Measurement of the $\gamma + {}^4$He Total Photoabsorption Cross-Section using a Gas-Scintillator Active Target

Ramsey Al Jebali

A thesis presented for the degree of
Doctor of Philosophy

Nuclear Physics Group
School of Physics and Astronomy
University of Glasgow
Scotland
June 2013

Abstract

A large number of experiments have been performed in the past 60 years in an attempt to understand the near threshold photodisintegration of ^{4}He. Available experimental data are inconsistent and do not provide reliable guidance for theoretical calculations for the total and partial cross-sections in the energy regime near breakup threshold. Even with the most recent experimental work done on the subject, the situation still has not been fully clarified.

This thesis reports a measurement of the total cross-section for photodisintegration of ^{4}He below π-production threshold, carried out in 2009 at the up-graded tagged photon facility at MAX-lab in Lund, Sweden, in collaboration with the Photonuclear group of Lund University. The aim of this measurement is to provide a reliable and precise set of data so that the accuracy of theoretical models can be judged reliably. The experiment was performed using a **H**elium **G**as-**S**cintillator **A**ctive **T**arget (HGSAT), built and developed at the University of Glasgow. The helium target acts also as a detector of the ^{4}He photodisintegration charged products. A photon beam, energy tagged in the range $\sim 11 - 68$ MeV, was directed towards the HGSAT, which operated at a pressure of 2 MPa, at room temperature. The resultant scintillation is collected and detected by a number of photomultiplier tubes (PMT) mounted on the HGSAT. 12 external neutron detectors and two 10" sodium iodide (NaI) detectors were used during the experiment to distinguish $^4\mathrm{He}(\gamma, n)^3\mathrm{He}$ and $^4\mathrm{He}(\gamma, \gamma')^4\mathrm{He}$ events, although these events have not been analysed here.

The tagged photon coincidence signal was separated from random background using two methods: background filtering and fitting procedure. The two methods produced similar results. A Geant4-based Monte-Carlo simulation was developed to derive the HGSAT detection efficiency. Trigger thresholds needed in the simulation were estimated by evaluation and matching the normalised yield to previously measured $\gamma + {}^4$He cross-sections above 40 MeV where more consistency in the dataset is observed, hence the results presented in this thesis are preliminary and will remain so until the absolute detection efficiency is determined.

The preliminary total $\gamma + {}^4$He cross-section obtained in this work peaks at $\sim$2.85 mb at a photon energy (E_γ) of $\sim$27 MeV, falling to $\sim$1 mb at $\mathrm{E}_\gamma = 60$ MeV. The measured cross-section is compared with previous data and recent theoretical calculations made using the **L**orentz **I**ntegral **T**ransform (LIT) technique. The present cross-section is already in reasonable agreement with the theoretical calculations and a number of previous experimental data. Future work to reduce systematic uncertainties will include analysis of the pulse height response of the HGSAT and further lower intensity experimental runs.

Declaration

The work in this thesis is based on research carried out within the Nuclear Physics Experimental Group, School of Physics and Astronomy, University of Glasgow, Scotland and with a collaboration of Lund University, Lund, Sweden. No part of this thesis has been submitted elsewhere for any other degree or qualification and it is all my own work unless referenced to the contrary in the text.

Contents

List of Figures

List of Tables

Chapter 1

Introduction

Nuclear reactions induced by energetic photons are known as *photonuclear* reactions. In such interactions, the electromagnetic field of the photon couples to the internal charges and currents of the nucleus of an atom in a process called *photoabsorption* leaving the nucleus in an excited state. If the energy of the incident photon is greater than the binding energy of the nucleus, the photoabsorption process may lead to the break-up of the nucleus into two or more fragments and the process in this case is referred to as *photodisintegration*. To characterise the probability of photons inducing such interactions, the term *cross-section* (σ) is used[1].

In this chapter, a brief overview on a number of topics will be given, without going into detail, to help provide better understanding of the motivation behind the work presented in this thesis.

1.1 Photonuclear Reactions

The first photodisintegration reaction was observed in 1934 by Chadwick and Goldhaber. They used the photodisintegration of the then newly discovered isotope, the deuteron, to demonstrate that the mass of a neutron is greater than that of a proton by obtaining the deuteron binding energy, knowing its mass and that of the proton. The significance of this work was that it was the first indication that a neutron is not a complex particle made of a proton and an electron as previously supposed but rather an elementary particle[2] [1]. The experiment of Chadwick and Goldhaber, which became the basis of all photonuclear studies, investigated the following reaction:

$$\gamma + D \rightarrow p + n \tag{1.1}$$

[1] Cross-section, as the name implies, is an area. It is the area that the nucleus effectively presents to the incident beam.

[2] Now we know that neutrons are not elementary particles but made up of three more fundamental particles called quarks.

The photon source used at that time was a naturally occurring 2.62 MeV gamma-ray produced from the decay of ^{228}Th[3]. The γ rays irradiated a deuterium filled ionisation chamber allowing the detection of the break-up protons. Only a few months after this experiment, Bethe and Peierls published the first theoretical calculation describing the photodisintegration of the deuteron (known then as the Diplon) [2]. Their calculated cross-section agreed qualitatively with the cross-section obtained from the experiment of Chadwick and Goldhaber. The work of these four people contributed enormously to the early understanding of nuclear structure and the nature of nucleon-nucleon (NN) interactions and indeed marked the beginning of photonuclear physics, highlighting its potential to illuminate nuclear structure.

Photonuclear reactions continue to provide an excellent means to investigate and understand the nuclear many body system. The well understood electromagnetic interaction with nuclear constituents is well suited to study nuclear structure. This is because the electromagnetic interaction is relatively weak making perturbative methods sufficiently accurate for theoretical calculations and ensuring that the entire volume of the nucleus is probed by the photon. As technology to produce energetic photons was developed, the field of photonuclear physics flourished and it continues to be important to this day.

Research in photonuclear physics is not only confined to fundamental physics, photonuclear cross-section data for instance are being used in various applications, ranging from radiation shielding design, safeguard applications and nuclear waste transmutation to astrophysical nucleosynthesis and high-energy γ ray therapy. These applications led to a major experimental effort to provide a reliable photoabsorption cross-section database for many nuclei. Most of these data are available in computerised libraries such as EXFOR[4] [3]. Despite these efforts, discrepancies in the magnitudes and energy dependencies of cross-sections are observed [4]. This was attributed in Ref. [4] to three factors: actual differences in photon spectra; absolute normalisation of cross sections; and calibration of photon energies. To deal with this issue, better experiments are needed. Using tagged photons removes much of the uncertainty in photon flux and photon energy.

A number of evaluation methods were developed by different research groups based generally on combining and assessing both available experimental data and theoretical models. Evaluated data are available in different libraries such as the IAEA[5] Photonuclear Data Library [5] and the Japanese Evaluated Nuclear Data Library (JENDL) [6]. These libraries provided a compromise solution for applications where photonuclear data are urgently needed, such as in radiation transport

[3]Thorium-228 used to be known as Radiothorium (Rd). There is no clear indication of when and why the name was exchanged in literature.

[4]Experimental nuclear reaction database referred to as EXFOR (**EX**change **FOR**mat).

[5]International Atomic Energy Agency.

and shielding. However the discrepancies observed in different measurements are of real concern to both theoretical and experimental nuclear physicists. This will be discussed further in Sec. 1.4.

1.2 The Description of Atomic Nuclei and the Force that Binds them Together

The Nucleon-Nucleon interaction refers to the force between two or more nucleons (protons and neutrons). It was the discovery of the neutron by James Chadwick in 1932 [7] that made scientists realise the existence of this new type of force that holds the nucleons together in the atomic nucleus. Understanding the nature of this force and the structure of nuclei remains at the centre of nuclear physics even today almost 80 years after its discovery. This is indeed a clear indication of the complexity associated with the topic considering the enormous and impressive efforts that have been made in the field since then.

Progress in understanding the nature of the nuclear force and nuclear structure has evolved in many directions. Before the discovery of quarks and the development of the field theory Quantum Chromodynamics Dynamics (QCD), which underlies the strong nucleon-nucleon interaction, the nucleons were treated as elementary particles and models of the force operating between them were based mostly on a phenomenological or a semi-phenomenological description. In the traditional approach, interactions between nucleons are described by a potential whose parameters are optimised from a fit to nucleon-nucleon scattering data. More recently, the form of the potential is based on a model and its parameters are fitted to experimental data. Potentials constructed in the latter manner generally employ the idea that the strong force arises from exchange of a π meson. Similar to Quantum Electrodynamics (QED), where the force between two electrically charged particles results from an exchange of photons, the forces between two nucleons are considered to result from an exchange of particles called mesons[6]. This theory was first suggested by Hideki Yukawa in 1934 [8] in an attempt to explain the nature of the nuclear force. In his theory, the force acting between two nucleons is described by the Yukawa potential, which takes the following form:

$$V_{Yukawa}(r) = g^2 \frac{e^{-m_\pi c r/\hbar}}{r} \tag{1.2}$$

where g is a coupling constant which has the same role as the charge in the case of electrostatics, m_π is the mass of the π-meson (pion), c the speed of light, $\hbar$ is the Dirac constant[7] and r is the radial distance between two nucleons. If the mass of

[6] From Greek word *mesos* which means intermediate since their masses were predicted to be between those of electrons and those of protons.

[7] $\hbar = h/2\pi$, where h is the Plank constant.

the exchanged particle is zero, the Yukawa potential is reduces to the well-known Coulomb potential:

$$V_c(r) = -g^2 \frac{1}{r} \tag{1.3}$$

Remarkably, Yukawa's theory predicted the existence and the mass of the pion a decade before it was experimentally discovered in 1947. Yukawa was awarded the Noble prize two years later and his pioneering work led to the development of a class of models, known as Boson Exchange Models (BEM) which are still used today to derive highly sophisticated nucleon-nucleon (NN) potentials [9].

Today, Quantum Chromodynamics (QCD) is thought to be the field theory which underlies the strong nucleon-nucleon force. Nucleons are not elementary particles, but instead are made up of 3 quarks[8]: 2 up plus 1 down quarks for a proton and 2 down plus 1 up quarks for a neutron. The force that keeps the quarks bound within a nucleon is due to exchange of massless gluons. While QCD provides a fundamental description of the short range structure of hadrons, a direct QCD derivation of the nuclear forces has proven to be a real challenge in theoretical physics, if at all possible. This is mainly due to the intrinsic non-perturbative character of QCD at low energy ($E \lesssim 1\,\mathrm{GeV}$) where the quark-gluon coupling is too strong for perturbative treatment.

Alternatively, other approaches have been followed to deal with the limitation of QCD in the low energy regime. Of these, lattice QCD [10] and Chiral perturbation theory (χPT) [11] show great promise. In the former approach, the space-time continuum is "discretised" into a four-dimensional lattice, three-dimensional space plus time, and the resulting equations describing the interactions of quarks and gluons are solved numerically on super computers using Monte-Carlo techniques. The advantage of this approach is that it preserves the fundamental character of QCD without the need for simplifying assumptions. However, solving QCD numerically requires enormous computational resources and there is still a long way to go before lattice QCD can provide a realistic description of nuclear forces equivalent in accuracy to models based on meson exchange [12].

The second approach, Chiral perturbation theory (χPT), is an effective field theory[9] derived from QCD. The degrees of freedom in this approach are hadrons rather than quarks and gluons which is similar in a way to Yukawa's meson theory mentioned earlier. However χPT goes a lot further by providing a direct connection to QCD respecting its known symmetries. The dynamics of hadrons are described by an effective Lagrangian formulated in terms of the effective degrees of freedom,

[8] Quarks were found to come in six different flavours: up, down, strange, charm, top and bottom. The names were made to differentiate between quarks of different properties.

[9] An effective theory is an approximation to a more fundamental parent theory which uses certain degrees of freedom sufficient to describe a physical phenomenon without necessarily being able to model any of the causes which led to that phenomenon.

with the pion as the central plank. Calculating the χPT coefficients directly from QCD is not yet possible, and thus the parameters are determined from fits to experimental data [13]. At present, methods of deriving the nuclear force from chiral Lagrangians are making good progress in predicting the nucleon-nucleon (NN) interaction at next-to-leading order (NLO) extending up to the four-nucleon (NNNN) interaction at the fourth order (N^3LO), (see [14] for more details).

To summarise, the nucleon-nucleon force can be described effectively by potentials derived phenomenologically, based on Boson Exchange Models (BEM). Although potentials derived in this manner do succeed in describing the nuclear force with a good fit to NN data below pion production threshold, they provide no connection to the underlying fundamental theory, QCD. Potentials derived using χPT, do provide a link to QCD and are now employed in quantitative calculations of nuclear structure. Lattice QCD on the other hand is a promising approach to solve the equations of QCD numerically but still more effort is needed until it can provide a description of the nucleon-nucleon interaction comparable to the approaches mentioned earlier.

1.3 Photoabsorption Cross-Sections Below π Threshold

Photonuclear reaction observables are sensitive to the details of nuclear structure and thus provide an exacting test of models if the experiment is sufficiently accurate. Photoabsorption cross-sections are photon energy dependent and exhibit common features among all nuclei. Cross-sections below ~140 MeV photon energy (E_γ), the π-production threshold, are dominated by two excitation mechanisms: the so-called Giant Dipole Resonance (GDR) ($E_\gamma < 40$ MeV) and Quasi-Deuteron (QD) mechanisms (40 MeV $< E_\gamma <$ 140 MeV), which occur in the photon energy regions illustrated in Fig. 1.1.

The Giant Dipole Resonance (GDR) is a collective excitation mode of the nucleus resulting mainly from the electric dipole (E1) absorption of photons by the nucleus. The giant dipole resonance is one of a series of possible collective excitations. These are classified according to their quantum numbers: orbital momentum (ΔL), intrinsic spin (ΔS) and isospin (ΔT). The GDR has ($\Delta L = 1$, $\Delta S = 0$, $\Delta T = 1$) and hence is referred to as an Isovector Giant Dipole Resonance (IVGDR). Isovector means that the protons and neutrons oscillate out of phase. In almost all nuclei, the GDR region appears as a broad peak dominating the photoabsorption cross-section from reaction threshold up to ~40 MeV. The shape, amplitude and location of the peak in the GDR region depend on the type of absorbing nucleus. It is found to be centred between about 25 MeV for the lightest nuclei and about 13 MeV for the heaviest nuclei, and its shape can be approximated empirically by a

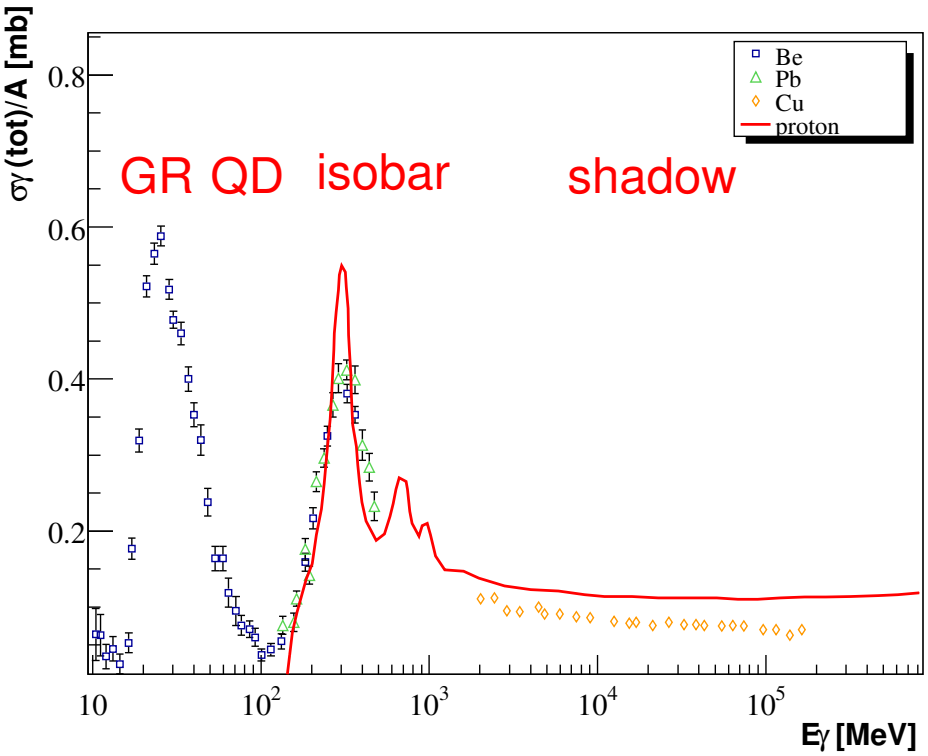

Figure 1.1: An illustration of the photoabsorption cross-section per nucleon as function of photon energy E_γ. The figure shows: the Giant Dipole Resonance (GDR) region (few MeV up to ∼40 MeV), the Quasi-Deuteron ($\sim 40-140$ MeV) and isobar and shadow regions at higher photon energies [15].

Lorentzian [16]:

$$\sigma_{abs}(E_\gamma) = \frac{\sigma_0 {E_\gamma}^2 \Gamma^2}{({E_\gamma}^2 - {E_i}^2) + {E_\gamma}^2 \Gamma^2} \tag{1.4}$$

where σ_{abs} is the photoabsorption cross-section, σ_0 is the peak cross-section in the GDR region, Γ is the width of the peak in the GDR region and $\mathrm{E_i}$ is the resonance energy. The incident photon wavelength in the GDR region is of the same order as the nuclear diameter so the photon is considered to interact with a nucleus as a whole. The phenomenon has been studied intensively [16][17][18] and several theoretical models have been proposed to describe the GDR macroscopically and microscopically. The first macroscopic description of the GDR, the Hydrodynamical model, was put forward by Goldhaber and Teller in 1948 [19]. The model was modified 2 years later by Steinwedel and Jensen [20] to overcome an issue with the GDR frequency prediction by Goldhaber and Teller model [21]. In the Hydrodynamical model, the nucleus is considered to be an ideal liquid drop, consisting of two components, protons and neutrons. In the original Goldhaber and Teller model, non-deformed proton and neutron spheres were assumed to oscillate with opposite phases, isospin $\Delta \mathrm{T} = 1$, keeping the nucleus centre of mass stationary. The restor-

ing force is proportional to the change in nuclear surface area and the resonant frequency $\omega \propto A^{-1/6}$ [18], where A is the atomic mass number. In the modification by Steinwedel and Jensen, both protons and neutrons are considered as compressible droplets which oscillate out of phase inside a sphere with a fixed surface. The restoring force is given by the volume symmetry energy and the frequency varies as $A^{-1/3}$. This prediction was not consistent with the experiential data [22]. The first microscopic description of the IVGDR was suggested by Bohm and Pines [23] in 1952. The so-called Random Phase Approximation (RPA) model, proved to be more successful in matching experimental data. In the RPA, nuclear excitations are considered as a coherent superposition of particle-hole vibrational states with respect to the ground state in closed shell nuclei, or two quasi-particle excitations in open shell nuclei. The model is based on a time-dependent Hartree-Fock approximation of the ground state and it is the simplest microscopic approach that includes correlation corrections. Self-consistent RPA calculations start from the nuclear ground state wave-function. The energy is determined by Hartree-Fock and relevant equations are solved to derive physical quantities that describe the giant resonances, such as transition strengths and amplitudes [22]. A comprehensive description of the RPA approach is presented in Ref. [24].

The Quasi-Deuteron (QD) region starts at about 40 MeV photon energy and extends up to the pion production threshold at 140 MeV, as illustrated in Fig. 1.1. The photoabsorption cross-section in this region shows a structureless steady decrease as photon energy increases. The excitation mechanism is different to that of the GDR region since the incident photon wavelength is smaller than the nucleus. This is known as the Quasi-Deuteron (QD) mechanism where the photon is considered to interact with a pair of nucleons within the nucleus, most probably proton-neutron pairs as proposed by Levinger in his Quasi-Deuteron (QD) model [25][26]. Photon absorption by nucleon pairs helps to remove a potential momentum mismatch between an incident photon and outgoing nucleon. In the QD model, the nuclear photoabsorption cross-section $\sigma_{\mathrm{qd}}(\mathrm{E}_\gamma)$ is described phenomenologically in terms of the deuteron photoabsorption cross-section [15]:

$$\sigma_{qd}(E_\gamma) = \frac{L}{A} N Z \sigma_d(E_\gamma) \tag{1.5}$$

where L is the so-called Levinger constant, N , Z and A are the neutron, proton and atomic mass numbers respectively and σ_d is the photodisintiegration cross-section for the deuteron. The Levinger constant is a parameter that gives the probability of two nucleons being close to each other in a complex nucleus compared with that in a deuteron. This parameter can either be estimated theoretically [25] or from fits to data. With the success of the QD model, Gottfried [27] developed the model into a more microscopic form to derive, the angular correlation of the emitted pair and differential cross-sections of protons and neutrons, in addition to the total photoabsorption cross-section as in Levinger's original theory. The cross-section takes the following form:

$$d\sigma = (2\pi)^{-4} F(P) S_{fi} \delta(E_f - E_i) d^3k_1 d^3k_2 \tag{1.6}$$

where the first term is for the available phase space, F(P) is the probability of finding a correlated two nucleon pair with a total momentum P = $\mid k_1 + k_2 - \omega \mid$ where k_1 and k_2 are the momenta of the emitted nucleons and ω is the photon momentum. S_{fi} is the transition matrix which contains all the information of the reaction dynamics. E_f and E_i are given by $\omega - B_t$ and $\epsilon_1 + \epsilon_2 + E_s - B_r + \epsilon_r$ respectively, where B_t, B_r are the ground state binding energies of the target and residual nuclei respectively, ϵ_1, ϵ_2 and ϵ_r are the kinetic energies of the two photonucleons and the residual system, E_s is the excitation energy [27]. Gottfried assumed that the terms in Eq. 1.6 could be factorised, but subsequent work by Ryckebusch at al. [28] showed that this approximation may induce some error.

1.3.1 ^{4}He Photodisintegration Reaction Channels

Absorption of energetic photons by an atomic nucleus leaves it in an excited state which decays into one of the possible reaction channels. There are five different reaction channels involved in the photodisintegration of ^{4}He below the π production threshold[10]. These are, according to their production threshold order, two-body break-up (γ, p), (γ, n) and (γ, d), three-body break-up $(\gamma, pd)n$ and finally four-body break-up $(\gamma, 2p)2n$. The photoabsorption cross-section for each reaction channel has a different photon energy dependence. The reaction threshold energies are determined by the mass difference between the break-up products and the parent nucleus ^{4}He, see Sec. 4.4.1. It is obvious that any total photoabsorption measurement must account for all of these reaction channels simultaneously. The photoabsorption cross-section of ^{4}He in the GDR region is dominated by the (γ, p) and (γ, n) channels, which have approximately equal strength. Above ∼40 MeV, contributions from three-body and four-body break-up become significant. Many experiments on ^{4}He photodisintegration concentrated on detailed comparison of (γ, p) and (γ, n) with a view to investigating the charge symmetry (CS) of the nuclear force, (see Ref. [29]). This yielded to a relatively large dataset on two-body breakup reactions but rather fewer concerned the total photoabsorption cross-section which is more difficult to measure. Today however, the situation is very different with the increased interest in the total ^{4}He cross-section due to the current advances in the theoretical techniques allowing full microscopic calculations on the ^{4}He system to be performed. This will be discussed further in the next section.

1.4 ^{4}He Total Photoabsorption Cross Section Theory and Experiment

^{4}He is the second most abundant isotope in the universe. Its nucleus consists of 2 protons and 2 neutrons with a notably high binding energy of 7.1 MeV/nucleon due

[10] There is also a single non-breakup channel, Compton scattering ^{4}He$(\gamma, \gamma')^4$He whose cross-section is much lower than the break-up channels.

to the saturation of the nuclear force [11]. This last feature is of real interest and makes ^{4}He unique in the sense that it is a few-body nucleus, which has much in common with more complex nuclei. Therefore, it may be considered as a bridgehead from which to commence microscopic calculations on more complex nuclear systems with A>4. With recent advances in theoretical techniques such as the Lorentz Integral Transform (LIT) method [31], *Ab initio* microscopic calculations of the ^{4}He system are possible for given NN and NNN potentials. Such calculations are extremely important in the fundamental understanding of the nuclear many-body system. More practically, these calculations can be used to derive experimental observables such as the binding energy or cross-sections against which the model may be tested.

The ^{4}He photodisintegration cross-section has a long and continuing history of controversy, from both an experimental and theoretical point of view, despite the fact that the first measurement of this kind was reported over 60 years ago [32]. The heart of the dilemma lies in the location and the size of the peak in the GDR region in both inclusive γ+^{4}He and exclusive (γ, p) and (γ, n) cross-sections. Previous theoretical calculations (see [33][34][29][35] and references therein) showed contradictory results, with some showing a pronounced peak in the exclusive (γ, n)[12] cross-section while others showed a flattened distribution. However, the theoretical situation appears to be getting closer to a settlement. *Ab initio* calculations are now capable of handling realistic Argonne V18 (AV18) NN[36] plus the Urbana IX (UIX) NNN [37] potentials [38] and calculations based on NN plus NNN potentials derived from χPT theory [14] have more recently been published. The experimental situation, on the other hand, seems to suffer from "chronic" inconsistency. The available dataset shows a large spread in values. Even with the most recent ^{4}He(γ, n) measurements [39] and [35], the situation still has not been clarified. While Nilsson et al. [39] correspond closely with recent theoretical calculations and a new measurement of HIgS[13] [40], Shima et al. [35] on the other hand showed a disparity with any theoretical or experimental results (see Fig. 1.5). This situation is confusing to theorists who are waiting to test their current calculations.

In the following, a short description of theoretical methods will be given along with a brief overview of the most recent measurements on the topic.

[11] The term "saturated" is given to the nuclear systems where the remainder of the binding energy that hold the nucleons within the nucleus is used to bind clusters of α-particles, 2 protons and 2 neutrons. It is believed that nuclei favour this structure, *α-clusters* within the nucleus, especially in nuclei $<^{16}$O [30].

[12] Which is half the total photoabsorption cross-section in the GDR region.

[13] High Intensity Gamma-Ray Source.

1.4.1 Current Theoretical Status

Ab initio[14] calculations are a major step forward in nuclear physics. Initially they have concentrated on few nucleon systems (A⩽7), but now are spreading to more complex systems. The important step for reaction calculations came with the introduction of the Lorentz Integral Transform (LIT) method in 1994 by Efros et al. [31][41]. With the LIT approach one avoids all difficulties associated with a continuum calculation and basically transforms the difficult continuum problem into a solvable bound-state like problem. This method has been used recently to calculate the γ+^{4}He total cross-section from break-up threshold up to pion production threshold. The total photoabsorption cross-section equation may be given by[15]:

$$\sigma_{tot} = 4\pi^2(e^2/hc)E_\gamma R(E_\gamma) \tag{1.7}$$

where the response function R(E_γ) depends on the ground state and final state wavefunctions Ψ_0,Ψ_f and is defined as follows:

$$R(E_\gamma) = \int df |\langle \Psi_f | D_z | \Psi_0 \rangle|^2 \delta(E_f - E_0 - E_\gamma) \tag{1.8}$$

where $D_z = \sum_{i=1}^{A}(\tau_i^3 z_i^{'})/2$, τ_i^3 and $z_i^{'}$ are the third components of the ith nucleon isospin and centre of mass frame position [38]. E_0 and E_f are the energies of the ground and final states respectively. Direct solution of this equation for the four-body system is only possible below 3-body breakup threshold and as Efros [31] stated, "The difficulty is related to the fact that in these cases a great number of continuum spectrum states Ψ_f contribute to R(E_γ) and the structure of these states is very complicated.". Here the LIT method comes into play as it allows calculation of the response function R(E_γ) by evaluation and the inversion of its Lorentz integral transform:

$$L(\sigma_R, \sigma_1) = \int dE_\gamma \frac{R(E_\gamma)}{(E_\gamma - \sigma_R)^2 + {\sigma_1}^2} = \left\langle \tilde{\Psi} | \tilde{\Psi} \right\rangle \tag{1.9}$$

where $\tilde{\Psi}$ is the localised solution of the Schrödinger-like equation:

$$(H - E_0 - \sigma_R + i\sigma_1)|\tilde{\Psi}\rangle = D_z|\Psi_0\rangle \tag{1.10}$$

where H is the Hamiltonian of the system. With Eq. 1.10 one avoids solving the difficult continuum-state-problem and is faced instead with a bound-state-like problem whose solution is possible using an appropriate method such as the so-called Effective Interaction Hyperspherical Harmonic (EIHH) approach [43] or the No Core Shell Model (NCSM) approach [44]. Once the solution becomes available, the total

[14] "*Ab initio*" according to Merriam-Webster.com. 2013. http://www.merriam-webster.com (13 Feb. 2013) is a Latin word for *from the beginning*. When coined with calculations in science the term implies that the calculation was performed from first principles with no additional assumptions.

[15] A "straightforward" derivation of this equation can be found in [42].

cross-section σ_{tot} can then be calculated directly using Eq. 1.7. The most advantageous feature of the LIT method is that it only requires a model of the nuclear potential and an operator of the electric dipole transition as an input for an *ab initio* calculation to be performed. A comprehensive review on the LIT method is provided in Ref. [31] therefore no further detail will be given here.

Over the years there have been a variety of theoretical attempts to describe the photodisintegration of ^{4}He, both inclusive and exclusive reactions. Two of the most recent are the calculations made by Gazit et al. using the EIHH approach with realistic potentials AV18+UIX [38] and those done by Quaglioni et al. using the NCSM approach and NN+NNN potentials derived from χPT theory [14]. The two calculations include the three-body force effect NNN. While NN potentials describe the dominant nuclear binding effect, they clearly fail on their own to reproduce the binding energies of light nuclei. With the AV18 NN potential for example, the binding energy of ^{4}He was calculated to be 24.25 MeV [45] which is noticeably lower than the experimental value of 28.30 MeV. Including the UIX NNN potential leads to a more accurate value of 28.5 MeV [45].

Gazit et al. Calculation

The Gazit et al. calculation of the total photoabsorption cross-section of ^{4}He [38] is the first of its kind to utilise realistic nucleon-nucleon potentials. In this calculation, the four-body system is solved taking the NN AV18 and the UIX NNN potentials. The continuum-state problem is reduced to a bound-state-like problem using the LIT method which is then solved using expansion in hyperspherical harmonics (HH) using the Effective Interaction HH (EIHH) approach. The computed total photoabsorption cross-section (σ_{tot}) with and without the three-body force effect NNN, is shown in Fig. 1.2. A previous calculation using the semi-realistic Malfliet-Tjon (MT) NN potential [46][47] is also shown for comparison. One can clearly see the effect of including the three-body force effect in the calculation: a decrease in the cross-section peak height by about 6% and a shift in the peak position by about 1 MeV, in addition to a significant increase in the cross-section beyond ~50 MeV. As Gazit pointed out, this is rather surprising if one is to compare this with the effect of NNN in the lighter nuclei ^{3}H and ^{3}He where including the NNN effect reduces the peak amplitude by ~10%. A larger NNN effect would be expected in ^{4}He and indeed NNN has a 17% effect on the ^{4}He binding energy, compared to ~10% for ^{3}H and ^{4}He. This is not yet fully understood.

Quaglioni et al. Calculation

Quaglioni et al. [14] used a slightly different approach in their γ+^{4}He total cross-section calculations. The many-body wave function is derived from potentials based on Chiral effective field theory χEFT and is solved in the framework of the No Core Shell Model (NCSM) approach. Fig. 1.3 shows the results of Quaglioni et al. for the

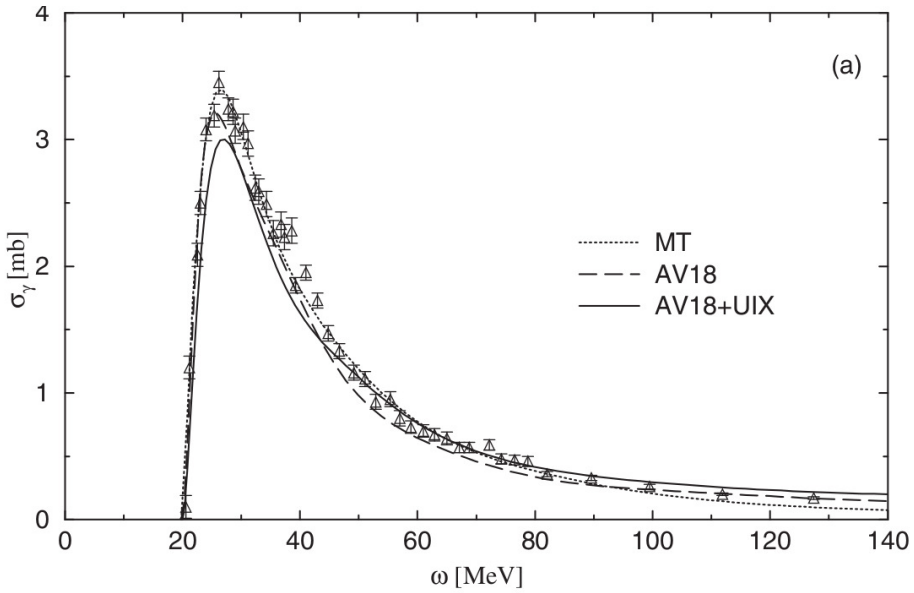

Figure 1.2: The total photoabsorption cross-section of ^{4}He as calculated by Gazit et al. [38] using: realistic NN potential AV18, realistic NN AV18+NNN UIX potentials and finally a former calculation using the semi-realistic Malfliet-Tjon (MT) NN potential. The triangles are experimental data from Arkatov et al. [48].

total γ+^{4}He cross-section with and without the thee-body force effect. The figure also includes the calculations of Gazit et al. for comparison. In the χEFT/NCSM

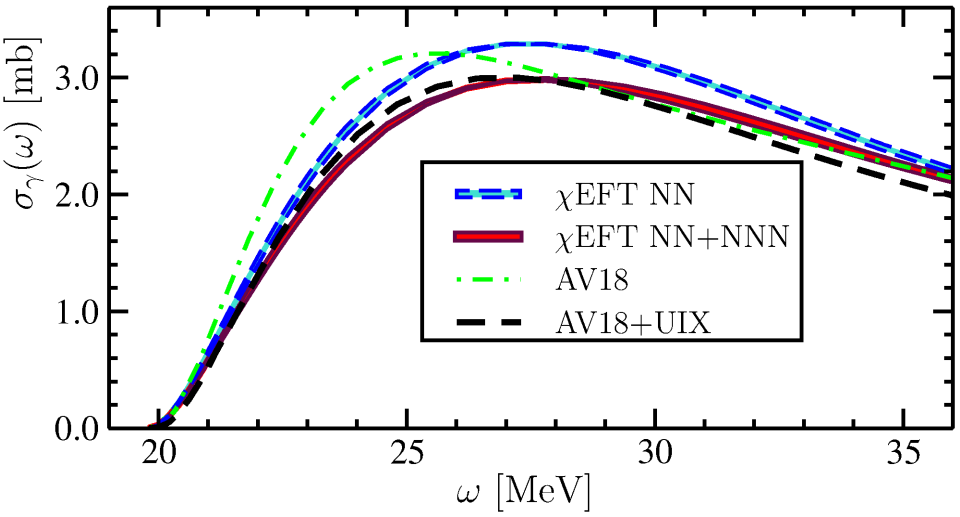

Figure 1.3: The computed total photoabsorption cross-section (σ_{tot}) of ^{4}He by Gazit et al.,with and without the three-body force effect NNN (AV18 and AV18+UIX respectively), in comparison with that of Quaglioni et al. also with and without NNN effect (χEFT NN and χEFT NN+NNN respectively) [14].

calculation NNN reduces the peak height in the GDR region by about 9%, but the

peak position is not shifted significantly. In the EIHH calculation NNN reduces the peak in the GDR region by ∼6% and shifts the peak position upwards by >1 MeV. The overall similarity between the two calculations is still remarkable considering the different approaches used to reach these results.

1.4.2 Previous Measurements

Measurement of the photodisintegration of ^{4}He spans over 60 years. Early experiments concentrated on the exclusive (γ, p) and (γ, n) reactions partially in an attempt to verify the charge symmetry (CS) of the nuclear force. However, significant discrepancies between different experimental datasets has been observed, particularly in the GDR region (see Ref. [29]). The situation led Calarco et al. [34] to review all existing (γ, p) and (γ, n) datasets available prior to 1983 and come up with recommended cross-sections for both reactions based on their selection of experiments which they considered to be most reliable. The Calarco et al. recommendation is shown in Fig. 1.4.

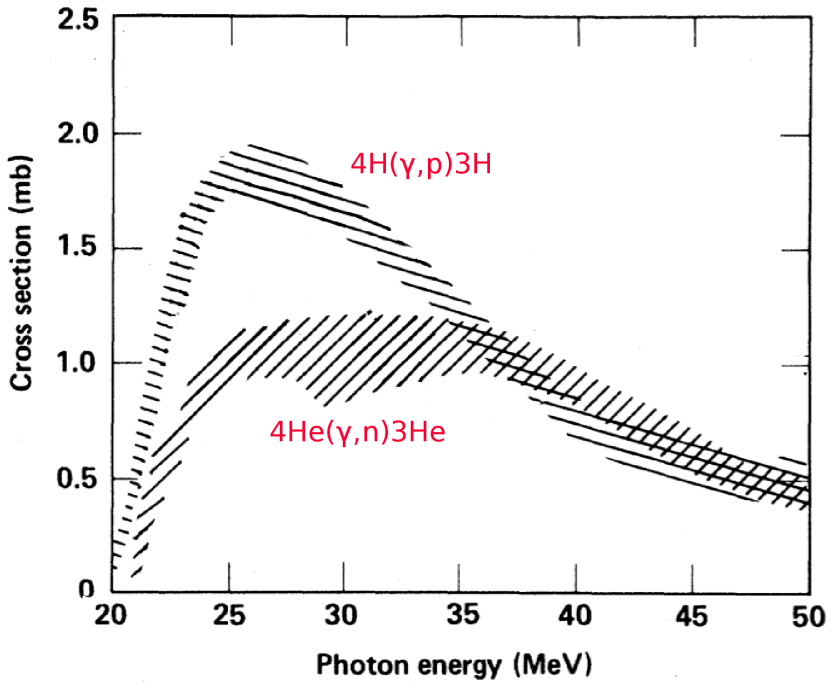

Figure 1.4: Recommended ^{4}He$(\gamma, p)^3$H and ^{4}He$(\gamma, ^3$He$)n$ cross-sections by Calarco et al. [34].

The Calarco et al. review was received with mixed reactions since it supported the hypothesis of the charge symmetry breaking (CSB) in the GDR region. As a consequence several theoretical attempts were made to reproduce these findings without much success. This situation stimulated further experimental activities in the late 80's and early 90's which yielded three measurements of the ^{4}He$(\gamma, p)d$ cross-section: Bernabei et al. in 1988 [49], Feldman et al. in 1990 [50] and Hoorebeke

et al. in 1993 [51] and one measurement on the $^4\mathrm{He}(\gamma,{}^3\mathrm{He})n$ cross-section: Komar et al. in 1993 [52]. Of these measurements, two $^4\mathrm{He}(\gamma,p)d$ datasets, Bernabei et al. [49] and Feldman [50], disagreed with Calarco et al. showing rather a flat peak at ∼1.3 mb while the $^4\mathrm{He}(\gamma,p)d$ measurement by Hoorebeke et al. [51] showed a pronounced peak, agreeing with Calarco et al. The $^4\mathrm{He}(\gamma,{}^3\mathrm{He})n$ measurement by Komar et al. [52] showed a flattened distribution, also agreeing with Calarco et al. An additional measurement came from a Compton scattering experiment on ^{4}He by Wells et al. in 1992 [53]. The forward Compton cross-section can be related to the total cross-section via the Optical Theorem and the inferred total $\gamma + {}^4\mathrm{He}$ total cross-section showed a pronounced peak at 2.86 mb in the GDR region which agreed with the recommended cross-section sum $(\gamma,n)+(\gamma,p)$ of Calarco et al.. This puzzling situation motivated the $^4\mathrm{He}(\gamma,n)^3\mathrm{He}$ cross-section measurement preformed by Nilsson et al. and the results were published in 2005 [39]. These results suggest that the (γ,p) and (γ,n) cross-sections are very similar, implying that charge symmetry is respected. During the same year interesting results on the $^4\mathrm{He}(\gamma,p)^3\mathrm{H}$, $^4\mathrm{He}(\gamma,{}^3\mathrm{He})n$ and the total ^{4}He photoabsorption cross-sections were published by Shima et al. [35]. While Nilsson et al. appears to be in an overall good agreement with the most recent theoretical calculations mentioned in the previous section, the Shima et al. measurement on the other hand shows a complete disagreement. The unexpected results of the Shima at al. measurement led to another wave of experimental activities to verify the situation: Nakayama et al. [54] published in 2007, Raut et al. [55] and Tornow et al. [40] both published in 2012. The former measurement was conducted before the experiment reported in this thesis was carried out, while the last two were published after. The most recent measurements are displayed in Fig. 1.5 along with some older data and the sum of the recommended $\sigma(\gamma,n)$ and $\sigma(\gamma,p)$ cross-sections of Calarco et al. [34]. Since most previous data focused on the exclusive $^4\mathrm{He}(\gamma,p)d$ and $^4\mathrm{He}(\gamma,{}^3\mathrm{He})n$ cross-sections, exclusive cross-sections have been simply multiplied by factor of 2 with the assumption that charge-symmetry is not violated. As can be seen in the figure, none of the most recent measurements reproduced the results of Shima al el.. The measurement of Nakayama et al. [54] is in a rough agreement with $\sigma(\gamma,n)$ from Nilsson et al. and the recommended cross-section sum of Calarco et al. while $\sigma(\gamma,p)$ from Raut et al. [55] and $\sigma(\gamma,n)$ from Tornow et al. [40] deviate from the Carlo et al. recommendation, showing a sharp peak of ∼3.5 mb at 26.5 MeV photon energy. This is ∼15% higher than the recent theoretical predictions which include the three-body NNN effects, see Sec. 1.4.1. For a summary of previous data, refer to Nilsson et al. [29]. A short summary on the most recent measurements is given below.

Nilsson et al. 2005

The Nilsson et al. $^4\mathrm{He}(\gamma,n)^3\mathrm{He}$ cross-section measurement [29][39][58] was carried out at the pre-upgrade MAX-lab tagged photon facility in a collaboration of the University of Glasgow and Lund University in 1995. A quasi-monochromatic photon beam was generated by means of bremsstrahlung radiation in the energy range (E_γ) of $23-42$ MeV. The photon beam was directed toward a liquid ^{4}He target stored

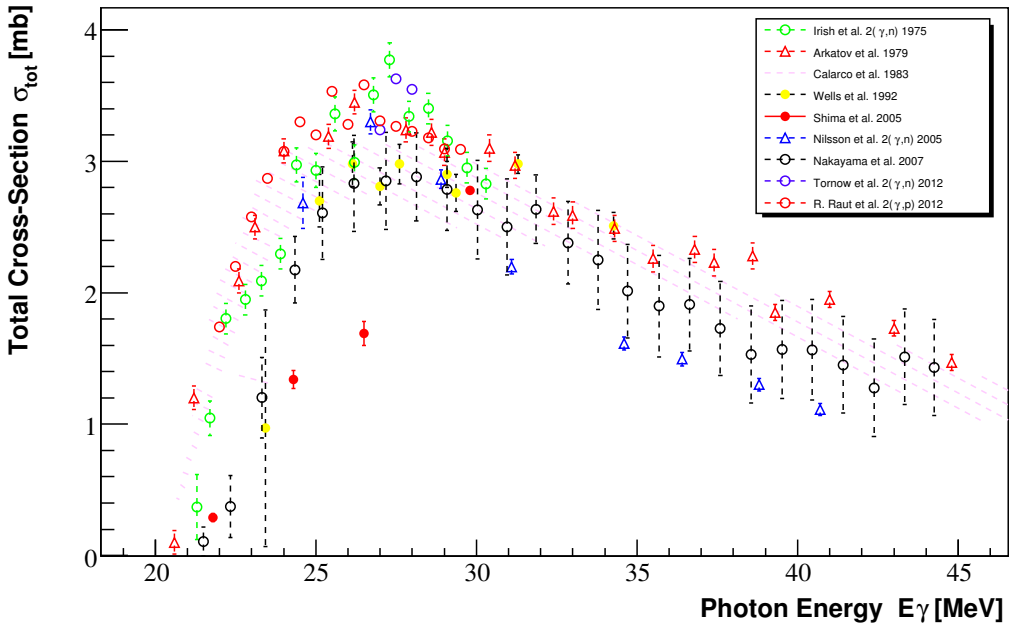

Figure 1.5: Previous experimental data: Irish (1975)[56], Arkatov (1979)[48], Wells (1992)[53], Shima (2005)[35], Nilsson (2005)[39] Nakayama (2007)[54], Tornow (2012)[40] and Raut (2012)[55]. The dashed region is the sum of the recommended (γ, p) and (γ, n) based on an evaluation of the dataset made by Calarco at el. in 1983. All of the experimental data are retrieved from the EXFOR online library [57].

in a cylindrical 90 mm diameter×75 mm height container. Neutrons were detected via two 3×3 arrays of 20×20×10 cm liquid scintillators placed 2.6 m away from the target at 60° and 120° with respect to the photon beam. Coincidences between the tagger focal plane hodoscope and neutron detectors were used to determine the photon beam energy (photon tagging) and neutrons were identified via time of flight and pulse shape discrimination (PSD).

Shima et al. 2005

The measurement of Shima et al. [35] was conducted using a pulsed-Laser Compton backscattering (LCS) photon beam at the National Institute of Advanced Industrial Science and Technology (AIST) in Japan. Two and three-body photodisintegration cross-sections were measured using the active target concept. Charged break-up products were detected using a near-4π time projection chamber filled with ^{4}He. The time projection chamber has a drift area of 60×60×250 mm and determines track and times using multiwire proportional counter (MWPC). The gas target was 80% natural helium and 20% methane pressurised at ∼133 kPa. γ+^{4}He charged break-up products ionise the gas and the resultant electrons drift toward the MWPC. Signals generated by the electrons arriving at the MWPC are collected by the cathode/anode wires which provide information on the charged particle $x-y$

position. The z position is determined from the drift time of the electrons recorded via a time-to-digital converter (TDC). Photodisintegration charged particles were identified from tracking information and reaction kinematics. Shima et al. checked the apparatus by measuring the well-studied photodisintegration of the deuteron at 22.3 MeV photon energy. The measured deuteron cross-section of 0.56 mb agrees with previous experimental data. Nonetheless their ^{4}He data has a radically different form to all other measurements.

Nakayama et al. 2007

Nakayama et al. employed an alternative approach in their ^{4}He total photodisintegration measurements [54]. They used ^{4}He(^{7}Li,^{7}Be) reaction[16] observables to derive the total photodisintegration cross-section of ^{4}He. The measurement was carried out at the Research Centre for Nuclear Physics (RCNP) at Osaka university in Japan using a 455 MeV $^3Li^{3+}$ beam bombarding a ^{4}He gas target cooled to ∼10K. The gas target is pressurised at ∼150 kPa and has a thickness of 7 mg/cm^2 contained in a cell equipped with two Aramid $(C_{14}O_2N_2H_10)_n$ beam entrance/exit windows. The scattered ^{7}Be particles were momentum analysed using a magnetic spectrometer placed at 0° and 3° and were detected, with and without coincidence with the 0.43 MeV γ from decay of the ^{7}Be excited state using two multiwire drift chambers backed by a ΔE/E plastic scintillator telescope. The 0.43 MeV γ was detected via 18 Gd_2SiO_5(Ce) (GSO) scintillator detectors. Scattered ^{7}Be particles are produced either in the ground ($^7Be_0$) or in the first excited state (0.43 MeV $^7Be_1$). The ground state is produced by both ΔS=0 and ΔS=1 transfer while the first excited state only proceeds via ΔS=1 transfer. Using this information, Nakayama et al. deduced the ΔS=0 spectrum over a wide range of excitation energy by subtracting the spectra obtained from the scattered $^7Be_1$ and $^7Be_0$. The ΔL=1 transfer is confirmed by measuring the angular distribution at forward scattering angles. The ΔS=0 spectrum with ΔL=1 reflects the photodisintegration cross-section. The obtained cross-section was normalised to previous cross-section measurements at a photon energy of ∼40 MeV, where existing photodisintegration data appear to agree well with each other.

Raut et al. 2012

Raut et al. measured the ^{4}He$(\gamma, p)^3$H cross-section using Laser Compton backscattering (LCS) photons at energies between $22 - 30$ MeV [55]. The measurement took place at the High-Intensity Gamma-ray Source (HIgS) at Duke University in the USA. The detection was performed using the active target concept where the target is also a detector for the reaction break-up products. The target consisted of ^{4}He+Xe gas pressurised at ∼5 MPa and contained in a stainless steel vessel 5.1 cm in diameter with 1 mm wall thickness. The inner structure of the gas vessel was coated with a white reflector (MgO) and was viewed by a single PMT via a Pyrex

[16] This type of reaction is referred to as charge-exchange spin-flip (CESF) reaction.

window. Charged photodisintegration products were detected via scintillation. The ^{4}He$(\gamma, p)^3$H channel was identified from the energy deposited in the reaction for the given incident photon energy. Xenon gas was added at various ratios ranging from 7 to 47% depending on the incident photon energy, to increase the target stopping power for protons. The photon energy was determined using a calibrated NaI detector. Background effects were evaluated using an identical gas cell filled with pure xenon pressurised to the xenon partial pressure used in the gas mix during the experiment.

Tornow et al. 2012

The Tornow et al. measurement of the ^{4}He$(\gamma, ^3$He$)n$ cross-section [40] was conducted at the HIgS facility using the same experimental method and apparatus but with a minor optimisation to the ratio of gas mix. This overcame an issue with pulses generated by electrons, produced via Compton scattering of the incident photon at low energy overlapping with the small pulses generated by the recoiled ^{3}He ions. The optimisation was done by minimising the stopping power for charged particles by reducing the Xe content. However this made it difficult to measure the ^{4}He$(\gamma, p)^3$H cross-section simultaneously since the produced protons end up depositing only a fraction of their energy within the gas volume. The total pressure of the ^{4}He+Xe mixture was ∼4.9 MPa and contained 5.5% Xe. The ^{4}He$(\gamma, ^3$He$)n$ cross-section was measured at four photon energies 27, 27.5 and 28.5 MeV.

1.5 Motivation of this work

The theoretical importance of ^{4}He and the inconsistency in the experimental datasets on the inclusive and exclusive photoabsorption cross-section on ^{4}He inspired J. R. M. Annand and collaborators of the Universities of Glasgow and Lund to propose a series of high-precision measurements to clarify the situation in the early 1990's. The program began in 1995 with the first-generation experiment to measure the ^{4}He$(\gamma, n)^3$He cross-section at MAX-lab in Lund. This was published by Nilsson et al. [29][39] [58].

The measurement presented in this thesis is the second-generation of these investigations which aim to provide a direct precise measurement of the total ^{4}He photoabsorption cross-section from the break-up threshold to the π-production threshold with the hope of resolving and settling some of the inconsistencies in the existing dataset and making recommendations for future theoretical effort. The measurement was taken using the Active Target technique in 2009 at the MAX-lab tagging photon facility in Lund/Sweden in collaboration with the photonuclear group at Lund University.

Chapter 2

Helium Gas-Scintillator Active Target

The total $\gamma + {}^4\text{He}$ cross-section measurement reported in this thesis was performed using the active target technique, where the gaseous ^{4}He target was also used as the detection medium for photodisintegration products. The development along with the design and construction of the helium gas-scintillator active target was done at the University of Glasgow exclusively for this measurement. This chapter covers in some detail all of the development and construction aspects in addition to the underlying principle of operation and starts with a brief introduction and necessary background for the subject.

2.1 Introductory Background

Scintillation, in its simplest definition, is a flash of light emitted from certain materials when struck by energetic particles. The materials that exhibit scintillation are simply called *scintillators*. The scintillation phenomenon has been used extensively in detection of particles since its discovery more than a hundred years ago and to this day is still one of the most popular methods of particle detection in both nuclear and particle physics. In the early years of using this method, the light emitted from a scintillator was observed by the human eye through a microscope[1]. Birks [61, page. 4] mentioned a quaint story of how a famous laboratory of the time tested research students by placing them in a dark room to accurately count scintillations before they were accepted for nuclear research. At that stage, the method was unpopular for its awkwardness and usage difficulties [61], especially after the development of gas ionisation detectors in the 1930s despite the success of a series of experiments using scintillators performed by some of the brightest physicists of the twentieth century. It was only after the development of photomultiplier tubes in the

[1] The Spinthariscope (from *Spinthiras* Greek word for spark) invented by W. Crookes in 1903 [59] was the first known device to use this technique. It consisted of a zinc sulphide scintillator screen and a microscope. The device eventually ended up as an educational toy for children in the 1950s [60].

early 1940s that the full potential of using the scintillation phenomenon for particle detection was realised when Curran and Baker used a photomultiplier tube instead of the human eye in the Spinthariscope to detect 2 MeV α particles in 1944 [62]. Soon after the success of the Curran and Baker experiment interest in scintillation detectors grew rapidly and a chain of discoveries of new scintillation materials and enhancements to photomultiplier tubes ensued. By the mid 1950s scintillation detectors became common and reliable devices for detection of elementary particles.

Currently, there are several types of scintillators available with varied scintillation properties (scintillation yield, rise time, energy resolution, etc.), physical state (solid, liquid, gas or solid solutions) or chemical composition (organic or inorganic). However, there is no "official"classification of these scintillators since their properties often intersect and are not clearly separated. Probably the most practical classification to use is the one based on the scintillation mechanism which divides scintillators into three main categories: organic, inorganic and gas scintillators. The selection of a particular scintillator is highly influenced by the user requirements and the application type and it is a matter of compromising between these and the scintillator properties since it is usually not possible to obtain all desired features in a single scintillator.

2.1.1 Noble-Gas Scintillator Detectors (NGSD)

Research in using gas-scintillators for detection of charged particles began soon after Grün and Schopper developed the first gas scintillation detector in 1951 [61][2]. It essentially consisted of a gas cell viewed by a single photomultiplier tube (PMT) through a quartz window via a Plexiglas light guide. Since then scintillations of different gases and gas mixtures were investigated by several researchers, although most of the research efforts were quickly directed toward noble-gas[3] scintillators because of their excellent scintillation properties and potential applications with xenon and helium receiving most attention. Partly because of their exceptional fast rise time [61][62][67] early utilisation of these detectors was focused mainly in the detection and spectroscopy of fission fragments and heavy charged particles. Helium scintillators in particular were developed in the 1960s for neutron detection and polarimetry measurements where pressurised helium gas (often mixed with traces of Xe) served both as a scintillator and a target for incident neutrons [61][67]. However, interest in using gas scintillators declined soon after the development of semi-conductor detectors in 1960 [68] which offered much better energy resolution and were easier to handle [61][69]. As a result, progress in gas scintillator research slowed down but did not cease (notably due to one group at the University of Coim-

[2]According to Ward [63] and Al-Dargazelli et al. [64] Auderbert and Lormeau preceded Grün and Schopper in using a PMT with a gas scintillator in their research in 1949. It was not possible to verify this since it was not possible to locate the original publications [65] and [66].

[3]From German word Edelgas that refers to members of group eight elements on the periodic table: helium, neon, argon, krypton, xenon, radon, and ununoctium.

bra, Portugal, led by A. J. L. Policarpo [70]), and for some time it was mainly driven by research in fundamental atomic physics, and the physics of gas discharges and laser excitation rather than detector development. Nevertheless this slow progress eventually led to the development of the widely used gas-scintillation proportional detectors (GSPSD) in 1967 [71] and later gas-scintillation drift chamber detectors (GSDCD) in 1972 [72], which have dominated the applications of gas-scintillators for particle detection since then. These detector types employ an electric field for detection of the resultant secondary scintillation emissions. The devices are suited for detection of heavy ions [73–77] and also proved very useful for precision spectrometry of X-rays and soft gamma rays [70]. Fortunately advances in modern nuclear physics experiments in the 1970s drew attention back to NGSDs, mainly due to the limitations of semi-conductor detectors in active area, cost and their poor resistance to radiation damage. During the 1970s, substantial efforts were made by M. Mutterer et al. to show the potential of noble-gas scintillators as an effective detection medium for heavy ions with and without applying an electric field [70, 78], but this work was largely ignored. Nevertheless, interest in noble-gas element scintillators, in liquid, gas and solid phases, is growing, and at present they are used in a wide range of applications within medical physics, astrophysics, particle and nuclear physics. In nuclear physics high-pressure ^{3}He or ^{4}He NGSD are used extensively in the detection of thermal and fast neutrons. An extensive review of current applications of noble-gas scintillators can be found in Ref. [69].

Interest in noble-gas scintillators arises from the combined features they possess which makes them preferable to many other types of scintillators for the detection of particles. The most prominent of these are summarised below [61]:

- The scintillation response to energy deposited by ionising particles is almost linear over a wide range of dE/dx (energy loss per unit path length), which implies no quenching effects on signals from low energy particles.
- Fast response time. The scintillation rise time is very fast making gas-scintillators among the fastest radiation detectors.
- The simplicity of obtaining good 2π or 4π geometry.
- High flexibility, in terms of shaping and formation of the scintillation volume.
- The possibility of adjusting the stopping power by varying the gas pressure which can allow selective detection efficiency for particles of interest.
- High resistance to radiation damage.
- Transparency to their own scintillation light, unlike organic or inactivated inorganic scintillators.

- High scintillation yield, though the scintillation emission predominantly occurs in Vacuum Ultraviolet (VUV)[4] region.

However, one of the main challenges in using noble-gas scintillators as detectors is the difficulty associated with collection and detection of the scintillation light efficiently since it lies mostly in the VUV region and since the scintillation efficiency of noble-gases is relatively low overall [79]. Other difficulties include the requirements of high-purity, high-pressure gas and large volume (necessary to achieve reasonable detection efficiency), which may further complicate handling the detection system. Also, the cost can be immense for low abundance gases such as ^{3}He.

Further background on the developments of the scintillation detectors can be found in the review written by Birks [61], which is still considered one of the best references on the subject despite being written over 40 years ago.

2.2 Helium Gas-Scintillator Active Target

The helium gas-scintillator active target (HGSAT) used in this work is a segmented ^{4}He NGSD. It was first proposed to measure the total photodisintegration cross-section of ^{4}He by Annand of the University of Glasgow in 1997 [80]. It is part of an ongoing programme that is run at MAX-lab in conjunction with the Photonuclear Group at Lund University in Lund, Sweden to measure photodisintegration of few-body nuclei from breakup threshold to π-production threshold. This follows on from the first experiment in the programme to measure the $^4\mathrm{He}(\gamma, n)^3\mathrm{He}$ partial cross-section with high precision made by Nilsson et al. in 1995 using the tagged photon facility at MAX-lab [29]. The scientific motivation for the current $\gamma + {}^4$He measurement was discussed in the previous chapter.

The development of the HGSAT began soon after the experimental proposal was accepted by the Nuclear Physics Program Advisory Committee (PAC) at MAX-lab. Some investigations of the helium scintillation response were necessary to verify the feasibility of the experimental concept. For this purpose, serious efforts were made between 1998 and 2001 followed by more work between 2008 and 2009. These included the design and construction of two prototypes which provided the baseline design of the HGSAT (MKI and MKII), a number of bench tests in Glasgow and three in-beam tests in Lund. The focus of these efforts was mainly to enhance the weak scintillation signals and to maximise the light collection efficiency, both of which are vital to the detection of low energy ions associated with the ^{4}He photodisintegration near breakup threshold. Eventually, the design of the HGSAT was finalised and the construction was completed in Glasgow during a one month period in September 2008 with minor modifications at the hardware-level made one month before it was shipped to Lund for the experiment in March 2009.

[4] The VUV radiation wavelength ranges from 100 nm to 200 nm.

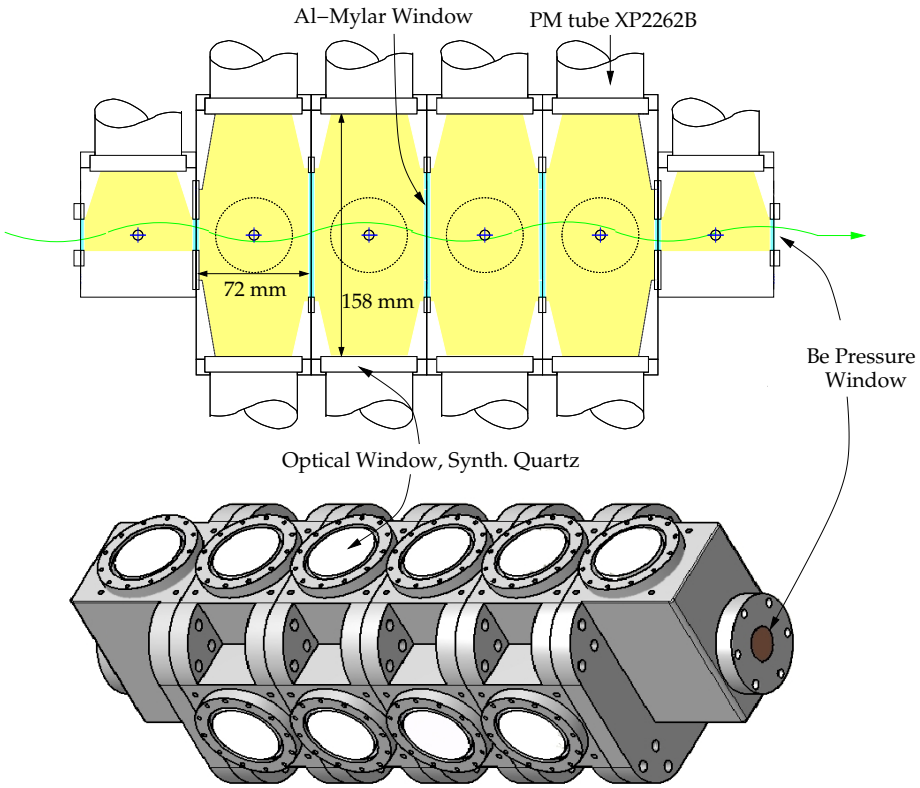

Figure 2.1: Schematic drawings of the Helium Gas-Scintillator Active Target (HGSAT).

2.2.1 HGSAT Description

The HGSAT is shown schematically in Fig. 2.1. It consists of four identical main cells machined from solid Al alloy. A central cylindrical cavity 72 mm long by 58 mm diameter constitutes the main body of the target and for tagged-photon studies is aligned with its axis parallel to and centred on the beam axis. Each cell is read out by 4 photomultiplier tubes (PMT) type XP2262B, viewing the gas cell through 10 mm thick synthetic quartz windows. A pressure-tight seal is made between the window and the body of the target using indium O-rings. The cell thickness is 72 mm, giving at 2 MPa pressure a target thickness of $\sim$110 mg/cm^2. Pressure-tight coupling between cells is done by a V-"ridge" on a copper gasket. The pressure between cells is equalised via a connecting aperture. The cells are optically isolated by 5 µm thick aluminised mylar inner windows. Two outer window isolation cells attached at either end of the HGSAT, have a single PMT attached to the target body as in the main-cell PMTs. The outer pressure-containment windows are of 0.5 mm thick beryllium.

2.2.2 Working Principle

Although complex in detail, the working principle of the HGSAT is straightforward and can be explained fairly easily as shown in Fig. 2.2. Charged particles result-

ing from a $\gamma + {}^4\text{He}$ disintegration event pass through the high-pressure monatomic helium gas target depositing their energy via ionisation. Consequently, numerous excited molecules[5] are created along the track of the charged particles via ionisation/recombination and direct excitation processes. A flash of light is emitted as the excited molecules decay to the monatomic ground state via a variety of different radiative mechanisms. The energy of the resultant scintillation emission is less than the first atomic excited state, therefore it can not be re-absorbed by the helium target. As with all noble-gas scintillators, most of the helium scintillation emission lies in the VUV region of the spectrum so a wavelength shifter is used to convert the emission spectrum to the visible region where standard PMTs are most sensitive. The scintillation light is collected and detected through 4 PMTs mounted on each target cell. The PMTs signals are then used to make the experimental trigger according to certain conditions which, when met, announce a valid $\gamma + {}^4\text{He}$ event and generate a signal which starts the Data Acquisition (DAQ) system and associated experimental electronics (see Sec. 3.7 for more details).

For the $\gamma + {}^4\text{He}$ total photodisintegration measurement presented in this thesis, employing the active target method is highly advantageous since detection of products near the breakup threshold region is difficult when using conventional separate target and detector systems. This is because low energy charged ions are very easily stopped in the target material before reaching the detector systems. The active target also offers a simplified experimental set-up with $\sim 4\pi$ coverage without resorting to the use of large and expensive detectors. Additionally, the active target provides a very convenient reference time for photon tagging and a start time for precise neutron time-of-flight (TOF) measurements when used in conjunction with external neutron detector(s). Otherwise neutron TOF requires a reference from the fast-counting photon tagging system, which registers substantial random-coincidence and other background. The active target was employed for the ${}^4\text{He}(\gamma, n^3\text{He})$ partial cross-section measurement that was run in parallel to the measurement reported here, and more recently the ${}^4\text{He}(\gamma, n)$ photon asymmetry (Σ) measurement that was separately performed in March 2011 [82]. The underlying concept of these measurements is to detect neutrons in coincidence with the associated charged particles detected in the target, which announce the occurrence of a photodisintegration event and provide the start signal for the TOF coincidence.

As indicated earlier, the HGSAT detection of the photodisintegration products is highly dependent on collection and detection of the helium scintillation. Details of the mechanisms that lead to scintillation are complicated and tend to be very specialised. These are of no particular interest to the measurement presented in this thesis apart from the resultant emission spectrum itself and such details can be found within various publications such as [61], [83], [84] and [85]. However, a

[5] These excited molecules are known as *Excimers* from **exci**ted di**mers**. The term was introduced by Stevens and Hutton in 1960 [81].

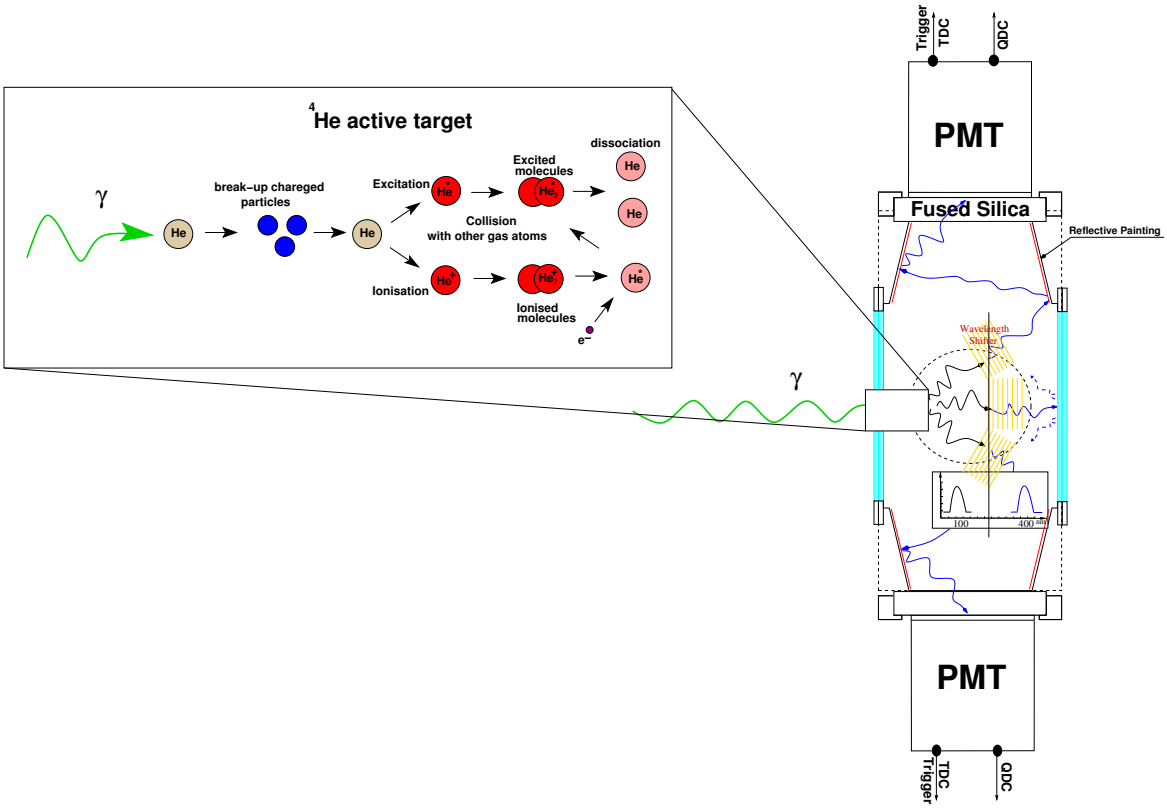

Figure 2.2: The working principle of the HGSAT. Charged ^{4}He photodisintegration products ionise helium gas atoms and consequently lead to scintillation. The wavelength of the scintillation is shifted from vacuum ultraviolet (VUV) to the visible (VIS) region via a wavelength shifter. The scintillation is collected and detected via 4 PMTs mounted on the target cell. Energy and timing information are stored via Charge-to-Digital converters (QDCs) and Time-to-Digital converters (TDCs). The scintillation signals are used to generate the experimental trigger.

simplified overview of the helium scintillation and some of its properties is given in the next section in order to provide a better sense of how the HGSAT functions and the difficulties confronted during the development phase.

2.3 Helium Scintillation and Emission Spectrum

The scintillation emission spectrum of helium, in common with all noble gases, is a complex system of lines, bands and continua, originating from many excited states and from various collisional and transfer processes. The spectrum extends from the Near-Infrared (NIR)[6] into the VUV [69] and is highly dependent on the gas pressure, the excitation modes and more obviously the energy of the ionising particle.

[6]The NIR radiation wavelength ranges from 780 nm to 3000 nm.

The process of scintillation can be described as follows: As a charged particle (R) passes through helium gas, it deposits its energy along the track. For relatively low gas pressure $< 0.1\,\mathrm{kPa}$ the energy is transferred mainly to the gas atoms producing excited atoms through two dominant processes:

Ionisation/Recombination

$$R + He \Longrightarrow e^- + He^+$$
$$He^+ + e^- \Longrightarrow He^*$$

or direct excitation

$$R + He \Longrightarrow He^*$$

These excited atoms decay to their ground state either via direct transitions which

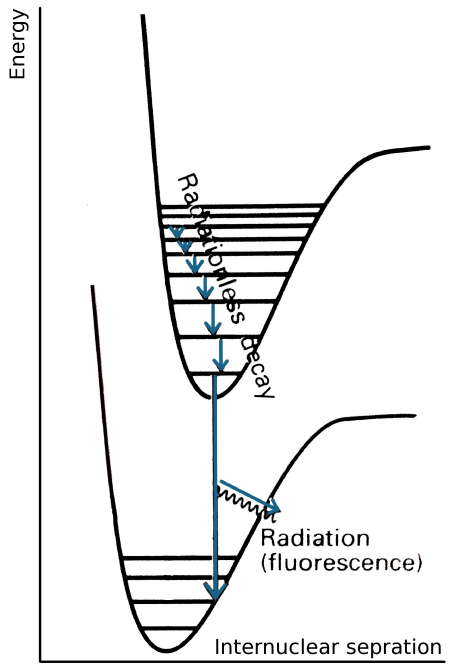

Figure 2.3: Non-radiative decay occur when upper vibrational states give up energy to nearby atoms and molecules, whereas radiative transitions occur from the vibrational ground state of the upper electronic state to ground electronic state [86].

lead to the emission of characteristic resonance lines, or by successive allowed transitions to lower excited states, with the emission of photons of corresponding energy, thus yielding the atomic line spectrum [61]. The former emission is in the VUV region and is effectively trapped via absorptions and re-emissions many times by neighbouring helium atoms and is eventually absorbed, whereas the latter emission occurs in the visible (VIS) and may extend to the NIR region:

$$He^* \Longrightarrow He + hv$$

This process is most likely be the responsible for the spectrum seen in Fig. 2.4. The spectrum was taken for 10 Pa of helium excited by 20 keV helium ions (He^+) [87].

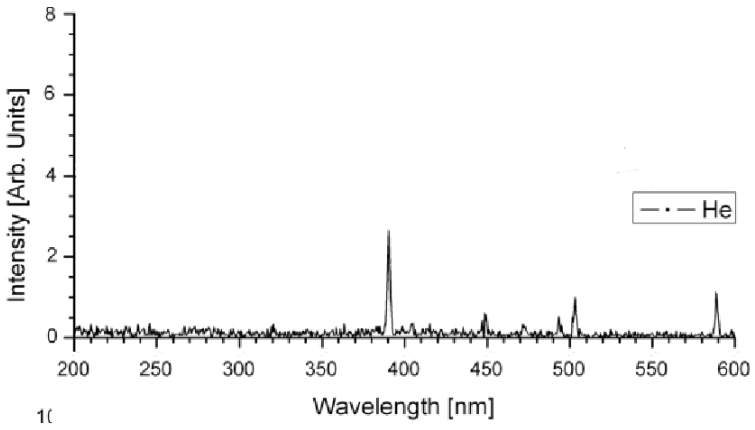

Figure 2.4: The scintillation spectrum of helium in the Visible (VIS) region at 10 Pa excited by 20 keV helium ions (He^+) [87].

At higher densities, in the high-pressure gas or liquid, the probability of double and triple collisions of excited/ionised atoms with surrounding ground state atoms increases. This essentially leads to the formation of excimers [88]:

directly

$$He^* + 2He \Longrightarrow He_2^* + He$$

or through associative ionisation/recombination processes similar to those leading to the production of excited atoms:

$$He^+ + 2He \Longrightarrow He + He_2^+$$
$$He_2^+ + e^- \Longrightarrow He + He^*$$
$$He^* + 2He \Longrightarrow He + He_2^*$$

These excimers are formed in many different excited states with various vibrational levels, mainly singlets ($^1\Sigma_u^+$) and triplets ($^3\Sigma_u^+$). The singlets in helium come in two different excited states: ($D^1\Sigma_u^+$) and ($A^1\Sigma_u^+$) formed by three-body collisions involving ($^1P_2$) and ($^1S_2$) excited state atoms respectively [84][89], whilst triplets come in one state ($a^3\Sigma_u^+$) formed from ($^3S_2$) excited state atoms. The excimers either decay directly to the ground state by emitting photons, or undergo collisions with the surrounding molecules and atoms, giving up energy non-radiatively in the process. The non-radiative decays cause excimers to descend the ladder of vibrational

levels to the lowest vibrational level of the excited electronic state. Since the energy difference between the ground electronic state and the lowest vibrational level of the excited states is higher than the ability of the surrounding molecules and atoms to accept, the remaining excess energy is emitted as radiation:

$$He_2^* \Longrightarrow 2He + h\nu$$

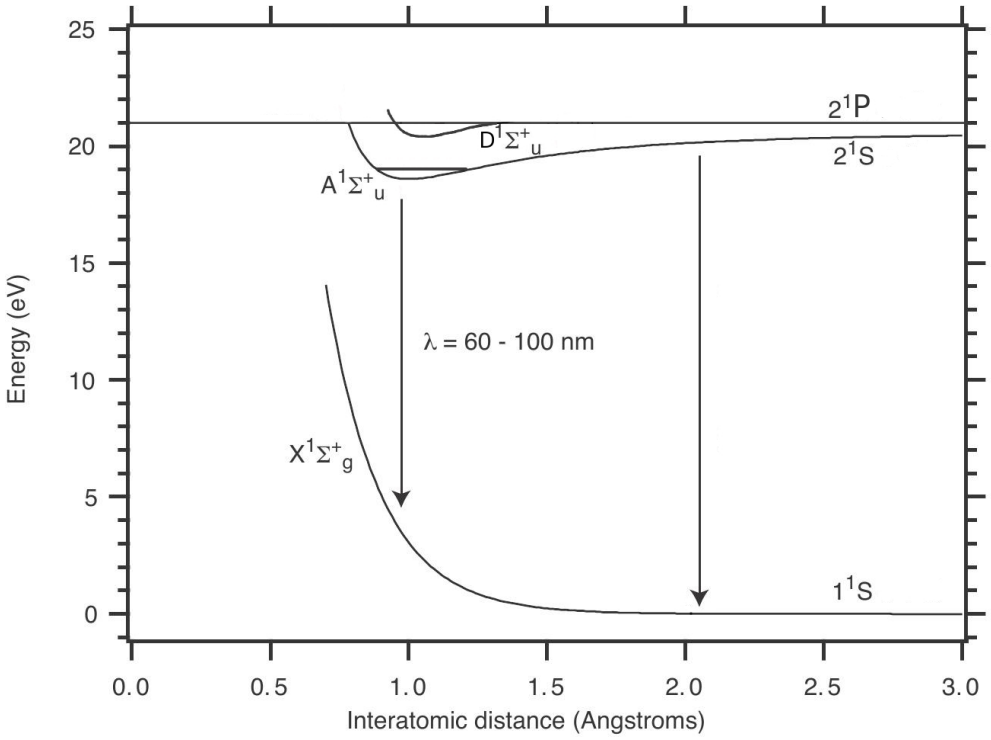

Figure 2.5: The potential curves of the $He_2(A^1\Sigma_u^+)$ and $He_2(D^1\Sigma_u^+)$ excited state and the ground state $He_2(X^1\Sigma_g^+)$ (equivalent to two free He atoms). Graph is modified from Ref. [90].

Overall, the energy of the resulting emission is less than that required to excite surrounding atoms (∼20 eV) which makes helium transparent to its own scintillation. A diagram illustrating the difference between radiative and non-radiative decay processes is given in Fig. 2.3.

The radiative decay of the resultant excimers into the monoatomic ground state leads to the generation of characteristic molecular continua in the VUV region, with two distinct continua: the so-called first and second continua. The first continuum in helium originates from the transition of the highest vibrational levels of the first excited states ($^1\Sigma_u^+$) to the ground repulsive state ($^1\Sigma_g^+$). This continuum appears as a narrow feature peaking at ∼60 nm in helium, close to the main atomic resonance line, and can be observed at relatively low pressure, typically $<$ 0.1 MPa [85]. The first continuum disappears in favour of the second continuum as pressure increases [91]. This is explained by the increased probability of excimer

collisions with other surrounding molecules and atoms, which effectively results in non-radiative vibrational de-excitation of these excimers as explained earlier. The second continuum corresponds to the decay of the lowest vibrational levels of $(^{1,3}\Sigma_u^+)$ to the ground repulsive state $(^{1,3}\Sigma_u^+) \Rightarrow (^1\Sigma_g^+)$. This continuum is broader than the first, extending from ∼60 to 100 nm and peaks at ∼80 nm. This large wavelength spread is attributed to the unbound state of the two reacting helium atoms. In the Oppenheimer approximation, helium nuclei do not change position during fast electronic transitions, therefore the amount of energy released as photons depends on the distance between the two helium nuclei at the time of radiative decay [90].

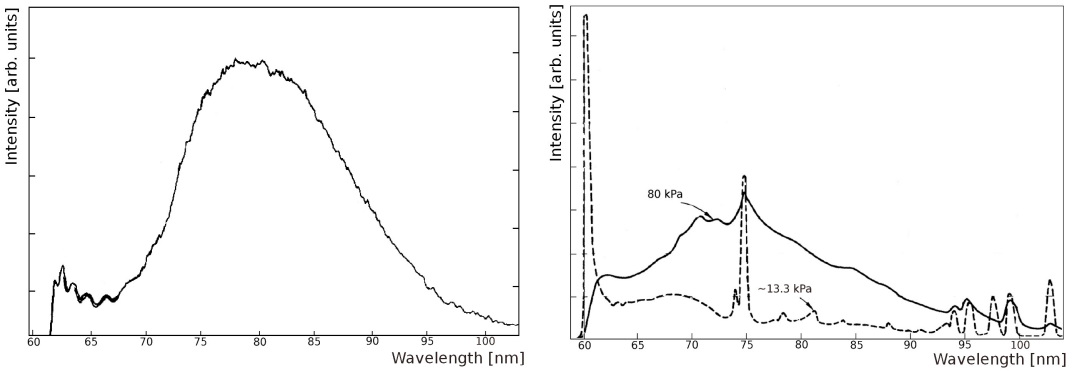

Figure 2.6: Left: ultraviolet emission spectrum of a high-pressure helium discharge lamp [92]. Right: emission spectrum of proton-excited helium at ∼13.3 and 80 kPa [93], the difference in shape is due to the different scintillation mechanisms taking place (see Sec. 2.3.2).

The second continuum (Fig. 2.6) dominates the emission spectrum at higher pressure, > 100 kPa, driven mostly by the decay of the $(A^1\Sigma_u^+)$ singlets[7]. Two other distinct continua extending approximately from 105 to 400 nm and from 210 to 650 nm in helium were first discovered by Tanaka et al. [96] and Huffman et al. [97] respectively. Tanaka observed the 105-400 nm continuum using an AC discharge of helium at low pressures ranging from ∼0.1 to 10 kPa, and cooled at liquid nitrogen temperature, while Huffman observed the 210-650 nm continuum using a self-triggering helium discharge at pressures of ∼10 to 100 kPa. Boichenko [98] referred to these two continua as the third continuum of helium[8]. In any case, the mechanism and kinetic processes leading to the emission of these continua are different from the first and second continua. The mechanisms responsible for the emission

[7]The contribution of $(D^1\Sigma_u^+)$ and $(A^1\Sigma_u^+)$ singlet decay in the helium second continuum is known as the Hopfield continuum [85][94][95]. The potential curves of the $He_2(A^1\Sigma_u^+)$ and $He_2(D^1\Sigma_u^+)$ excited states are given in Fig. 2.5

[8]Langhoff [99] and Griegel [100] refer to a different continuum that peaks at 60 nm as the third continuum of helium. That continuum is based on an ab initio calculation of Yagisawa et al. [101] and was not observed experimentally since it coincides with the first continuum.

of the third continuum are not fully understood with two competing hypothesis suggesting that it originates either from the decay of either doubly charged (He_2^{2+}) or from highly excited singly (He_2^{+*}) charged ionic molecules [98][102]. The calculations of Hill [103] suggest that the molecular transition from the lowest vibrational levels of the singly charged $He_2^+(C^2\Pi_u^+)$, formed from ($^3P_2$) and He^+, to the ground repulsive state $He_2^+(A^2\Sigma_g^+)$ is the origin of the Tanaka continuum, whereas the Huffman continuum originates from the same molecular transition but from higher vibration levels. It is worth mentioning that the third continuum is likely to be observed at low gas pressure with heavy ion beam excitation since energy loss per unit path length is higher leading to a higher density of excited ionic molecules.

It is clear from what was mentioned above that the scintillation of helium is not directly usable at high pressure for detection of ^{4}He photodisintegration products since it mostly lies in the VUV region where most photon sensors are almost blind. On the other hand, the detectable visible scintillation signals of helium can only be observed at very low gas pressure. At this low level, the gas density is too thin to be an effective target especially for photo-nuclear reactions with relatively low cross section, the aim of the measurement reported in this thesis. As a result, employing an appropriate wavelength-shifter was unavoidable to boost the detectable scintillation signals as will be shown in Sec. 2.4.1.

2.3.1 Scintillation Time Structure

The HGSAT is to be placed directly in an intense bremsstrahlung photon beam where a high counting rate can be expected. This could put some restrictions on the maximum beam intensity allowed in the experiment if the scintillation pulses are not fast enough to avoid pile up effects. For this reason, information on the scintillation time-structure and its dependencies are important and they are highlighted briefly below.

The timing characteristics associated with helium scintillation are complicated due to the different processes involved and the existence of diverse forms of excited molecules and atoms produced in various excited states. Practically, the scintillation time structure is governed by the formation time of these excited species and their lifetimes. The formation time is highly pressure dependent, particularly in the case of the ionisation/recombination process, ranging from a few nanoseconds to a few microseconds, whereas the decay time is determined by the characteristics of the initial and final states. What stands out is that the lifetimes of the two dominant excited molecular states, singlets ($^1\Sigma_u^+$) and triplets ($^3\Sigma_u^+$), differ substantially. In superfluid helium, the lifetime of the ($A^1\Sigma_u^+$) state was measured to be $\sim$1 ns and 13$\pm$2 s for the ($a^3\Sigma_u^+$) state [94]. This huge difference arises from the fact that the triplet ($^3\Sigma_u^+$) radiative transition to the dissociative ground state ($^1\Sigma_g^+$) is forbidden according to the spin selection rule. However, the presence of spin-orbit coupling breaks down the selection rule allowing such transitions to take place weakly result-

ing in a comparatively long decay-time. The spin-orbit coupling scales roughly as the fourth power of the effective nuclear charge (Z) which explains the large difference between the He($a^3\Sigma_u^+$) lifetime and the lifetimes of the triplets in neon (6.6 µs), argon (3.2 µs), krypton (350 ns), and xenon (50 ns) [104].

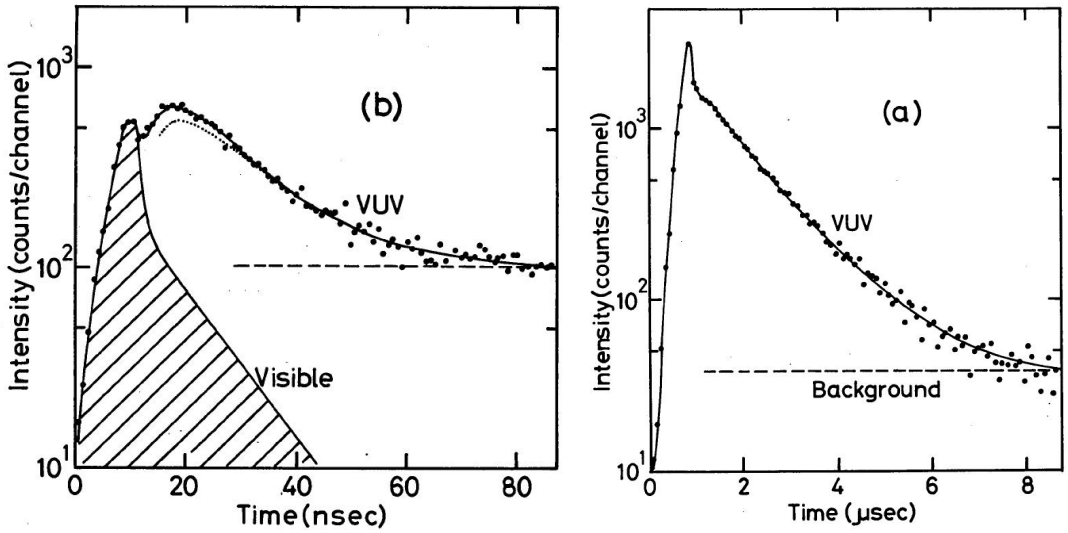

Figure 2.7: Time dependence of the scintillation in helium at ∼100 kPa [84]. Left: the fast component. Right: the slow component.

Studies on scintillation time dependence of helium at relatively low pressure show two separate components arising primarily from the two different singlet states, ($D^1\Sigma_u^+$) and ($A^1\Sigma_u^+$), as suggested by Bartell et al. [93] and Iida et al. [84][9]. The formation and the de-excitation of the ($D^1\Sigma_u^+$) state leads to a component with a decay-time of a few nanoseconds, whereas in the case of the ($A^1\Sigma_u^+$) state the formation and de-excitation, along with decay of ($^1S_2$) atomic state via a two-body collision results in a slower component lying in the range of a few microseconds. These components are highly pressure dependent as will be shown later, and are known, for obvious reasons, as the fast and the slow components of helium respectively. These components are shown in Fig. 2.7. It is likely that the time difference of the two components derives from whether the decaying excimer originated in a single or multi stage three-body collision constrained by the state of the interacting atoms forming the excimer, as explained in section 2.3. The formation of excimers from ionised atoms involves an additional route of a three-body collision and an ion-electron recombination compared to excimers formed from directly excited atoms. This can certainly increase the apparent decay-time of the excimer produced in this manner at very low pressures and clearly explains the high pressure dependence

[9]Hill [85] disagrees with this suggestion, arguing that the ($D^1\Sigma_u^+$) state radiates at lower wavelength than the one observed by Bartell et al. He proposed a lower vibrational ($A^1\Sigma_u^+$) state instead.

since the density of nearby electrons and atoms obviously increases as pressure increases.

The long decay-time of triplets and the slow component could lead to pile-up problems for an in-beam detector which could effectively limit the beam intensity that could be utilised usefully in the experiment. However, there are a number of ways to improve the timing of the scintillation pulses as will be shown in the next few sections.

2.3.2 Pressure Dependence

The HGSAT is required to act both as a target and a detector for the charged particles resulting from the ^{4}He photodisintegration reactions. For this purpose, the gas pressure should not only be sufficient to stop the photo-nuclear reaction products within the gas volume as with most conventional detectors, but also be set as high as possible to increase the effective target thickness and hence counting rate. This is advantageous in other respects since increasing the pressure also improves the scintillation signals as explained later.

Early empirical investigations on the pressure effects on pure helium scintillation showed clearly that the scintillation pulse height is increased with increasing pressure. Esterling [105] found that the increase in the pulse height goes up to a saturation level of ∼2 MPa (Fig. 2.8[left]). According to Birks [61] this concurred with the findings of Rubbia and Toller [106] who reported no variation in pulse height for helium between ∼2 and 10 MPa. On the contrary, Aamodt [107] reported a continuing increase of pulse height up to ∼100 MPa (Fig. 2.8[right]). This discrepancy may simply be due to impurity contamination of the gas used by the former as the latter appears to have made substantial efforts to eliminate impurities in the tested sample. Esterling provides a convincing explanation for the increase in the pulse height as mostly due to variation in the timing of the output light. However, work by Saito et al. [108] on argon, xenon and krypton indicates that the scintillation yield[10] also increases as pressure increases. Saito attributes this to the positive correlation of the intensity of the ion/recombination scintillation contribution and the pressure. This in principle should also be valid for helium.

The primary effect of increasing the pressure is the increased probability of collisions between excited and ground state atoms and molecules at the expense of direct excitation simply because of the increased density. This essentially suppresses all of the VIS and NIR emission as a result of depletion of the corresponding excited atoms via formation of excimers through double and triple collisions as was explained in Sec. 2.3. Furthermore, increased collision probability results in non-radiative relax-

[10]Scintillation yield is defined as the number of photons emitted per unit energy deposit. The units are MeV^{-1}.

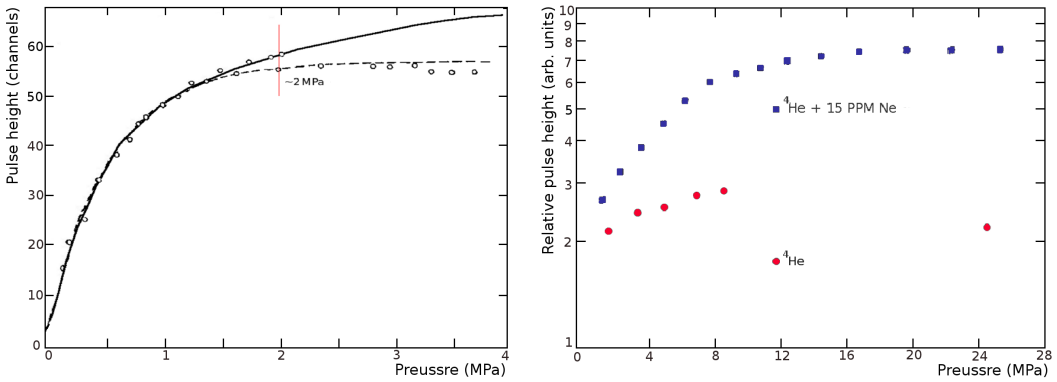

Figure 2.8: Pressure dependence of the scintillation in helium. Left: Esterling measurement using a 5.4 MeV α source. The solid curve is a least-squares fit of the data points below 20 atm [105]. Right: Aamodt measurement using 5.1 MeV α source [107].

ation of high vibrational excimers to the lowest levels, minimising the probability of direct transition to the repulsive ground state ($^1\Sigma_g^+$). This leads to the disappearance of the VUV ~60 nm first continuum while intensifying the second continuum $\sim 60-100$ nm at pressures of more than 50 kPa.

In Ref. [85], it was stated that the contribution of singlet ($D^1\Sigma_u^+$) decay on the scintillation decreases steadily with pressure until by 10 kPa it is not observed, mainly due to the depletion of the ($^1P_2$) excited atoms. This is in an agreement with studies made by McKinsey [94][90][104][109] on the scintillation of liquid helium which shows that the scintillation is mainly due to singlet ($A^1\Sigma_u^+$) and triplet ($a^3\Sigma_u^+$) decay with no contributions from the decay of singlet ($D^1\Sigma_u^+$) states. This evidence is in direct contradiction to the supposition of Bartell et al. [93] and Iida et al. [84] on the origin of the fast component (see Sec. 2.3.1). Furthermore, the work of Iida et al. shows that the experimental emission intensities of the fast and slow components increase proportionally as pressure increases in the range ~10 to 160 kPa. This suggests that Hill's proposal that the fast component is due to the lower vibrational level of singlet ($A^1\Sigma_u^+$) states rather than ($D^1\Sigma_u^+$) is more likely to be correct. However, what is more relevant here is that experimental investigations on the time dependence of pure helium scintillation clearly show that the "slow" component eventually becomes very fast at higher densities, down to ~10 ns at 1 MPa [110] (as can be seen in Fig. 2.9) from ~30 µs at 10^{-2} MPa [85]. This is attributed primarily to the sharp decrease in the formation time of the radiative species while their natural lifetime is not affected as much. This also means that increasing the pressure will not have much effect on the long-lived triplet states ($a^3\Sigma_u^+$) decay-time (~13 s in liquid helium). It is worth stressing again that these radiative species contribute slightly to the second continuum region ($\sim 60-100$ nm) that dominates the helium scintillation emission at high pressure. This contribution is limited by collisions between pairs of these states in the so-called Penning ionisa-

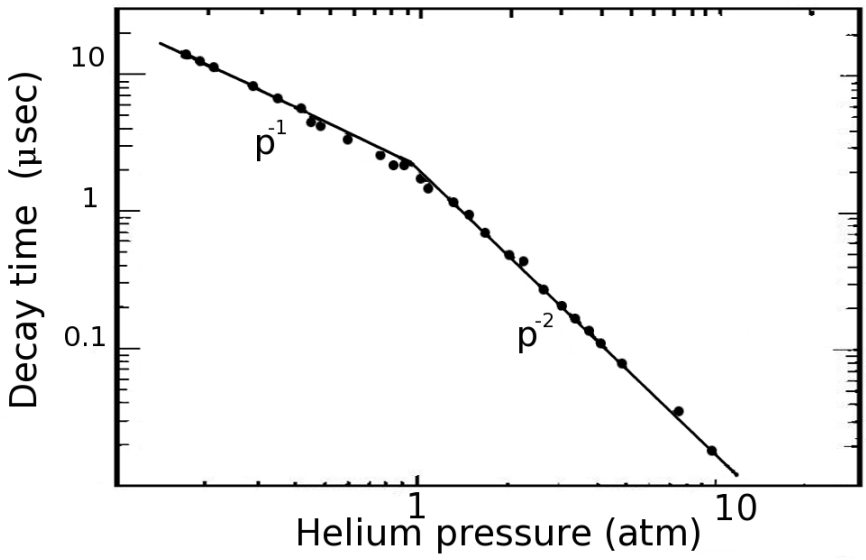

Figure 2.9: Decay time of helium VUV scintillation as a function of pressure [110].

tion, and also collisions with container walls [104]. On the other hand, it was found that these triplet states are very sensitive to impurity concentrations of even one part per million as a consequence of a sizeable cross-section for energy transfer [89]. There follows a section on the impurity dependence of the scintillation.

2.3.3 Impurity dependence

The impact of impurities on noble-gas scintillation was realised from the earliest investigations where trace impurities were generally present and difficult to avoid in the gas samples used. Despite their quenching effects on the scintillation, it was found that adding a small trace of certain gases improved the scintillation time structure and acted as a wavelength shifter of the VUV emission into the UV and VIS region where the sensitivity of most commercial PMTs peaks. Generally this happens through energy transfer from noble-gas excimers and/or exited atoms to some excited levels of the molecules of the added gas trace. This effectively stimulates the latter and leads to the appearance of their own emission at the expense of the noble-gas primary emission. At high pressures, this process occurs in a variety of ways [111]: charge exchange with atomic and molecular ions, collision with excimers, electron impact and photoionisation. Early investigations of the effects of impurities on noble-gas scintillation are reported in Ref. [61].

The effect of adding a trace of a gas impurity on helium scintillation depends on the nature of the added impurity, the total pressure of the gas mixtures and most important the concentration, i.e., the partial pressure of the impurity. An optimum combination of these parameters is required to minimise quenching effects associated with non-radiative transitions and emission of non UV/VIS photons by the impurity molecules. Xenon and nitrogen in particular were widely considered for boosting the

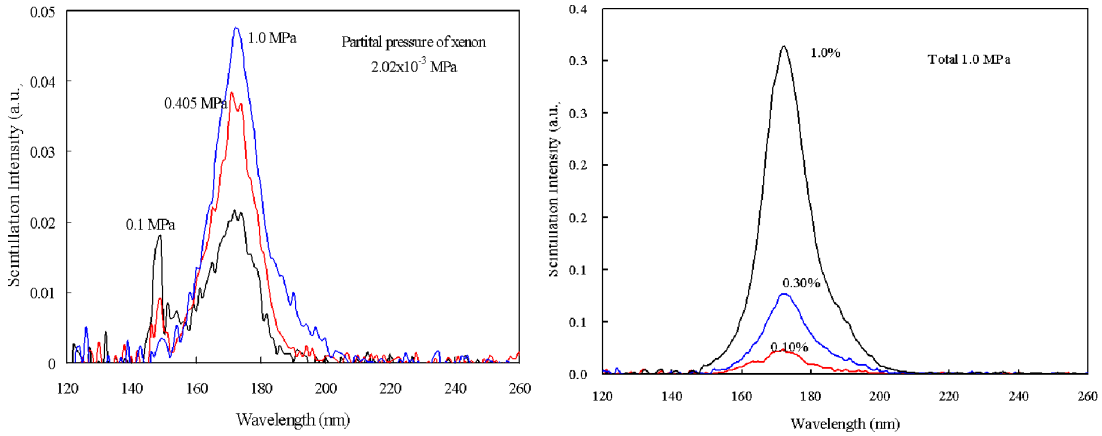

Figure 2.10: Emission spectrum in He + Xe mixture taken at various system total pressure (left) and various xenon concentrations (right) [112].

scintillation signals of helium. For xenon this was due to the high light yield and high stopping power. Nitrogen investigations were motivated by the fascinating blue emission at extremely low concentrations. Fig. 2.10 and Fig. 2.11 show the effect of adding traces of xenon and nitrogen respectively with various concentrations and different total gas mixture pressure. Full details of the measurements can be found in the references quoted below the corresponding figure. It should be noted that the experimental conditions and the method of excitation are different and one should only treat the figures as indicators of the effect of changing the pressure and concentration of the added impurity on the scintillation.

The presence of other types of impurity provide no real advantage and their existence seems only to quench the scintillation signals. In fact, the presence of these types of impurity may result in a significant reduction of the light yield. These types of impurities are named "scintillation poisoners" and their presence should be eliminated if at all possible. This is of particular importance when dealing with wavelength shifter paints where impurities due to out-gassing are a common by-product. To eliminate these undesirable effects, the gas container and associated gas-filling system should be kept as clean as possible. Further a high quality of vacuum is also required before the filling of the gas scintillator. The gas, and any desired added impurities, should be of the highest purity. Additionally, a continuous purification of the gas scintillator may become necessary in the case of wavelength shifter paints.

Morii et al. [115] studied the quenching effects of oxygen, carbon dioxide and methane in order to eliminate nitrogen scintillation that was causing a noise problem to his detector. Fig. 2.12 shows the results of these studies on the effect of O_2 and CO_2, the two most common impurities present in air, on the light yield of nitrogen scintillation as the concentration increases.

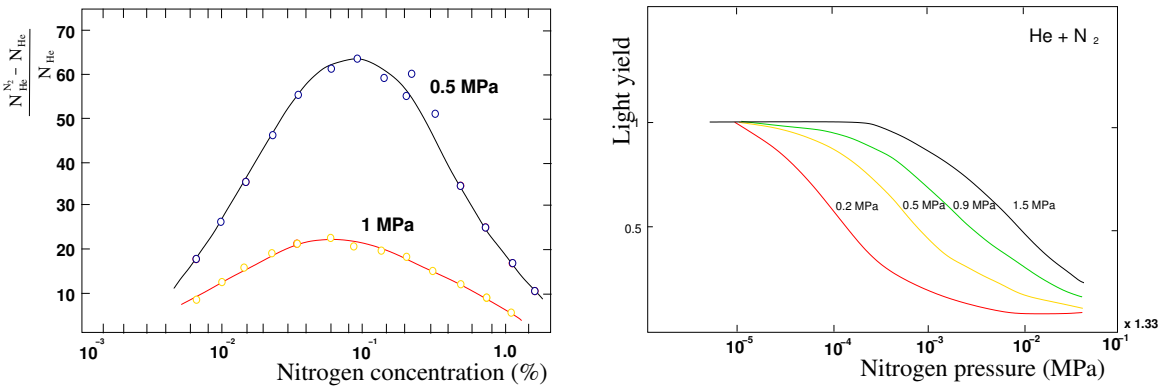

Figure 2.11: Left: Relative scintillation intensity for a He + N_2 mixture and pure He. N_{He} and $N_{He}^{N_2}$ are the scintillation counting rates for pure helium and the He + N_2, mixture respectively [113]. Right: Light yield in the quenching region for He + N_2 mixture at He pressure indicated in the figure. The curves are normalised at the lowest N_2 pressure [114].

2.4 HGSAT Development

The HGSAT relies heavily on collection and detection of the scintillation in detecting $\gamma + {}^4$He photodisintegration products. It was shown in the previous sections how detection of helium scintillation is difficult and can be challenging. For this reason, a substantial portion of the development process of the HGSAT focused mainly on two objectives: maximising the light collection efficiency through optimisation of the detector geometry, and effectively shifting the primary VUV helium scintillation emission to match the response spectrum of the standard bialkali-cathode PMTs available to use for the experiment reported in this thesis. This section provides a summary of these efforts along with a description of the construction process of the HGSAT.

2.4.1 Investigation of Helium Scintillation

A number of tests were performed in Glasgow in order to study the properties of helium scintillation taking into consideration previous investigations reported in the literature. This started using a small test cell designed originally for neutron polarimetry. The cell was equipped with a single PMT type XP2020Q and housed an open ^{241}Am α source. The helium gas was filled at 0.2 MPa pressure and the scintillation signals were viewed directly via a digital oscilloscope. The preliminary test confirmed that efficient transport and collection of the helium scintillation is difficult [116], therefore applying a proper fluorescent material was indeed necessary.

Wavelength Shifter

A number of wavelength shifting techniques was investigated [116]. We first examined a commercial wavelength-shifting paint type EJ-298 [117]. The paint consists

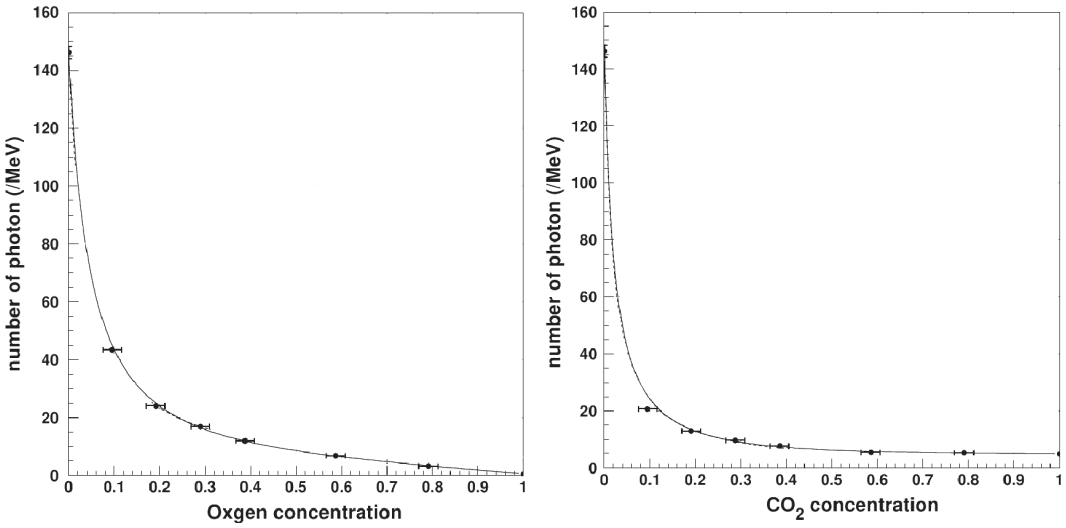

Figure 2.12: Quenching effects on N_2 scintillation [115]. Left: quenching effect on nitrogen as a function of oxygen contraction. Right: quenching effect on nitrogen as a function of carbon dioxide concentration.

of a polyvinyltoluene binder and $C_2H_4(CH_3)_2$ fluorescent dopant dissolved in a xylene solvent and is commonly used in plastic scintillators. The dopant blue emission spectrum peaks at ∼420 nm which is a perfect match to the response spectrum of most commercial PMTs. In order to increase the reflectivity, the internal structure of the cell was first coated with TiO_2 and then the wavelength shifter paint was applied on the top of the reflector and the surface of the quartz window. The paint did boost the scintillation signals significantly as can be seen in Fig. 2.13[left]. However, considerably stronger signals were observed when the cell was evacuated (Fig. 2.13[right]) implying the paint itself was scintillating. This was most likely due to α particles striking the cell walls directly. For this reason, the EJ-298 paint was abandoned [116].

A better solution was to use a trace of fluorescent gas. This was successfully used in the past in several application with helium as frequently reported in literature (see Sec. 2.3.3). We have investigated nitrogen, xenon and a mixture of both with different concentrations and for various total gas system pressures. Investigation on the effect of nitrogen on the scintillation of helium was performed in 1999 and was repeated and confirmed to give the same results in 2008 alongside further investigation with xenon and nitrogen-xenon mix. The apparatus used during these investigations is shown in Fig. 2.14 and the technique employed for the gas mixture preparation is described in Sec. 3.6.2. Research-grade[11] gas samples and a purpose-built prototype (MKII) viewed by 4 PMTs type XP2262B (see Sec. 2.4.2) were used in all of these investigations.

[11]Gas purity index equivalent to ∼99.995% purity.

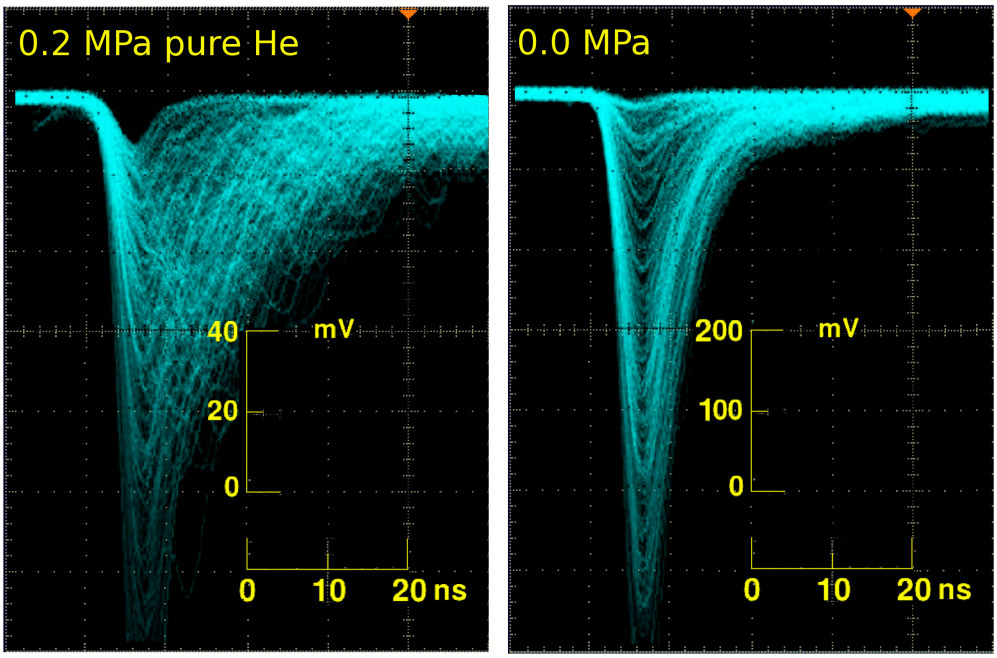

Figure 2.13: Test-cell pulse forms using the EJ-298 wavelength shifter and a ∼5.4 MeV α source [116]. Left: scintillation observed at 0.2 MPa of pure helium. Right: stronger scintillation signals observed using an evacuated cell.

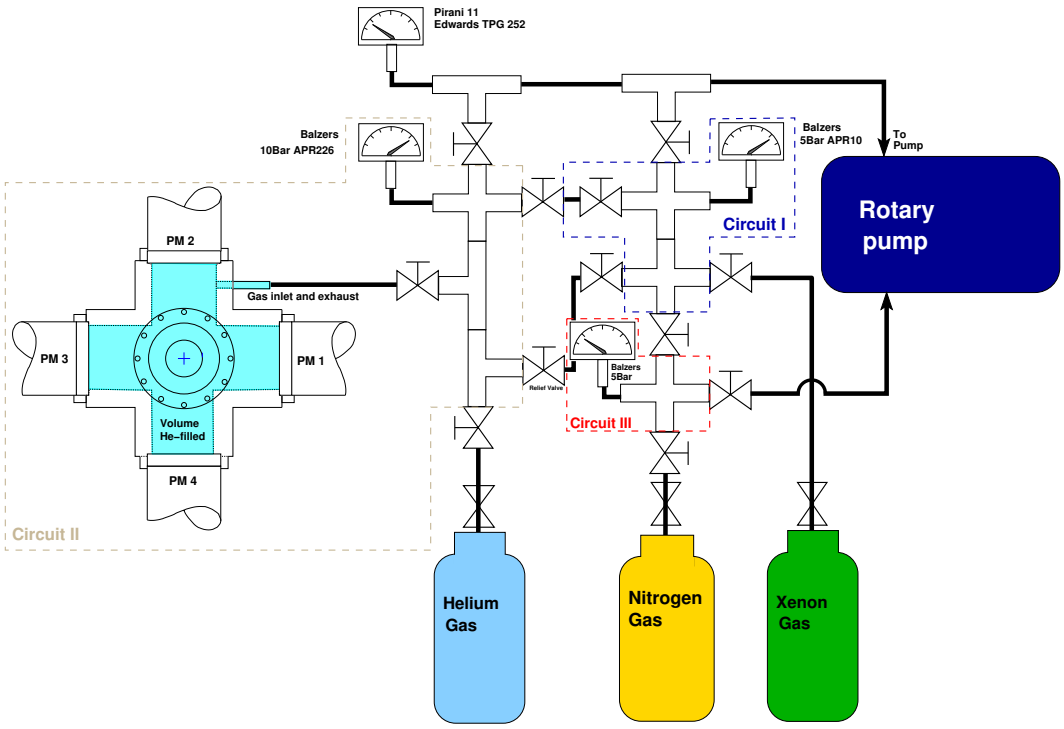

Figure 2.14: Schematic diagram of the gas filling system used during investigations of the effect of adding trace amounts of nitrogen and xenon.

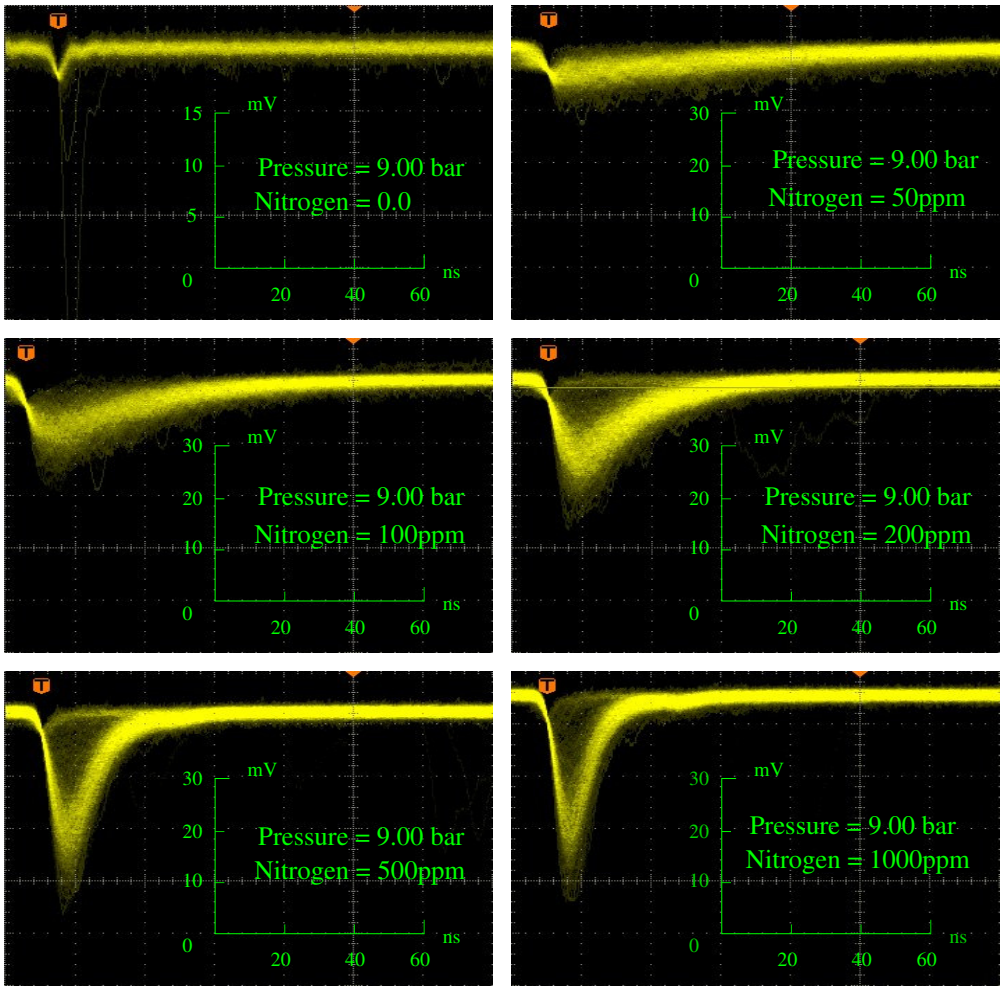

Figure 2.15: Helium scintillation response as a function of nitrogen concentration, to ∼5.4 MeV α particles at 0.9 MPa total constant pressure.

Fig. 2.15 shows the gas scintillation response to ^{241}Am ∼5.4 MeV α particles as a function of nitrogen concentration at a total system pressure of ∼0.9 MPa. The figure shows conspicuously the strong dependence of the pulse shape on N_2 concentration up to ∼500 ppm, but thereafter up to 1000 ppm the pulse shape seems quite stable. These findings are consistent with the optimum N_2 concentration of $\sim 200-500$ ppm commonly reported in publications in this area of research [111, 113, 118, 119]. The observed ∼420 nm emission spectrum consists of a contribution from both N_2 second positive ($C^3\Pi_u^+$) and the N_2^+ first negative ($B^2\Sigma_u^+$) systems. The scintillation decay time of ∼60 ns at 200 ppm N_2 concentration is the distinct signature of the decay of the N_2^+ first negative system. This appears to dominate the emission spectrum at low N_2 concentration up to 200 ppm but rapidly decreases with further increase in N_2 concentration in favour of the N_2 second positive emission. At a concentration of 500 ppm the resultant emission appears to arise entirely from the decay of the N_2 second positive system with corresponding decay time of ∼30 ns (see Fig. 2.16). It

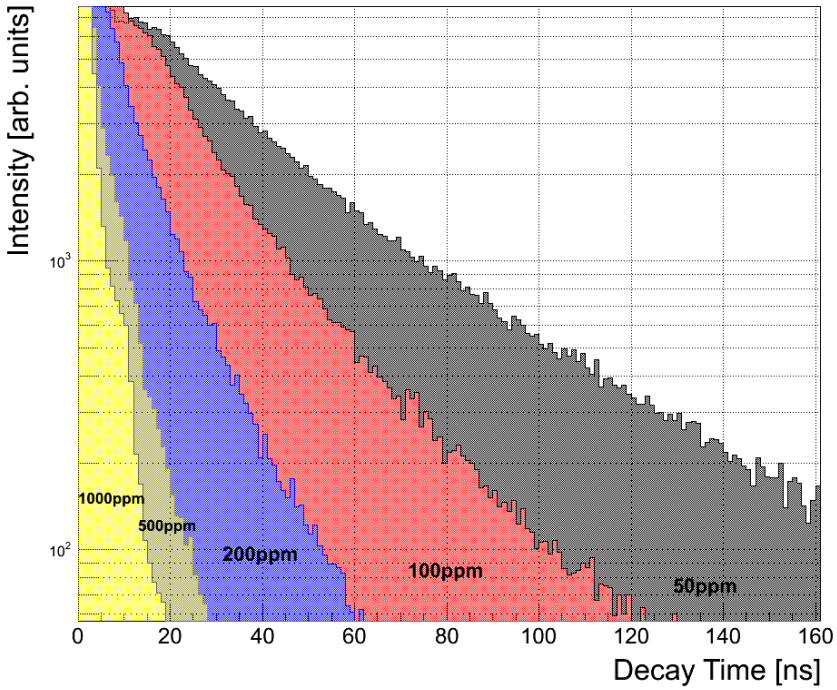

Figure 2.16: Scintillation time-profile at different nitrogen concentrations and a constant total pressure of ∼1 MPa.

is worth noting the absence of any clear sign of the long-lived triplets $He_2^*(a^3\Sigma_u^+)$ in the emission spectrum. This is most likely due to their destruction through collision with the N_2 impurity molecules suppressing all of the slow scintillation component in the process. The mechanism that leads to nitrogen two emissions is distinctly different due to the different energy levels responsible (Fig. 2.17). The formation of the N_2^+ first negative system band is believed to be due to total charge exchange excitation of N_2^+ by the molecular ion He_2^+ [61][111]:

$$He_2^+ + N_2(^1\Sigma_g^+) \Longrightarrow N_2^+(B^2\Sigma_u^+) + 2He$$
$$N_2^+(B^2\Sigma_u^+) \Longrightarrow N_2^+(X^2\Sigma_g^+) + hv$$

whereas the formation of the N_2 second positive band is attributed most probably to electron impact:

$$e^- + N_2 \Longrightarrow N_2(C^3\Pi_u^+) + e^-$$

and/or through destruction of triplets $He_2^*(a^3\Sigma_u^+)$:

$$He_2^*(a^3\Sigma_u^+) + N_2 \Longrightarrow N_2(C^3\Pi_u^+) + 2He$$

which then decay giving rise to the corresponding emission:

$$N_2(C^3\Pi_u^+) \Longrightarrow N_2(B^3\Pi_g^+) + hv$$

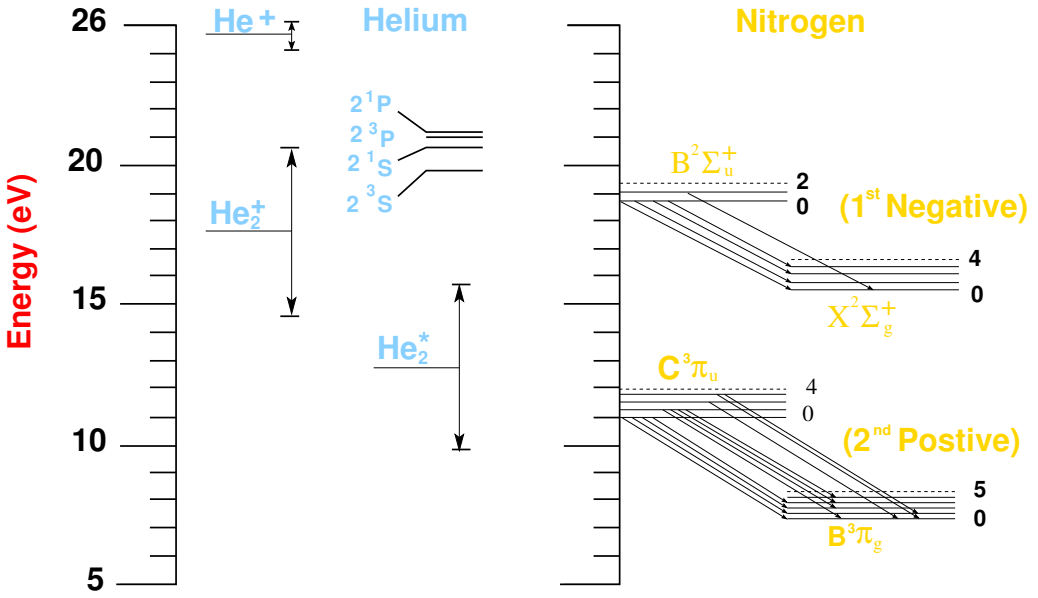

Figure 2.17: Schematic of helium energy levels responsible for nitrogen impurity excitation. The observed N_2 second positive and N_2^+ first negative transitions are also shown [111].

The exact details and interpretation of these processes are complicated and somehow irrelevant to the measurement reported in this thesis, therefore, the reader is referred to [111] and [120] as a good starting point on this subject. Fig. 2.18 shows the two-dimensional distribution of the signals from two perpendicular PMTs at 500 ppm trace of N_2. The scintillation response sits on a background from non-scintillation events, such as direct interaction in the PMTs and Čerenkov interactions in the quartz optical windows. Real scintillation signals can be seen in correlation, while the background can be seen as separated bands parallel to the axes.

We intended to enhance the scintillation signals even further by investigating the effect of xenon and N_2 - Xe mixture additives at various concentrations on the scintillation of helium. It was realised at the start of these investigations that adding xenon alone would not be of a great benefit using the XP2262 PMTs since the dominant xenon scintillation emission is centred at ~173 nm, a region beyond the sensitivity of those PMTs. The aim of these investigations was to examine whether adding xenon would maximise energy transfer efficiency from helium to nitrogen molecules through dual energy transfer He⇒Xe⇒N_2. Adopting the same apparatus used during nitrogen investigation we tried various concentrations of xenon at the optimum nitrogen concentration of 500 ppm and compared them with the same concentrations of xenon alone in helium. This was not successful in boosting the scintillation signals as can be seen in Fig. 2.19. In fact, adding 500 ppm of N_2 trace appears to quench the scintillation signals in the N_2 - Xe mixture in helium. There could be "magic" ratios in which these gases are mixed, as can be concluded from the work of Tornow [121]. However, at this stage we decided not to take

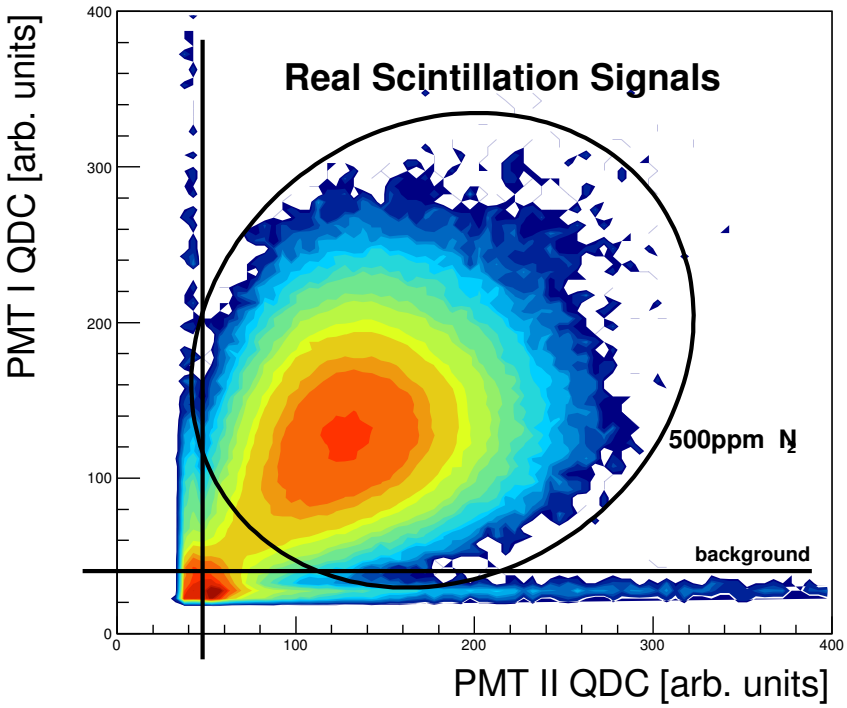

Figure 2.18: Two-dimensional distribution of helium scintillation signals from two perpendicular PMTs. The scintillation is produced from ∼5.4 MeV alpha particles striking the helium gas pressurised at ∼0.9 MPa and with 500 ppm trace of N_2. The two lines parallel to the x and y axes are drawn to highlight the background.

these investigations any further since the conditions of the scintillation pulses with 500 ppm nitrogen and 1 MPa were satisfactory for an in-beam pilot measurement at the MAX-lab tagged photon facility.

Pressure Effects

The desire to have a high density target in photo-nuclear experiments was briefly discussed in Sec. 2.3.2. It was shown that the scintillation of helium is highly pressure dependent due to the formation of different radiative species as the pressure varies. The observed nitrogen emission at low concentrations in helium is directly related to helium excitation, therefore, one would expect a complex pressure dependence since the scintillation emission of both nitrogen and helium are pressure dependent. This can be seen clearly in Fig. 2.15 which shows the effect of increasing nitrogen partial pressure on the observed scintillation.

We studied the effect of increasing the total gas system pressure on the scintillation signals at 1000 ppm of nitrogen. Fig. 2.20 shows the variation in scintillation response as the pressure is raised from 0 to 1 MPa (maximum allowed pressure for the MKII prototype). The pulse height appears to increase proportionally with pressure

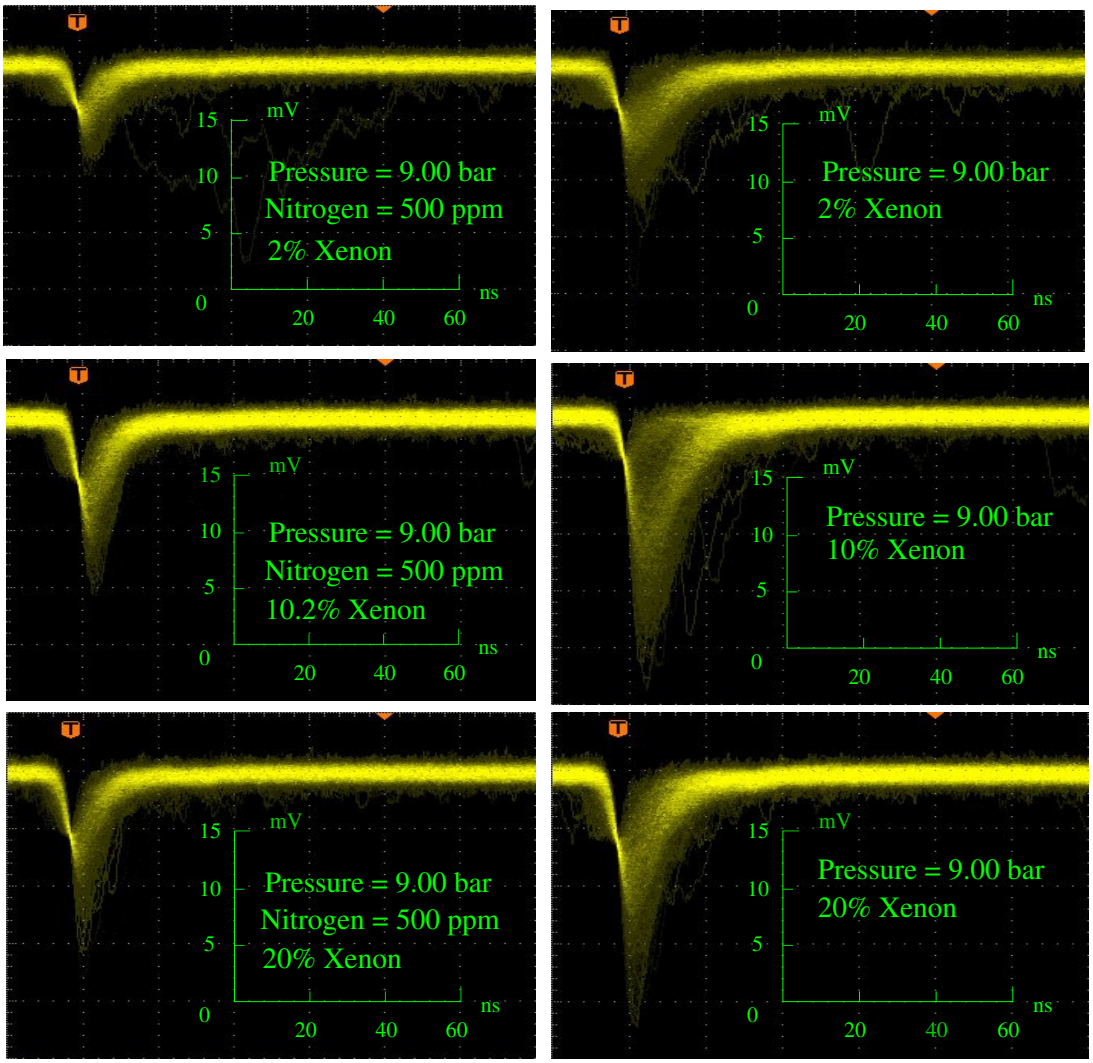

Figure 2.19: Helium scintillation response as a function of xenon concentration (right column) and xenon-nitrogen mix (left column), to ∼5.4 MeV α particles at ∼0.9 MPa total constant pressure.

up to about 0.5 MPa but decreases slightly at double the pressure. This evidently indicates a change in the dominant processes leading to scintillation. However an exact explanation of the pulse shape behaviour as a function of pressure is difficult due to the many dependencies involved in the process. One could roughly single out two main processes responsible for this behaviour: helium pressure dependence and the increased ionisation density as pressure increases. It is worth noting that the pressure required to stop α particles entirely within the gas volume in the MKII prototype was approximately 0.2 MPa.

All of these investigations were verified with the HGSAT MKIII cell and ^{241}Am α source prior to the experiment detailed in this thesis. The results were confirmed to be the same as from the MKII prototype for all N_2 concentrations and pressures

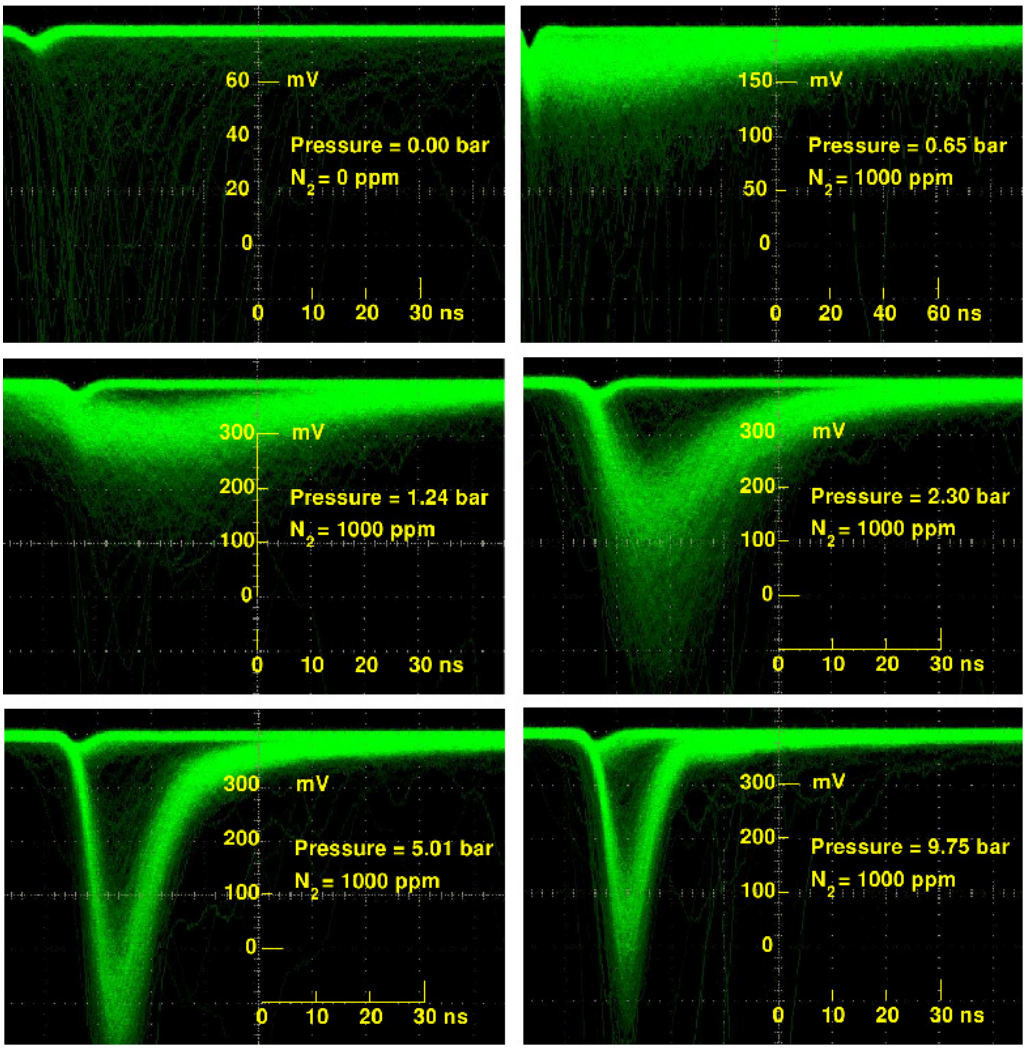

Figure 2.20: Helium scintillation response as a function of the gas pressure, to ∼5.4 MeV α particles at constant nitrogen trace of 1000 ppm [33].

up to 1 MPa. However a reduction of roughly 15% in pulse height at 2 MPa compared to that at 1 MPa was observed. This was most likely due to the nitrogen quenching effect (see Sec. 2.3.3). On the other hand, the timing profile was found to be improved approximately by the same percentage. The scintillation decay time was found to be ∼25 ns at 2 MPa opposed to ∼30 ns at 1 MPa.

2.4.2 Geometry Modification and In-Beam Tests

The HGSAT was developed using the MKI [122] and MKII [123] prototypes. The design was eventually finalised and the MKIII cell was built for the HGSAT used in the measurement reported in this thesis. A schematic view of the gas-volume cell of the two prototypes and the MKIII cell is displayed in Fig. 2.21.

The MKI was the first purpose-built prototype and was used in all of the initial

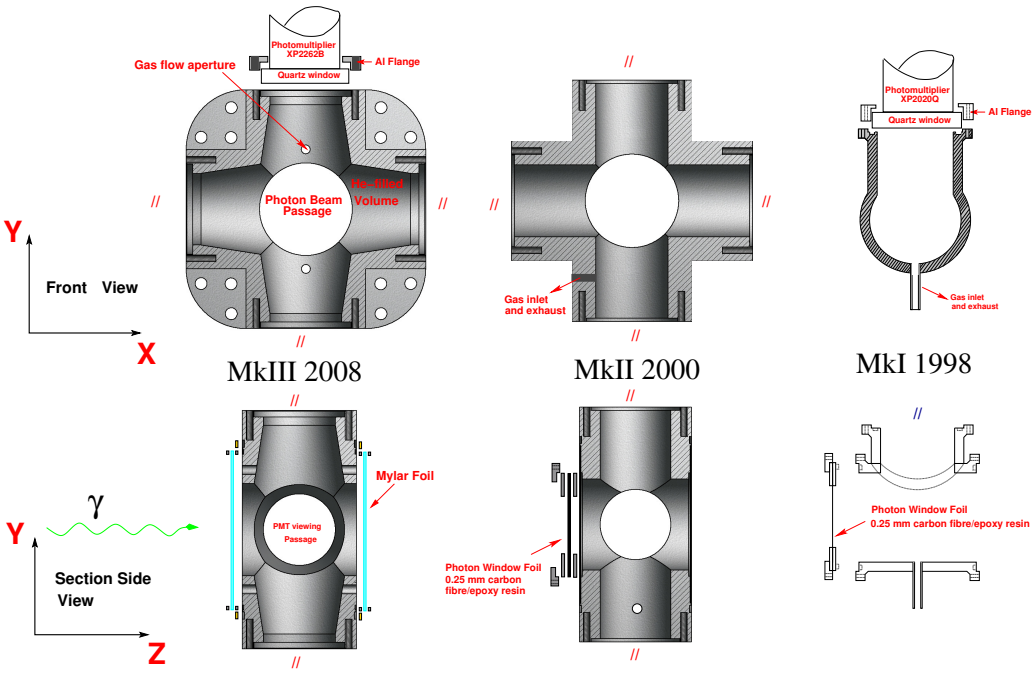

Figure 2.21: A schematic view of (left to right): the MKIII cell, the MKII and the MKI prototypes.

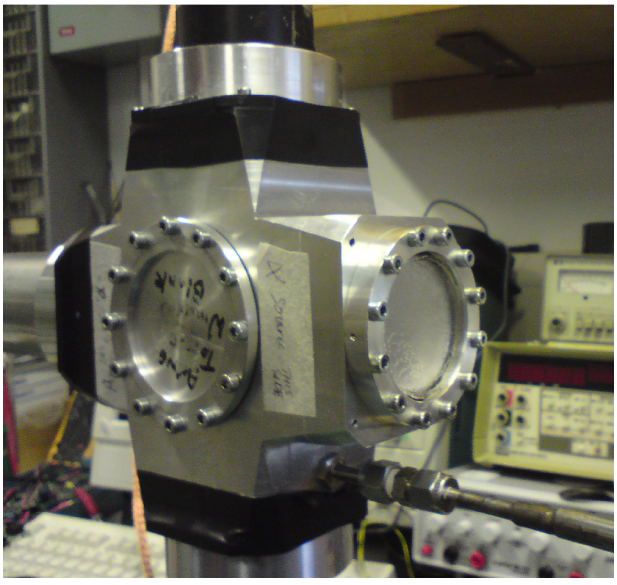

Figure 2.22: The MKII prototype. The beam entrance and exit carbon windows were replaced by Al disks for all bench tests with ^{241}Am α source.

investigations with the wavelength shifter paint. The MKI prototype consists of a pressurised gas-volume cell viewed by a single PMT type XP2020Q and operates at maximum pressure of 1 MPa. The main body of the cell is 72 mm long × 58 mm diameter machined from a solid aluminium block. Beam entrance and exit windows are a 0.25 mm-thick, carbon-fibre, epoxy-resin composite and the scintillation viewing window is 1 cm-thick, fused silica. Standard rubber O-rings and Al flanges were used to provide the seal between the fused silica windows and the Al body. In-beam tests with this prototype showed significant sensitivity of the PMT to non-scintillation events such as Čerenkov light produced in the quartz optical windows by relativistic electrons and direct electron interactions in the PMT electrodes. Nevertheless, following the unsuccessful experience with the wavelength shifter paint the prototype was found to be unusable.

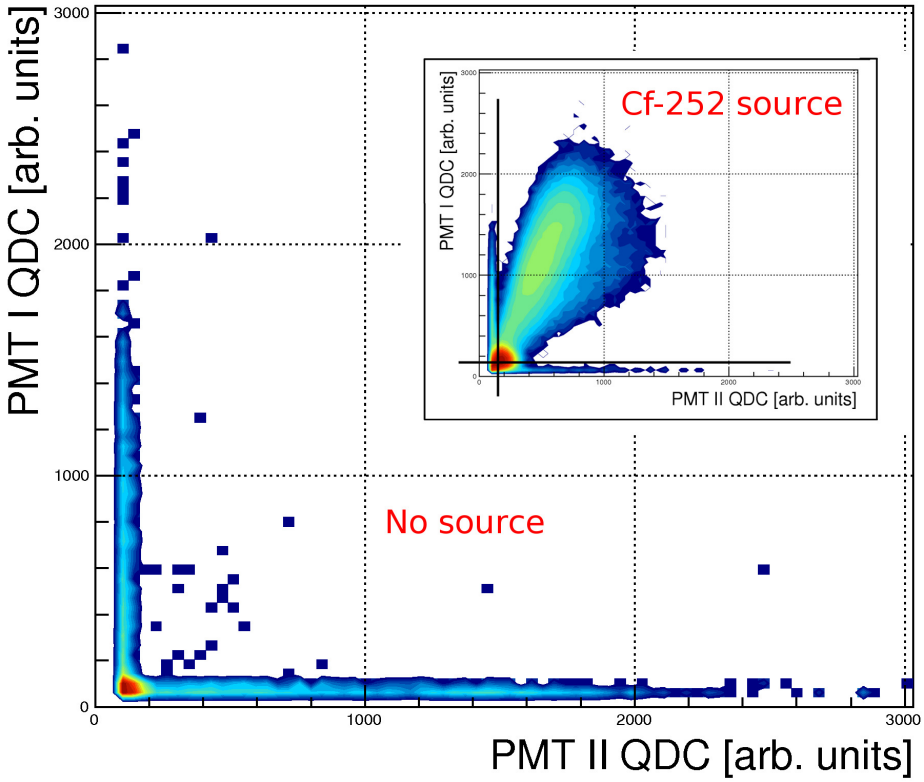

Figure 2.23: Comparison between the scintillation response with and without ^{252}Cf source. Real scintillation signals can be seen in correlation between two perpendicular PMTs, where the background can be seen as separated bands parallel to the axes.

The MKII prototype was constructed in 1999 at Lund in conjunction with the photo-nuclear group at MAX-lab. The dimensions and design of the MKII prototype is similar to that of the MKI prototype with a modification to the geometry to house three extra PMTs. This was done in order to reduce the sensitivity to interactions in the quartz windows by viewing correlated gas-scintillation signals in

two perpendicular PMTs. This was found to be very effective in identifying real scintillation events as can be seen in Fig. 2.18 and Fig. 2.23. The inside walls of the main body were painted with a bright white paint consisting of titanium dioxide pigment and a water soluble paint (EJ-510) [117]. The MKII prototype was used in all of our investigations with nitrogen and xenon where the beam entrance and exit carbon windows were replaced by Al disks. In-beam tests revealed that contributions from particles produced in the carbon-fibre windows of the prototype were also detected along with ^{4}He photodisintegration products and empty target-cell subtractions are not possible for an active target. Moreover, the prototype target thickness of 13 mg/cm^3 was adequate for total cross-section measurements, but rather thin for coincidence, exclusive measurements that were planned to run in parallel to the experiment detailed in this thesis. More details can be found in [33]. A photograph of the MKII prototype is displayed in Fig. 2.22.

The construction of the MKIII cell was made in 2008 to overcome the drawbacks of all of the previous prototypes. The beam entrance and exit windows were isolated from the main HGSAT cells by two auxiliary cells so that signals from particles produced in the entrance and exit windows are reduced. The outer carbon-fibre windows were replaced by 0.5 mm thick beryllium which are stronger. The target thickness was increased by a factor of 4 using a multi-cell design and a further factor of 2 by increasing the operating pressure to 2 MPa. The cells are optically isolated via thin aluminised mylar and are maintained at the same pressure by applying a connecting aperture throughout the cells. Light collection efficiency was increased by approximately 10% by machining truncated-cone shaped PMT viewing passages. The HGSAT MKIII is shown schematically in Fig. 2.1 and construction and assembly are described briefly in the following subsections.

2.4.3 Pilot Measurements at MAX-lab

Measurements with the MKII prototype were made at the pre-upgraded MAX-lab tagged photon facility in May 2001. MAX I, operating in pulse stretcher mode (see Sec. 3.4.2), delivered a ∼50% duty-factor, 93 MeV electron beam at a maximum current of ∼50 nA. The photon beam was generated via a broad-band tagging spectrometer in the energy range of E_γ = 11 - 70 MeV. Experimental details including the electronic setup and data acquisition are given in [33] and [124]. Preliminary $\gamma + {}^4$He yield and HGSAT-Tagger coincidences obtained from the 2001 data are shown in Fig. 2.25 [116]. A way of eliminating contributions from beam entrance and exit carbon-fibre windows was to take data with single and triple-thickness beam window to provide a basis to linearly extrapolate to zero window contribution (see Fig. 2.25[left]).

The preliminary analysis of inclusive $\gamma + {}^4$He and exclusive $^4\mathrm{He}(\gamma, n)^3\mathrm{He}$ measurements gave confidence that the active target technique will effectively yield cross section measurement close to the two-body breakup threshold and is likely to achieve

Figure 2.24: Experimental setup for the pilot measurements at the MAX-lab tagged photon facility in May 2001 [123].

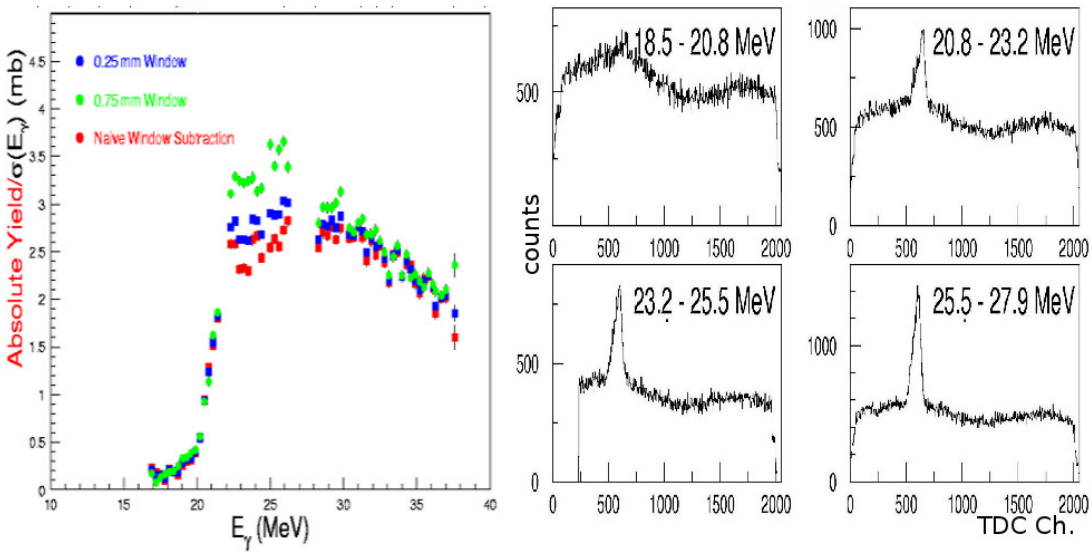

Figure 2.25: Left: Absolute yield measured with HGSAT (MKII) prototype. Right: Tagger time spectra for 4 tagged photon energies [116].

a high level of precision. Based on these grounds, measurement of the $\gamma + {}^4\mathrm{He}$ total photoabsorption cross section using HGSAT was approved and construction of the upgraded multi-cell HGSAT was given the go-ahead.

2.4.4 HGSAT Construction

The HGSAT was constructed at the workshops at the Kelvin building of the University of Glasgow over a one month period in September 2008, with the assistance of a 5 axis CNC (Computer Numerical Controlled) machine. The CAD (Computer-aided design) drawings of the HGSAT were fed into a CAM (Computer-aided manufacturing) programme which generated a compatible code that operates the CNC. The main cells were manufactured from 6 single blocks of solid aluminium alloy (6082-T6), measuring 150×150×80 mm. Upon finishing the mechanical work, each cell was washed several times with soapy water and cleaned with methanol and acetone sequentially. The inside structure of each cell was polished, hand painted with EJ-510 and then was left to dry for a period of one week at room temperature. A photograph taken during the construction of one of the main cells of the HGSAT can be seen in Fig. 2.26.

Figure 2.26: Construction of one of the main cells of the HGSAT using a 5 axis CNC machine.

2.4.5 Seal Design

A leak-tight seal of the HGSAT operating at 2 MPa pressure was difficult to obtain. Two different approaches were used to seal quartz to aluminium and aluminium

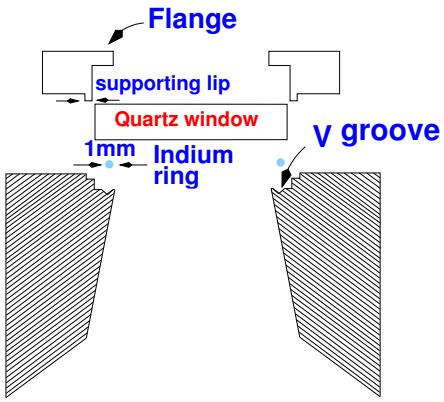

Figure 2.27: The semi-trapped indium O-ring seal used in all of the quartz-aluminium coupling.

to aluminium. Joined cells were sealed using a copper gasket pressed into a 1 mm depth × 110 mm diameter double knife-edge machined around the beam entrance and exit aperture of each cell. This approach was simple and proved very successful in holding the pressure. A high purity 1 mm diameter indium O-ring was used to seal the quartz optical windows to the HGSAT Al body. The seal design is shown in Fig. 2.27 and is known as a "semi-trapped indium O-ring" seal. In this design the indium is fixed in place via a V-groove but allowed to increase its contact area with the quartz when the flange bolts are tightened. Quartz windows and mating surfaces have to be exceptionally clean in order for this seal to work. Special treatment to the indium O-rings as recommended by [125] was also required.

2.4.6 Photomultipliers (PMTs) and Voltage Dividers (VD)

The 18 PMTs used in the HGSAT are the XP2262 type manufactured by PHOTONIS [126]. These PMTs were selected from 40 new PMTs purchased in two different batches. All of the PMTs were examined individually using a dark box, a 5 kHz nanoflash LED and one voltage divider (VD) base. Each PMT was connected to a generic counter consisting of a discriminator and a scaler and was housed in a μ-metal shield before it was placed in the dark box covered with a light-proof cloth. The PMTs operating voltage was determined by adjusting the high voltage (HV) in increments of 30 V, starting at the PMT "response voltage" and up to the maximum value as suggested by the supplier ∼2050 V, and noting the count rate which becomes relatively constant as the voltage is increased above the PMTs usual operating range. The corresponding pulse form was observed in each step via a high resolution digital oscilloscope. The pulse height versus HV measurements were also used to crudely equalise the pulse height of the PMTs by registering the HV required to give the average pulse height obtained. For dark noise measurements, the nanoflash LED was switched off and the PMT to be tested was left to "cool down" for ∼30 min. The dark noise rate was then simply measured by counting for 10 minutes. The PMTs were selected based on an optimisation between the PMT

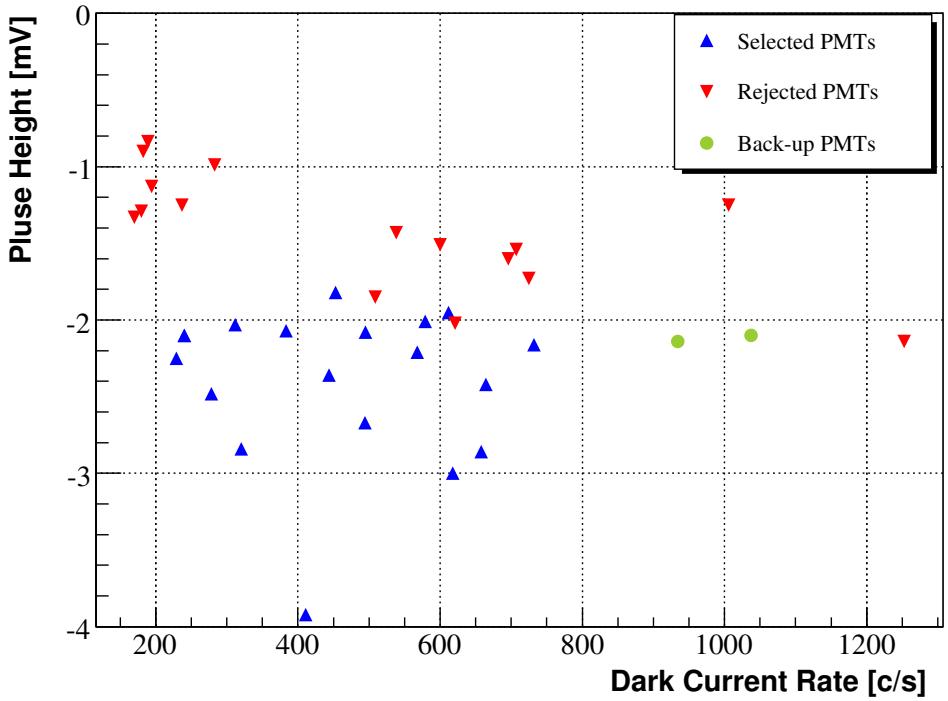

Figure 2.28: The pulse height and the dark noise rate obtained for all of the 40 tested PMTs operated at 1810 V. The up blue triangles show the selected PMTs. The two green circles represent the PMTs which were kept aside as a back-up. These two had slightly more dark current the the rest but were chosen since they came from the same batch as most of the selected PMTs.

gain and the associated dark noise rate as can be seen in Fig. 2.28.

The VD needed to distribute the high voltage to each dynode in the PMT was custom designed in Glasgow. The designed circuit consists of a series of 13 resistors, 5 capacitors and 3 zener diodes. Different configurations were tested prior to the experiment detailed here using a test XP2262B PMT and the same apparatus employed for the PMTs testing mentioned above. The VD circuit was optimised for the maximum pulse height and minimum pulse shape variation with amplitude. The VD circuit is shown in Fig. 2.29.

2.4.7 Full Assembly and Integration

The assembly of the HGSAT involved bolting the 6 cells together with copper gaskets and ∼5 µm thick mylar foils, held by two thin aluminium frames, in between. Indium was treated and cleaned according to [125] and then cut in a pre-specified purpose-made groove, pressing the two ends of the indium wire against each other to make the joint. The indium O-ring would then be placed in a V-groove at the bottom of each quartz-window recess stepping. Two 1 mm thick Teflon washers were used

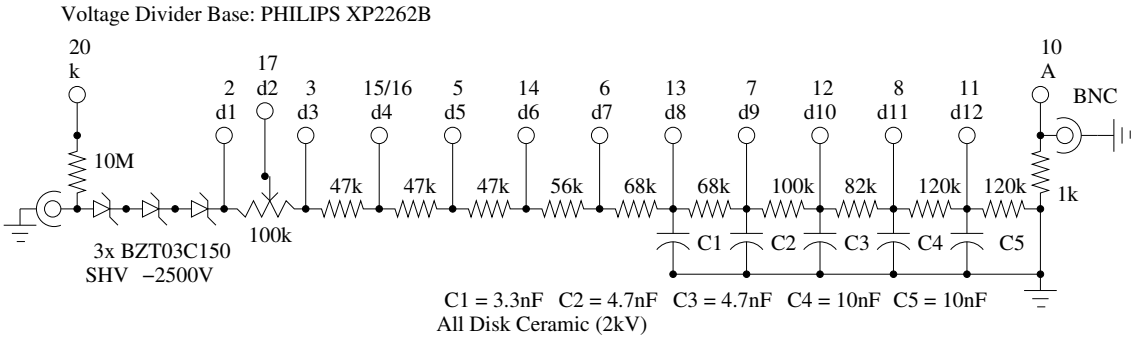

Figure 2.29: PMT voltage divider (VD) circuit diagram.

at the top of each quartz window to prevent the quartz window from coming into direct contact with the flange which could produce a localized area of high stress. The assembly concluded by fitting four XP2262B Photonis PMTs to each cell using standard optical grease. A μ-metal shield was then fitted to each of the PMTs to reduce the effect of stray magnetic fields. The μ-metal is held in place by two springs. Fig. 2.30 shows the fully assembled HGSAT under vacuum and ready to be filled with the gas mixture just before the experiment.

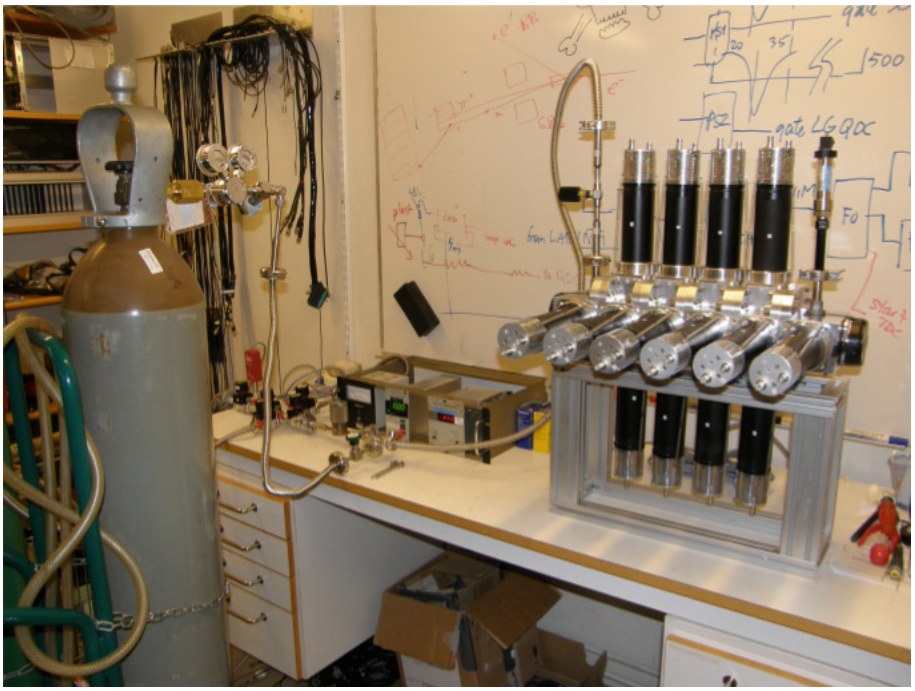

Figure 2.30: The fully assembled HGSAT under vacuum and ready to be filled with the gas mixture before the experiment.

Chapter 3

Experimental Details

3.1 Overview

The total $\gamma + {}^4\mathrm{He}$ cross-section measurement detailed in this thesis was performed using the Helium Gas-Scintillator Active Target (HGSAT) (see Ch. 2). This measurement required access to monochromatic photons with a relatively low energy, ranging from just below the breakup threshold ($\sim 20\,\mathrm{MeV}$) up to the pion production threshold. Such a photon beam may be generated by a variety of techniques, with two of the most common methods being either by means of bremsstrahlung radiation or Compton back-scattering techniques through specialised electron accelerators. Many of these accelerators are located within different research facilities worldwide, however only a limited number of these facilities are capable of delivering photons in the required energy range due to the nature of the research conducted at these facilities and technical limitations. Prominent among these facilities are the MAX-lab tagged photon facility in Sweden [127], Laser Compton backscattering (LCS) at the National Institute of Advanced Industrial Science and Technology (AIST) in Japan [128] and the High Intensity Gamma-Ray Source (HIgS) in the USA [129].

The Glasgow NPE group has been involved for many years in a collaboration with the Photonuclear Physics group at the University of Lund in Sweden. That led to a series of successful experiments for a variety of measurements, such as those on the (γ, n) reaction in light nuclei by Akkurt et al. in 1998 [130], on the ${}^4\mathrm{He}(\gamma, n){}^3\mathrm{He}$ reaction by Nilsson et al. in 2003 [29] and on differential photoneutron cross-sections for neutron dosimetry by Reiter et al. in 2004 [131]. These measurements were all made using the MAX-lab facility where tagged-photon energies from $\sim 10 - 80\,\mathrm{MeV}$ were available [29]. Details of other measurements conducted at MAX-lab can be found on their website [127]. The experiment presented here is the latest and not the last in this collaboration and was carried out over a period of four weeks between March and September 2009 at the upgraded (see Sec. 3.3) MAX-lab tagged photon facility.

The total $\gamma + {}^4\mathrm{He}$ cross-section as a function of photon energy (E_γ) is given by the following equation:

$$\sigma(\mathrm{E}_\gamma) = \frac{\mathrm{Y_x}(\mathrm{E}_\gamma)}{\varepsilon_\mathrm{x}(\mathrm{E}_\gamma)\varepsilon_\mathrm{tagg}(\mathrm{E}_\gamma)\varepsilon_\mathrm{s}(\mathrm{E}_\gamma)\mathrm{N_e}(\mathrm{E}_\gamma)\mathrm{N_A}\rho\mathrm{t}/\mathrm{m_{He}}} \tag{3.1}$$

where $\mathrm{Y_x}(\mathrm{E}_\gamma)$ is the reaction yield, $\varepsilon_\mathrm{x}(\mathrm{E}_\gamma)$ is the HGSAT detection efficiency, $\varepsilon_\mathrm{tagg}(\mathrm{E}_\gamma)$ is the tagging efficiency, $\varepsilon_\mathrm{s}(\mathrm{E}_\gamma)$ is the tagger stolen coincidence correction, $\mathrm{N_e}$ is the number of electrons counted in the focal plane (FP) detector corresponding to photon energy (E_γ), $\mathrm{N_A}$ is Avogadro's constant (mole^{-1}), ρ is the target density ($\mathrm{g.cm}^{-3}$), t is the thickness of gas in the path of the photon beam (cm) and $\mathrm{m_{He}}$ is ${}^4\mathrm{He}$ atomic mass ($\mathrm{g.mole}^{-1}$). The product of $\mathrm{N_e} \,.\, \varepsilon_\mathrm{tagg}$ defines the number of incident photons on the target (N_γ).

This chapter focuses on the details of that experiment and covers a brief overview of the MAX-lab tagged photon facility and its accelerator system, the photon tagging system and the principle of tagging, along with a detailed description of the detectors used in the experiment and concludes with an explanation of the associated electronic set-up and Data Acquisition system (DAQ). A summary of the experimental runs is also given at the end.

3.2 Bremsstrahlung Tagging

In the photon tagging technique the bremsstrahlung electron energy is measured to obtain the energy of the corresponding bremsstrahlung photon. The photon is said to be "tagged" by the electron. The earliest utilisation of the tagging technique to produce photons of known energy was reported by J. W. Weil and B. D. McDaniel in 1953 [132] who produced photons of $\sim 200\,\mathrm{MeV}$ for proton photoproduction studies using a single tagging counter and a target inside a 310 MeV synchrotron. Despite the difficulties and the unenthusiastic evaluation [132], the technique hugely inspired many experimentalists at the time and it was adopted for different experiments using single tagging counters [133–135]. Later in 1964, Caldwell et. al. developed the first multi-tagging counter, a 19 counter hodoscope, to produce 2 to 5 GeV tagged photons using a positron beam and a radiator buried inside the tagging magnet [136]. In the following years the apparatus used for the tagging technique continued to improve [137–139] and since the development of high duty-cycle electron accelerators in the late 1970's and early 1980's, tagging of bremsstrahlung photons has become one of the most successful techniques for producing photons of known energy [4]. The concept is well understood and the apparatus is fully developed and it is being routinely used in various photonuclear experiments.

3.2.1 Photon Tagging and Coincidence Measurements

The concept of the bremsstrahlung tagging technique is straightforward. A beam of monoenergetic electrons with energy ($\mathrm{E_e}$) generated through an accelerator sys-

tem is directed onto a thin metal foil radiator, a small fraction of the electrons are decelerated by the radiator nuclei generating photons (E_γ) in the forward direction via the bremsstrahlung process. The energy transferred to the radiator nuclei is negligible [140].

Since the radiator is very thin, the majority of the incident electrons pass through the radiator almost undisturbed and are deflected directly by a magnet into a beam dump, while the corresponding bremsstrahlung electrons ($E_{e'}$) are deflected to an array of detectors known as the "focal plane" array where they are detected and counted via scalers. The position where the bremsstrahlung electron hit the focal plane array is determined by its momentum, thus the electron energy is identified from the hit position in the array. That produces a signal that announces the production of a photon with energy (E_γ):

$$E_\gamma = E_e - E_{e'} \tag{3.2}$$

The photon beam is collimated and directed towards the target in the experimental area causing a photo-induced reaction that yields a signal triggered by the detection of one or more reaction products in the experimental detector. The time coincidence between the bremsstrahlung electron signal and the reaction signal indicates that the observed reaction was caused by a photon of energy (E_γ). Practically, this is done by connecting each detector of the focal plane array and, the experimental detector to a time-to-digital converter (TDC) module that measures the time difference between the arrival of the experimental detector signals and an electron detected in the corresponding focal plane detector. The resultant TDC spectrum of this time difference consists of a peak representing true coincidences superimposed on a background of random coincidences between uncorrelated bremsstrahlung electrons and the experimental detector signals. The yield of the photo-induced reaction is then simply determined by integrating number of events under the true coincidence peak after background subtraction for each of the TDC spectra. A schematic diagram of the bremsstrahlung tagging technique and coincidence measurement is illustrated in Fig. 3.1.

3.3 MAX-lab Tagged Photon Facility

MAX-lab is a high-energy electron and synchrotron radiation source based in Lund, southern Sweden. It is a Swedish National Laboratory for research, operated by Lund University under a contractual agreement with the Swedish Research Council (Vetenskapsrådet, VR) [141]. The name "MAX" comes from the days when the laboratory utilised a Microtron and a storage ring for X-ray and tagged photons in the early 1980's, that is **M**icrotron **A**ccelerators for **X**-Rays [142]. The microtron is no longer being used and it was replaced with a new injector in 2004 consisting of an electron gun and two linear accelerators (LINAC). As well as for Nuclear Physics research, MAX-lab is being used in two other discrete research areas: Accelerator Physics, and Synchrotron Radiation applications. As a result, the time at the facility

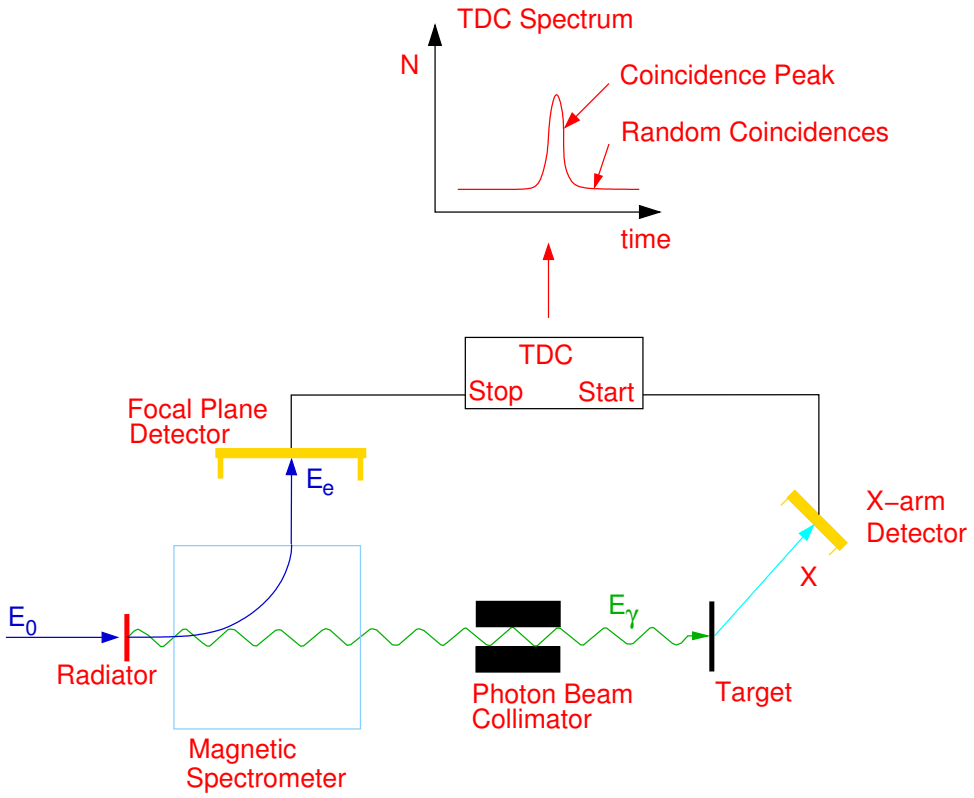

Figure 3.1: Schematic diagram of the bremsstrahlung tagging technique [4].

is shared between groups working within these three fields. In total, eighteen weeks of beam time were used for the Photo-nuclear Physics programme during 2009 [141], four of these weeks were dedicated exclusively to this experiment between March and September.

MAX-lab runs three main accelerators- a 550 MeV storage/pulse-stretcher ring MAX I commissioned in 1986, and two third-generation electron-storage rings 1.5 GeV MAX II and 700 MeV MAX III commissioned in 1997 and 2008 respectively. These three rings, with MAX I being in storage mode, are used to produce synchrotron radiation for research in the UV, VUV and soft X-ray regions using various spectroscopic techniques. Only MAX I, in pulse-stretcher mode, is part of the tagged photon facility at MAX-lab and used for experiments relating to nuclear physics. Thus, details on MAX II and MAX III will not be discussed here and the reader is advised to refer to Refs [143] and [144] for more details of those rings while, additional information on the facility can be found in Refs [127] and [141].

The Tagged Photon facility at MAX-lab comprises of the Accelerator system where the electron beam is generated and made suitable to use for photo-nuclear physics experiments, beam transportation system and the Tagging system located in the basement where the tagging process takes place. The facility was upgraded in connection with the construction of MAX III in 2004. The upgrade included

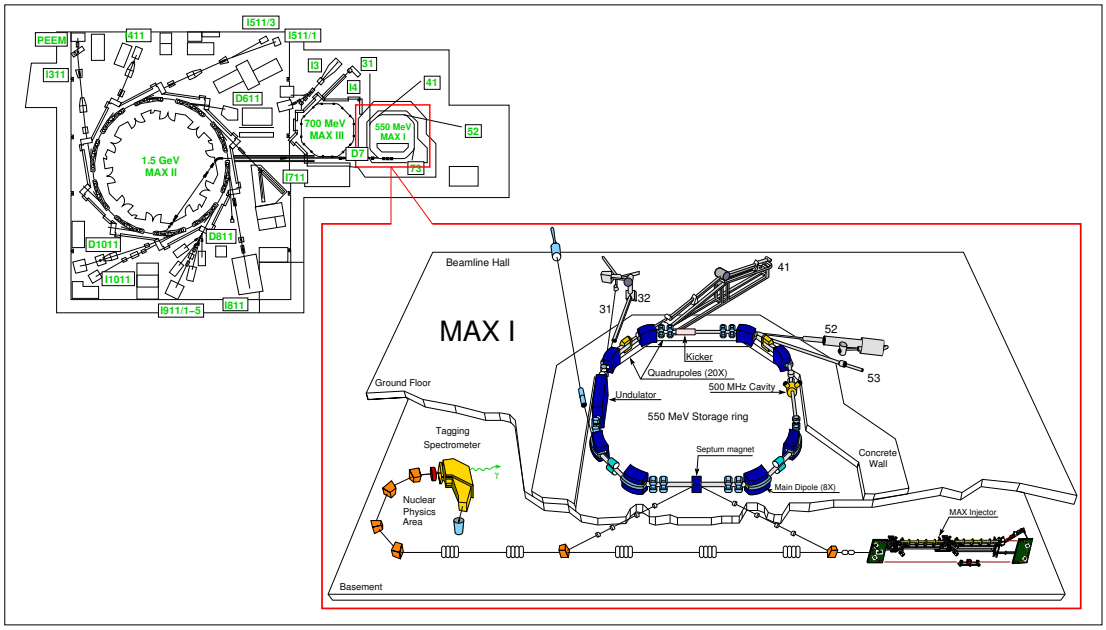

Figure 3.2: An overview of the MAX-lab facility showing the MAX I,II and III rings [141]. MAX I is zoomed in to show the Nuclear physics area located in the basement [29].

an installation of a new injector that increased the injected electron energy from 140 MeV to 250 MeV. The nuclear physics experimental hall was also enlarged to allow more space for larger detection systems and longer flight paths for time-of-flight measurements. A new achromatic beamline was installed together with the tagging spectrometers formerly used at the Saskatchewan Accelerator Laboratory (SAL). The first stretched beam after the upgrade completion was delivered in May 2006. Since then the tagging facility and the MAX I stretcher ring have been used for photo-nuclear experiments with a high degree of precision and the efforts are pursued within an international collaboration with around fifty members [145]. An overview of MAX-lab showing the MAX I,II and III rings as well as a zoomed view of MAX I and the nuclear physics area are shown in Fig. 3.2. The following sections focus on the details of the tagged photon facility components and their method of operation.

3.4 Accelerator System

The accelerator system utilised for this experiment consists of a 250 MeV electron injector (the MAX injector) and the MAX I ring running in pulse-stretcher mode. A detailed description of the MAX injector can be found in Ref. [146] while details on MAX I can be found in [147] and [148]. Thus, only a brief overview is given in the next few sections.

3.4.1 MAX Injector

The MAX injector is used to feed electrons to MAX I as well as to the other two rings and to the Free Electron Laser (FEL) experiment set-up inside the ring of MAX II [127]. Electrons are emitted initially in short pulses ($\sim$ 3 ps wide [146]) from a BaO cathode via a 3 GHz thermionic RF-gun and pre-accelerated to approximately 1.6 MeV [149]. A solenoid magnet at the gun exit is used to compensate for the defocusing caused by space charge effects and the electron beam is treated in a double bend achromat (DBA) structure containing two 60° bending magnets and five quadrupoles to filter out low energy electrons (an undesirable effect associated with all thermionic guns), that results in a 50% reduction of the gun output [150]. Upon leaving the gun, the electrons are further accelerated by two 5.2 m linear accelerators (LINACs) each having an energy gain of up to 100 MeV with 125 MeV maximum. It is at the LINACs where the final electron beam energy delivered to the nuclear physics area is determined. In this experiment, two electron beam energies were used, 142.9 MeV in March and 164 MeV in September of 2009 that produced tagged photon beams an with energy range of $12.7 - 60.5$ MeV and $13.7 - 68.8$ MeV respectively [141].

The electron beam leaves the MAX Injector in pulses of approximately 150 ns width and at a repetitive rate of 10 Hz thus a duty factor[1]of $\sim 1.5 \times 10^{-4}$%. The beam is then injected through the beamline to the Pulse-Stretcher Ring (MAX I) situated above the injector via a Lambertson injection septum [152].

3.4.2 Pulse-Stretcher Ring MAX I

The need for a stretcher ring comes from the fact that high intensity pulsed beam coming directly from the injector is not suited to carry out photo-nuclear physics experiments where cross-sections for the reactions are very low. A beam with such extremely poor duty factor would not only saturate the data acquisition system, tremendously increase data processing dead time and make the real to random ration too poor, but would also result in bad statistics and poor data quality. The pulse stretcher ring is therefore used to improve the duty factor by converting the injector pulsed beam into a semi continuous-wave (CW) form.

The Lambertson septum magnet bends the incoming beam 30° in the vertical plane until it enters parallel to the stretcher ring MAX I median plane and is captured in the ring orbit with the aid of the injection kicker and a 500 MHz RF cavity to compensate for the energy losses by synchrotron radiation [148]. The injection

[1]Duty factor in its general definition is the ratio of the pulse duration to its repetition time. The term is commonly used in accelerator physics to describe how continuous an accelerator pulsed beam is. That is the fraction of time that particles actually strike a particular target [151]. As an example, if an electron beam with a 50% duty factor strikes a particular target for a specific period of time, electrons in that beam will only hit the target half of the time the beam is present.

of a ∼150 ns pulse is done over two turns in the MAX I ring which has a ring circumference of 32.4 m, corresponding to 108 ns flight time for relativistic electrons. Since the pulse width is not exactly 150 ns but oscillates between 100 and 200 ns, uneven filling of the ring occurs resulting in some modulation of the stretched beam by the revolution frequency of the ring [153]. The ring current recorded during the experiment varied between 5 mA to 20 mA [154] depending on the machine status, operation conditions and the type of measurement.

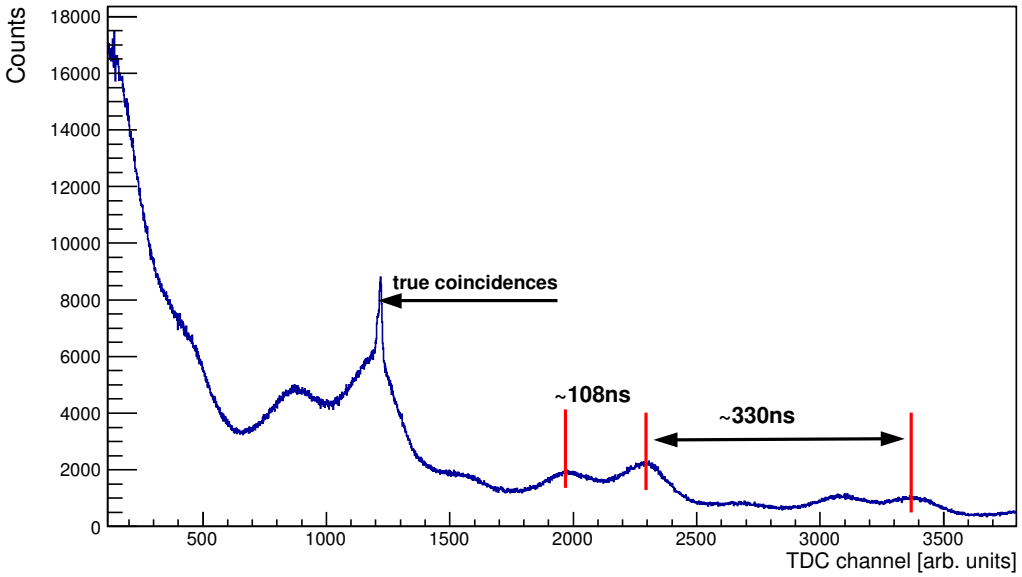

Figure 3.3: An uneven filling of the MAX I ring and the 3 MHz extraction RF-Kicker cause modulation to the stretched beam, the ∼108 ns and the ∼330 ns structures in the stretched beam time profile respectively. The ∼2 ns period caused by the 500 MHz accelerating cavity requires higher timing resolution to be observed. The plot also shows the $\gamma + {}^4\mathrm{He}$ true coincidences peak at around 1200 TDC channel (see Ch. 5).

Once the injection to MAX I is completed, the electrons are then driven towards the third betatron resonance by a RF-kicker that is operated at the same resonance frequency and slowly extracted by the extraction magnets over a 100 ms period, that is until the next pulse from the injector arrives. Extracting the beam this way improves the duty factor by a factor of $\sim 10^5$, and in perfect conditions a duty factor of 100% is possible, but due to the synchrotron losses and other accelerator related factors (beyond the scope of this thesis), the duty factor currently achieved at MAX-lab is in the range of $40-80\%$ [155]. The extracted beam is then bent down 30° by the magnetic septum and directed to the nuclear physics experimental hall located in the basement where it is bent back into the horizontal plane. Finally, the beam is guided toward the tagging spectrometers by a further 50° bend in the same

horizontal plane. The stretched beam current was about 15 nA on average during this experiment [154].

The 500 MHz accelerating cavity and the 3 MHz extraction RF-Kicker both cause a further modulation to the stretched beam due to their operating frequency. That results in clear 2 ns and 330 ns structures in the stretched beam time profile. These effects, along with the one caused by the uneven filling of the ring mentioned earlier (see Fig. 3.3), will have a direct impact on the experiment data analysis as will be shown in the next chapter.

3.5 The Bremsstrahlung Tagging System

The tagging system at MAX-lab (Fig. 3.4) is used to produce bremsstrahlung photons solely for nuclear physics experiments. The main component of the tagging system is the Tagging Spectrometer, "the Tagger", which is composed of the spectrometer magnet and the Focal Plane (FP) hodoscope. The tagger spectrometer is used to measure the energy of photons in a bremsstrahlung spectrum, as will be described in the next few sections. There are two tagging spectrometers currently being used at MAX-lab tagged photon facility. The so-called Main Tagger (MT) which covers a wide range of photon energies corresponding to $\sim 10-70\%$ of the incoming electron beam energy, and the End point Tagger (ET) with $\sim$30 MeV tagged range which is used to tag photons as close as 10 MeV from the endpoint of the bremsstrahlung spectrum [156]. As only one tagger system can be used at a time for any experiment the same focal plane hodoscope is used for both systems. For this work, the main tagger was used for its broad energy range coverage. The two tagging spectrometers, along with their focal plane hodoscope, were designed and used at the Saskatchewan Accelerator Laboratory (SAL) during the 1990's. After its closure in 1999, the two tagging spectrometers were taken to MAX-lab. Full technical details of the main tagger can be found in Ref. [157].

3.5.1 The Spectrometer Magnet

The Main Tagger (MT) magnet is a large clam-shell dipole magnet with a large momentum acceptance covering $\pm 40\%$ of the central momentum (P_0), which has a maximum value of 200 MeV at 1.25 Tesla and bend angle of 110°. The magnet is used to steer the primary non-interacting electron beam toward an external movable dump magnet where the beam is dumped into a Faraday cup [155], and to focus the post-bremsstrahlung electrons outside the magnetic field at the magnet exit into a vertical plane known as the tagger focal plane where the electrons are momentum analysed in the focal plane hodoscope. The focal plane is flat over the range of $0.8\,P_0$ to $1.4\,P_0$ but curved over the range $0.6\,P_0$ to $0.8\,P_0$.

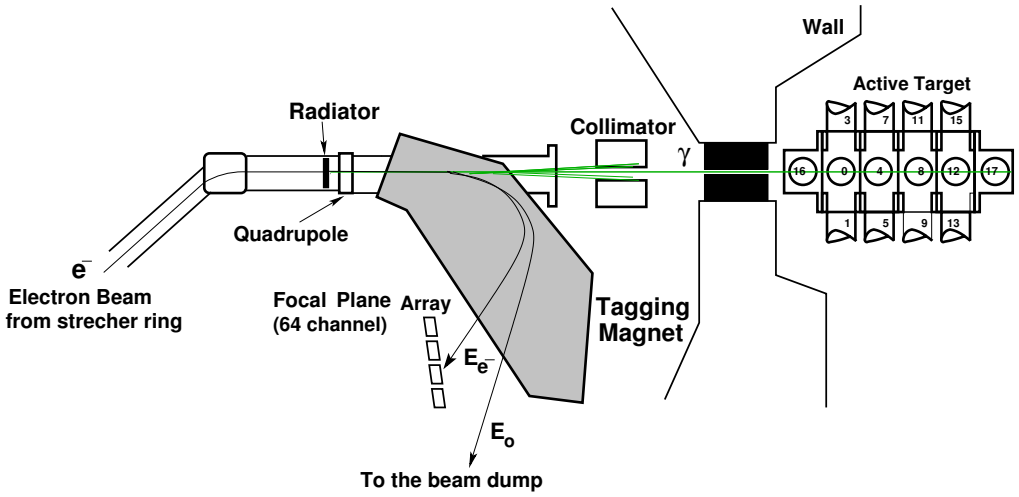

Figure 3.4: A schematic of the tagging system.

3.5.2 The Focal Plane (FP) Hodoscope

The focal plane hodoscope is an array of 63 scintillation counters arranged in two overlapping rows with 31 counters in the front row and 32 in the back. Each scintillation counter consists of a 3 mm thick 25×50 mm plastic scintillator connected to a Philips XP1911 photomultiplier tube via a Lucite light-guide. The overlapping area between the two rows is adjustable depending on user requirements. The need for this overlapping arises because demanding a coincidence between the signals of two scintillators can effectively suppress background and improve the energy resolution. In this experiment, the overlap was 50% of the scintillators's width in the projection perpendicular to the trajectories of electrons exiting the dipole as shown in Fig. 3.5. Each overlapping section represents a tagger channel with ~ 850 keV energy resolution (ΔE_γ). A tagged electron hit is generated by coincident hits in two overlapping scintillators, thus the full focal plane hodoscope has 64 coincidence tagging channels in total. The focal plane hodoscope is positioned next to the tagger magnet exit window where post-bremsstrahlung electrons are detected. Since the focal plane hodoscope covers only a portion of the bremsstrahlung spectrum of $\sim 48 - 55$ MeV tagging range known as the "tagger bite", for a typical incident electron beam energy of 145 MeV, the focal plane hodoscope must be shifted along the focal plane in order to get the full energy coverage. This procedure was not necessary in this experiment as the tagged energy range provided by a fixed focal plane hodoscope was $\sim 12 - 61$ MeV which is sufficient for this experiment. The electron count rate of the focal plane was in the range of 1 to 2.5 MHz per channel [154] constrained by rate limitations of the XP1911 PMTs used.

3.5.3 Photon Tagging

The stretched electron beam (see Sec. 3.4.2) directed toward the tagging system strikes a thin metal foil radiator upstream of the tagging spectrometer delivering

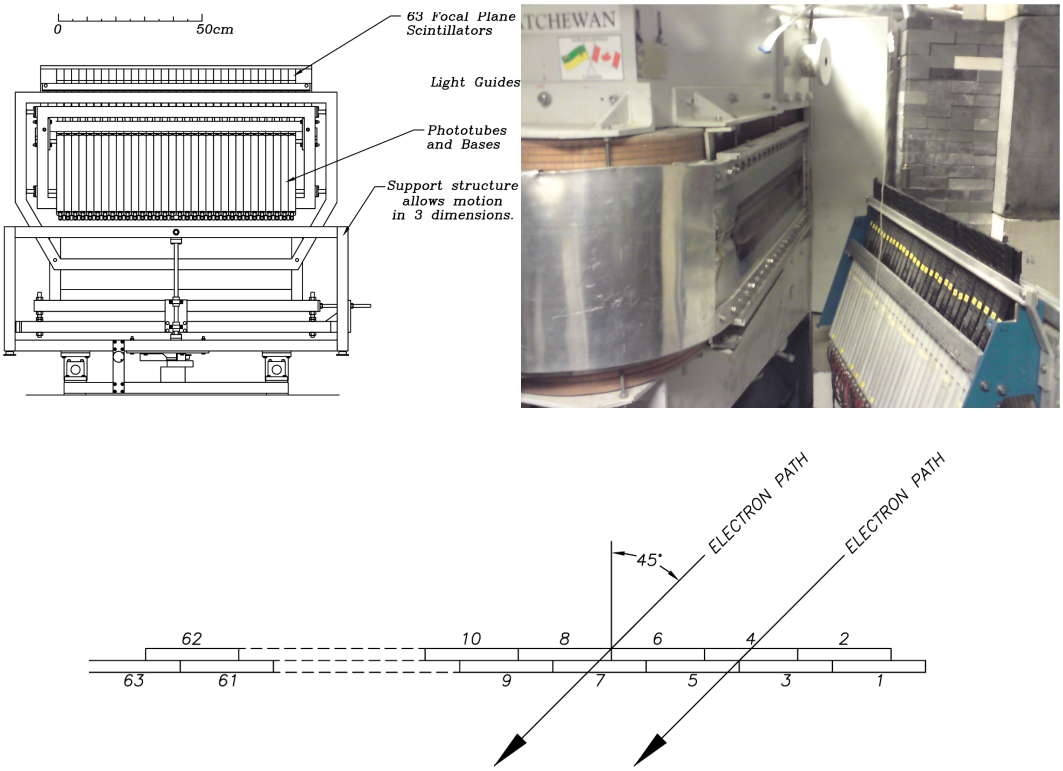

Figure 3.5: The focal plane hodoscope is shown next to the main tagger. Up left: The detector array and support structure [158]. Up right: The focal plane hodoscope is positioned in a defined place for the selected tagger bite of the bremsstrahlung spectrum. Bottom: The staggered scintillators arrangement [158].

bremsstrahlung photons, approximately within a cone half-angle of

$$\theta_\gamma \approx \frac{1}{E_e/m_e} \tag{3.3}$$

where m_e and E_e are the electron rest mass and beam energy respectively. During this experiment a 50 μm thick aluminium foil radiator was used. For such a thin radiator, slightly less than 0.1% of incident electrons produce bremsstrahlung photons with a corresponding opening angle of ∼3.6 and 3.1 mrad for an incident electron energy of 142.9 and 164.8 MeV respectively. The radiator products, both post-bremsstrahlung electrons and bremsstrahlung photons as well as primary non interacting electrons, enter the MT spectrometer. The primary non-interacting beam is steered directly into a well-shielded[2] Faraday cup of the beam dump with the aid of an external dump magnet allowing the beam current to be monitored. The post-bremsstrahlung electrons with momenta within the momentum acceptance of the tagger magnet are bent via the tagger magnetic field towards the focal plane hodoscope. The position of the electron hit along the focal plane is directly related to its momentum. For a given tagger setting, the momentum of the electron may be related to the hit position on the focal plane by the following relation [153]:

$$w_i = a{x_i}^5 - b{x_i}^4 + c{x_i}^3 + d{x_i}^2 + ex_i - f \tag{3.4}$$

Where w_i is the fraction of the electron beam energy associated with the tagger channel i, x_i is the central position of the tagger channel i along the focal plane and a, b, c, d, e, and f are constants specific to the main tagger:

$a = -9 \times 10^{-10}$, $b = -2 \times 10^{-8}$,
$c = \ \ 4 \times 10^{-6}$, $d = 1.3 \times 10^{-3}$,
$e = 6.4 \times 10^{-1}$, $f = -6 \times 10^{-4}$,

The post-bremsstrahlung electron energy at the centre of the tagger (E_0) for a given electron beam is then given by the following relation [159]:

$$E_0 = 198.6419\frac{E_e}{S} \tag{3.5}$$

where S is a number indicating the setting of the dump magnet (S = 345 for both March and September 2009 experimental runs) and E_e is the incident electron beam energy. Thus, the bremsstrahlung photon energy corresponding to each tagger channel ($E_{\gamma(i)}$) is then calculated using the following equation which is identical to equation 3.2:

$$E_{\gamma(i)} = E_e - w_i \times E_0 \tag{3.6}$$

The photon beam passes through the tagging spectrometer unaffected by the magnetic field of the tagger magnet and enters into the experimental hall through a

[2] To reduce the beam dependent background in the experimental hall by absorbing photons and neutrons produced by interactions of the energetic electrons.

4.5 mm diameter collimator 1828 mm downstream of the bremsstrahlung radiator. The usage of the collimator was necessary to ensure the photon beam spot is kept within the 25 mm diameter of the entrance/exit windows. The fraction of photons $\alpha(\psi)$ remaining after collimation is roughly given by the following relation [131]:

$$\alpha(\psi) = \frac{\int_0^{\psi} \frac{d\sigma_{(brem)}}{d\Omega} d\theta}{\int_0^{\pi} \frac{d\sigma_{(brem)}}{d\Omega}} = \frac{1}{1 + (\theta_\gamma/\psi)^2} \tag{3.7}$$

where ψ is the opening angle of the bremsstrahlung photons at the target entrance and $\mathrm{d}\sigma_{(\mathrm{brem})}/\mathrm{d}\Omega$ is the angular distribution. For the given radiator-collimator-target distances (see Fig. 4.17) the angle (ψ) was $\sim$ 1.1 mrad giving a beam spot of $\sim$9 mm on the target, thus the fraction of photons expected to reach the target after collimation is approximately 8.5% and 11% for the 142.9 and 164.8 MeV electron beam energy respectively.

During the two runs of this experiment, the photon beam was available Tuesday morning through Monday morning the following week with some interruptions in between due to a variety of machine operation problems, see Ref. [154] for more details. In addition, there were two breaks a day to allow for filling the two storage rings MAX II and MAX III. In an average week, $\sim$ 120 hours of stretched beam is delivered to the nuclear physics area [156].

3.5.4 The Tagged Photon Beam

The energy distribution of bremsstrahlung photons is continuous, ranging from zero and up to the end-point energy[3] [140]. During this experiment, 142.9 MeV and 164.8 MeV incident electron beams were used in March and September of 2009 respectively. The difference in energy was due to machine operation factors and was of no significance to the experiment.

The bremsstrahlung photon distribution for an incident electron beam energy of 164.8 MeV striking a 50 µm Al radiator and the tagged photon regions are shown in Fig. 3.6. The spectrum was calculated using the equations in Ref. [160], implemented by Ref. [153] and re-written in C++ by the author. The bremsstrahlung photon distribution for 142.9 MeV electron beam is similar to that of 164.8 MeV but with a different end-point value and with a slightly different tagged photon region.

3.5.5 Tagging Efficiency Measurement

The number of tagged photons inducing reactions in the experimental target is related to the sum of post-bremsstrahlung electrons detected in the focal plane hodoscope for each tagger channel i. Practically, the photon flux is reduced by a certain factor due to the use of the collimator downstream of the radiator to ensure

[3] End-point energy is the energy of the incident electron beam ($\mathrm{E_e}$).

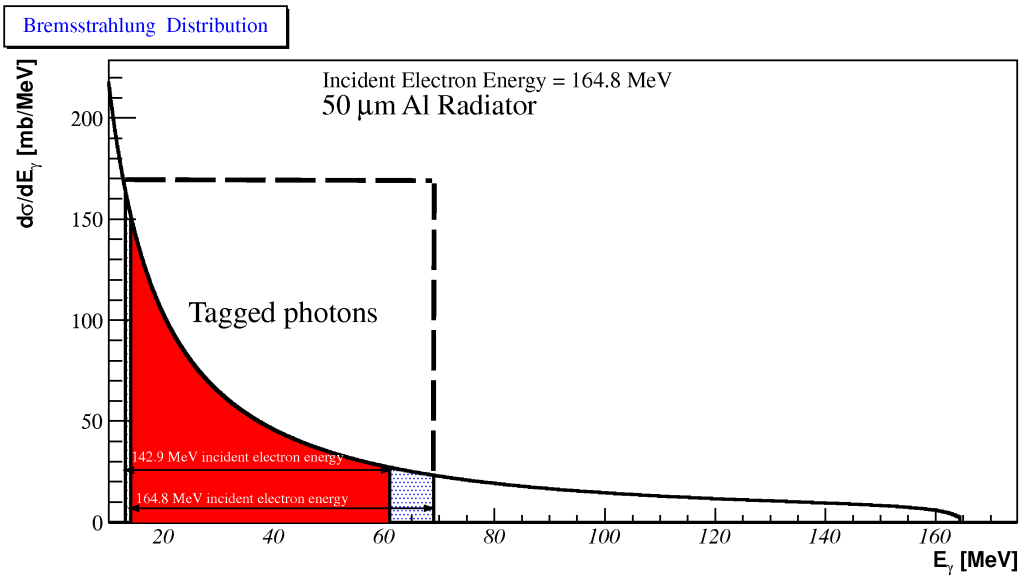

Figure 3.6: The bremsstrahlung distribution using the 50 μm Al radiator and a 164.8 MeV electron beam energy, with the tagged-photon energy range for this experiment highlighted in red for the 142.9 MeV electron beam energy and the dashed blue area for the 164.8 MeV electron beam.

the beam spot is kept within the target. The losses in the photon flux must be taken into account for precise cross-section measurement. This is done experimentally by the measuring the so-called "tagging efficiency (ε_{tagg})", which for each tagger channel i is defined as follows:

$$\varepsilon_{tagg(i)} = \frac{N_{\gamma(i)}}{N_{e'(i)}} \tag{3.8}$$

where $N_{\gamma(i)}$ is the number of tagged photons after collimation counted in coincidence and $N_{e'(i)}$ is the total number of electrons counted in focal plane hodoscope element i.

Tagging efficiency measurement has became a common practice in almost all photonuclear experiments to determine the number of tagged photons passing through the target, which is needed to normalise the cross-section as will be discussed in Ch. 5. The measurement was done with the aid of a lead/scintillating fibre (Pb/SciFi) detector [161], known as the "Spaghetti" detector, placed directly in the photon beam line downstream of the target to measure the total number of tagged photons passing through the target after collimation (N_γ). As the name implies, the detector is made of a uniform array of plastic scintillating fibres embedded in lead alloy and has ∼100% photon detection efficiency and good timing characteristics. It was originally developed for use in the CERN Low-Energy Antiproton Ring (LEAR). Full technical details of the detector can be found in Ref. [161]. Tagging efficiency depends on the collimator diameter and how far it is positioned from the radiator, the incident electron beam energy, and how well the target and the beam are aligned along the collimator axis. It also depends slightly on the photon energy

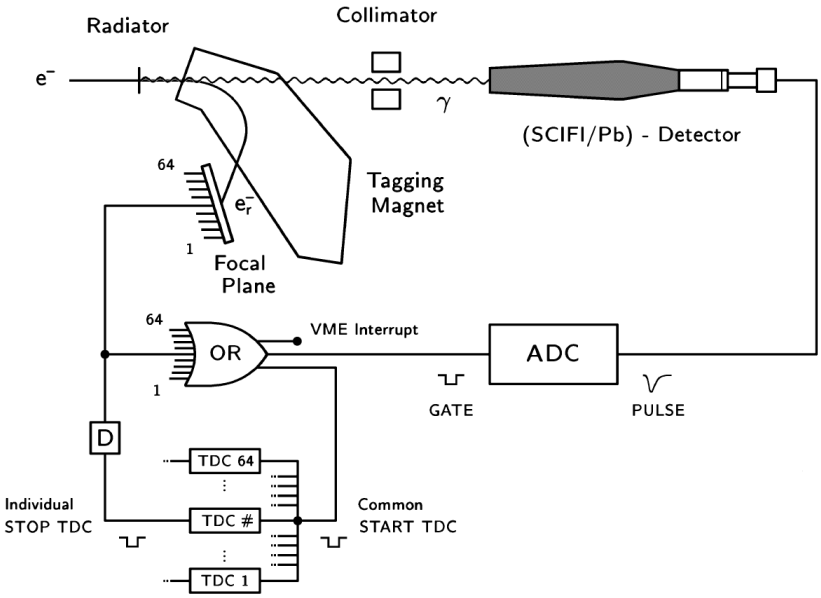

Figure 3.7: Schematic illustration of the set-up for the tagging efficiency measurement. The TDCs are stopped after suitable delay [29].

since it is directly related to the photon opening angle. Tagged photons with higher energy have a smaller opening angle minimising the probability of being terminated in the collimator, and vice-versa. This energy dependence means there are different values of tagging efficiency $\varepsilon_{tagg(i)}$ for each of the 64 tagger channels and they must be measured individually.

The layout of the experimental set-up for the tagging efficiency measurement is displayed in Fig. 3.7. The measurement is based on the coincidence technique (see Sec. 3.2.1), where the tagged photon is detected in coincidence with corresponding post- bremsstrahlung electron. During the measurement, the electron beam intensity was reduced to about 5×10^{-3}% of the normal beam intensity to avoid pile-up in the Pb/SciFi detector and to greatly reduce random coincidences normally associated with high beam intensities. Two trigger methods were used for each set of tagging efficiency runs:

- The focal-plane OR trigger, where a signal from any of the focal plane hodoscope detectors is used to trigger the data acquisition system (DAQ) and to generate the QDC (Charge-to-Digital Converter) gate for the Pb/SciFi detector. For each tagger channel i, the tagging efficiency $\varepsilon_{tagg(i)}$ is the ratio of real (above pedestal) to total counts in the corresponding Pb/SciFi QDC spectrum.

- The Pb/SciFi detector trigger, where a signal from the Pb/SciFi detector triggers the DAQ and starts tagger-Pb/SciFi coincidence TDC (Time-to-Digital Converter). The TDC is stopped by a delayed signal generated by the corresponding electron hit in a particular tagger channel i. The number of counts

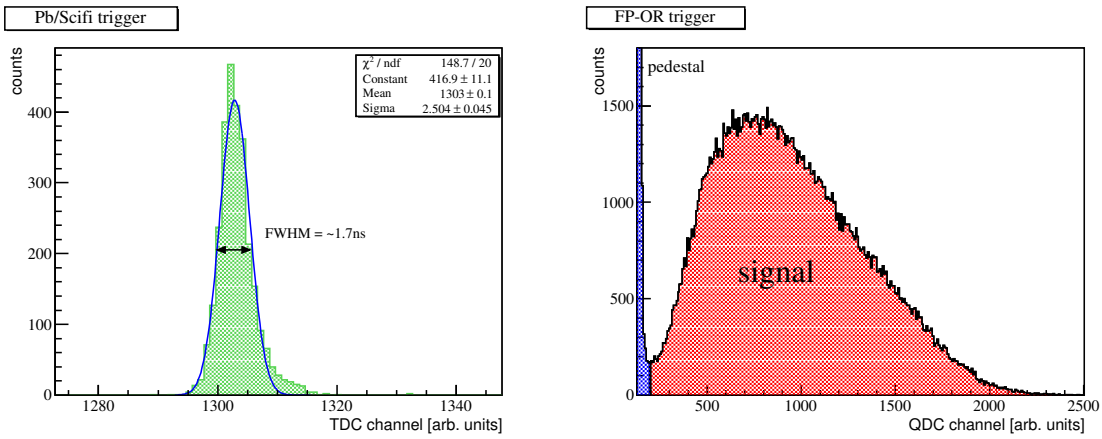

Figure 3.8: Left: The prompt peak in TDC spectrum obtained in a typical tagging efficiency measurement. The time resolution, obtained from a Gaussian fit, is ∼1.7 ns. Right: The QDC spectrum obtained from one of the tagging efficiency measurements.

in the TDC(i) coincidence peak corresponds to the number of tagged photons reaching the target since the Pb/SciFi detector is a ∼100% efficient. Thus, the ratio of TDC(i) coincidence peak counts to focal plane scaler counts for each tagger channel i gives the tagging efficiency $\varepsilon_{tagg(i)}$. This method requires runs with beam switched off to correct for background scaler rates.

Tagging efficiency measurements were performed twice daily on average, normally after each of the two injections of MAX II and MAX III which stops the electron beam delivered to the nuclear physics area. The Pb/SciFi detector was placed away from the photon beam line at the end of each run to protect the detector from high intensity beam used during normal data production runs.

3.6 Experimental Set-Up

The $\gamma + {}^4$He total photoabsorption cross-section measurement reported in this thesis made use of MAX-lab tagged photon facility over 4 weeks of beamtime in 2009. The experiment was performed using the helium gas-scintillator active target (HGSAT) and 12 external neutron detectors arranged in three groups of four to investigate ${}^4\mathrm{He}(\gamma, n^3\mathrm{He})$ differential cross-section. Additionally, two big sodium iodide doped with thallium "NaI(Tl)" detectors were used to look for Compton scattering ${}^4\mathrm{He}(\gamma, \gamma')$. A plan view of the experimental layout is shown in Fig. 3.9 and a description of the apparatus is given in the following sections.

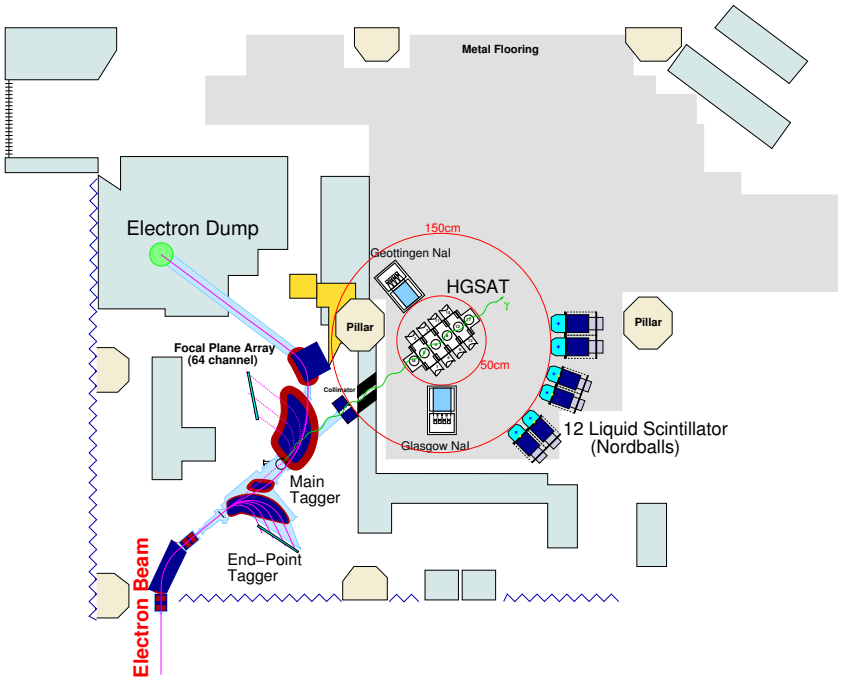

Figure 3.9: Floor plan of HGSAT set-up (unscaled), showing the in-beam target, NaI detectors and the Nordball liquid scintillators in the experimental-hall. Drawings of the tagging system and the Nordballs are made by J. R. M. Annand [162].

3.6.1 The Helium-Gas Scintillator Active Target (HGSAT)

The HGSAT (Figs. 3.10 and 3.11) consists of a 2 MPa[4] pressurised gas volume of research-grade helium-4 and a trace of ∼500ppm nitrogen acts as a wavelength shifter. The volume is contained in four identical aluminium-alloy cells bolted to-

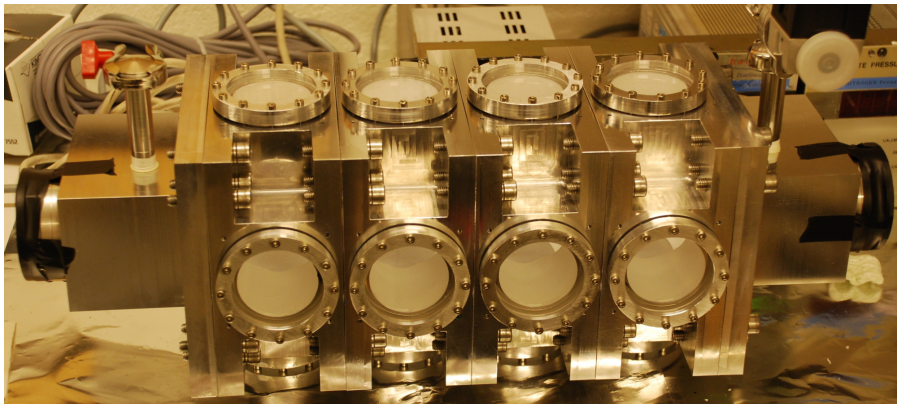

Figure 3.10: View of the multi-cell HGSAT before the photomultipliers tubes were connected. Figure courtesy J. R. M. Annand.

[4] 2 MPa = ∼19.74 atm (atmosphere).

gether with copper gaskets in between to provide the seal. A 5 mm diameter aperture connecting the four cells was made to maintain equal pressure throughout the target. The pressure of the gas target was constantly monitored by a pressure sensor attached to one of the target cells. Readings were recorded every 10 minutes over the experiment running period which allowed a continuous monitor of the target density (ρ). Measured day/night temperature fluctuations of around 4 °C in the experimental hall led to ∼10 kPa pressure fluctuations over the experimental run period. A small leak occurred at the quartz-aluminium coupling and resulted in a pressure loss of slightly less than 10% over the three weeks run period in March 2009 and ∼0.7% for the one week run in September of the same year as can be seen in Fig. 3.13. A detailed description of the HGSAT design, construction, and how it works is given in Ch. 2.

The HGSAT was placed on the photon beamline 3873 mm downstream of the bremsstrahlung radiator. The 4.5 mm diameter collimator was used to suit the 25 mm diameter of the entrance/exit windows.

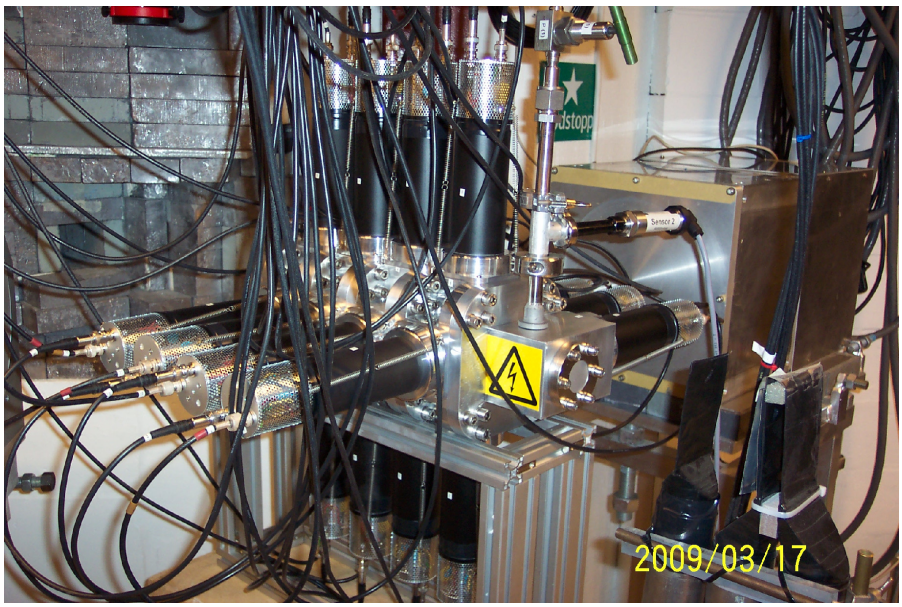

Figure 3.11: The fully assembled in beam HGSAT with all cabling and PMTs fitted, the Göttingen NaI detector can also be seen right of the target.

3.6.2 Gas-Handling System

A gas-handling system was used to fill helium gas into the HGSAT cells and add a 500 ppm trace of nitrogen in order to shift the scintillation wavelength to the detectable region of the PMT's. The gas-handling system is shown schematically in Fig. 3.12. It consisted of two research-grade gas bottles of nitrogen and helium with their specific gas regulators, three high pressure valves, five Edwards vacuum valves, a PRL-10 Pirani vacuum sensor, a 5 bar Balzer pressure sensor, a 50 bar Balzer high

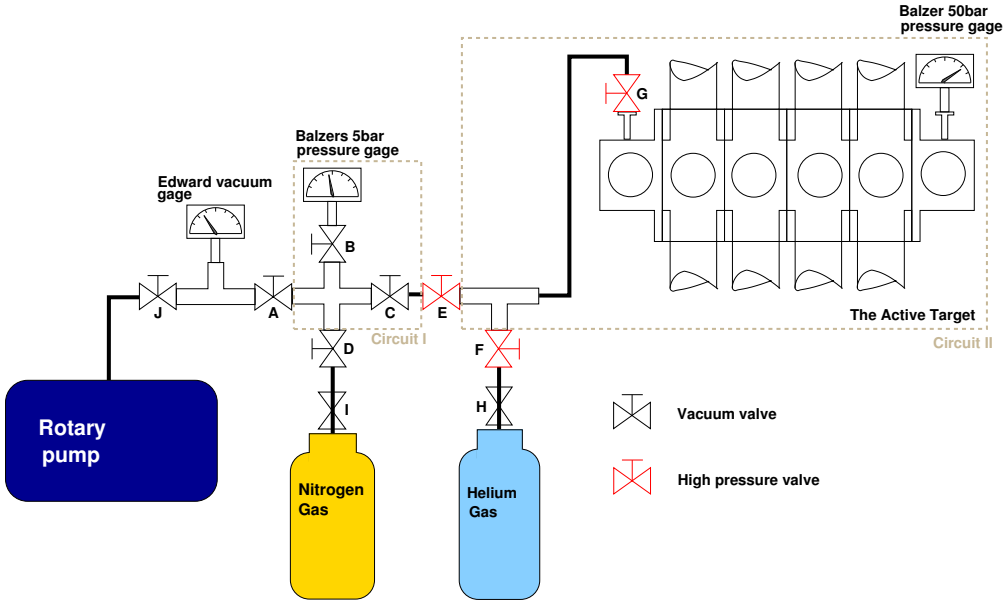

Figure 3.12: A schematic drawing of gas-handling system used to during the experiment.

pressure sensor and a regular rotary pump. Standard rubber O-rings were used in all connecting joints. The system was designed in such a way as to ensure precise control of a small volume of gas and to withstand the operating pressure of 2 MPa. The two Balzer pressure sensors were calibrated one week before the experiment with the aid of the reference guide supplied by the manufacturer. For the pressurised volume preparation, the HGSAT and the gas-handling system were pumped down to slightly less than 0.2 Pa monitored by the Pirani vacuum sensor[5]. During the process, the helium and nitrogen feeds (I)(D) and (H)(F) were evacuated and then re-pressurised to 300 kPa. The (D) and (F) valves were then half-opened separately for 45 seconds each to allow the gas to flow in while the system is evacuating. This "flushing" procedure was necessary to remove residual air[6] from the system. To obtain the 500 ppm trace of nitrogen, an initial 1 MPa (p_1) of nitrogen is allowed in (A)(B)(E)(D) highlighted as circuit I in Fig. 3.12 and then let it to flow into circuit II. When the gas was settled, the pressure in circuit I and II (p_2) was measured and the gas volume ratio in circuit I to that in circuit II is determined according to Boyle's law:

$$p_1 V_1 = p_2 V_2 \tag{3.9}$$

where p_1 and p_2 denotes the pressure of circuit I and II, V_1 and V_2 denotes the volume of the gas before and after it expanded to circuit II. Since the V_1/V_2 ratio is constant, the pressure required to give 500 ppm of nitrogen in the system can

[5]The process takes approximately 12 hours to reach the highest possible vacuum quality achieved by the rotary pump used.

[6]Oxygen is well known for its strong quenching effect on scintillations

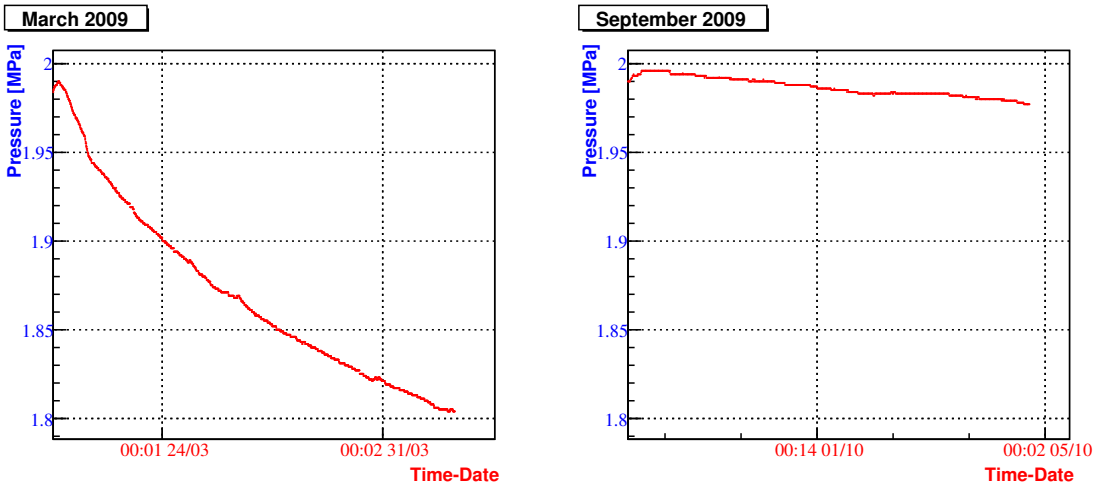

Figure 3.13: The pressure performance of the HGSAT during the experimental run period of March (left) and September (right) of 2009. A small leak at the quartz-aluminium coupling resulted in a pressure drop of ∼9% and ∼0.7% in March and September run periods respectively.

be calculated and allowed into circuit I and then let into the system. In this experiment, the calculated partial nitrogen pressure was 61.5 kPa. The pressure was monitored while the gas was flowing into circuit II and was confirmed to be 1 kPa after it was fully settled. Helium was then allowed slowly into the system with the rate of ∼1 kPa/s up to the total system pressure of 2 MPa at a room temperature of 21°C.

The gas filling process took place in the small user room outside the experimental hall. When the gas-filling process was completed, the target was decoupled from the gas-handling system and was carefully transported to the experimental hall.

3.6.3 Nordball Array

An array of neutron detectors known as the "Nordball array" was placed around the HGSAT to detect neutrons coincident with charged recoils in the target. The detectors were originally developed and built for the Nordball detection system [163] at Chalmers University of Technology in Göteborg, Sweden [164]. The array consists of five pentagon and seven hexagon shaped detectors filled with BC-501 organic liquid scintillator. The scintillator responds differently according to the ionisation density of the interacting particle. Pulses generated by recoiling protons have a relatively larger slow component compared to those generated by electrons, thus, neutrons can be identified against electron and photon background in the experiment if a pulse shape discrimination method is employed. The BC-501 scintillator is held in a 2 mm stainless steel container with a glass window occupying one of its six sides and all other surfaces are internally coated with white reflector paint. The hexagonal detectors have a detection radius of 8.4 cm and carry 3.33 litres of liquid

scintillator, while the radius of the pentagonal detectors is 7.0 cm and they carry 2.57 litres. Both detectors have a thickness of 160 mm. A Philips 5" photomultiplier XP2041 is coupled to the glass window of the container and fitted with a μ-metal shield. The PMT and its voltage-divider are housed in a plastic cover and the whole detector is mounted on an aluminium frame. The two different shapes were built in order to form a 2π geometrical coverage around a target when they were previously used as a neutron filter for the Nordball project [163] which is not related to this experiment. The Nordball array is capable of detecting neutrons of energies as low as 1 MeV kinetic energy. Schematic drawings of the two different shapes of the Nordball array detectors are shown in Fig. 3.14. Details on the performance and efficiency of the Nordball array is well documented and can be found in the work done by Reiter [131], Navirian [165] and Karlsson [166].

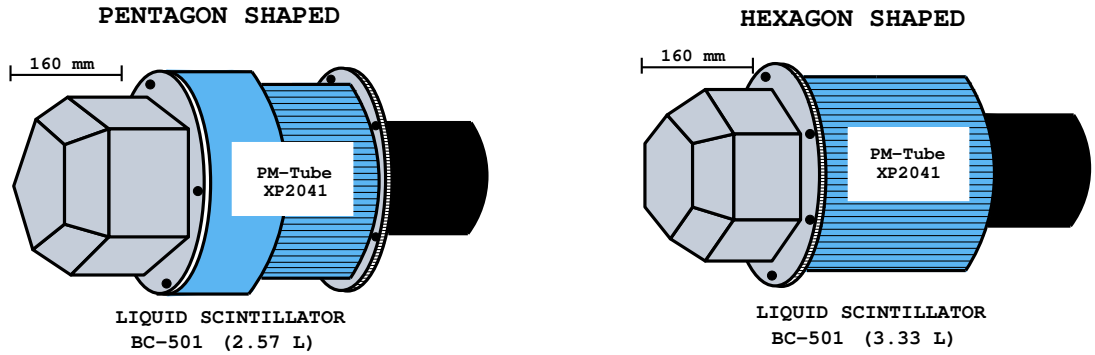

Figure 3.14: Schematic drawings of the hexagon and pentagon shaped liquid scintillator detectors.

The Nordball array was segmented into three clusters of four detectors arranged in two rows. The array was placed at a flight path of 150 cm from the target and at angles of 30°, 60° and 90° with respect to the incoming photon beam. Two clusters were constructed of three hexagonal and one pentagonal detectors while the third cluster was made of three pentagonal and one hexagonal detectors. The array was placed so that the centre row was at the same height as the incoming photon beam. The Nordball PMT anode signals were used to trigger the DAQ system during Nordball calibration measurements but were not included in the trigger during data production.

3.6.4 NaI Detectors

Two large (254 mm diameter × 254 mm thick) NaI(Tl) detectors provided by Glasgow and Göttingen were used to investigate Compton scattering $^4\mathrm{He}(\gamma,\gamma')$. Each detector consists of a cylindrical crystal encased inside an air-tight Al frame. The crystal is read out by seven photomultipliers and the combined signal is processed. The Göttingen detector is supplied by a single HV channel distributed via potentiometers to the individual PMTs, while the Glasgow detector is supplied by 7 HV

channels [167]. The height of the two NaI detectors was adjusted to 141.5 cm so that

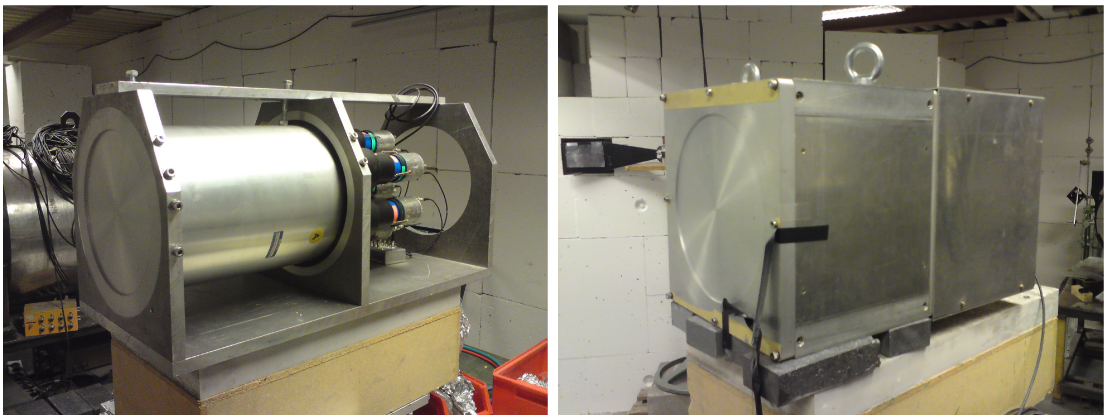

Figure 3.15: The Glasgow (left) and Göttingen (right) NaI detectors.

the beam height was the same as the centres of the crystals. Both detectors were placed 50 cm from the centre of the target with the Göttingen positioned at angle of 90° while the Glasgow detector was placed at 135° with respect to the incoming photon beam. The two detectors are shown in Fig. 3.15. As with the Nordball array, the NaI detectors were not included in the trigger system apart from when they were calibrated.

3.6.5 The In Beam Monitor detector (IBM)

The In-Beam Monitor detector (IBM) was used to constantly monitor fluctuations in the photon beam intensity. The detector consists of three 0.5 mm thick 70×100 mm scintillators (I_1,I_2 and I_3), each connected to a single photomultiplier tube via a light-guide. A thin aluminium foil is placed at the front of the middle scintillator acts as a gamma/pair-production converter for the downstream scintillators. Photons are identified through charged particles detected in coincidence in (I_2) and (I_3) with the upstream scintillator (I_1) set in anti-coincidence mode to veto charged-particles. A count is generated according to the following logical relation [29]:

$$!I_1 \ \& \ (I_2 \ \& \ I_3) \ \Rightarrow count \tag{3.10}$$

The count rate of the IBM is directly proportional to the photon beam intensity, thus, a continuous monitor of the photon flux upon the target is achieved by connecting the IBM discriminator outputs to scalers and feeding them into the recorded data stream. The IBM detector was placed in the photon beamline a few centimetres downstream the target. An overview of the IBM detector electronics together with a photograph of the detector are shown in Fig. 3.16.

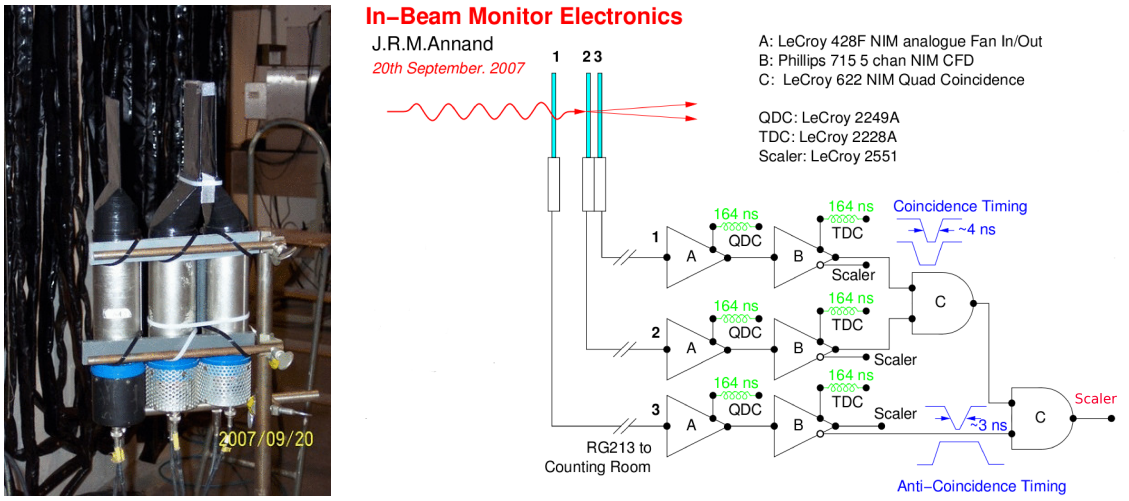

Figure 3.16: A schematic describing the front-end electronics for the In-Beam Monitor (IBM) detector together with a photograph. The IBM output was fed to a scaler. Figure courtesy J. R. M. Annand.

3.7 Electronics and Data-Acquisition System

The Data-Acquisition (DAQ) system at MAX-lab was used to select, process and digitise signals of interest from all detectors used during this experiment. This was done via various NIM, CAMAC and VME electronics modules residing in three NIM crates, one VME crate and one CAMAC crate. The data was read and stored in a local computer allowing later retrieval for off-line analysis. There are two separate DAQ systems at MAX-lab that are exclusively used for nuclear physics experiments. The two systems are located in two different user rooms and can be run simultaneously and independently. This experiment made use of the "small" DAQ system, referenced by the room size, where the HGSAT was assembled and pressurised. The "small" DAQ system hardware is based on a GE 616 (formally known as SBS 616) PCI/VME bus adapter [169] that connects the VMEbus to the PCIbus plugged into a 2.4 GHz/512 MB RAM linux PC via an 8 m cable [170]. The CAMAC crate controller is connected to the VME crate via a CAMAC branch driver. The software that controls and runs the DAQ system, created and developed at MAX-lab for nuclear physics experiments, is based on ROOT[7]. The DAQ software has an interface that allows for data acquisition start/stop and for a basic on-line data analysis to monitor the detection system for any anomalies during data production. Experimental data were read out after each event trigger and stored in a ROOT standard data-file format in the DAQ computer hard drive. The data were then transferred manually to Glasgow using a commercial external USB hard drive. A schematic diagram of the DAQ system is given in Fig. 3.17.

[7]A C++ object oriented framework developed at CERN for large scale data analysis [171].

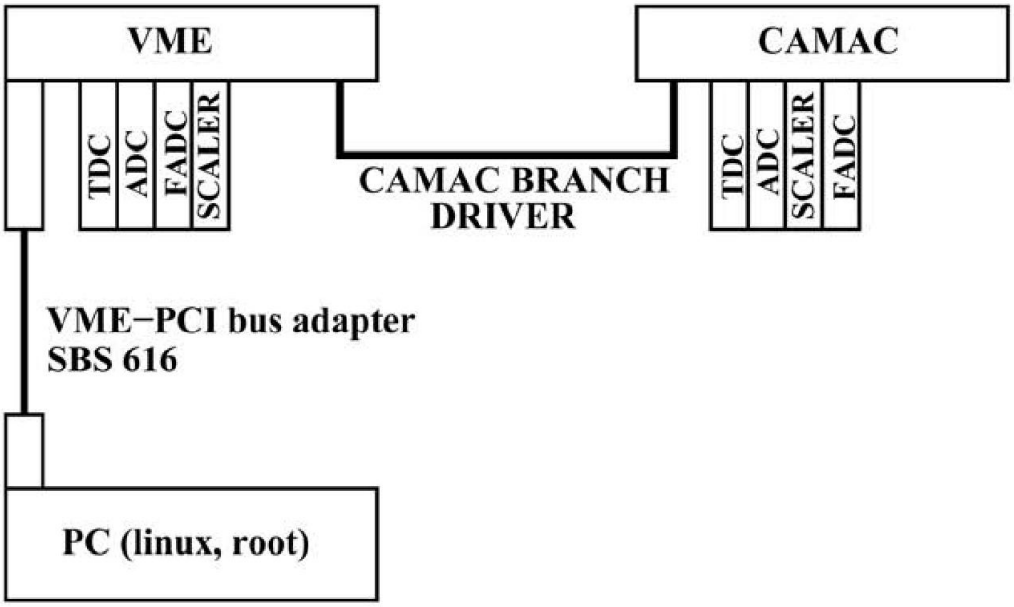

Figure 3.17: Schematic drawing of the Data Acquisition (DAQ) System [168].

3.7.1 Electronics Set-up

The read out electronics set-up was designed and implemented by J. R. M Annand [167]. For the total $\gamma + {}^4$He measurement, the aim was to measure correlated hits in the focal plane array and the HGSAT. This was done by simply connecting the HGSAT and each of the 64 focal plane elements to a TDC. Each focal plane channel corresponds to a specific photon energy. A trigger generated by the HGSAT starts each TDC and is stopped by signals generated by the relevant focal plane element. In a spectrum of time intervals measured in this manner, correlated events appear in a limited region which produces a peak riding on a random background. The number of counts above background in the peak is proportional to the $\gamma + {}^4$He reaction yield. For the ${}^4\mathrm{He}(\gamma, n{}^3\mathrm{He})$ and ${}^4\mathrm{He}(\gamma, \gamma')$ measurements, the same method was employed. The HGSAT announces the start of the reaction, generates the system trigger which starts the TDCs connected to the Nordball and the NaI detectors. The TDCs are stopped by signals generated by these detectors upon detecting neutrons or photons respectively.

To this end, timing and energy information from each detector in the experimental set-up were recorded via QDC and TDC modules gated or stopped by the system trigger. A detailed diagram of the electronics set-up used to process detector signals and generate a trigger is given in Fig. 3.18. Although the diagram looks fairly complicated, the principle is quite straightforward. For the HGSAT and NaI detectors, the analogue signal of each detector is actively split into two signals using a LeCroy 428 linear fan-in/out. The first signal is delayed (allowing time for the triggering decision to be made) and fed to a QDC where the energy information is digitised. The second signal is passed to a leading edge discriminator (LED). A logic signal

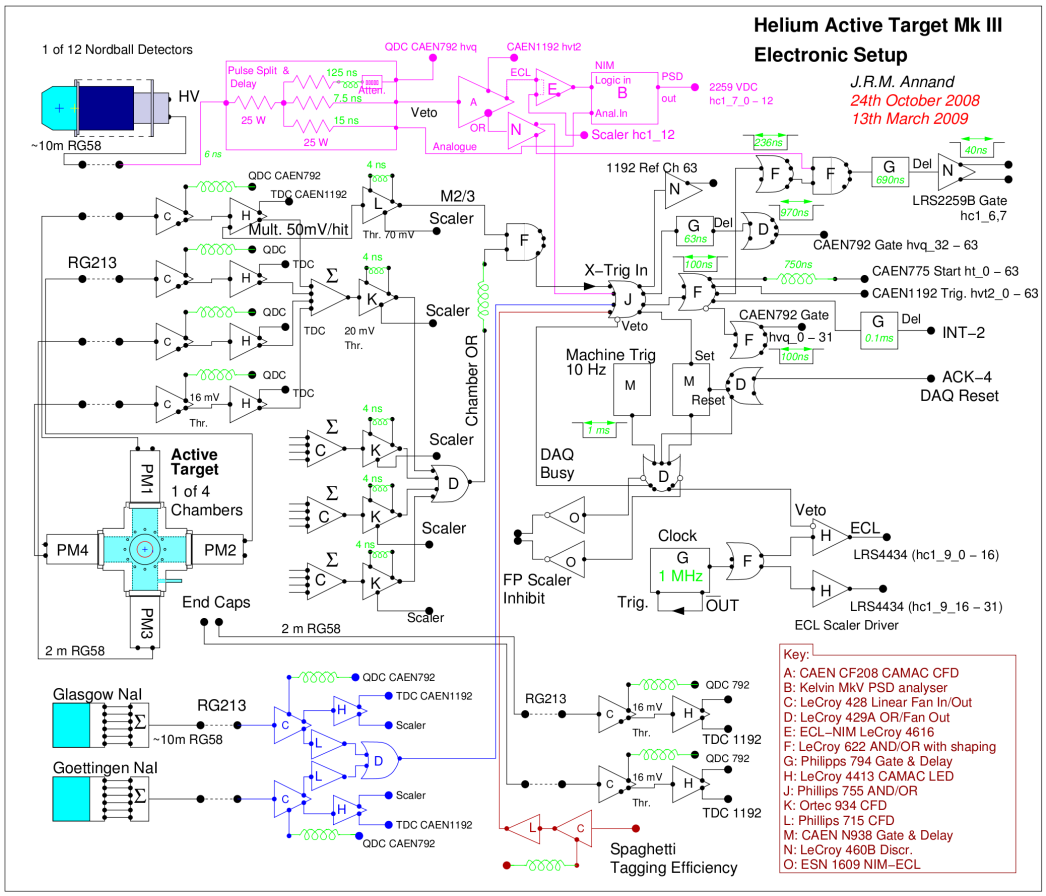

Figure 3.18: Electronics to process detector signals for recording and for trigger generation. Designed and drawn by J. R. M. Annand March 2009.

is generated at the moment the analogue signal crosses the discriminator threshold value. One output of the discriminator forms the secondary system trigger through a chain of NIM modules. The other output of the discriminator is fed to the relevant TDC for timing information. The primary trigger is made by the sum signal of 4 PMTs which feed into a CFD.

A 64 channel CAEN V1190B multi-hit TDC module [172] was used for all of the experiment detectors TDCs, while two 32 channels CAEN V775 TDC modules were used for the focal plane elements TDCs. Two 32 channel CAEN V792 QDC modules were used for digitising the charge information for each of the 18 HGSAT PMTs, the 12 Nordball array detectors, the 2 NaI detectors and the Pb/SciFi detector with one of the modules dedicated entirely to the 18 HGSAT channels. VME scalers were used to monitor the event rate of the detectors in real time and to count the number of times the system triggered. The scalers were also used to determine the DAQ system processing time (dead-time) and the photon flux in the experiment. This was done as follows:

- A self triggered Philips 794 Gate/Delay Generator module was adjusted to

run as 1 MHz clock. The clock output was sent to two scalers one of which was inhibited when the DAQ system was busy. The ratio of the counts in the two scalers provided the live-time fraction of the experiment.

- Logic pulses from the focal plane discriminators were fed to scalers which registered the number of electron hits in focal plane elements which is eventually used to calculate the photon flux in the experiment. Since the focal plane scalers were inhibited while the DAQ system is busy, no correction for the dead-time losses was needed.

The electronics set-up for the Nordball detectors was slightly different since neutrons are detected through the pulse-shape discrimination method that uses the timing and the shape of the pulses. A pulse split and delay module was used instead of the LeCroy 428 Fan-in/out to passively split the analogue signal of each of the Nordball elements into three signals. The first signal was delayed, attenuated and then fed to the QDC for charge digitisation. The second signal was passed through a CAEN CF208 constant faction discriminator which compensates for time walk related to variable amplitude of the input pulse. The third signal was fed directly to the Pulse-Shape Discrimination (PSD) module. The three outputs of the CFD discriminator were sent to the TDC, the trigger unit "the Nordball trigger" and to the start input of the PSD module (designed and developed by J. R. M. Annand [173]). The PSD module uses the PSD properties of the BC-501 scintillator for neutron identification by analysing the scintillation decay time. Briefly, the module equally splits the analogue pulse from the Nordball detector into two and integrates one with a short gate and the other with a long gate. The resultant charges are converted into voltages via capacitors and fed to a fast comparator that provides a logic decision on particle type based on the decay time. The voltages of the two charges are also subtracted via a fast difference amplifier to give a "pulse shape" analogue output whose pulse height is related to the effective scintillation decay time. When the pulse shape signals are plotted against the pulse height from the QDC in a 2D plot, a clear separation between different particles is seen. The PSD analogue output was fed to a LeCroy 2259 VDC (Voltage-to-Digital Converter) for digitisation. The tricky part dealing with the PSD module was to properly adjust the length of the two gates and to correctly set the voltage threshold at the hardware level. Alas, a lack of a suitable neutron source at the start of the experiment prevented a precise adjustment of the module. It is worth mentioning that this module was used successfully by A. Reiter for his work on neutron cross-sections using the same Nordball array detectors [131].

3.7.2 System Triggers

The time the DAQ system requires to process events is not negligible. During this processing period, the DAQ electronics are blind to any further events. This period is known as the experimental dead-time and it depends on the complexity and the processing power of the electronics used.

The fractional dead-time is minimised considerably by using a suitable trigger that places constraints on accepting events by making the decision on when the DAQ system should start accumulating data. Seven different triggers were used during this experiment depending on the run mode. For the Nordball array and NaI detectors calibration runs, the Nordball and the NaI triggers were used respectively. Two different triggers were employed for tagging efficiency measurement runs, the FP and the Pb/SciFi triggers. How the Nordball and the NaI triggers were generated is discussed in the previous section, and the tagging efficiency triggers are discussed in Sec. 3.5.5. A description of the three HGSAT triggers is given below in some detail:

HGSAT (OR/OR+M_n) trigger

The HGSAT signals were used to generate the main triggers during production running. The trigger comes in three different conditions:

- HGSAT OR+M_1
- HGSAT OR+M_2
- HGSAT OR+M_3

The "OR" component of the trigger was generated by adding the 4 PMT anode signals from each cell of the HGSAT and feeding the sum to a constant fraction discriminator Ortec 934 module. The 4 cell-sum logic signals were ORed, hence called the "OR", and fed to a LeCroy 622 AND gate. The hit-multiplicity "M_n" component, where n denotes to the minimum number of simultaneous PMT hits from the target, was produced by feeding the 16 PMT anode signals into a LeCroy 4413 leading-edge discriminator (LED) module. The Σ output of this module has an amplitude of $x\times50\,\mathrm{mV}$, where x is the number of activated channels [167]. The value of multiplicity n was simply selected by sending the Σ output to a CFD with the threshold set to $< \mathrm{n}\times50\,\mathrm{mV}$. For M_1, M_2, and M_3 the threshold was set to 40, 70 and 120 mV respectively. The CFD output is then sent to join the "OR" component at the LeCroy 622 AND gate and the output produces the OR+M_n trigger that is sent to the trigger unit, a Philips 775 AND/OR module. Ideally,the OR+M_1 trigger would be used for all of the data production runs since it should have the smallest threshold effects on the detection efficiency. However, running at such an open trigger increased the DAQ system dead-time to ∼80%, even with a reduced beam intensity. This is due to many spurious signals which arise from direct electron interactions in the PMTs and Čerenkov light produced in the optical components in addition to the HGSAT scintillations [174]. For this reason the more restricted OR+M_2 and OR+M_3 triggers were employed as a compromise between the DAQ system live-time and the effect of the trigger threshold on the detection efficiency. For normal data production runs, the OR+M_3 trigger allowed ∼90% live-time and gave a trigger rate of ∼250 Hz. At a reduced beam intensity, the OR+M_2 and the OR+M_1 triggers gave ∼60% and ∼20% live-time respectively.

When a trigger signal is generated, it provokes a chain of signals that makes all QDC gates and TDC starts as well as initiating the read out of the QDC and TDC modules. The trigger signal also activates a CAEN N93B Gate/Delay Generator module that vetos the Philips 755 trigger unit so any further events that might arrive and perturb the processing are blocked. The module also sends an INHIBIT signal to the tagger focal plane scalers and the gated clock scaler while the DAQ is processing events. When the DAQ finishes processing the event, a RESET signal is sent to the Gate/Delay Generator, thereby allowing a new system trigger to be made. Finally, it is worth noting that the scaler modules are independent of the triggering decision. They are read out and cleared at pre-determined intervals.

3.7.3 Experimental Summary

The initial construction of the HGSAT was finished in October 2008. A week of beam time for electronic set-up and proof of concept was taken a few days after the initial construction was completed. The target was then sent back to Glasgow for modifications at the hardware level. Four weeks in total of beam time was allocated to this experiment during 2009. Data were taken over a period of three weeks in March which ran mainly using the restricted OR+M_3 trigger and with incident electron beam energy of 142.9 MeV while the extra week in September was used to evaluate the triggers effect on the detection efficiency. It was run with different triggers but mainly focused on the OR+M_2 trigger and used an electron beam energy of 164 MeV. A summary of the "effective" beam time utilised over the experiment running period along with different run modes is given in Table 3.1.

Description		∼Time (hr)		Total (hr)	∼Off-beam time (%)	Run mode
		Mar. 2009	Sep. 2009			
Trigger	**OR+M1**	-	13	13	6.5	Data production
	OR+M2	3	38	41	20.5	Data production
	OR+M3	133	14	147	73	Data production
	Nordball	3.5	2	5.5	-	Calibration
	NaI	8	1	9	-	Calibration
	Focal plane	-	2	2	-	Tagging efficiency
	Spaghetti	4	2	6	-	Tagging efficiency
Total		151.5	72	223.5 (9.3 days)	100	-

Table 3.1: Experimental Runs Summary A.

Each beam day consists of about 20 hours of beam delivered to the experimental hall interrupted by the two daily injections of MAX II and MAX III, each of which takes 1 to 1.5 hrs. Tagging efficiency measurements taking 20 to 30 minutes were performed twice a day, normally after each injection since it was more convenient to start the beam with a lower intensity then switch to full intensity for data taking. The calibration of the Nordball and the NaI detectors was done at the start and the end of the experiment since these calibration runs were performed with the photon

beam switched off. However, a few days were lost during testing, beam tuning, electronics set-up, maintenance, etc. A break down of the experiment time duration is given in Table 3.2 and an on-line track of the evolution of the experiment can be viewed at the Electronic Logbooks for Nuclear Physics at MAX-lab [154].

Description	∼Time (Days)		Total (Days)	Notes
	Mar. 2009	Sep. 2009		
MAX II/III Injections	2.5	0.5	3	2 per day (∼3 hr)
Maintenance days	3	1	4	1 per week (Every Monday)
AT Testing	2	0.5	2.5	setting up the HGSAT and tune electronics
Beam Tuning	2	0.5	2.5	after each injection (time varies)
Losses	5	-	5	collective of all unaccounted factors (machine problems, Corrupted data, testing...ect)
MAX I power failure	-	1.5	1.5	total shut down of the facility
Data Production	6.5	3	9.5	solid data taking duration
Total	21	7	28	-

Table 3.2: Experimental Runs Summary B.

Chapter 4

HGSAT Geant4 Monte-Carlo Simulation

Calculation of the detection efficiency(ε_x)[1] of the HGSAT is one of the major steps required to convert the measured $\gamma + {}^4$He reaction yields to cross-sections, the goal of the work presented in this thesis. To do this, a Geant4 based Monte-Carlo simulation was developed as part of the experimental part of this project. The simulation was also used to quantify systematic effects which distort the yield measurements and to gain a better understanding of the processes taking place within the HGSAT. In this chapter, a comprehensive overview of the HGSAT simulation and how it was constructed is given. A detailed description of the steps followed to calculate the detection efficiency and studies on the performance of the HGSAT are also provided.

4.1 A Brief Overview of Geant4

Geant4 (**GE**ometry **AN**d **T**racking) is a well established C++ object-oriented Monte-Carlo simulation package developed at CERN [175] originally for high energy physics experiments. However, since its first release in late 1998, the software toolkit has been extensively used in various scientific disciplines ranging from nuclear and medical physics to space applications. The software capability of modelling optical photon transportation makes it suited for simulations on the HGSAT. There are nine main releases of the software including several subversions in between with 9.5 being the latest at the time of writing this text. The simulation described here was developed and ran on 64 and 32-bit Fedora Linux machines using releases 9.0 through 9.5 with no significant compatibility issues.

Geant4 is partitioned into eight semi-independent class categories. Each category consists of a cluster of closely related classes that handles one specific task within the simulation. These categories are responsible for handling the detector geometry, tracking, detector response, run management, visualization and user interface. The

[1] A quantity defined simply as the ratio of detected to actual events.

categories provide the "skeleton" on which the user simulation is built. In extremely simplified terms, the user defines the detector geometry with all associated materials and then chooses the appropriate models of particle interactions to include from 32 predefined physics libraries. Elements of the detector geometry, where events of interest are registered, are declared "sensitive" volumes. This allows the user to request any kind of information for interactions taking place within the sensitive volume to be recorded. The user specifies the details of the events to be generated using either the Geant4 generic event generator or an external generator. For each generated event, the particle(s) are given initial momentum and position and are then tracked through the geometry. Recorded information can be stored in various formats including the ROOT [171] tree format for further analysis if desired. Geant4 is well documented in Ref. [176] and [177], therefore details of the software structure and its class categories will not be discussed any further.

4.2 The HGSAT Simulation Structure

The detection technique used in the HGSAT relies primarily on detection of the scintillation resulting from energy loss of the ^{4}He photo-disintegration products in

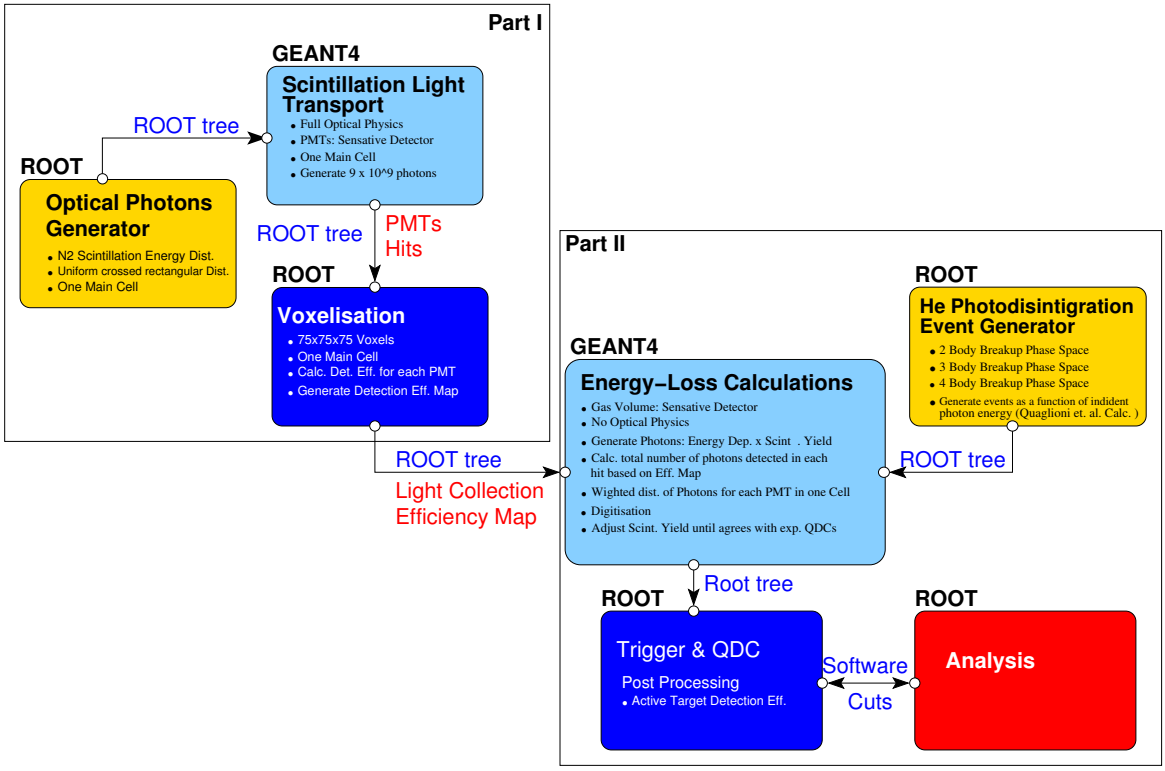

Figure 4.1: The two main simulation parts are presented in light-blue coloured boxes. The output of part II was used to determine the HGSAT detection efficiency (ε_x) by applying the experimental discriminator thresholds and the software cuts.

the gas volume of the target as discussed in Ch. 2. A realistic simulation of the

HGSAT response entails modelling of the scintillation processes, scintillation light transport and optical boundary characteristics as well as calculating the energy loss of γ+^{4}He reaction products. This was fully implemented at an early stage of the development of the HGSAT simulation but found to be computationally expensive and impractical for running a satisfactory number of events. Hence, a more efficient approach was employed by splitting the simulation into two parts. The first part was used to map the scintillation transport efficiency as a function of position of the primary scintillation which was then fed into the second part where energy-loss calculations are made. These calculations were used to determine the HGSAT pulse amplitude response and hence detection efficiency (ε_x) by applying the experimental discriminator thresholds and software cuts in the analysis of the event-by-event data generated by the simulation. Two external Monte-Carlo event generators were written in C++ using ROOT. The generated events were fed separately into each of the two parts of the simulation in the form of a ROOT tree. Initially the simulation was developed for $\gamma + {}^4$He total photoabsorption cross-section measurement. The modelling of the whole experimental setup including the 12 Nordball liquid scintillators and the 2 NaI detectors will be done when the analysis of exclusive reaction data is performed. The structure of the HGSAT simulation is shown in Fig. 4.1. The next few sections first describe all of the simulation common components and finishes with a discussion of the two parts of the simulation in Sec. 4.3 and 4.4.

4.2.1 Geometry

The geometry of the HGSAT is shown in Fig. 2.1 and Fig. 3.10. The fully assembled detector consists of 8 components. These are:

- 4 Identical Al main cells.
- 2 Auxiliary Al cells.
- Reflective paint (EJ-510).
- 5 Aluminised mylar foil optical isolators.
- 18 Quartz windows (HOQ-310).
- 18 PMTs. Modelled as 18 photo-cathodes and 18 PMT glass windows (Schott-270).
- 18 Al window retaining rings
- 2 Flanged beryllium windows.

The detector geometry was initially derived from the actual Computer-Aided Design (CAD) file that was used in machining of the HGSAT (see Fig. 4.2(right)). This was done by converting the CAD STEP[2] file into Geometry Description Markup Language (GDML) format supported by Geant4 with the aid of the FASTRAD V3 trial

[2]Acronym for **ST**andard for the **E**xchange of **P**roduct. A standard CAD output format.

version [178]. GDML is a specialised **E**xtensible **M**arkup **L**anguage (XML) [179] based language developed by CERN and designed as an application-independent persistent format for describing the geometries of detectors associated with physics measurements. It serves to implement "geometry trees" which correspond to the hierarchy of volumes a detector geometry can be composed of, and to allow for the identification of the position of individual solids, as well as to describe the materials from which they are made. Importing CAD files into Geant4 was not a straightforward task. It involved several instances of code debugging to avoid overlapping between different volumes of the detector which currently poses problems in Geant4. The exact details of how to convert CAD files into GDML format are lengthy and beyond the scope of this thesis, however further details can be found in the GDML manual at the CERN website and Ref. [180] where similar procedures to the one used here were reported.

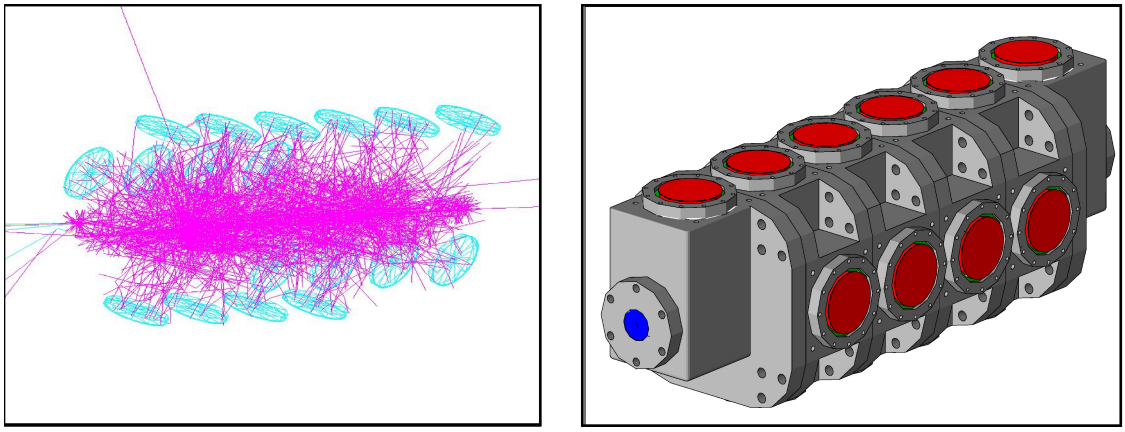

Figure 4.2: Left: overview of scintillation photons across the HGSAT visually showing no reflection is taking place. Right: a Geant4 model of the HGSAT as imported from the CAD file used in the machining stage.

Despite all of the efforts to avoid overlapping volumes, generating scintillation photons across the HGSAT cells showed that the majority of photons were not reflected as expected and a few were even able to penetrate the aluminium walls of the cell which is plainly non-physical (see Fig. 4.2(left)). Increasing the tolerance of a built-in overlap surface checker[3] and stripping the geometry to one cell showed overlapping occurs within the same tessellated unit volume. Although this was found in two of the four main cells, excluding them did not resolve the problem. A similar issue was reported by Alvarado [181] who simulated with two geometries. The first was a tube coded via Geant4 predefined primitive volumes while the second was imported from a CAD file. The latter showed the same problem experienced here. This leads to the conclusion that Geant4 is not yet well suited to handle tessellated volumes imported from CAD files when dealing with scintillation photons. For this reason,

[3] A Geant4 built-in overlapping checker first introduced in release 9.2.

it was decided to abandon this method.

As an alternative the HGSAT geometry was "hand" coded using a combination of GDML predefined geometric primitives called "solids" such as boxes, cones and tubes. These basic geometries are described by a minimal set of parameters necessary to define the shape and size. Volumes of the aluminised mylar foils, quartz windows and PMTs (photo-cathodes + PMT glasses) were created from basic solids "tubes" using the same dimensions as specified on the CAD drawings. The gas-cells, retaining rings and flanged beryllium windows were more complicated and required boolean operations where a combination of subtraction and unification of different solids is performed. Each main cell was created from two distinguishable volumes: a cell Al body and an inner gas-volume. The first volume was constructed by combining two perpendicular cuboid solids and forming a space for quartz windows at the top of each end by subtracting an equivalent volume. The gas-volume was created by unifying 4 identical truncated cones, each rotated by 90° sequentially about the same axis, and attaching them to a horizontal central tube. The combined gas-volume was then placed inside the cell Al body volume. Similarly, auxiliary cells were modelled by combining two perpendicular tube solids of different dimensions placed inside two combined perpendicular cuboid solids. Window retaining rings and flanged beryllium windows were modelled using the same concept. It is sufficient to describe only one volume for a group of identical volumes which can be then "copied" as many times as needed. Each volume is assigned a material in the same GMDL file and placed in its location within the detector geometry using a position transformation matrix. The GDML file was read by the Geant4 integrated GDML parser which imports the detector geometry and makes it ready to use in the simulation. The full HGSAT geometry as used in the simulation is presented in Fig. 4.3 below.

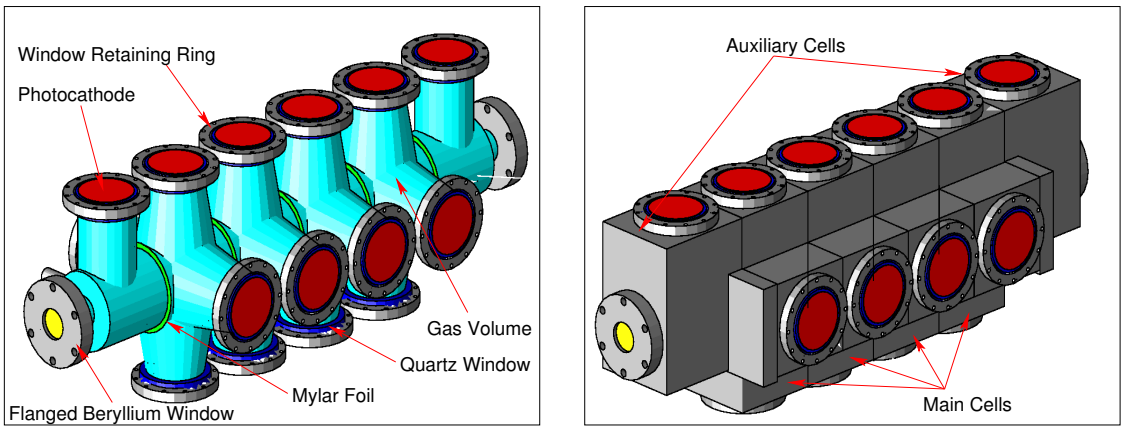

Figure 4.3: The HGSAT geometry as used in the simulation. Left: the gas volume in cyan. Right: the Al container.

The detector response to scintillation photons was checked both visually and at the software level by reading-out processes occurring at the boundaries of each com-

ponent. This confirmed that the alternative method works well and scintillation photons were reflected as expected with no penetration into the Al walls. A transparent overview of the HGSAT geometry showing scintillation photons emerging from the viewing windows is displayed in Fig. 4.4.

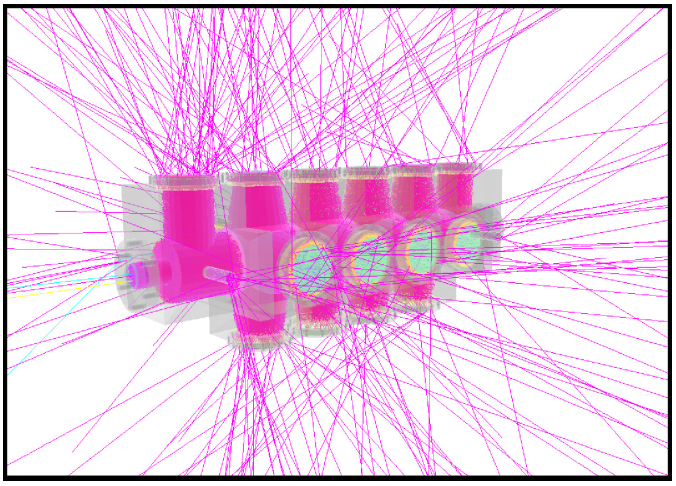

Figure 4.4: Transparent view of the HGSAT showing scintillation photons in one simulation run.

4.2.2 Materials and Optical Properties

The materials of the different volumes of the detector were defined in a separate XML file read by the GDML parser. In Geant4, materials are defined from an element or a mixture of elements by specifying the density of the material and either the atomic composition as presented in the chemical formula or by giving the weight fraction of each element. All elements and composites used in this simulation were taken from the NIST[4] database [182]. The compositions of elements necessary to define commercial materials such as Quartz windows (HOQ310) were taken from the manufacturer's data-sheet.

For simulations involving transport and tracking of scintillation photons, optical properties and boundary characteristics, such as absorption length, refraction and reflection at medium boundaries, must be defined for all materials involved in the process as a function of optical photon energy. These properties were taken from each component's specification-sheet provided by its manufacturer. These include the EJ-510 coating paint reflectivity (Fig. 4.5(left)), and transmission and the refractive index for each of the quartz windows (HOQ-310) and XP2262 PMT glass (Schott B270) (Fig. 4.6(left) and Fig. 4.7 respectively). The helium-gas refractive index (Fig. 4.6(right)) was taken from the calculations of Chant and Dalgarno [183].

[4]National Institute of Standards and Technology.

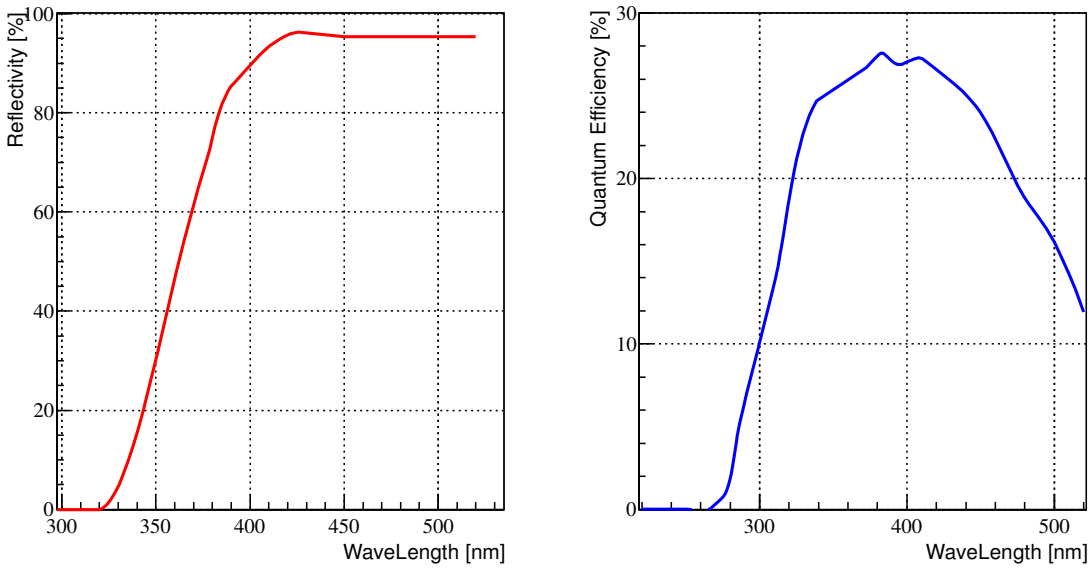

Figure 4.5: Left: the EJ-510 coating paint reflectivity spectrum [185]. The spectrum provided by the manufacturer was extrapolated to cover photon wavelengths below 370 nm. Right: the XP2622 PMT photo-cathode quantum efficiency spectrum [126].

The reflectance and transmission of the aluminised mylar foils were measured using a Cary 300 UV-Visible Spectrophotometer [184] and found to be almost constant at ∼95% and ∼ 0% respectively[5] over the range of the nitrogen scintillation emission spectrum. In addition, the quantum efficiency[6] of the employed XP2262 PMTs is required and was defined as a function of photon wavelength as shown in Fig. 4.5(right).

4.2.3 Optical Photon Processes

Scintillation photons are classified as "optical" in Geant4 to differentiate them from higher energy gamma rays which are subject to different types of processes. Optical photons are handled by four main processes described according to the user's input. This input includes a number of empirical parameters such as characteristics of the scintillation emission and the optical properties of the detector components (explained in Sec. 4.2.2). The processes involving optical photons are explained in detail in Ref. [188], and thus, only a brief description will be given below, with a focus on the settings implemented particularly in the HGSAT simulation.

[5] Implies ∼5% absorption in the aluminised mylar foil.

[6] The number of photoelectrons produced at the PMT photo-cathode divided by the total number of incident (optical) photons.

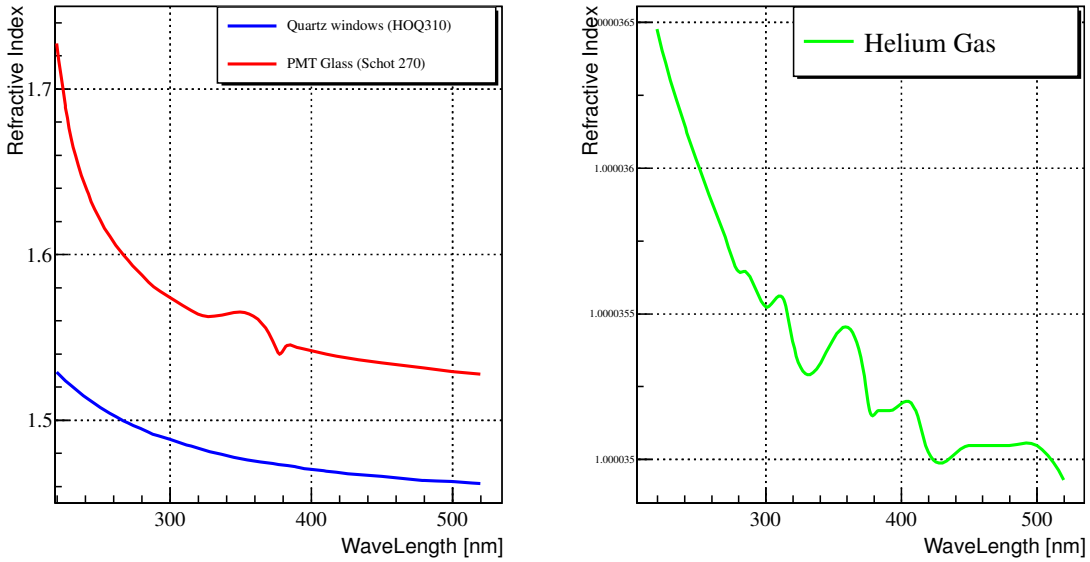

Figure 4.6: Left: Refractive Index of the XP2262 PMT glass (Schott B270) (red) [186] and the Quartz windows (HOQ310) (blue) [187]. Right: Refractive Index of helium-gas as calculated in Ref. [183].

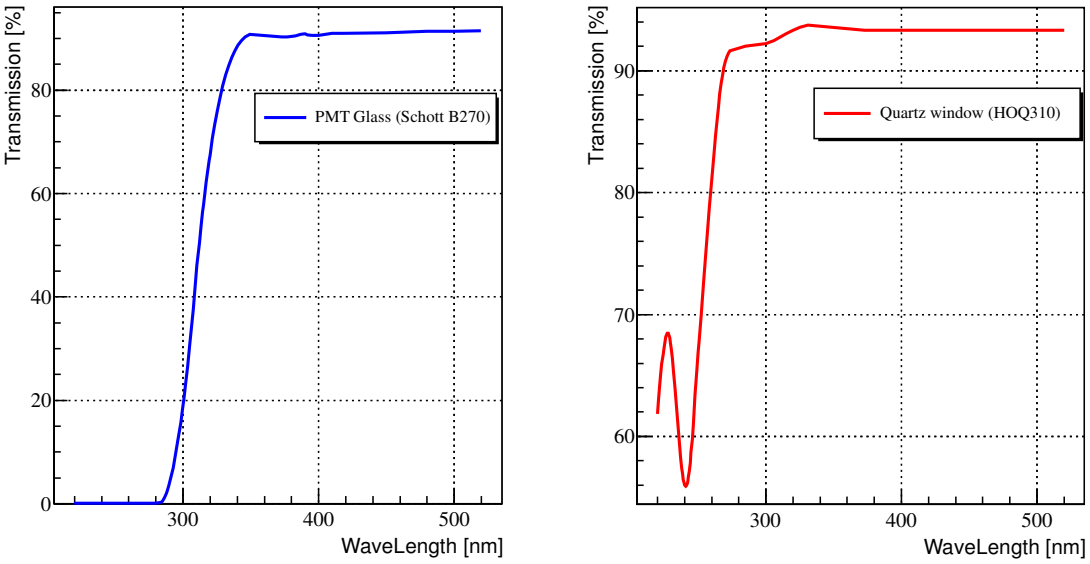

Figure 4.7: Left: Transmission spectrum of PMT glass (Schott B270) [186]. Right: Quartz window (HOQ310) [187]. At wavelengths above 450 nm the transmission was assumed to be constant.

Production of Scintillation Photons

Scintillation photons are produced when a charged particle deposits part of its energy in the helium gas contained within HGSAT. The generated number of photons are given a Gaussian distribution if they were more than 10, or a Poisson distribution otherwise, with a mean value $N(E_{dep})$ determined according to the following relation:

$$N(E_{dep}) = E_{dep} \times Y_{scint}$$

where E_{dep} is the energy deposited and Y_{scint} is the light yield of the scintillator. An additional statistical fluctuation around the average yield can be added if necessary to fit the observed intrinsic resolution of the scintillating material. Photons are emitted isotropically along the track segment with random linear polarisation, with wavelength according to the specified emission spectrum and with a time dependence characterised by an exponential decay.

Alternatively, scintillation photons can be generated "manually" by specifying the characteristics of the scintillation emission and an angular distribution. This in particular was used to study the detector light collection efficiency, as will be described in Sec. 4.3.

In this simulation the characteristic scintillation emission of nitrogen, including its emission spectrum and the time structure, was used since the observed scintillation in the HGSAT comes from the nitrogen fluorescence emission (see Ch. 2). The slow and fast components were taken as 60 ns and 30 ns respectively, though the relative strength of the fast component as a fraction of total scintillation yield was set to 100% since the fast component is dominant for the conditions in which the HGSAT was operated (see Sec. 2.4.1 for more details). The scintillation yield of nitrogen can vary considerably depending on many factors such as pressure, impurities and quenching effects resulting from non-radiative species. For pure nitrogen at $\sim$ 100 kPa and room temperature the scintillation yield has been measured to be $\sim$ 145 photons/MeV [115] and about 10 times higher at 1 kPa as measured in Ref. [189] where a more detailed study of nitrogen scintillation yield as a function of gas pressure was performed. However, the situation is different with nitrogen acting as a wavelength shifter, particularly concerning the wavelength shifting efficiency, and the uncertainty associated with the scintillation yield of helium itself, currently not well covered in literature. Investigation of the scintillation pulse height of helium mixed with 500 ppm nitrogen at various pressures during HGSAT calibration tests showed that the pulse height (a direct indication of scintillation yield) is inversely proportional to the pressure (see Fig. 4.29) which is consistent with Ref. [189] mentioned above[7]. By calibrating the number of photons registered by one PMT to

[7]This is not to be confused with Fig. 2.11 (right) which shows an increase in the scintillation yield for the same nitrogen partial pressure in helium as total system pressure increases. The

values in terms of QDC channels (see Sec. 4.2.5) it was estimated that the "effective" scintillation yield (Y_{eff})[8] was ∼100 and ∼60 photons/MeV at 1 and 2 MPa respectively.

However, information on the scintillation yield and timing structure were used for testing and to optimise the simulation since photons were generated "manually" following the nitrogen emission spectrum to construct a position map of the scintillation transport efficiency that was fed back into the ion energy-loss calculation as will be explained in the next few sections.

Absorption Process

Absorption produces a loss in intensity of scintillation photons travelling through a dielectric medium. It is implemented simply by attenuating the photon flux according to the medium's absorption length[9] defined as a function of the photon wavelength. Neglecting the insignificant absorption in the helium gas, there are two components of the detector in which this process is significant: the optical quartz windows (10 mm thick) and the PMTs glass (∼3 mm thick). The absorption length of the two components were calculated from the transmission spectra shown in Fig. 4.8 based on the Beer-Lambert law:

$$P(x, E) = e^{-x/\lambda(E)}$$

Where P(x,E) is the transmission probability, x is the thickness or the distance travelled by the photon, λ(E) is the absorption length[10] and E is the photon energy. Since noble-gases are transparent to their own scintillation emission the absorption length of the gas mix was set arbitrarily high to avoid any significant absorption of scintillation photons within the gas volume.

Boundary Processes

These processes determine the behaviour of optical photons crossing the boundaries of different media in terms of energy and polarisation and depend on the nature and the optical properties of the adjacent media. An optical photon crossing a boundary of a dielectric medium is faced with two possible scenarios: it either goes to another dielectric medium or is confronted with a metal surface. In the first scenario, the photon can undergo total internal reflection, refraction or reflection, depending on

measurement reported in that particular reference was made using a wavelength shifter, thus, the scintillation of helium was also detected, which scintillation yield increases proportionally with pressure as explained in Sec. 2.3.2.

[8] Reduced absolute scintillation yield of He/N_2 mix due to all of the quenching effects. $Y_{eff} = Y_{scint} \times Q_L$, where Q_L is the quenching loss factor.

[9] The average distance travelled by a photon before it is absorbed by the medium.

[10] Equivalent to the inverse of the linear attenuation coefficient (α).

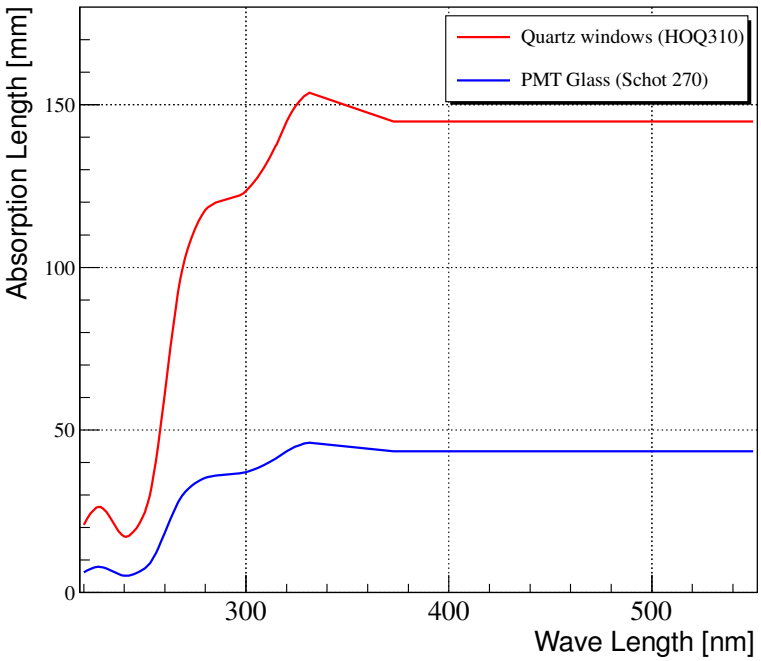

Figure 4.8: Absorption length in mm of quartz windows and PMT glass calculated from the transmission curves shown in Fig. 4.7 and as implemented in the simulation.

the photon's wavelength, angle of incidence, and the refractive indices on both sides of the boundary. For a perfectly smooth interface between two dielectric materials, no further input is needed for this scenario other than the absorption length and refractive indices of the two materials. For more demanding surfaces, Geant4 offers the UNIFIED [190] model which has a range of different reflection mechanisms that deal with all aspects of surface finish and reflector coating. In the second scenario, the photon can either be reflected back into the dielectric medium or absorbed at the metal surface. If the receiving medium is declared a "sensitive detector" e.g. a photocathode, absorbed photons can be registered as "detected" depending on the defined quantum efficiency of that medium. Optical reflection at a dielectric-metal boundary interface is handled via the GLISUR [191] model that provides two options for the surface finish type: *polished* or *ground*. There are two choices in setting optical properties in Geant4, one can either assign these properties to a surface between two volumes or a assign them to an entire single volume. In Geant4 terminology, in the former the boundary is referred to as a "*border*" surface whereas in the latter it is called a "*skin*" surface.

In this work, surfaces of quartz optical windows and PMT glasses were assumed to be perfectly smooth since they were supplied professionally polished and were coupled using optical grease during the assembly of the HGSAT. For this reason, it was sufficient to define the refractive index and transmission probability, given

in Sec. 4.2.2, in this case. On the other hand, reflectivity of the coating paint (Fig. 4.5(left)), aluminised mylar foils (80%) and photo-cathodes (0%) was assigned using the *skin* surface concept. This meant that for the cell Al body the entire volume was given the same optical properties as the coating paint. This was found to be the most practical solution since scintillation photons were only generated and propagated inside the gas-volume and nothing penetrated outside of the cell Al body. The GLISUR model and surface type dielectric-metal were used for all of these components setting the surface finish to *polished* for the aluminised mylar foils and photo-cathodes and *ground* in the case of the reflective coating paint. The Al window retaining rings were also considered since a small number of photons were able to propagate to these rings. Information on the reflectivity of these rings was not available, but investigating several values between 50% and 100% showed no significant effects on photon counting in the simulation. Thus the reflectivity was set to 80% which is around the lower end of values commonly reported in literature for unpolished aluminium reflectivity for the present emission spectrum.

Čerenkov Effect and Rayleigh Scattering

Geant4 is capable of simulating Čerenkov radiation when charged particles move faster than the speed of light in a given medium [188]. There are two potential places in the HGSAT where the Čerenkov radiation can be produced: optical quartz windows and PMTs glass. The Čerenkov photons are emitted in a cone centred on the direction of the incident charged particle. The cone opening angle (θ) is given by the following relation:

$$cos\theta = \frac{1}{\beta n} \tag{4.1}$$

where β is the particle velocity relative to the speed of light and n is the refractive index of the medium. Information on the Čerenkov light emission, such as flux, spectrum and polarisation, are calculated automatically by Geant4.

Implementation of the Rayleigh scattering process was not necessary in this simulation because of its small differential cross-section for optical photons, that is $\sim 0.2\,\mathrm{b}$ for 200 nm photons in N_2 or O_2 which gives a Rayleigh interaction length of 1.7 km in air and 1 m in quartz [192].

4.2.4 Physics Processes For Energetic Particles

To create a realistic simulation, one needs to define interaction processes for all of the particles produced when energetic gamma rays strike the HGSAT. To this end, Geant4 comes with an extensive set of physics processes which model particle interactions over a wide energy range. The software is being used in a broad range of scientific disciplines, from high energy physics to space science, and thus a large range of models are required to cover many different energy domains. In Geant4 the selection of interaction processes and the models which describe these is entirely the choice of the user. This is performed via "physics lists". Pre-compiled lists are

available, or alternatively users may compile their own custom lists. These physics processes are grouped in 7 main categories in Geant4: electromagnetic, hadronic, decay, photolepton-hadron, optical, parametrisation and transportation. A description of these processes is given in detail in Ref. [192], and thus only a brief overview of the relevant processes will be described.

There are two physics processes considered to be of major importance to the HGSAT $\gamma + {}^4\text{He}$ total photoabsorption simulation: propagation of optical photons, described in details in Sec. 4.2.3, and energy loss of the low energy ^{4}He photodisintegration products inside the gas volume. Hadronic interactions of low energy neutrons are also important for the analysis of the (γ,n) reaction channel and studies on the effects of the thin Be foils used in the beam inlet/exit windows. These processes are described in Geant4 by:

- Low Energy Electromagnetic (LEM) physics models.
- Hadronic physics that includes: the High-Precision neutron models (HP) ($<$ 20 MeV), the Pre-compound model ($>$ 20 MeV) and Low energy parametrised (LEP) Models.

Furthermore, Geant4 is said in Ref. [192] to be capable of simulating photonuclear interactions, including photonuclear disintegration relevant to the simulation presented here. It uses parametrised "total" photonuclear cross-sections and the ChIPS model for final states generation. The photonuclear package was examined and found to be inadequate to use for the purpose of this study. This will be discussed briefly in Sec. 4.5.2.

Low Energy Electromagnetic Physics

The Low Energy Electromagnetic (LEM) package is one of two main packages available in Geant4 to simulate electromagnetic interactions. It is specifically designed to handle electromagnetic interactions down to 250 eV, making it well suited for low energy applications up to 1 GeV. The package had undergone a major re-construction since the release of Geant4 (during the work on this simulation) to allow a better compatibility between the different sub-packages and to permit combination of different models within the electromagnetic main packages.

The models contained in the LEM package employ evaluated data libraries and analytical approaches to describe the electromagnetic processes of electrons, positrons, photons, charged hadrons and ions. The models used in this simulation for photons and electrons are based on the so-called "Livermore" library which in turn was extracted by Geant4 from a set of publicly distributed evaluated data libraries EADL, EEDL and EPDL97[11]. Electromagnetic processes of photons include Compton and Rayleigh scattering, pair production and the photo-electric effect. For

[11] **E**valuated **xx** **D**ata **L**ibrary, where **xx** is for **A**tomic, **E**lectrons and **P**hotons respectively.

electrons and positrons, bremsstrahlung, ionisation, multiple scattering, δ-ray production, positron annihilation and synchrotron radiation are considered. Charged hadrons and ions interact according to models of multiple Coulomb scattering and ionisation. The energy loss process manages the continuous energy loss of particles due to bremsstrahlung and ionisation using different models depending on the type and charge of a given particle. For charged hadrons with scaled energy [12] above 2 MeV the Bethe-Bloch formula is used, below 2 MeV parametrised models based on the NIST data bases are used if available, otherwise the ICRU'49[13] based parametrised models are used. Corrections due to the molecular structure of materials, the effect of the nuclear stopping power and the Barkas effect[14] are also taken into account [193]. Ionisation and energy loss calculations for charged ions heavier than helium are handled via the Ion parametrised energy loss model ($G4IonParametrisedLossModel$) which uses the ICRU'73 stopping power data up to 1 GeV. For ion-material combinations not included in the ICRU'73 data, the stopping powers are computed using the effective charge approach as in the so-called Geant4 "Standard" Electromagnetic (EM) package. This is explained in more detail in Ch. 12 of Ref. [192].

Hadronic Interactions

As explained above, Geant4 handles hadronic interactions via an extensive set of processes and models. Most of these models are applicable in limited energy ranges with some only suited to certain types of hadrons. Therefore more than one model is often needed to cover the energy range of interest for all the different types of hadron involved. The transition between different models is done via random selection of a model in the overlapping energy region. Generally speaking, Geant4 hadronic models provide descriptions of hadronic elastic and inelastic scattering (0 - 1 TeV), capture, fission, radioactive decay (at-rest and in flight), photo-nuclear ($\sim$ 10 MeV - 1 TeV), and lepto-nuclear reactions ($\sim$ 10 MeV - 40 TeV) [194]. The models governing these interactions are classified into three distinct types: data driven models, theory based models and parametrised models based on parametrisation and extrapolation of cross-sections.

In this simulation, interactions of neutrons from thermal up to 20 MeV are handled via the high-precision neutron library (HP). These interactions include radiative capture and elastic and inelastic scattering. Since the databases cover only certain elements, parametrised models (less accurate) are used if data on a particular element is missing. For neutrons above 20 MeV, the low energy parametrised

[12] To save memory Geant4 constructs tables for energy loss calculations only for certain charged particles called base particles: protons, antiprotons, muons, pions, kaons, and generic Ions. For all other charged hadrons and ions, Geant4 uses the same tables by scaling the particle kinetic energy to one of the base particles. More detail is found in Ref. [192].

[13] International Commission on Radiation Units & Measurements.

[14] Stopping power dependency on the particle charge.

models are used for elastic scattering and capture, whereas for inelastic scattering the Pre-compound model, recommended for neutrons and protons of energies below 170 MeV, is used.

Although not important for the present application, processes of elastic and inelastic scattering were assigned to all proton, deuteron, triton and alpha particles. For elastic channels the same process, *G4LElastic* inherited from GEANT3 GEISHA models, was used. For inelastic channels, these were defined individually for each particle/ion type. For this simulation, the process handling this type of interaction is based primarily on Low Energy Parametrised (LEP) models for light ions and alpha particles, whereas the Pre-compound model is used in the case of the inelastic scattering of protons. The Low Energy Parametrised models include *G4LEDeuteronInelastic*, *G4LETritonInelastic* and *G4LEAlphaInelastic*. These models are derived from the low energy part of GEISHA and are said to be valid in the energy range of 0 to 100 MeV on the Geant4 collaboration website [195].

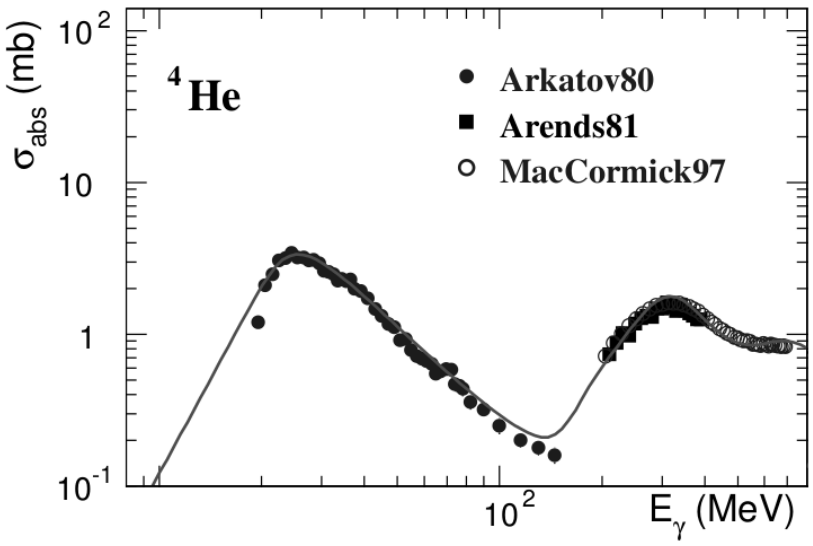

Figure 4.9: Geant4 approximation to the $\gamma + {}^4$He total photoabsorption cross-section as modified from Ref. [196] compared to measurements by Arkatov [197], Arends [198] and MacCormick [199].

There are two important processes to consider in modelling photonuclear interactions in Geant4. These are computation of the photonuclear cross-section and generation of the final states, which are done independently. Geant4 includes parametrised photonuclear cross-sections for all nuclei and all incident photon energies from breakup threshold upwards, including the γ+^{4}He total photoabsorption cross-section. The parametrisation employs interpolations and extrapolations from measurements on a large number of nuclei. It is done using five different functional forms, each covering a specific energy region. The regions relevant to this study are the Giant Dipole Resonance (GDR) region that covers the photon energy

from 10 MeV up to 30 MeV and the "quasi-deuteron" region which extends from ∼ 30 MeV up to the pion threshold. Details on how these approximations are made can be found in Ref. [196]. Fig. 4.9 shows the Geant4 approximation to the γ+^{4}He total photoabsorption cross-section compared with the measurement of Arkatov [197] for photon energies of ∼20 MeV to ∼150 MeV.

4.2.5 Hits Processing and Digitisation

"Hits" are created as particles pass through volumes declared as sensitive detectors. In each hit, information on the traversing particle such as position, momentum or energy deposited are recorded. Certain conditions can be applied to when hits are created, e.g. minimum energy below which a particle is not tracked.

In this simulation, the initial coordinates and kinetic energies of the incident particles are recorded at the beginning of each event and filled in a ROOT tree. Photons reflected or absorbed at the boundaries are counted and included in the simulation output sequentially. The gas and photocathode volumes are set to be sensitive detectors. A gas hit is created whenever the particle deposits part of its energy within the gas volume. The particle type, energy deposited, particle momentum, and the vertex position are recorded and filled directly in the ROOT tree. Photons arriving the photocathode volumes produce photoelectrons (photon hits) depending on the photocathode QE spectrum shown in Fig. 4.5. Photon hits contain information on the photon arrival time, photon energy (i.e wavelength), and finally the PMT identification index. Photon hits are converted to pulse heights in terms of QDC channels in what is known as "digitisation" in Geant4.

Digitisation

The digitisation is performed in a simple manner within the simulation. First, the number of photoelectrons produced in individual PMTs (N) are used to simulate the corresponding charge according to the following relation:

$$Q(i) = N(i) \times g(i) \times Qe \tag{4.2}$$

where Q(i) is the charge collected by PMT(i), g(i) is the PMT(i) gain (electrons/photo-electron) and Qe is the electron charge, 1.602×10^{-19} Coulomb. To compensate for fluctuations and other smearing effects, the gain for individual PMTs is chosen randomly from a Gaussian distribution centred around the gain given by the PMT manufacturer for the applied operating voltage and with a standard deviation of 30%[15]. The resultant charge spectrum is then converted to a QDC spectrum on the basis of the QDC module calibration factor (k) (charge/channel) and adding the intrinsic pedestal QDC channel:

$$QDC(i) = Q(i) \times k + QDC_{pedestal} \tag{4.3}$$

[15] A smearing factor that gives the best fit to the pulse height spectrum measured from a ^{241}Am source, see Sec. 4.5.3.

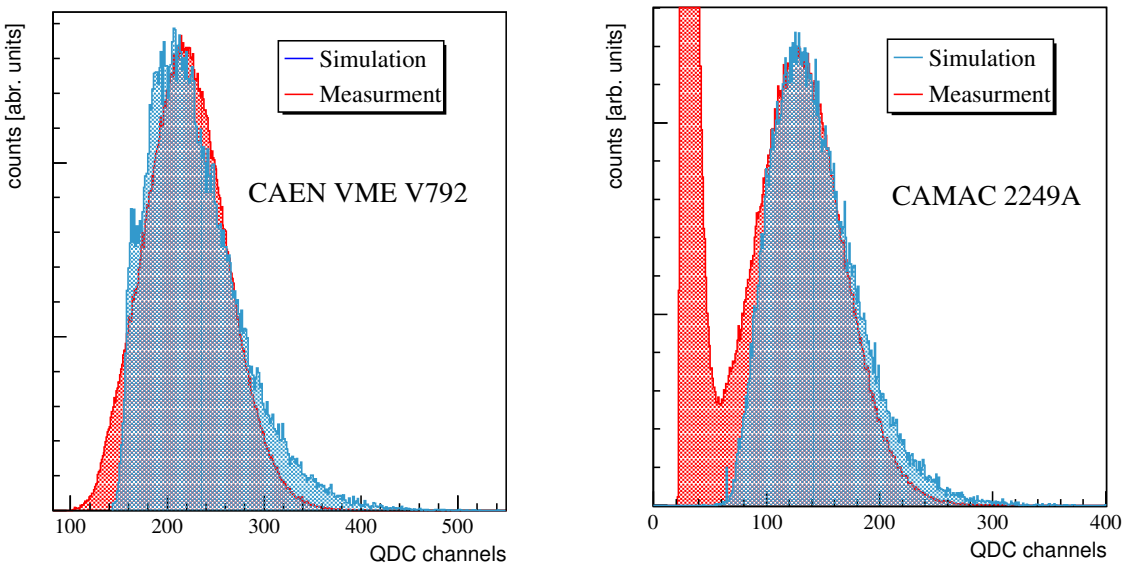

Figure 4.10: The simulated QDC spectrum of one PMT superimposed on the spectrum measured using the 5.45 MeV α-particles from a ^{241}Am source placed at the centre of one of the the HGSAT main cells and using two different QDC modules: a CAEN VME V792 (left) and a CAMAC LeCroy 2249A (right). The latter was used during bench-tests at Glasgow whereas the former was used in Lund for calibration and during the experiment. The intrinsic pedestal channels of the two modules are 88 and 40 respectively. The bench-tests were performed at half the pressure of that used during the experiment and calibration, therefore, the scintillation yield was adjusted accordingly (see Fig. 4.29). The mean gain used in this simulation is 2×10^7 for the simulated Lund data and 3×10^7 for the Glasgow data as the PMTs were operated at slightly different HV.

The width of the pedestal distribution shows the level of electronic noise on the signal which would also add a width to the signal distribution. This approach seemed to work quite well as can be seen in Fig. 4.10. However, a more careful selection of the parameters of the photoelectrons $\Rightarrow$ QDC channel conversion could have led to a better match and will be attempted when the analysis is refined for publication.

4.3 Light Collection Efficiency

The light collection efficiency is defined as the number of photoelectrons produced by a PMT divided by the total number of photons generated at a given location. The light collected by the HGSAT PMTs depends on the position at which the scintillation occurs and this in turn leads to a position dependence of the detection efficiency for photodisintegration reaction products. Thus a quantitative study of optical photon transport through HGSAT was necessary to obtain a cross-section.

For the light collection studies, it was sufficient to declare the photocathodes as sensitive and to include only the optical photon processes in the physics lists. Running the simulation with this setup proved to be computationally efficient. The light collection efficiency was then mapped by generating optical photons with a random distribution in the entire gas volume and counting how many of those photons were successfully detected in the photocathodes. This is explained in more detail in the following subsections.

4.3.1 Generation of Optical Photons

Due to the geometric shape of the HGSAT, Geant4 generic particle generators were inadequate for the purpose of generating optical photons. Alternatively, a basic event generator was written in C++ which was fed into Geant4 in the form of a ROOT tree. To map out the light collection efficiency, approximately 8×10^9 optical photons following the nitrogen emission spectrum[16] were generated isotropically and

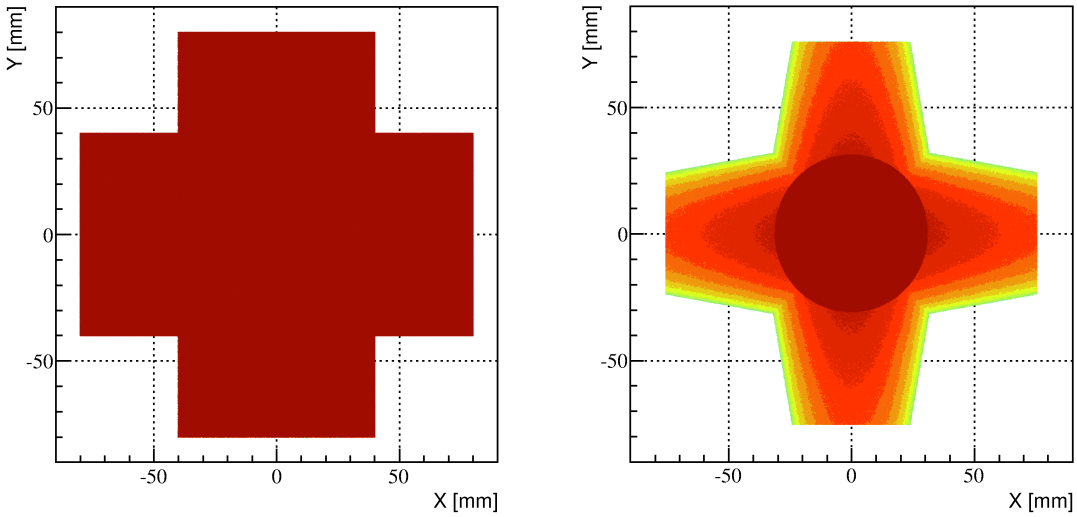

Figure 4.11: Left: the lateral distribution of the optical photons produced by the event generator. Right: the distribution of optical photons as generated in a simulation run, photons generated outside the gas volume are terminated in the simulation immediately. More events are seen in the central cylinder because of the shape of the gas cell, see bottom right of Fig. 4.12.

distributed randomly in the shape of a two crossed rectangular volumes measuring 80 mm × 80 mm × 160 mm as can be seen in Fig. 4.11(left). To further investigate

[16]The nitrogen emission spectrum was approximated to 22 entries with the following strength: ∼ 20% at 220 - 320 nm, ∼ 60% at 320 - 390 nm and ∼ 20% at 390 - 520 nm [200].

the light collection position dependency, sets of 10^5 photons were generated sequentially along the x, y and z axes in steps incremented by 0.5 mm. Photons generated outside the gas volume were excluded during the run of the simulation. Fig. 4.11 shows the photon distribution as produced by the event generator (left) and those allowed in the simulation (right).

4.3.2 Position Dependent Light Collection Efficiency

Photon hits on individual PMTs, as well as the sum on all PMTs of each cell, were recorded and plotted against the initial position of every event. Fig. 4.12 and 4.13

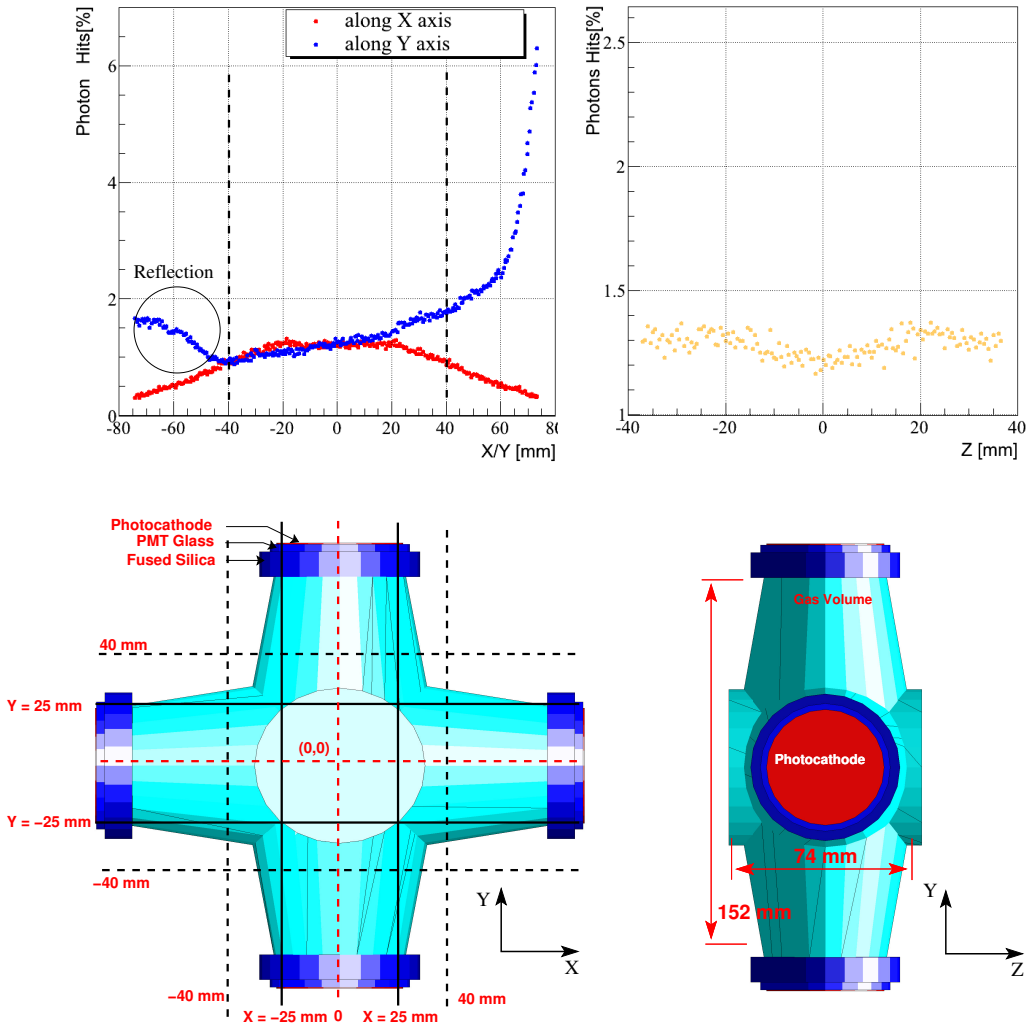

Figure 4.12: The position dependent light collection efficiency of the top PMT as a function of the photon generation position along x, y (left) and z (right) axes.

summarise the simulation results on the position dependent light collection efficiency of a single PMT, the top PMT in this case. The upper two plots in Fig. 4.12 show the percentage number of photoelectrons as a function of initial position along the x, y

and z axes. The four PMTs on each cell of the HGSAT are positioned symmetrically, which means that the response of one PMT is identical to the other three but with the x and y axes rotated. The rise in the light collection efficiency along the y axis at $y <$ -40 mm is a direct effect of back reflections from the optical window. The light collection is maximum when photons are generated close to the PMT due to the large solid angle coverage. As photons are generated away from the PMT, the solid angle becomes smaller and their probability of being detected in the other three PMTs is increased, resulting in less photons making it to the initial PMT. The high light collection efficiency at the two sides of Fig. 4.13 (x,$y <$ -50 mm and x,$y >$ 50 mm) is mainly due to photons being generated close to one of the four PMTs, thus, giving a higher solid angle coverage.

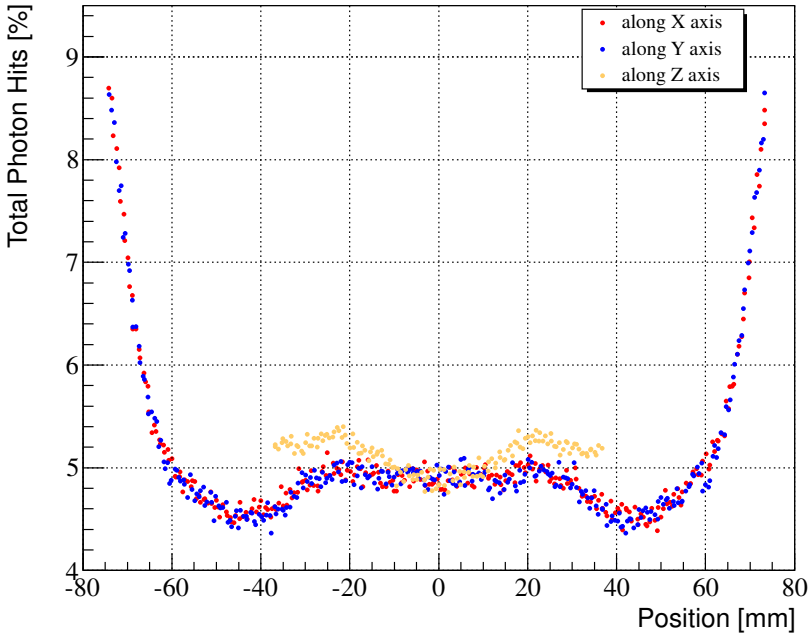

Figure 4.13: Percentage of photoelectrons in all of the PMTs as a function of photon generation position along x, y and z axes.

The light collection efficiency of the HGSAT is low overall, ranging from ∼4% up to a maximum of less than 9%, but it must be remembered that this efficiency includes the PMT QE which is only ∼27% at maximum.

4.3.3 Three Dimensional Light Collection Efficiency Map

Voxelisation

To map out the light collection efficiency in three dimensions, the gas volume was divided into 421875 three dimensional ∼ 2 × 2 × 1 mm pixels known as "vox-

els"[17]. Taking an input of 8×10^9 photons, generated at random positions within the HGSAT, the number of photons generated within each voxel is counted, as well as the number of photoelectrons produced by each of the four PMTs. The voxelisation was performed using a ROOT tool. The voxel size was sufficiently small to cope with the rate of change of light transport efficiency with position and was compatible with the available computational power.

Light Collection Efficiency Map

The three-dimensional light collection efficiency map was constructed by looping over all voxels, dividing the number of photoelectrons produced by the PMTs (photon hits) by the total number of photons generated in that particular voxel. Fig. 4.14 shows the mapped light collection efficiency for the top PMT. The figure shows a plot for each coordinate axis averaged over the other two axes. As mentioned in the

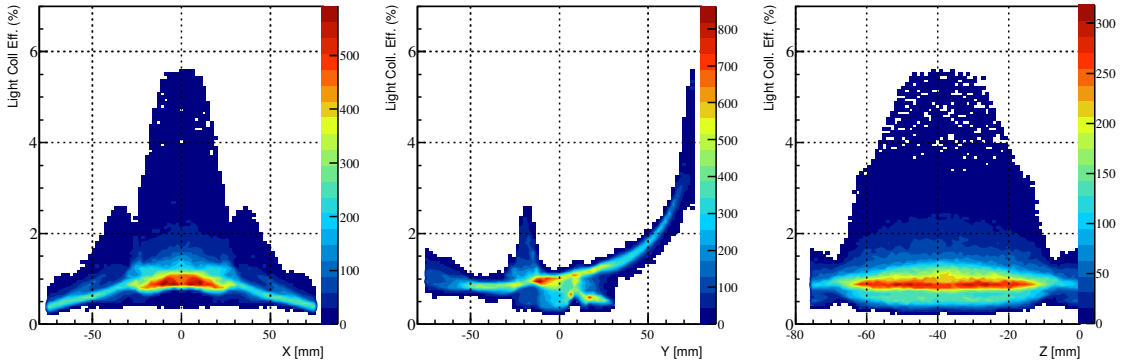

Figure 4.14: The three-dimensional light collection efficiency map of the top PMT for each coordinate axis averaged over the other two axes. The intensity scale presents the number of detected photons.

previous subsection, the PMTs are positioned symmetrically making Fig. 4.14 also valid for the other three PMTs. The light collection efficiency of one of the HGSAT cells is displayed in Fig. 4.15, where the sum of the four PMTs hits is divided by the total number of photons generated for each voxel. The light collection map is stored in the form of a ROOT tree which carries information on the voxel identification number and the corresponding light collection efficiency for individual PMTs.

4.4 $\gamma + {}^4$He Reaction Products Energy-Loss

The number of scintillation photons produced in a $\gamma+{}^4$He photo-disintegration event is proportional to the energy deposited by reaction products and depends on the

[17] Hence the term "voxelisation".

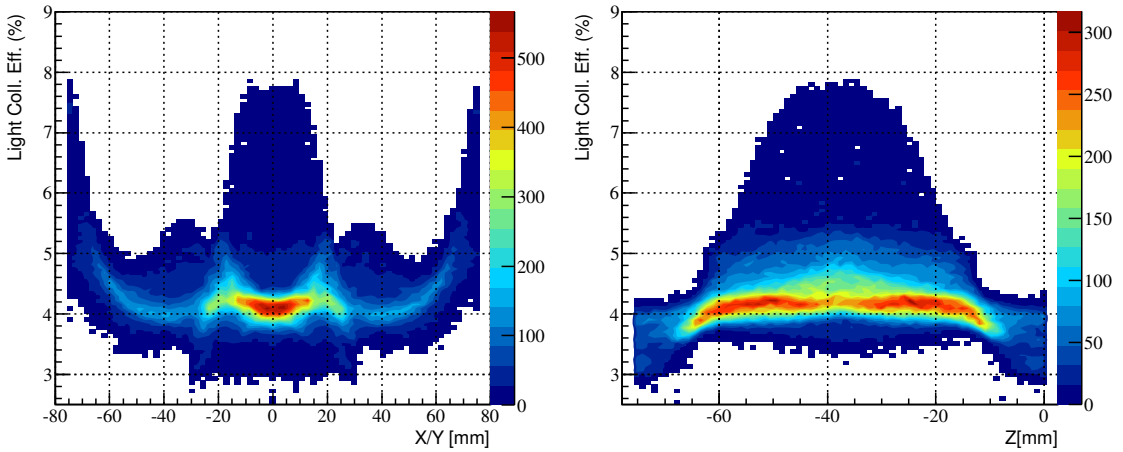

Figure 4.15: The total light collection efficiency of one of the HGSAT cells. The HGSAT is symmetric with respect to the x-axis and the y-axis, therefore, the x and the y plots are identical. The intensity scale presents the number detected photons.

scintillation characteristics of the He+500 ppm N_2 gas mix such as the scintillation yield and N_2 wavelength shifting efficiency. $\gamma + {}^4$He photo-disintegration events are detected if the energy deposited by reaction products is higher than a certain threshold. This threshold is set by the experimental discrimination levels and influenced by the light collection efficiency of the detector.

In the energy loss simulation, $\gamma + {}^4$He photo-disintegration events are generated separately and fed into the simulation. Modelling of all optical properties and light transport is substituted by the light collection efficiency map described in Sec. 4.3. For each step along the track of a charged particle in the helium gas (see Sec. 4.2.5) a voxel index is obtained from the vertex position. The total number of photoelectrons (photon hits) produced by the PMTs is calculated from energy deposited, scintillation yield and the corresponding light collection efficiency in the given voxel. Photon hits on individual PMTs are then calculated by randomly distributing the total number of photoelectrons around the PMTs, weighted by the light collection efficiency of each single PMT. The 4-momentum, energy deposited and particle type are recorded for all particles propagating through the gas volume as well as the vertex positions.

4.4.1 Event Generation

An event generator based on ROOT was written to simulate $\gamma + {}^4$He photodisintegration events. Partial cross-sections of different break-up reaction channels are specified and for each channel the reaction product four momenta are sampled according to the kinematic phase space. The event generator output is stored in a ROOT tree and includes: an index which specifies the particular reaction channel,

4-momentum components and particle type for each reactant and final product as well as the co-ordinates of the reaction vertex.

Photo-Reaction Modelling

$\gamma + {}^4$He photodisintegration below pion production threshold includes four main reaction channels: ${}^4\mathrm{He}(\gamma, p{}^3\mathrm{H})$, ${}^4\mathrm{He}(\gamma, {}^3\mathrm{He})n$, ${}^4\mathrm{He}(\gamma, pd)n$ and ${}^4\mathrm{He}(\gamma, 2p)2n$. The break-up thresholds of these reactions are 19.81 MeV, 21.57 MeV, 26.0 MeV and 28.3 MeV respectively. The ${}^4\mathrm{He}(\gamma, dd)$ reaction channel is neglected due to its tiny cross-section compared with the rest, measured to peak at ∼3.4 μb at 30 MeV photon energy [197]. Below the three-body break-up threshold, the total photoabsorption cross-section of ^{4}He is practically the sum of the ${}^4\mathrm{He}(\gamma, p{}^3\mathrm{H})$ and ${}^4\mathrm{He}(\gamma, {}^3\mathrm{He})n$ partial cross-sections. The total photoabsorption cross-section is taken from Quaglioni et

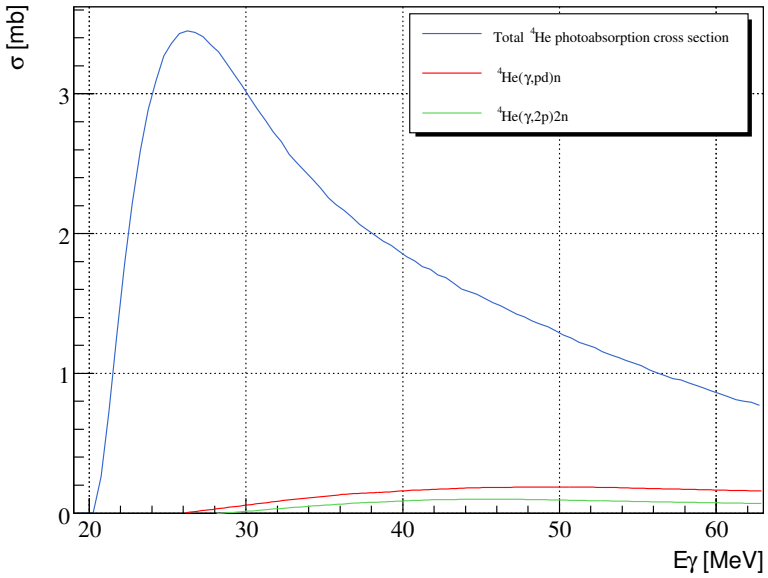

Figure 4.16: The total $\gamma + {}^4$+He cross-section as implemented in the event generator showing also the three (red) and four (green) body break-up cross sections. The event generator generates events according to the total photoabsorption cross-section. Events are then distributed into different reaction channels according to their partial cross-sections.

al. calculations using the *Lorentz Integral Transorm* (LIT) method with the $Malfliet - Tjon$ (MTI-III) potential [201]. A 1:1 $(\gamma, p)/(\gamma, n)$ ratio is assumed for the 2-body break-up channel. The 3-body and 4-body break-up cross-sections are taken from a naive fit to data in the Quaglioni review [201]. Partial cross-sections of the 3-body and 4-body reaction channels along with the total cross-section as used in the event generator are given in Fig. 4.16.

Generating $\gamma + {}^4$He photo-disintegration Events

To simulate the angular divergence of the collimated bremsstrahlung cone, interaction vertices are determined by taking random points along the 304 mm length of the HGSAT within a cone of half angle 1.1 mrad defined by the photon collimator. The radiator-collimator-target geometry are illustrated in Fig. 4.17. The distribution of vertex positions as produced by the event generator is shown in Fig. 4.18.

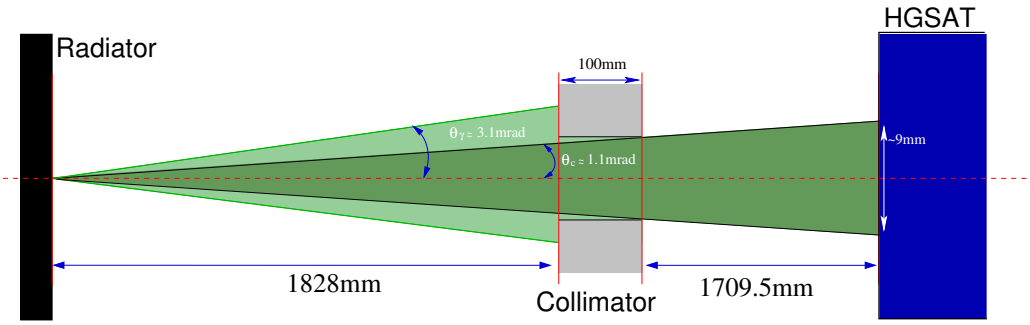

Figure 4.17: The radiator-target distance and the collimation angle (θ_c) as used in the event generator. θ_γ is the half opening angle of the bremsstrahlung photons.

The photon beam energy is selected randomly from a $1/E_\gamma$ bremsstrahlung distribution ranging between 13 to 63 MeV corresponding to the experimental energy range. However only events above the breakup threshold are accepted and the random selection is weighted by the total cross-section distribution. When the beam energy is selected a "parent particle" is formed by summing the four momenta of the beam photon and the (at rest) target ^{4}He. A particular reaction is then just the "decay" of this parent into 2, 3 or 4 daughter particles.

Generation of the daughter-particle four momenta is handled via the ROOT "*TGenPhaseSpace*" class. It takes the 4-momentum of the beam + target parent particle and the rest masses of the decay products as input parameters. Events are generated according to phase space in the centre-of-mass frame, and then the decay products are boosted to the lab frame [202]. Fig. 4.19 shows generated event distributions for different reaction channels as a function of photon energy.

4.4.2 Energy Loss

Energy loss calculations on the $\gamma + {}^4$He breakup products are performed in Geant4 using a combination of the well-known Bethe-Bloch formalism and parametrised models at lower energies as described in Sec. 4.2.4. The simulation was run with events generated by the event generator for a target density of $\sim$3.5 mg/cm^3, reading out the corresponding photon energy E_γ and energy deposited in each $\gamma + {}^4$He reaction channel as well as the range and energy deposited by individual break-up particles.

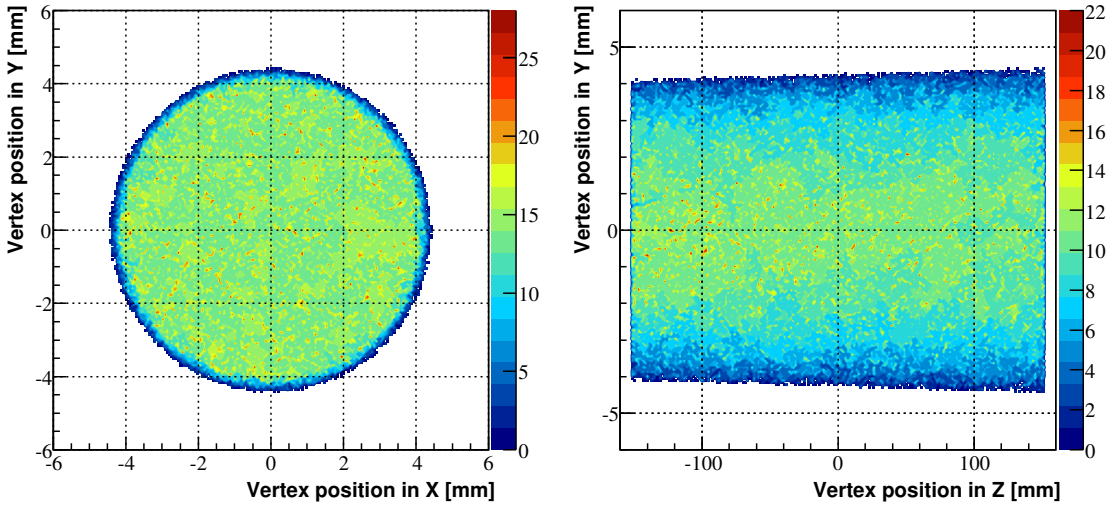

Figure 4.18: Distribution of vertex positions as produced by the event generator in the XY (left) and the YZ (right) planes. The XY plane plot also corresponds to the beam spot size.

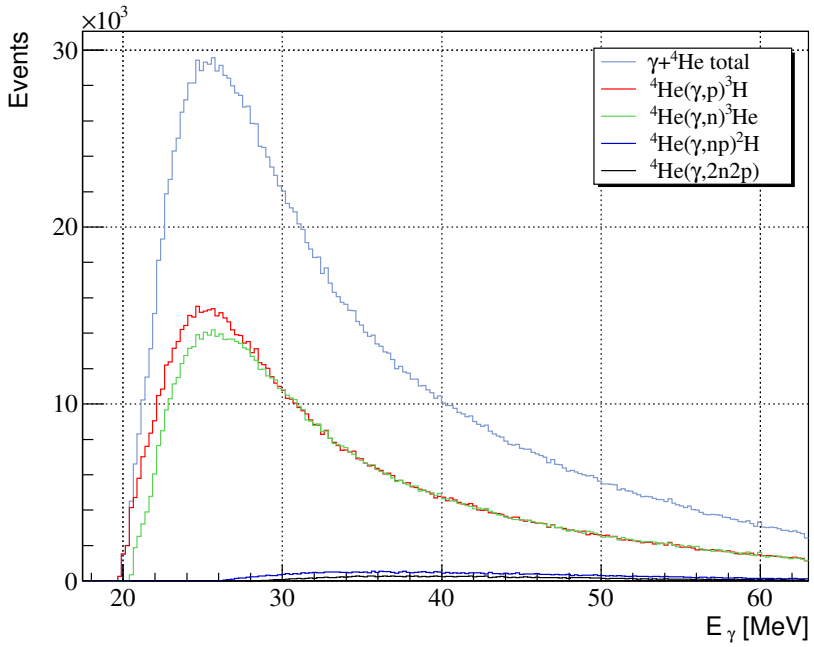

Figure 4.19: Generated events for different $\gamma + {}^4$He reaction channels as a function of photon energy.

Range and Stopping Power

The stopping power[18] and the range[19] of all $\gamma + {}^4$He breakup products, with kinetic energies extracted from the event generator, were obtained using SRIM[20] [203] in order to cross check the simulation data. Fig. 4.20 shows the expected range of

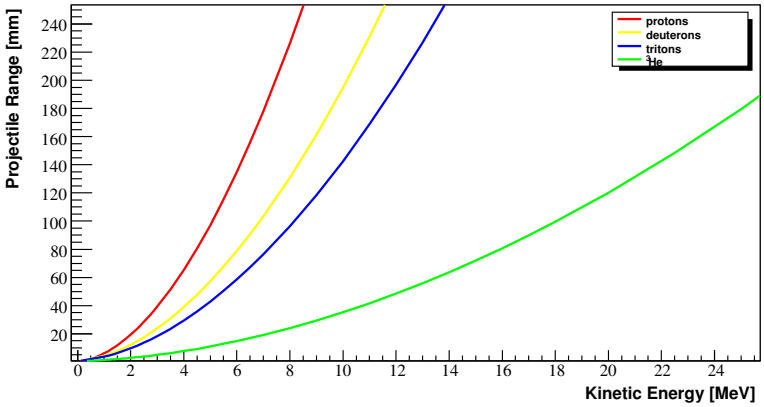

Figure 4.20: Expected range of $\gamma + {}^4$H breakup products as a function of particle energy. Data derived from SRIM [203].

γ+^{4}He breakup products as a function of particle energy. The active volume of the detector is ∼8×8×16 cm, meaning that most of the $\gamma + {}^4$He products will not deposit all of their energies within the gas volume for the employed target density and photon energy. Fig. 4.21 shows the range of $\gamma + {}^4$He products as produced by the simulation (left) and their corresponding kinetic energy as a function of photon energy (right). Fig. 4.22 shows tracked particles inside the gas volume. It can be clearly seen that particles with enough energy are escaping the gas volume. The escape energy thresholds of different particles correspond closely to the SRIM calculations.

Energy Deposited

Fig. 4.23 shows the energy deposited in the gas volume in the $^4\mathrm{He}(\gamma, p)^3\mathrm{H}$ reaction channel as a function of photon energy. The shape comes from the sum of the energy deposited by protons and tritons. The decrease in the energy deposited seen at >25 MeV and >45 MeV for protons and tritons respectively is due to these particles having enough kinetic energy to escape the gas volume, i.e. less and less energy being deposited as the photon energy goes up as explained in the previous subsection. Fig. 4.24 show energy deposited in $^4\mathrm{He}(\gamma, {}^3\mathrm{He})n$, $^4\mathrm{He}(\gamma, pd)n$ and $^4\mathrm{He}(\gamma, 2p)2n$

[18] Stopping power of a charged particle passing through a given material is defined as the differential energy loss per unit distance (dE/dx).

[19] The mean path length of a particle in target matter before coming to rest.

[20] Stopping and Range of Ions in Matter

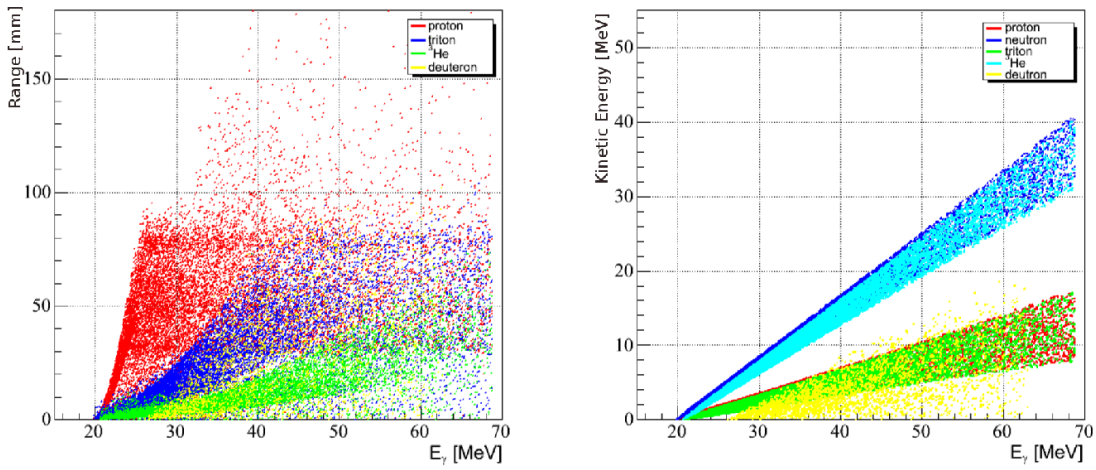

Figure 4.21: Left: range of $\gamma + {}^4$He break-up products as produced by the simulation. Right: corresponding kinetic energy as a function of photon energy.

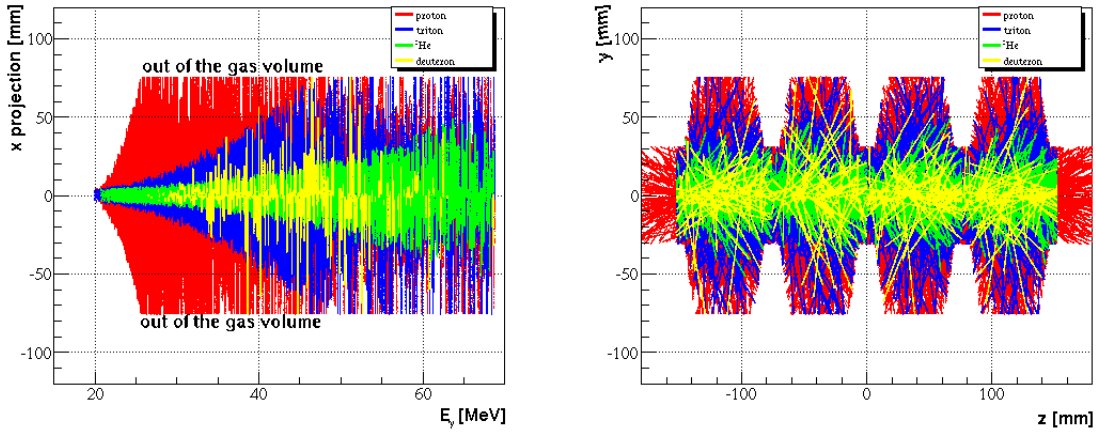

Figure 4.22: $\gamma + {}^4$He break-up particle tracks inside the active volume of the detector. Left: x projection as a function of photon energy (E_γ). It can be seen that at above 25 MeV photon energy, protons have enough energy to escape the gas volume. The escape thresholds for deuterons and tritons are E_γ >40 MeV and E_γ >45 MeV respectively. The corresponding particle kinetic energy can be obtained from Fig. 4.20(right). The target density at 2 MPa is high enough to stop all of the ^{3}He ions within the gas volume. Right: track projections on the yz plane.

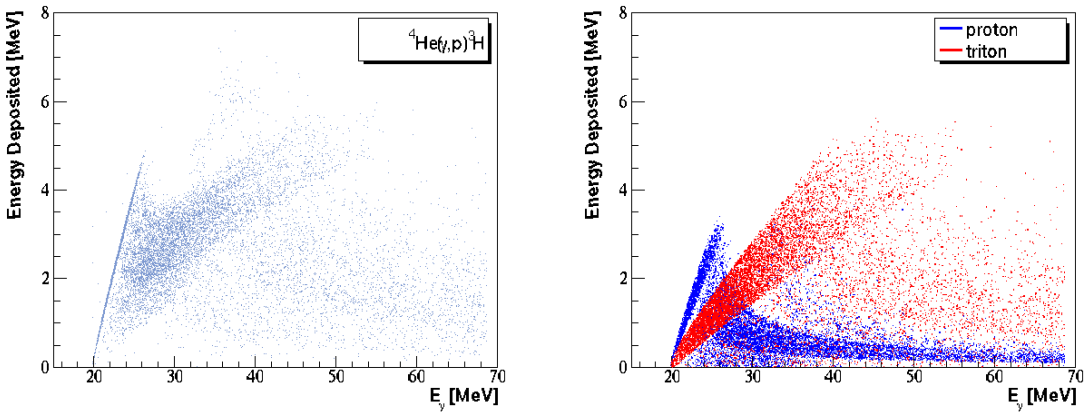

Figure 4.23: Left: The total energy deposited in the helium gas at 2 MPa pressure in the $^4\mathrm{He}(\gamma, p^3\mathrm{H})$ reaction. Right: the contribution of the two reaction products in the total energy deposited.

reaction channels also as a function of photon energy. The energy deposited in the (γ, n) channel comes primarily from energy loss of ^{3}He nuclides which are stopped entirely in the gas volume for all incident photon energies.

4.5 Detection Efficiency

The detection efficiency is simply the ratio of detected events to the total number of events that hit the detector. Determination of this quantity is required to convert the yield into cross-section. The HGSAT means of detection relies on the energy deposited by charged $\gamma + {}^4$He breakup products within the active volume of the detector. The energy deposited must be above a certain threshold[21] in order for the experimental triggers to fire and start the data acquisition. Therefore, there are two pieces of information needed to determine the HGSAT detection efficiency: total energy deposited in each $\gamma + {}^4$He event and the discrimination thresholds used to create the experimental triggers.

4.5.1 Discriminator Thresholds

The trigger used in the experiment is made of two levels:

- The first level trigger is made from the sum of the 4 signals from one cell. The sum feeds a CFD set at 30 mV. The 1$^{\mathrm{st}}$ level is the "OR" of the 4 CFDs (4 cells).
- The second level trigger uses the PMT multiplicity ($\mathrm{M_n}$), where "n" is the number of PMTs that record a signal above threshold. The $\mathrm{M_n}$ is derived

[21] This threshold is determined by the discriminator levels set during the experiment.

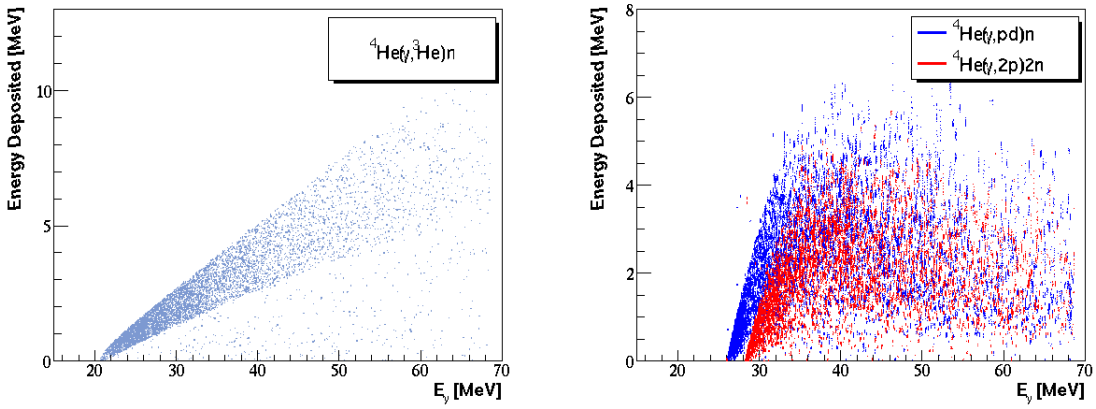

Figure 4.24: Left: energy deposited in the $^4\mathrm{He}(\gamma, ^3\mathrm{He})n$ reaction. The energy deposited in the reaction comes mainly from the ^{3}He ions. Right: energy deposited in the $^4\mathrm{He}(\gamma, pd)n$ (blue) and $^4\mathrm{He}(\gamma, 2p)2n$ (red) reactions.

from the single PMT discriminators. The multiplicity signal comes from the "Σ" output of the discriminator. Σ is 50 mV per simultaneous hit and feeds a discriminator which is adjusted to 40 mV for the M_1, 70 mV for the M_2 and 120 mV for the M_3.

Running with an open trigger caused the DAQ system to saturate at the standard beam intensity. More detail is given in Sec. 3.7.2.

Discrimination effects appear as cuts to energy deposited and therefore to the number of photoelectrons produced by the PMTs. Fig. 4.25 shows simulated total energy deposited (left) and number of PMT photoelectrons (right) as a function of incident photon energy. Although all of the discrimination thresholds were set in terms of mVs during the experiment, it was not straightforward to convert these in the offline analysis into values in terms of MeV needed to set the energy cuts in the Monte-Carlo simulation. Absolute determination of this conversion requires a calibration procedure which is currently being put together. Nevertheless, various energy and multiplicity cuts were evaluated using the simulation in order to estimate the discrimination effects on the detection efficiency as will be described in Sec. 4.5.4. Fig. 4.26 shows the HGSAT energy response as a function of E_γ as measured at MAX-lab [204]. The plot shows similar features, the increase in the pulse height as E_γ increases and the cusp at $25-30$ MeV E_γ, to those produced by the Monte-Carlo simulation shown in Fig. 4.25(left).

4.5.2 Geant4 Photonuclear Interactions

Geant4 photonuclear interactions were enabled and tested to compare with events produced by the customised event generator. A photon beam with a flat energy distribution between 12 and 65 MeV, corresponding to the photon energies used

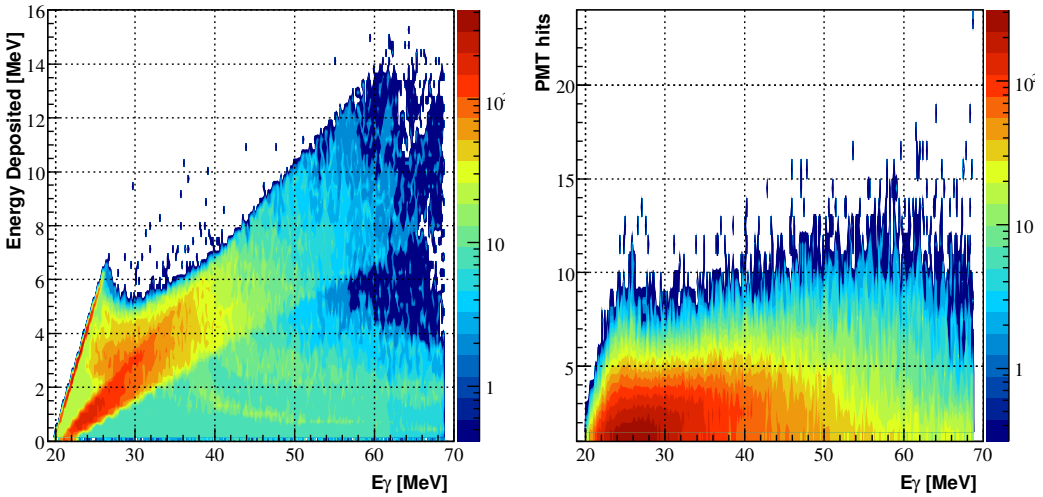

Figure 4.25: Left: total energy deposited in the helium gas at 2 MPa pressure by $\gamma + {}^4\mathrm{He}$ events as a function of photon energy. Right: number of photoelectrons produced by one PMT (PMT hits) as a function of photon energy. A discriminator threshold is effectively a value on the y axis.

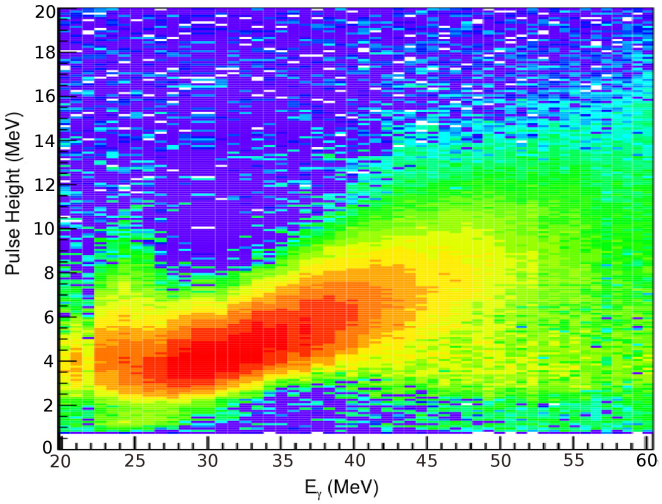

Figure 4.26: HGSAT energy response as a function of E_γ as measured at MAX-lab [204]. The measured distribution is distorted somewhat by the variability in the efficiency of the tagger channels.

during the experiment, was generated and directed toward the gas target. Energy deposited, reaction channel index and photon energy were all recorded in an event by event basis.

The simulation results show that Geant4 generates $\gamma + {}^4\mathrm{He}$ photodisintegration events according to the cross-section approximation shown in Fig. 4.9 as can be seen

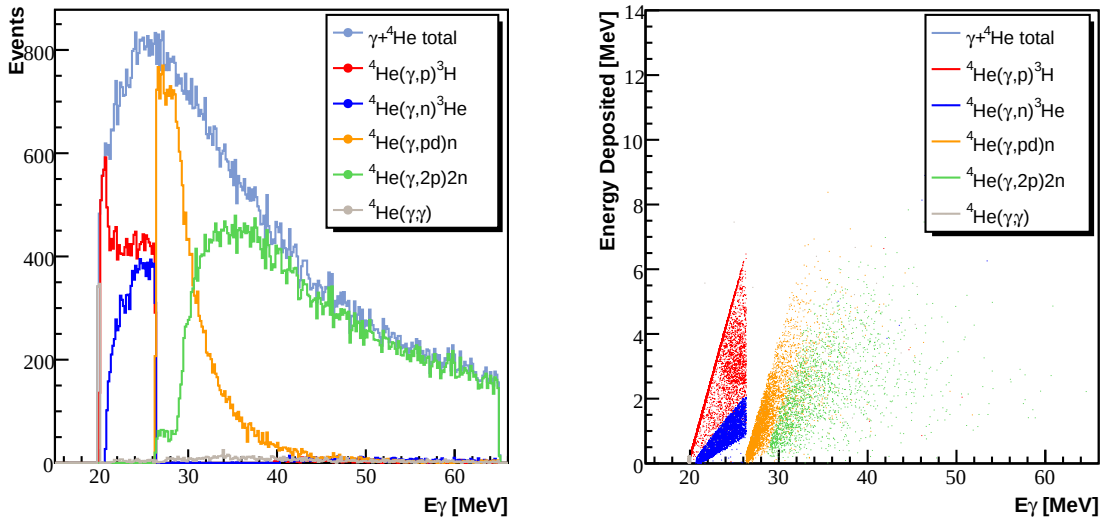

Figure 4.27: Left: Geant4 generated $\gamma + {}^4$He photodisintegration events broken down to the different reaction channels. The ratios of the reaction channels are clearly wrong though the total number of generated events does follow the ^{4}He total photoabsorption cross-section given in Fig. 4.9. Right: total energy deposited in the helium gas at 2 MPa by $\gamma + {}^4$He events as a function of photon energy. The cut-off seen at ∼27 MeV is due to a fault in Geant4 partial cross-section calculations.

in Fig. 4.27. The breakup thresholds of all reaction channels seem to be calculated correctly though some 4-body breakup events appeared below the corresponding breakup threshold. Energy deposited by $\gamma + {}^4$He breakup products is consistent with the one derived from the event generator. However, partial cross-sections of different reaction channels are incorrect as shown in Fig. 4.27(left). The ratios of different reaction channels are of real importance to this study since the detection efficiency is directly related to how much energy is deposited in the detector which can vary significantly from one reaction channel to another. It is possible for the user to input partial cross-sections directly to Geant4 by hand, however it was decided to not take these investigations any further at this stage.

4.5.3 Calibration

The HGSAT was energy calibrated using α sources. The same experimental setup, operating conditions and gas handling system described in Ch. 3 were used. The purpose of these measurements was to obtain input parameters needed in the Monte-Carlo simulation including the QDC channel to MeV conversion factor and an approximation to the effective scintillation yield.

The calibration was performed using ∼390 kBq ^{241}Am and ∼12 kBq ^{252}Cf sources.

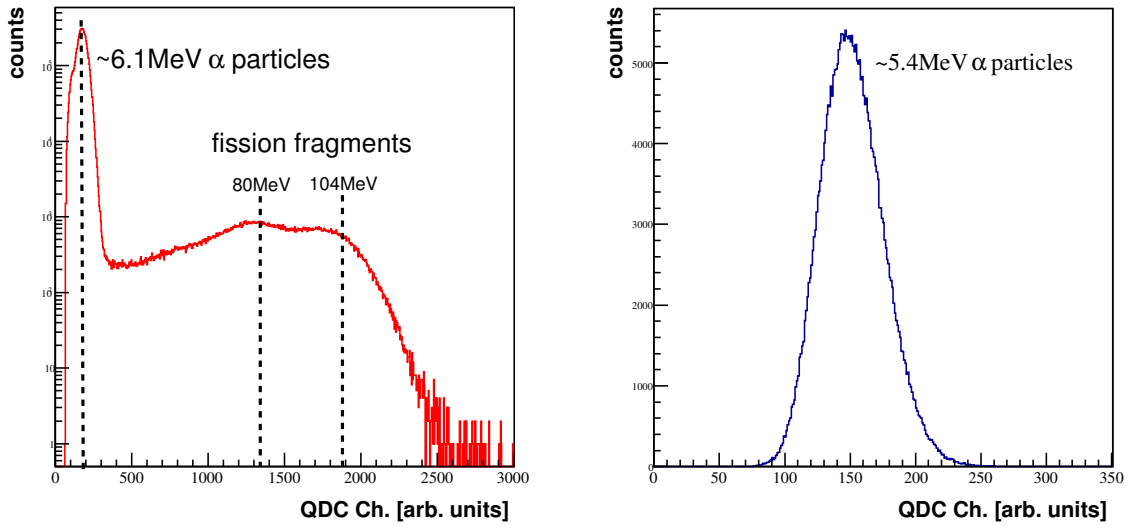

Figure 4.28: HGSAT (1 cell) response to: ^{252}Cf ∼6.1 MeV α particles and fission fragments the broad peaks at ∼80 MeV and ∼104 MeV [205] (left) and ^{241}Am ∼5.45 MeV α particles (right).

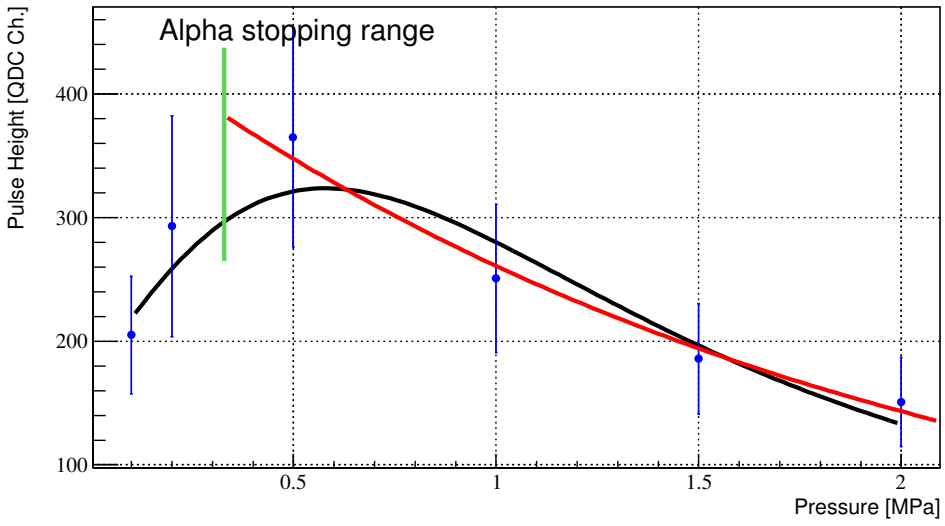

Figure 4.29: Scintillation pulse height in terms of QDC channels versus gas pressure. At ∼0.3MPa, the pressure is high enough to stop α particles entirely within the gas-volume. The red and the black curves are fits to data.

The sources were placed alternately[22] at the centre of one cell of the HGSAT using a source holder which is covered with aluminised mylar. Data was acquired the same way as with the data production using the same trigger conditions. The HGSAT response to charged particles is displayed in Fig. 4.28. The response is almost linear for both α particles and fission fragments. There is a slight mismatch between the ^{241}Am and ^{252}Cf QDC to MeV conversion which is likely due to the series of tests to investigate Xe and N_2 doping at different concentrations prior to measurement with the ^{252}Cf source. The gas system was evacuated and filled relatively fast due to the limited time available at the testing facility thus, the slight mismatch is likely to be due to quenching effects of residual impurities. The QDC to MeV conversion is done by subtracting the pedestal from the prompt peak location and then assigning the peak QDC channel number to the mean energy value of the used source, that is 5.45 MeV ^{241}Am α particles and 6.1 MeV, 80 and 104 MeV for α and fission fragments of the ^{252}C source respectively.

Variation of the pulse-height recorded for the ^{241}Am 5.45 MeV α peak as function of the gas pressure is displayed in Fig. 4.29. At 0.5 MPa helium gas pressure, 5.4 MeV α particles have a range of ∼4.5 cm and are completely stopped within the gas volume. Quenching effects of nitrogen at higher gas pressure can be clearly seen from the figure. The effective scintillation yield was estimated by running the simulation with different scintillation yield values and comparing with measurements taken at 1 MPa pressure. The value that led to the best match was then taken and used to extrapolate the corresponding scintillation yield at 2 MPa using the dependency relation shown in Fig. 4.29. The obtained value was then fed back to the simulation. The simulated QDC spectra output at 2 MPa were in good agreement with the spectra measured at that pressure. The effective scintillation yield was estimated to be ∼100 and ∼60 photons/MeV at 1 MPa and 2 MPa respectively.

4.5.4 Detection Efficiency Curves

Almost all beam events generate some energy in the target gas creating at least one hit in the PMTs as can be seen in Figs 4.30 and 4.31. The question is if they generate sufficient energy and enough PMT hits to make a trigger. To answer this, different energy and multiplicity cuts were evaluated to estimate the influence of discriminator thresholds on the detection efficiency. Fig. 4.30 shows the fraction of simulated events that pass different energy cuts. Events with energy deposited above these cuts are counted and then divided by the the total number of generated events for each photon energy bin. The multiplicity cut is slightly more complex containing two parameters: the threshold applied on the number of photoelectrons produced by a single PMT to register a hit (PMT threshold) and the minimum

[22] The ^{252}Cf source consists of $\sim 6.5 \times 10^{-5}$ µg californium oxide (Cf_2O_3) positioned on the top of a platinum clad nickel foil. The source is covered with 50 µg/cm^2 gold layer. Handling the source was done with caution to ensure no contamination to took place. More details on the source used in this work can be found in Ref. [166].

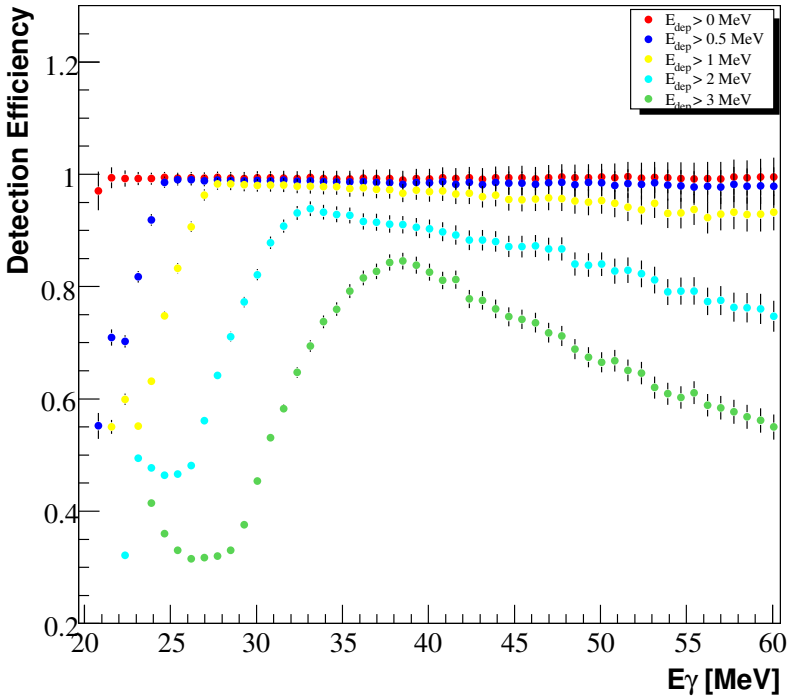

Figure 4.30: Detection efficiency for different energy cuts. For 0 and 0.1 MeV cuts, almost all generated events are detected. The low energy events at the GDR region are most affected by any energy cut of more than ∼200 keV. The minima observed around $25 - 28$ MeV photon energy for the 2 and 3 MeV energy cuts is mainly due to protons having sufficient energy to escape the gas volume, hence depositing less energy (see Figs 4.23 and 4.25(right)).

number of PMT hits to signal a scintillation event (multiplicity). The effect of these two parameters on the detection efficiency is displayed in Fig. 4.31. The three plots are for the M_1, M_2 and M_3 triggers. The different colours in each canvas are for the PMT threshold which is the minimum number of photons detected by the PMT to register a hit, that is 1, 2 or 3 which were chosen arbitrarily for illustration.

Discrimination effects are highly photon energy dependent. Events in the Giant Dipole Resonance (GDR) region are most sensitive to any applied discrimination. This is expected since events in that region are low energy events generally depositing $0 - 4$ MeV. Final detection efficiency curves are a combination between those displayed in Fig. 4.30 and Fig. 4.31.

4.5.5 Position Dependent Detection Efficiency

In addition to the incident photon energy dependency, the detection efficiency also depends on the position where the reaction takes place. $\gamma + {}^4\mathrm{He}$ events resulting

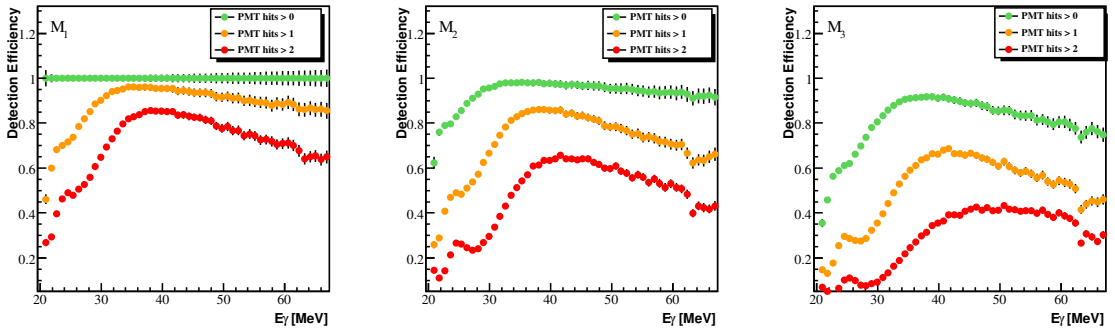

Figure 4.31: Detection efficiency for different multiplicity cuts at different PMT hits thresholds as a function of incident photon energy.

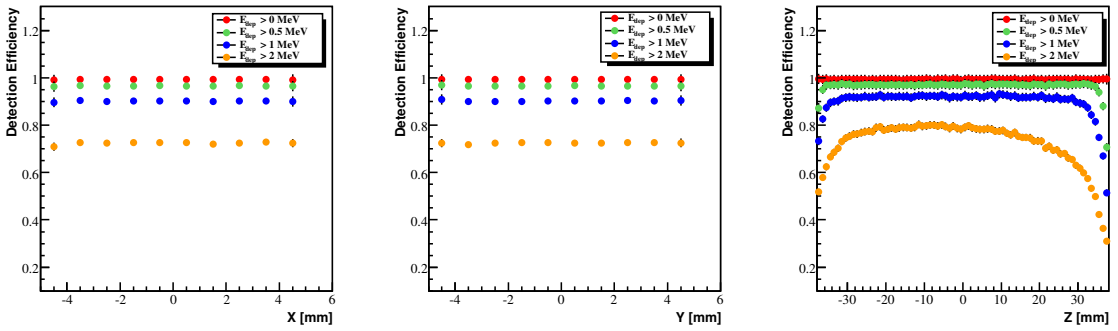

Figure 4.32: Position dependent detection efficiency averaged over all incident photon energies. Different energy cuts are presented in different colours. The stability in the detection efficiency along the x and y axes is due to the small size of the bremsstrahlung beam spot. As the beam illuminates the entire z-range of the target the position dependent effects are more apparent in this direction.

in breakup products close to the internal walls of the detector are less likely to deposit all of their energy within the gas volume than those associated with events which occur at the centre. Position dependency was evaluated for different energy and multiplicity cuts as can be seen in Fig. 4.32 and Fig. 4.33 respectively. As the bremsstrahlung beam is compact (∼9 mm diameter at the detector, Fig. 4.17) compared to the target cross-section there is little dependence on x and y in the relevant range. The case is different for the z axis (see Fig. 4.12 bottom right) where the detection efficiency averaged over all incident photon energies is higher in the centre ($z = 0$) than that near edges of the detector cell.

4.5.6 Be windows effect

The effect of possible contamination from photonuclear interactions in the Be windows, used to hold the gas pressure (see Ch. 2), on the measurement reported in this

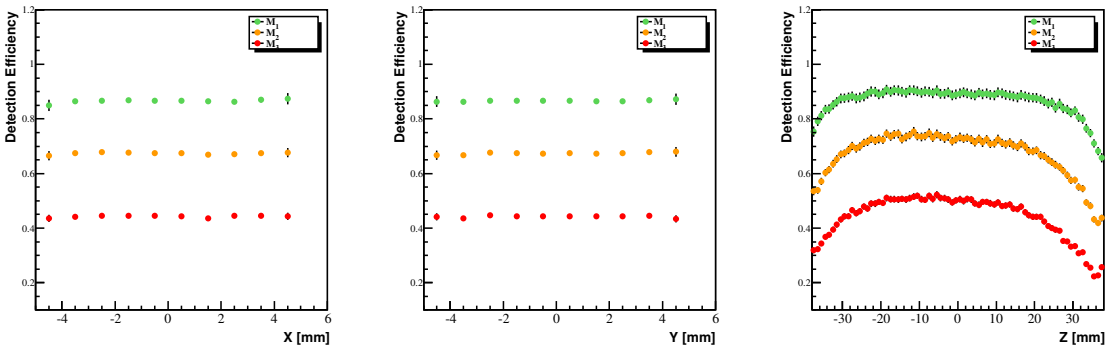

Figure 4.33: The same as with Fig. 4.32 but using different multiplicity cuts: M_1, M_2 and M_3. The minimum PMT hit threshold used in this plot is 2.

thesis was studied and simulated by J. R. M. Annand [204]. The two Be windows has a total thickness of about 180 mg/cm^2 compared to 103 mg/cm^2 for the helium target which may rise questions on the size of any background effects from the γ+Be reactions on the measured signals. The probability of photonuclear reactions products from ^{9}Be$(\gamma, p)^8$Li and ^{9}Be$(\gamma, pn)^7$Li produce a detectable signal in any of the HGSAT main cells was calculated via the Monte-Carlo simulation for the both the upstream and the downstream windows. The results of these are shown in Fig. 4.34. The distributions of the two Be windows are similar but 25% lower overall for the

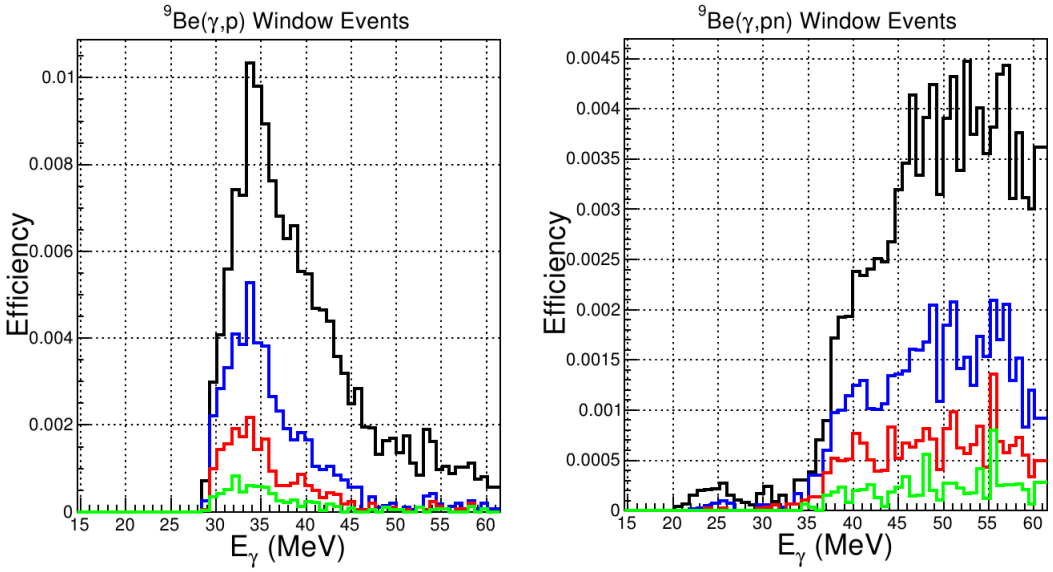

Figure 4.34: Detection efficiency for ^{9}Be$(\gamma, p)^8$Li (left) and ^{9}Be$(\gamma, pn)^7$Li (right) events as a function of incident photon energy E_γ. The different colours are for energy cuts of: 1 MeV (black); 2 MeV (blue); 3 MeV (red); 4 MeV (green). The PMT hit multiplicity is M2 [204].

downstream window [204]. For an energy cut of $\gtrsim$3 MeV, close to that estimated for

the actual experiment ∼2.5 MeV, the relative detection efficiency for γ+^{9}Be events in the HGSAT main cells is $\lesssim 0.5\%$ taking into account the thickness differences between Be and He. This was found to be small compared to other systematic effects described in Ch. 5. A further interesting finding of these studies was that around 80% of the detected γ+^{9}Be events occurred in the HGSAT outer main cells. Therefore, the small contamination from Be windows can be further reduced by excluding events in those two cells.

4.5.7 Summary

A Geant4 based Monte-Carlo simulation was developed to perform studies on the HGSAT and to determine the detection efficiency required in the absolute normalisation of the cross-section. Calibration and bench-test measurements were made to obtain a number of parameters used in the simulation and considerable effort was made to build a physics library relevant to the processes taking place within the HGSAT. The Geant4 photonuclear package was found to be inadequate for this case of study and therefore, a phase-space event generator was written to realistically generate $\gamma + {}^{4}$He events which are then fed to the simulation.

The simulation results showed that the HGSAT intrinsic detection efficiency can attain values close to 100%, but it is reduced substantially if practical discriminator thresholds are employed. Discrimination effects were evaluated and found to be highly incident photon energy dependent with events in the GDR region most affected. Absolute determination of the detection efficiency requires converting discriminator thresholds from mV to MeV. This was not performed in this work due to the limited time available. However, the work on this is still on-going and different approaches are currently being investigated. The detection efficiency for different discriminator thresholds was obtained and used to study the effect on the normalised cross-section as will be discussed in Ch. 5.

Chapter 5

Data Analysis

The aim of the analysis outlined in this chapter is to extract the total $\gamma + {}^4$He cross-section from the collected experimental data. Approximately 100 Gbyte of data in total were acquired over ∼9 days (*net*) of beam time distributed over two run periods in March and September of 2009. For the total $\gamma + {}^4$He cross-section measurement, the experimental data included:

- Coincidence times between the HGSAT and the 62 elements of the tagger focal plane detector.
- Pulse height and time from all PMTs attached to HGSAT.
- Scalers recording the counts in the tagger focal plane detector.
- Scalers recording rates in the trigger system and photon beam monitors.

The data is stored in a ROOT format and the entire analysis was performed using the ROOT data analysis framework [171].

This chapter focuses on the steps followed in extracting the cross-sections, along with a discussion of the systematic uncertainties.

5.1 Overview

The total $\gamma + {}^4$He cross-section as a function of photon energy (E_γ) is given by Eq. 3.1. Following background subtraction and data filtering, the $\gamma + {}^4$He reaction yield is determined by integrating the prompt peaks in all of the 62 HGSAT-tagger time spectra separately. Data filtering is performed by applying a series of cuts based on HGSAT QDC and TDC information, in order to identify real helium scintillation signals. Each of the 62 focal plane elements corresponds to a specific photon energy. The yield extraction, including background subtraction, is described in Sec. 5.2. The number of electron hits are recorded by scalers connected to the focal plane elements. The tagging efficiency, required to convert the number of electron hits on the FP detectors to the number of tagged photons incident on the target, is

obtained from dedicated coincidence measurements conducted in a similar manner to the main experiment as detailed in Sec. 5.3.1. Tagger rate-dependent corrections come in two types: the stolen coincidence correction and Ghost counts, the former is determined from information given by the 62 FP TDC coincidence spectra while the latter is ignored as it has a tiny effect, as explained in Sec. 5.6. A Geant4 based Monte-Carlo simulation is used to determine the detection efficiency by applying the experimental trigger conditions and software cuts to simulated data. The Geant4 Monte-Carlo simulation is discussed in detail in Ch. 4 and briefly in Sec. 5.7

The analysis was made easier by inhibiting the focal plane scalers at the hardware level during the DAQ system processing time, eliminating the need for dead-time correction. Tagged photon energies are determined from the energy calibration of the tagger magnet for each of the focal plane elements. This information is extracted and provided to the user by the Photonuclear physics co-ordinator at MAX-lab. This is discussed briefly in Sec. 5.5.

5.2 Yield Extraction

5.2.1 HGSAT-Tagger Coincidence Time Spectra

A typical HGSAT-tagger coincidences spectrum is shown in Fig. 5.1. The plot shows coincidences between the HGSAT and the 24^{th} FP channel corresponding to $\sim$30 MeV photon energy. Events in coincidence appear in the narrow peak between TDC channels 1190 and 1240 sitting on the top of the random coincidence background. Because the random rate depends on the beam intensity the time structure of the beam causes the structure observed in the random distributions in the TDCs. It is dominated by three components related to the way the electron beam was extracted. The 108 ns period oscillation comes from the non-uniform filling of the MAX I ring whereas the 330 ns period is due to the 3 MHz frequency of the RF-kicker magnet used to extract the beam from the storage ring (see Sec. 3.4.2). A third component of 2 ns period (not visible in Fig. 5.1[1]) comes from the 500 MHz accelerating cavity necessary to compensate for radiative energy losses of the electrons. The different structures in the stretched beam time profile is explained in more detail in Sec. 3.4.2.

Instability in the macroscopic time structure of the beam occurred a few times during the run in September 2009, as can be seen in Fig. 5.2. This was most likely caused by the de-optimisation of the timing of the accelerator trigger system in order to run at a reduced beam intensity. Running at standard stretched-beam intensities, the more relaxed trigger conditions OR+M_1 and OR+M_2 (see Sec. 3.7.2) caused the DAQ to saturate at around 1200 Hz [174], thus a reduction in the beam intensity was desirable. As a result, $\sim$73% of the data was accumulated using the more restricted

[1]Requires better time-resolution to be observed.

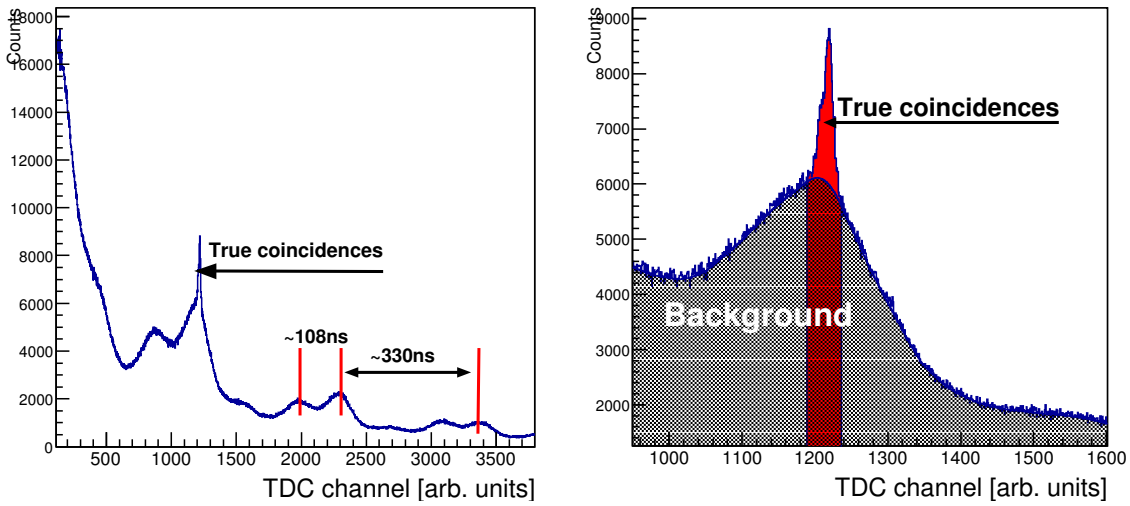

Figure 5.1: Left: Tagger-Target coincidence spectrum showing true coincidences (around channel 1180) sitting on the top of the stretcher-ring related structure of the random-coincidence background. Right: expanded detail of the time spectrum, showing a fit to the random background, used to extract the true-coincidence yield.

OR+M_3 trigger condition, ∼20% with the OR+M_2 and ∼7% with the OR+M_1[2]. The coincidence peak position was confirmed in very low-intensity runs where the random background was much reduced. The experimental run summary is given in Table 3.1 and Table 3.2 in Ch. 3.

Because of the instability in the beam time structure all of the data was carefully examined and those with the same time structure were grouped together and analysed separately. Intersection runs, where the change in the time structure took place, were excluded from the offline analysis. It is worth adding that running with optimised beam intensity and the OR+M_3 trigger, the time structure was a lot more stable.

5.2.2 Data Filtering and Event Selection

The occurrence of $\gamma + {}^4$He events is associated with scintillation signals in the HGSAT. Two sources of information are available to distinguish real scintillation events from random background: the energy and timing information of the 16 HGSAT PMTs, recorded by QDCs and TDCs respectively. This information is used to identify $\gamma + {}^4$He events by applying QDC and TDC cuts in the offline analysis.

[2]The beam time structure was more stable during the March 2009 run period where most of the data was accumulated using the OR+M_3 trigger and standard beam intensity.

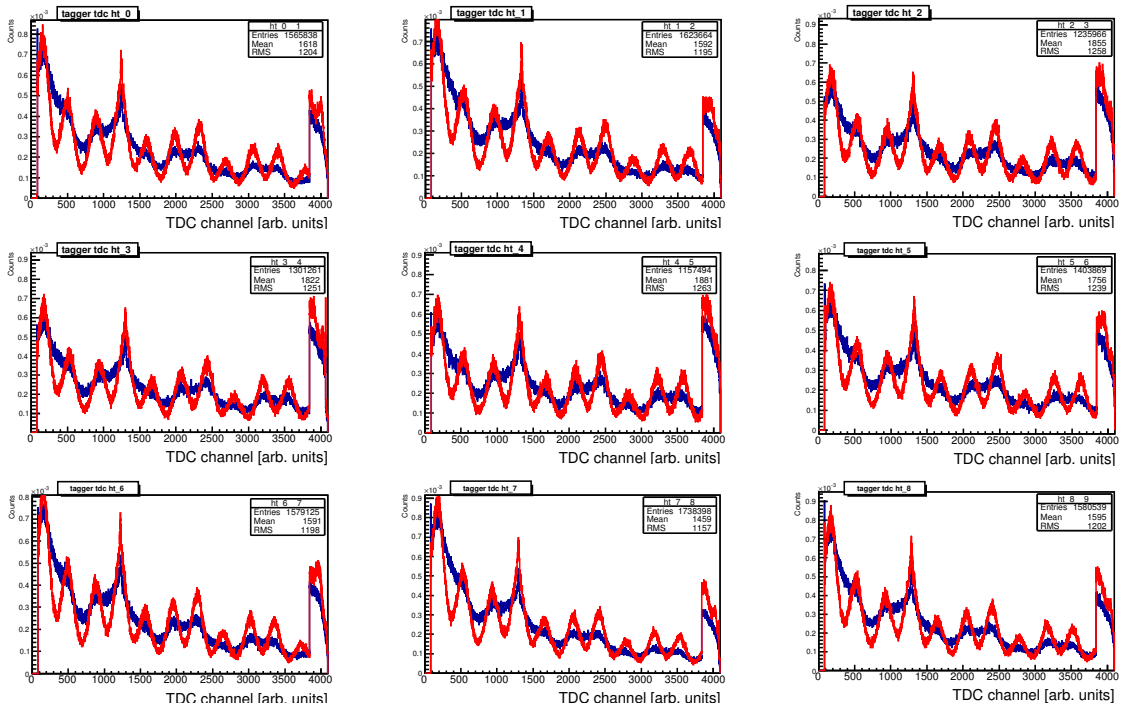

Figure 5.2: HGSAT-Tagger time coincidence spectra for the first 9 tagger channels from two consecutive runs taken with the OR+M_2 trigger. The two runs are presented in two different colours. The real coincidence peak is seen in a fixed channel at around 1250. The difference in shape of the beam time structure is clearly visible. The histograms were normalised for the sake of comparison of the time dependence.

QDC cuts

Previous work with the HGSAT showed that real scintillation signals can be identified using the QDC signals of any two orthogonal PMTs in a given cell[3]. In the two-dimensional distribution of these signals, highly correlated real scintillation signals appear as a distribution around the diagonal axis $y = x$, whereas the background is confined in separated bands parallel to the axes (see Sec. 2.4.1 and 2.4.2). 2D QDC cuts were defined from a visual inspection of all of the 16 correlation plots[4]. Each cut consists of two perpendicular lines as illustrated in Fig. 5.3[left]. Events which pass this threshold for any two orthogonal PMTs in any of the 4 cells of HGSAT are further checked using the TDC information.

TDC cuts

Signals generated in the PMTs due to scintillating $\gamma + {}^4$He events are correlated in time unlike singles random background events. This piece of information is used

[3]Orthogonal PMTs are chosen to minimise direct Čerenkov effects, i.e. minimising the possibility of Čerenkov light produced in one optical/PMT window being detected by the facing PMT.

[4]Four for each cell.

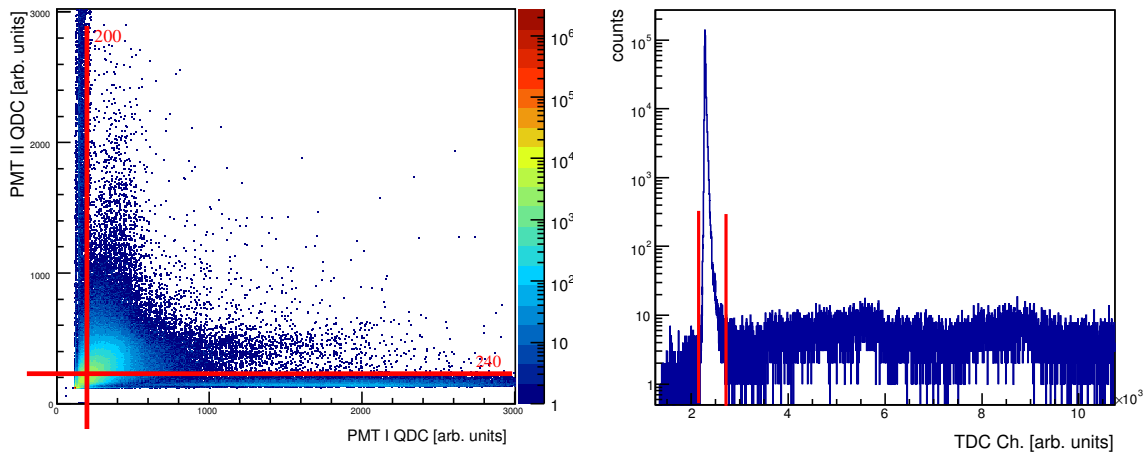

Figure 5.3: Left: typical two-dimensional distributions of signals measured in correlation between two perpendicular PMTs. The red lines indicate cuts applied to the data in the offline analysis. Right: TDC spectrum for an individual PMT. The red lines delimit the signal.

to further reject background by requesting a time correlation as well as an energy correlation.

Signal timing is recorded for all of the sixteen PMTs on the HGSAT using a CAEN V1190B multi-hit TDC module. Each PMT is connected to a leading edge discriminator that fires if the pulse height of the incoming signals is larger than the threshold. The TDC unit is started by the trigger and stopped by the output of the discriminator, hence, all of the timing information is recorded with respect to the trigger. The time difference recorded by the HGSAT TDCs appears as a prompt peak in the TDC time spectrum sitting on the top of a low level random coincidence background. A typical HGSAT TDC spectrum is shown in Fig. 5.3[right]. The TDC cut was made loose around the prompt peak for all of the 16 PMTs. Events which pass the TDCs cuts are accepted in the offline analysis.

Multiple Reactions

The probability of a second (or more) photon, inducing a γ+^{4}He reaction in addition to the one the that fired the trigger is low, but not completely negligible. A scan through the OR+M_3 data showed that less than 0.5% of all events had signals in more than one cell. Of these $\sim$ 98% were hits in 2 adjacent cells, which means there is a good chance that these hits originated from a single event. Nevertheless, it was decided to exclude these events in the offline analysis at this stage.

5.2.3 Tagger FP Signal Background Subtraction

Random background subtraction is non-trivial due to the complicated shape of the stretched beam time structure. Each of the 62 HGSAT-Tagger coincidence time spectra (see Fig. 5.1) is the time difference between the experimental trigger and an electron hit in the corresponding focal plane detector. At a high photon beam intensity the focal plane detectors register multiple electron hits unrelated to the photon that initiated the trigger. Their associated photons are either lost, due to the collimator, or simply failed to interact with the target. These accidental coincidences are responsible for the random background coincidences seen in the TDC coincidence spectra, including the region of the true coincidence peaks. The coincidence time resolution is about 11 ns (FWHM), influenced by the different propagation delays in the 16 HGSAT signals, which in principle can be corrected for.

Accidental background must be subtracted if the true $\gamma + {}^4\mathrm{He}$ yield is to be determined. For this purpose, two different approaches were employed in order to increase the confidence level and to estimate the systematic uncertainties on the extracted yield.

Background Fit

The background fit approach involves fitting the background with a 3^{rd} order polynomial and the prompt peak with a Gaussian. This was done for all of the 62 focal plane channels individually. The yield was extracted by subtracting the integral of background from background + prompt over a period of $\pm 3\sigma$ from the mean of the Gaussian fit to the prompt peak.

To fit the background accurately, the mean position of the prompt peak was first located using the "search" function of the ROOT TSpectrum class [206]. The algorithm searches for peaks in the spectrum for a given bin-count threshold and returns their positions on the x axis. The peak with the maximum bin content, corresponding to the prompt peak, is then chosen. In order to not confuse the background fitting the true coincidence peak region is effectively removed from the spectrum by setting the bin content to 0 over a period of $\pm 3\sigma$ and what is left is fitted with a 3^{rd} order polynomial function. The fitting parameters are fixed and used to define a combined 3^{rd} order polynomial+Gaussian function that is used to fit both of the prompt peak and the background within a range chosen empirically to cover both of the prompt peak and the background, $\pm 6\sigma$ in this case. The difference in the integral of the prompt peak and the background fit functions within the range of $\pm 3\sigma$ is the $\gamma + {}^4\mathrm{He}$ yield for the photon energy corresponding to the tagger TDC channel being processed. Fig. 5.4 shows the steps followed in implementing this approach.

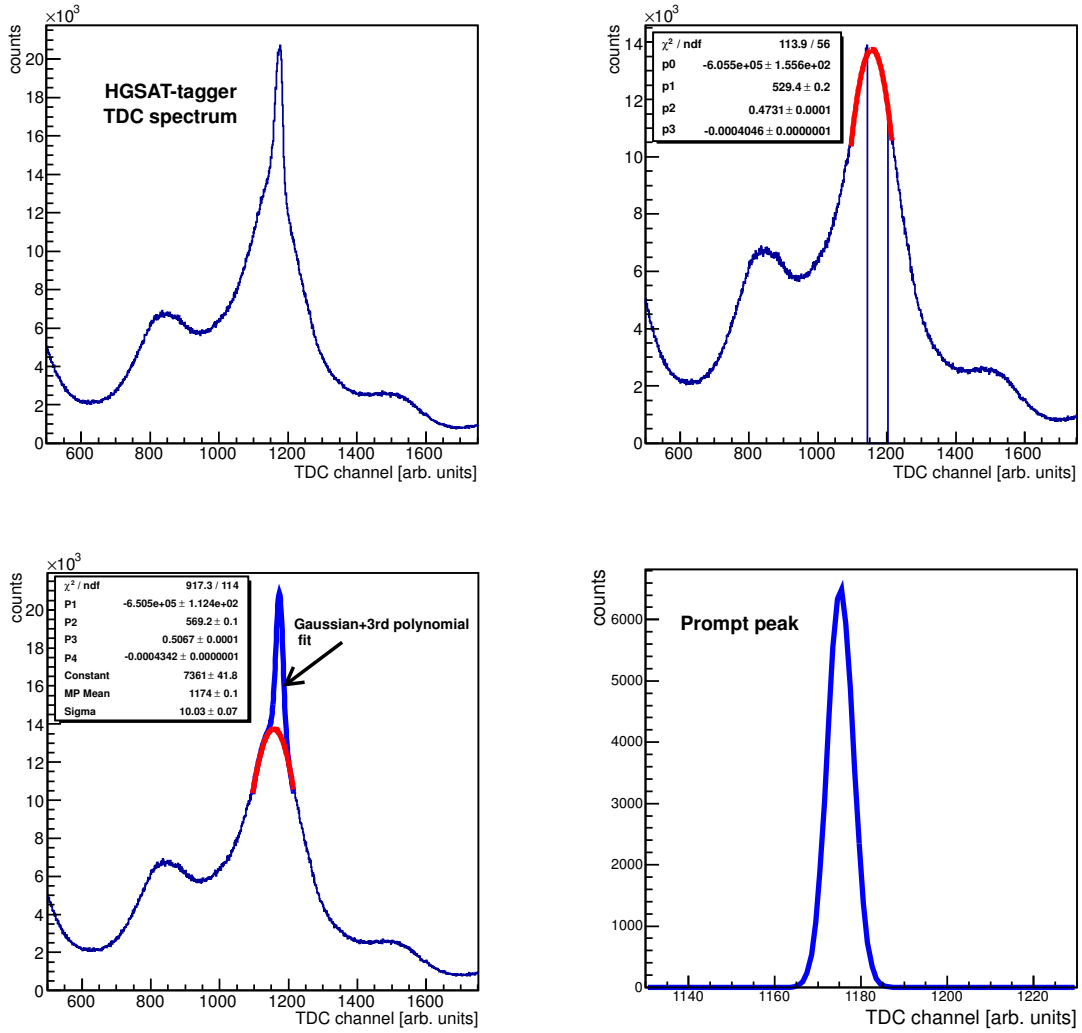

Figure 5.4: In the background fit, the yield is extracted by fitting both the prompt peak and the background (top left). The prompt peak region is excluded when fitting the background (top right). The background fitting parameters are fixed and combined with a Gaussian function to fit both the prompt peak and the nearby background (bottom left). The prompt peak resulting from subtracting background from background + prompt is shown bottom right. The HGSAT-tagger TDC spectrum shown is for the 24^{th} tagger channel.

Background Filter

The second approach is slightly different; the idea is to eliminate the random background in the HGSAT-Tagger TDC spectra using a sophisticated algorithm known as "*Sensitive Nonlinear Iterative Peak clipping*" developed by Morháč et al. [207] and Ryan et al. [208]. The algorithm is implemented in ROOT and can be used via the "background" function of the TSpectrum class [206]. The function takes two parameters, the source spectrum and the order of the noise filter. The latter was

determined by trial and error.

In this approach, an exclusive background spectrum is created and subtracted from the HGSAT-Tagger TDC source spectrum as can be seen in Fig. 5.5. The outcome of this is a clean prompt peak from which the yield can be extracted directly by integrating the peak region ($\pm 3\sigma$).

5.2.4 $\gamma + {}^4$He Yield

The $\gamma + {}^4$He yield as a function of the 62 tagger channels is displayed in Fig. 5.6. The yield shown is for March 2009 data that were taken using the M_3+OR trigger. The yield for the M_2+OR and the M_1+OR data was also extracted and showed the same trend as the M_3+OR data. However, after applying all of the software cuts, the statistics in the HGSAT-tagger TDC spectra were somewhat poorer and a time-consuming yield extraction by hand, channel by channel, was necessary. Therefore, it was decided to concentrate on the M_3+OR data in the analysis presented in this thesis.

The different colours in the plot show the comparison between the two extraction methods, described in the previous section, for the same data set. The two methods agree reasonably well. The plan was to make the extraction procedures as automated as possible for all of the tagger channels to avoid inconsistencies and possible bias in the extraction procedure. This was possible with the "background filter" approach, which only required the order of the noise filter as an input [206], but was more difficult with the "background fit" method. The background and prompt peak automated fitting failed occasionally when the prompt peak is small with respect to the background, i.e. below or above the peak in the GDR region where the cross-section is relatively low. In Fig. 5.6 for example, there are two channels, 49 and 56, where the background automated fitting has failed and the two points are off of the y-axis range.

5.3 Photon Flux

Determination of the photon flux incident on the target is required to normalise the $\gamma + {}^4$He yield into a cross-section. In photon-tagging experiments, the incident flux is determined from the number of associated electrons detected in the tagger focal plane detectors. This quantity is recorded for all of the 62 focal plane channels using scalers which are inhibited while the DAQ system is busy processing data. The scalers count all electron hits in the focal plane detectors including those whose associated photons are lost in the collimator. Thus, a correction is necessary in order the determine the true photon flux incident on the target.

To determine this correction, dedicated tagging efficiency measurements were performed at lower photon beam intensity, separate from the production data taking

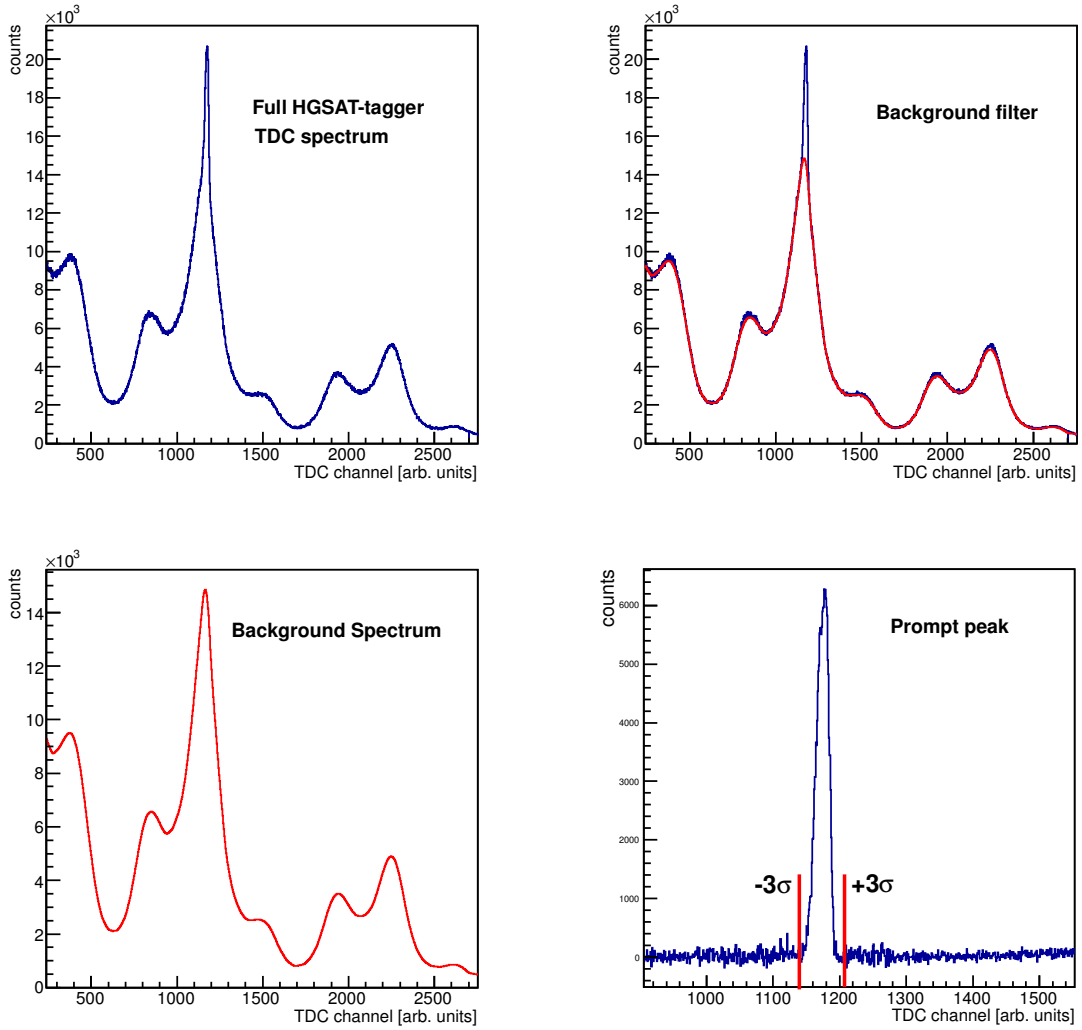

Figure 5.5: Background filter yield extraction approach. Excluding the prompt peak region, the entire HGSAT-tagger TDC spectrum (top left) is fitted using the "*Sensitive Nonlinear Iterative Peak clipping*" algorithm (top right) to create a separate background histogram (bottom left). Subtraction of the original and the background histograms results in a clean prompt peak (bottom right) from which the yield is extracted by integrating the peak region over a period of $\pm 3\sigma$. Background fluctuations underneath the peak are accounted for by subtracting a background sample from either side of the prompt peak. The HGSAT-tagger TDC spectrum shown is for the 24^{th} tagger channel.

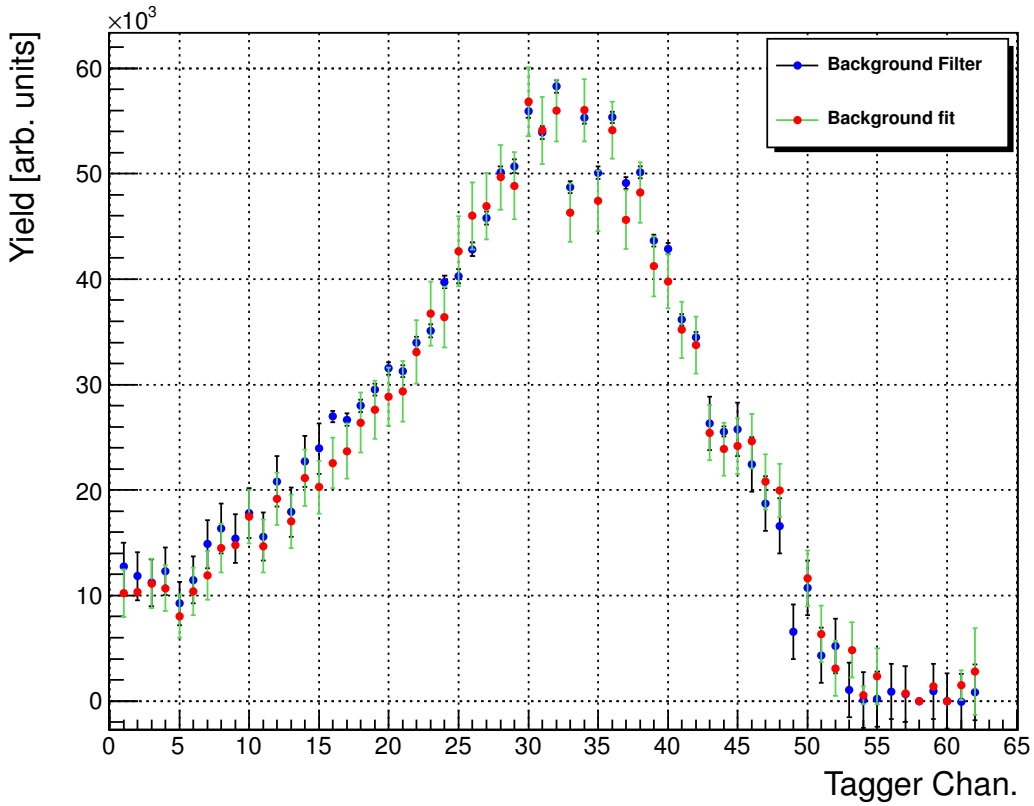

Figure 5.6: Raw excitation curve for photodisintegration of ^{4}He as a function of tagger channel. Extracted from the M_3+OR trigger data. Note that high tagger channel corresponds to low photon energy.

(see Sec. 3.5.5). In these measurements, all of the photons passing through the collimator are counted along with the electron hits in the focal plane detectors. The ratio of the two quantities for each tagger focal plane detector is the tagging efficiency for the corresponding photon energy.

5.3.1 Tagging Efficiency Determination

The tagging efficiency was measured twice daily on average, ∼30 min each, during the experimental runs as discussed in Sec. 3.5.5. In the September 2009 runs, two trigger configurations were used for each set of the tagging efficiency runs, that is the focal-plane OR trigger and the Pb/SciFi detector trigger. The former is used routinely for tagging efficiency measurements in Lund [174] whereas the latter is commonly used in the **MA**inzer **MI**krotron (MAMI) tagged photon facility in Mainz. After some adjustments to the automated script that is used in Lund the two methods gave approximately similar results. A comparison between the two methods was used for verification.

FP-OR trigger "Lund Method"

In this method, an electron hit in any of the focal plane detectors is used to trigger the DAQ and to generate the QDC gate for the Pb/SciFi detector.

If a photon is lost in the collimator the associated electron is still detected in one of the focal plane detectors generating the trigger and opens up the Pb/SciFi detector QDC gate. As a consequence, a count is registered within the pedestal peak[5] of the Pb/SciFi QDC spectrum. However, if the photon passed through the collimator and made it to the detector, which in principle has a ∼100% detection efficiency, a count is registered in the signal peak of the QDC spectrum. Therefore, the ratio between events above the pedestal to the those in the full QDC spectrum gives the percentage of electrons whose associated photons made it to the detector, i.e. the tagging efficiency. A typical Pb/SciFi QDC spectrum obtained during tagging efficiency measurements is shown in Fig. 5.7.

The Lund tagging efficiency was obtained using a script developed by J. Brudvik [209]. The idea was to have automated tagging efficiency evaluation for any standard tagging efficiency measurement taking place at MAX-lab. The script locates the positions of the true signal and the pedestal peaks and finds the local minimum in between via a 2^{nd} order polynomial fit. This was done for all of the 62 Pb/SciFi QDC spectra, one per tagger channel, each obtained by applying a cut on the coincidence peak in the corresponding tagger TDC spectrum. The local minimum was taken as the pedestal peak cut-off and it is optional in the script to either locate it by hand or via the fit. The automated fit cut-off is by eye slightly

[5] The QDC pedestal is the value registered if no input signal is given.

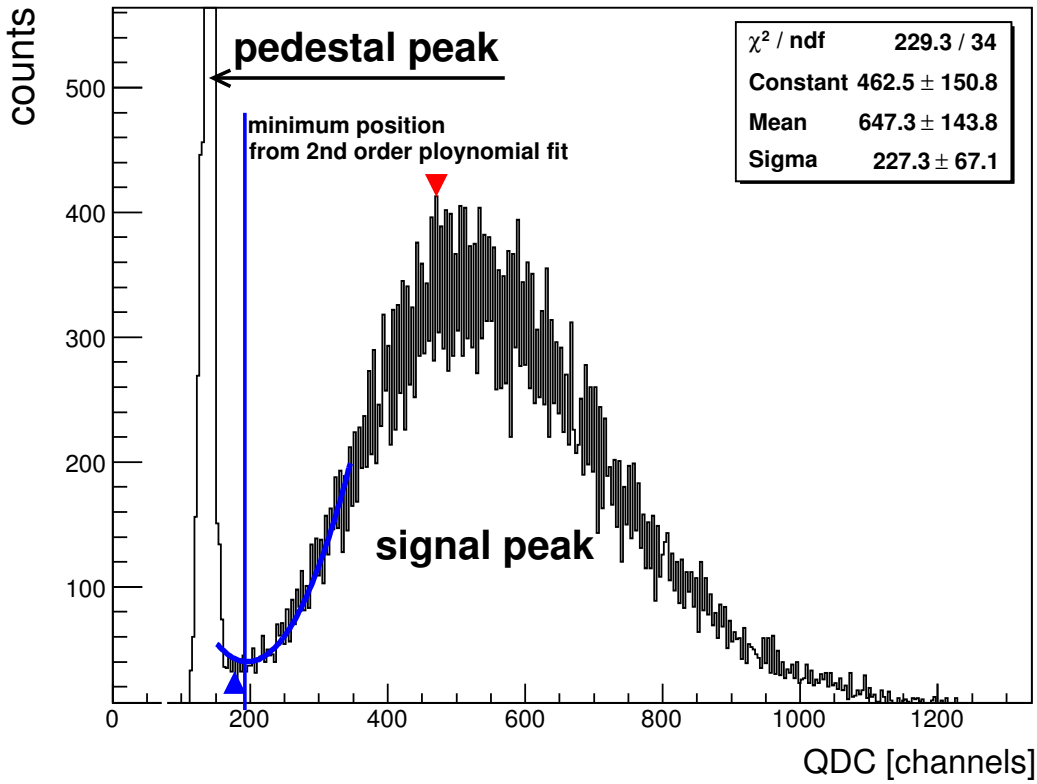

Figure 5.7: A typical Pb/SciFi QDC spectrum obtained from one of the tagging efficiency measurements. The ratio between events in the signal peak to the total events in the spectrum is the tagging efficiency for the tagger channel which generated the trigger. The red and blue triangles are the maximum and minimum bin contents respectively.

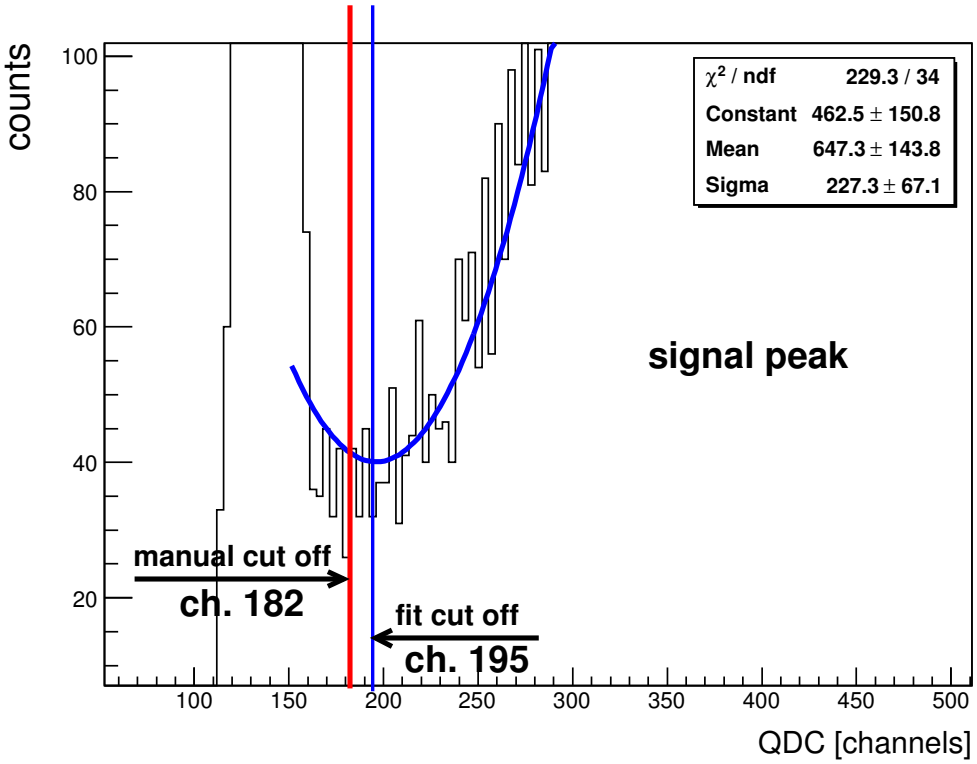

Figure 5.8: A zoomed in version of Fig. 5.7. The automated pedestal cut-off is slightly high. Shifting the cut by hand by a few channels (13 channels in this case) produced a good match with the "Mainz" method. The cut made by hand (red line) is well within the minimum region and far above the pedestal peak.

high and moving the cut by hand by few channels towards the pedestal distribution but still far from the pedestal peak channel (see Fig. 5.8) made a good match with Mainz-method tagging efficiency results as will be explained below.

Pb/SciFi trigger "Mainz Method"

The Mainz method uses the signals from the Pb/SciFi detector to trigger the DAQ system and start the tagger coincidence TDCs. The stop signal comes from an electron hit in the focal plane detectors. The number of tagged photons detected in the Pb/SciFi detector is determined from the number of counts in the coincidence peak of the tagger TDC spectra. The ratio of this value to the number of electrons recorded by the scalers for each tagger channel gives the tagging efficiency.

At low beam intensities the non-beam background scaler rate may become significant and a correction for this is necessary. To do this data were taken using the same experimental setup with beam switched off after every tagging efficiency measurement. The tagging efficiency expression 3.8 in Chapter 3 is modified to the

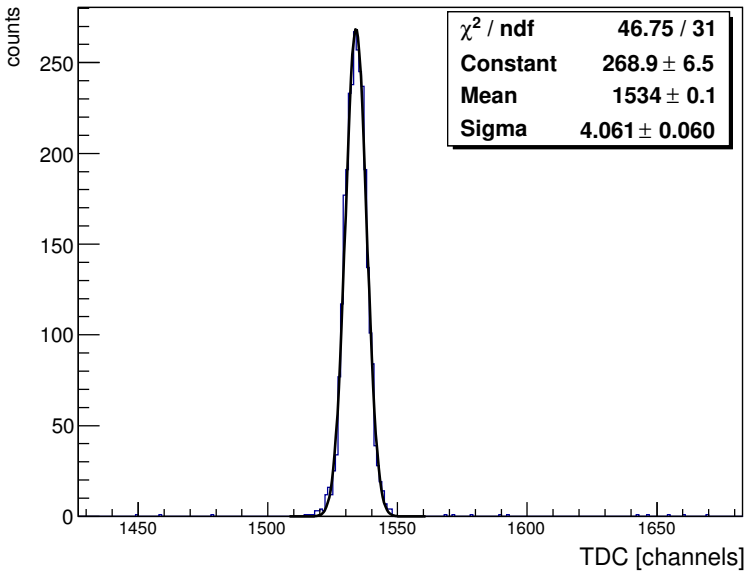

Figure 5.9: The prompt peak in the tagger TDC spectrum (tagger channel 24). The number of photons (N_γ) is determined from the number of events in the prompt peak. At low intensity, random background is negligible.

following form:

$$\varepsilon_{tagg(i)} = \frac{N_{\gamma(i)}}{N_{e'(i)_{beamOn}} - N_{e'(i)_{beamOff}}} \tag{5.1}$$

where $N_{\gamma(i)}$ is the number of tagged photons detected in the Pb/SciFi detector in coincidence with focal plane channel i, $N_{e'(i)_{beamOn}}$ and $N_{e'(i)_{beamOff}}$ are the number of electrons counted by the focal plane scalers in the same time interval with beam switched on and off respectively. The scaler counts in the background runs were less than 0.1% of those during tagging efficiency runs for all of the tagger channels which means the background correction could be neglected in practise.

Lund vs. Mainz Comparison

Fig. 5.11 shows a comparison between the tagging efficiencies extracted by the "Mainz" and the "Lund" methods. The two methods agree quite well after adjustments to the pedestal cut-off in the latter, as explained previously. The drop in the measured tagging efficiencies seen at higher tagger channels is mainly due to the loss of the detection efficiency of the Pb/SciFi detector at low photon energy. It is worth reiterating that both methods are directly affected by the detection efficiency of the Pb/SciFi detector, that is, if a photon arriving at the Pb/SciFi detector is not detected, the trigger will not be generated in the case of the "Mainz" method but the focal plane scalers will still count the associated electron, resulting in a drop in the measured tagging efficiency. Similarly, in the "Lund" method, an undetected

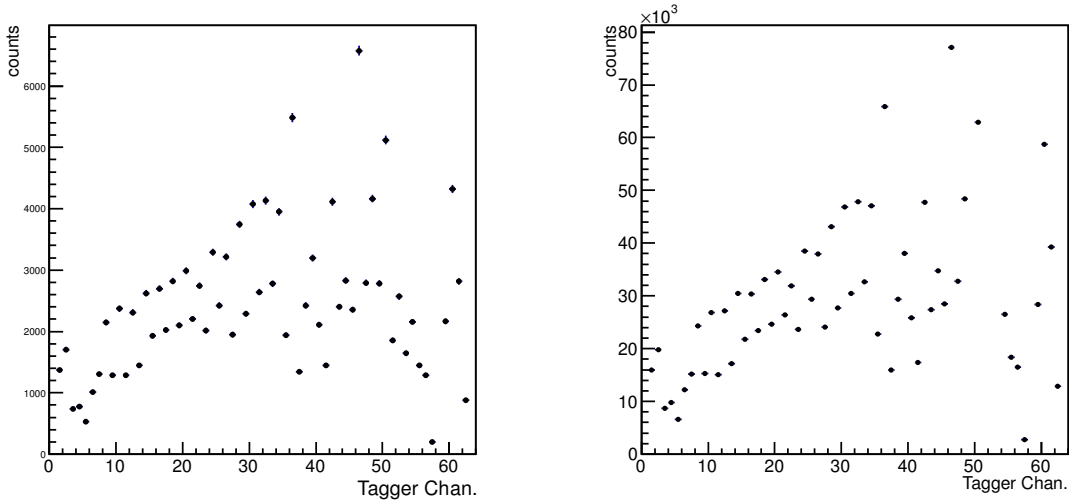

Figure 5.10: In the Mainz method, the number of photons (N_γ) are determined from the number of counts in the Pb/SciFi-tagger TDC spectrum for each tagger channel (left). The number of electrons ($N_{e'}$) is extracted from the tagger scalers (right). The spread in counting rates is partly due to variations in the detection efficiency of the FP counters and the detection efficiency of the Pb/SciFi counter. The systematic difference between odd and even-number channels results from an FP overlap coincidence requirement. These cancel when the TDC/scaler counting ratio is taken.

photon will register a count in the pedestal region of the Pb/SciFi detector that was triggered by an electron hit in any of the focal plane detectors, causing a drop in the measured tagging efficiency.

Stability of Tagging Efficiency

Drifts in the electron beam position at the radiator can affect the tagging efficiency. Such drifts are in fact quite common, occurring several times during the data production of the experiment reported in this thesis. Therefore, it is important to continuously monitor the tagging efficiency during the experiment.

To do that, the In-beam monitor detector (IBM) was employed as discussed in Sec. 3.6.5. In principle, if one can relate the count rate in the IBM to the tagging efficiency ($\varepsilon_{\text{tagg}}$) determined from the dedicated tagging efficiency measurements, then it is possible to have a continuous monitor of the tagging efficiency during data production. In dedicated tagging efficiency measurements, if α_{IBM} is defined as:

$$\alpha_{(IBM)}(i) = \frac{N_{\gamma(i)}}{N_{IBM}} \tag{5.2}$$

then a parameter directly related to the tagging efficiency, let's call it the IBM ratio and denote it with β_{IBM}, can be obtained for each tagger channel i continuously

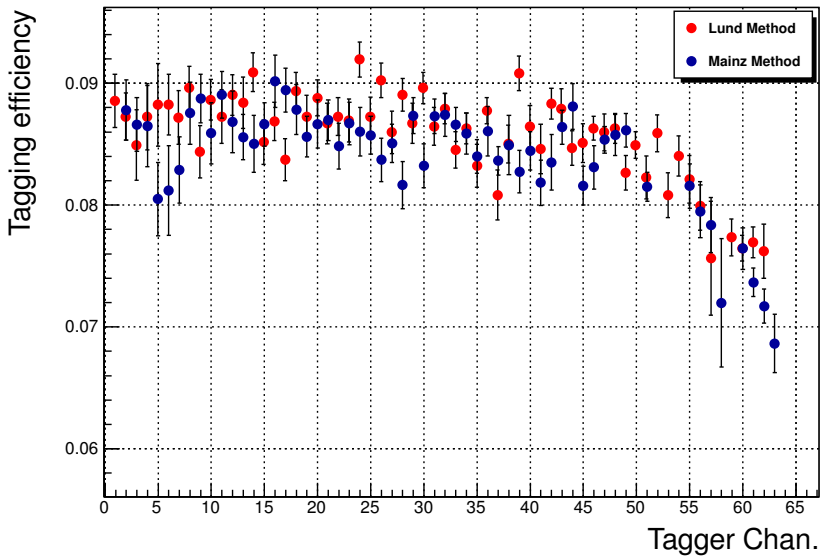

Figure 5.11: Comparison of tagging efficiency measured with the "Lund" (Run 328) and the "Mainz" (Run 329) methods. The systematic drop in the measured tagging efficiency at low photon energy ($E_\gamma < 21$MeV, correspond to tagger channels >50) is due to a loss of efficiency in the Pb/SciFi detector. This does not affect the measured total $\gamma + {}^4$He cross-section since the significant drop in the tagging efficiency occurs at incident photon energies below ^{4}He break-up threshold (∼20 MeV).

during data production:

$$\beta_{IBM}(i) = \alpha_{(IBM)}(i) \times \frac{N_{IBM}}{N_{e(i)}} \tag{5.3}$$

where N_{IBM} is the number of counts registered by the IBM, $N_{e(i)}$ is the number of electrons counted by the focal plane scaler channel i.

Fig. 5.12 shows the IBM ratio (β_{IBM}) for tagger channel 17 for most of the March 2009 runs. Runs below 75 were taken before the IBM was installed. The observed peaks show the results from the dedicated tagging efficiency measurements. The IBM ratio for all of the other tagger channels showed the same trend. The plot shows four features which merit some explanation:

- Firstly, the stability of the tagging efficiency during most of the production runs can be clearly seen. Due to beam instability it was decided that runs $96 - 98$ were unusable and were excluded from the analysis.
- Secondly, the drop in the measured tagging efficiency at and after run 103 is almost certainly due to shifts in the beam position on the radiator [153][210]. The drop was first noted during the tagging efficiency measurement run 122

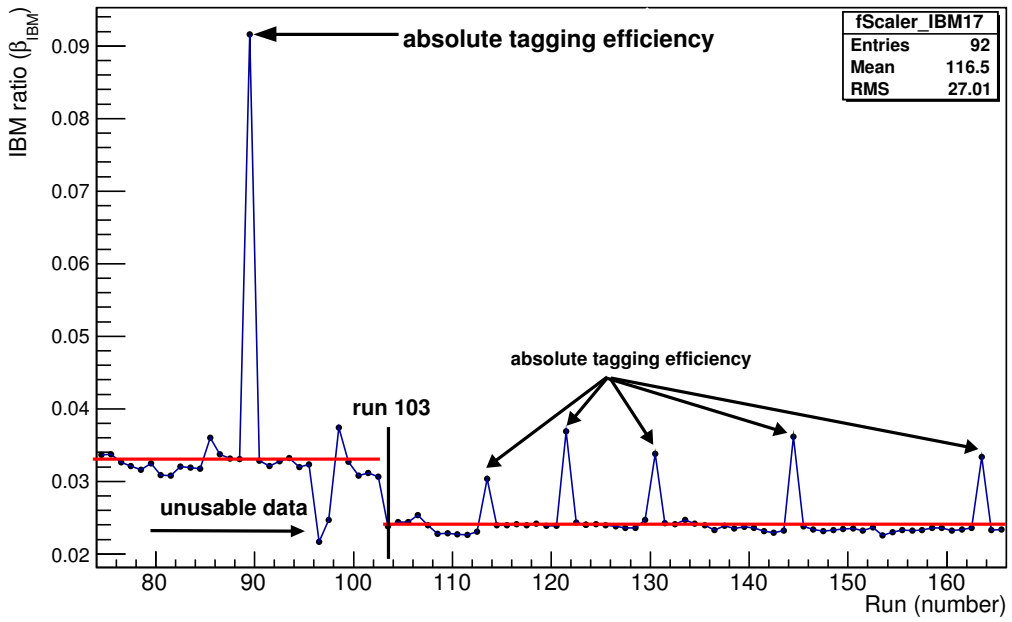

Figure 5.12: The IBM ratio (β_{IBM}) for most of March 2009 data. The peaks seen in the plot, referred to as absolute tagging efficiency, represent the tagging efficiencies from dedicated measurements. Runs before 75 were performed before the IBM was installed. The IBM ratio seems relatively stable between production runs before and after run 103. See text for more explanation.

which prompted us to check all of the Pb/SciFi settings with nothing to report [154](Message ID 39). Power issues with the accelerator and unstable beam were reported a few times around 103 run [154](Operators Message ID 17 and 18) which strongly suggests the drop seen in the measured tagging efficiencies is directly linked to something changed in the accelerator settings.

- Thirdly, the discrepancy between the IBM ratio (β_{IBM}) and the directly measured tagging efficiency where they should be the same in principle. The reason for this is most likely due to the reduced detection efficiency of the IBM counter at higher beam intensity. Quantitative studies on the IBM detection efficiency at high beam intensity are not available. Nevertheless, the IBM was used to monitor the beam stability and was not expected to measure tagging efficiency absolutely.

- Fourthly, β_{IBM} to tagging efficiency ratios before run 103 are higher than those after. The beam intensity was reduced to 60% after run 103 to overcome issues with the beam instability and the lower tagging efficiency also reduced the post-collimator photon intensity. This points toward the increased efficiency of the IBM at lower beam intensity.

As a result of the discrepancy in the tagging efficiency in the data before and after

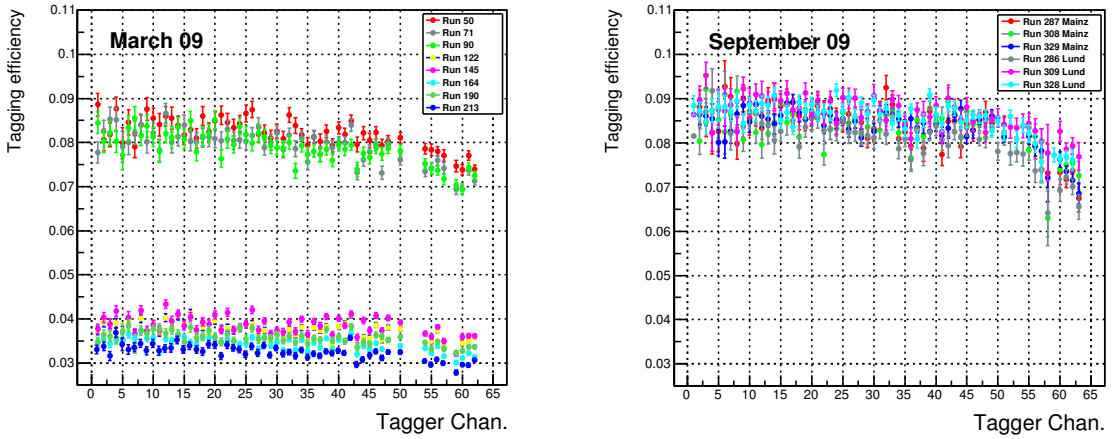

Figure 5.13: Tagging efficiency as a function of focal plane channel determined from all of the tagging efficiency measurements. Notice that the y-scale of the two plots starts at tagging efficiency of 0.025. The gap seen in March 2009 data is due to broken channels in the focal plane hodoscope 49, $51-53$ and 58. On the other hand, tagger channels 48, $50-52$ were unusable in September 2009 due to bad tuning of the focal plane discriminator thresholds. Tagging efficiencies for the September 2009 run show a good agreement (within $\pm 3\%$). March 2009 shows two different values of tagging efficiency with more than a factor of 2 difference. It is almost certain that this is due to shifts in the beam position on the radiator. Statistical uncertainties are shown as error bars.

run 103 during the March 2009 runs, the data were divided into two groups which were analysed separately.

Tagging Efficiency

Fig. 5.13 shows the tagging efficiency extracted from all of the tagging efficiency runs, including the "Mainz" and the "Lund" methods employed in the September 2009 runs. The deviation seen between different runs is most likely due to the instability and drifts in the electron beam position at the radiator. Background correction was not possible for the March 2009 runs since no data were taken directly before or after the beam was switched off. However, the size of this correction was found to be tiny (less than 0.1%) in the September 2009 runs and there is no reason to believe otherwise for the March 2009 runs. The data were analysed separately using the mean tagging efficiency for each data set, that is September 2009, March 2009 (pre 103 run) and March 2009 (after 103 run) data for the same trigger setup.

5.3.2 Tagger Scalers

The final step to determine the photon flux incident on the target is to extract the number of electron counts in the focal plane channels. This information is provided

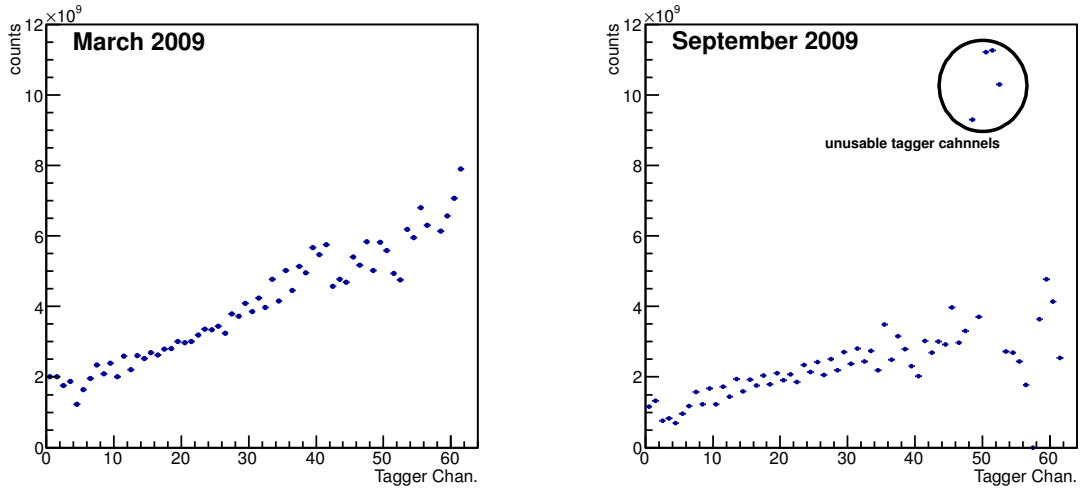

Figure 5.14: The tagger scalers as a function of focal plane channel. The broken tagger channels are excluded in the offline analysis. The statistical errors bars are included but are too small to be seen.

by scalers connected to each of the focal plane channels as explained in the previous few sections.

Scalers connected to the focal plane detectors were 32 bit counters and a correction for overflows[6] was necessary in the offline analysis as they were not cleared after a read. Determination of this correction is trivial, the number of times the scalers overflowed is counted in the offline analysis and the correction is simply calculated as: the number of overflows × overflow value, that is 4294967296, plus the scaler value at the end of the analysis run. Fig. 5.14 shows the tagger scalers as a function of focal plane channels for all of the M_3+OR March and September 2009 runs. The systematic difference between odd and even number tagger channels seen in the plot is due to the overlap between adjacent tagger FP channels (see Sec. 3.5.2). Some tagger channels were unusable during both the March and September 2009 data. The scatter seen in September 2009 data in channels > 34 is likely to be due to discriminator threshold effects and the gain applied to the focal plane PMTs. The higher tagger channels correspond to low energy photons.

5.4 Target Density

The target density was determined from measurements of the target pressure at room temperature. The target pressure was continuously monitored using a 5 MPa Balzer high pressure sensor which was calibrated and has a ±2% accuracy according

[6] An overflow occurs when the number of counts exceed the allowable range of the scaler.

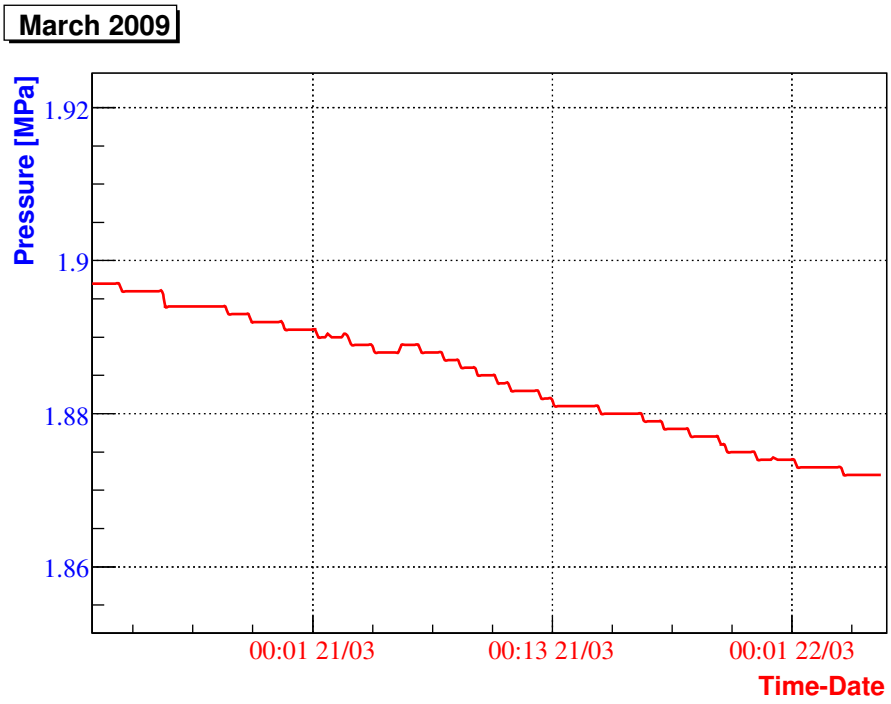

Figure 5.15: A small leak occurred in the quartz-aluminium coupling resulting in a pressure drop during the March 2009 experimental run. This drop was measured to be ∼1.5% for the data analysed and presented in this thesis.

to the manufacturer. The temperature in the experimental hall was also measured during a typical operational day and found to fluctuate between day-time and night-time by $\sim \pm 2°C$ around a mean of 21°C. A small leak in the pressurised vessel during the 3 week run period in March 2009 resulted in a total pressure loss of ∼9%[7] and ∼0.7% during the 1 week run in September 2009 (see Fig. 3.13). For the data used in the analysis presented in this thesis, only a ∼1.5% pressure drop was recorded as can be seen in Fig. 5.15.

The gas density was approximated using the ideal gas law:

$$\rho = \frac{P \times M}{R \times T} \tag{5.4}$$

where ρ is the gas density (g.cm^{-3}), P is the gas pressure (MPa), M is the Molar mass (4.002602 g.mol^{-1} for helium), R is the gas constant (8.314 cm^3 MPa.K^{-1}.mole^{-1}) and T is the gas temperature (K). The values used in the offline analysis are calculated from the pressure readings taken for each data set and used to calculate the target thickness in g.cm^{-2}

[7] ∼6% for runs before 103 and ∼3% after.

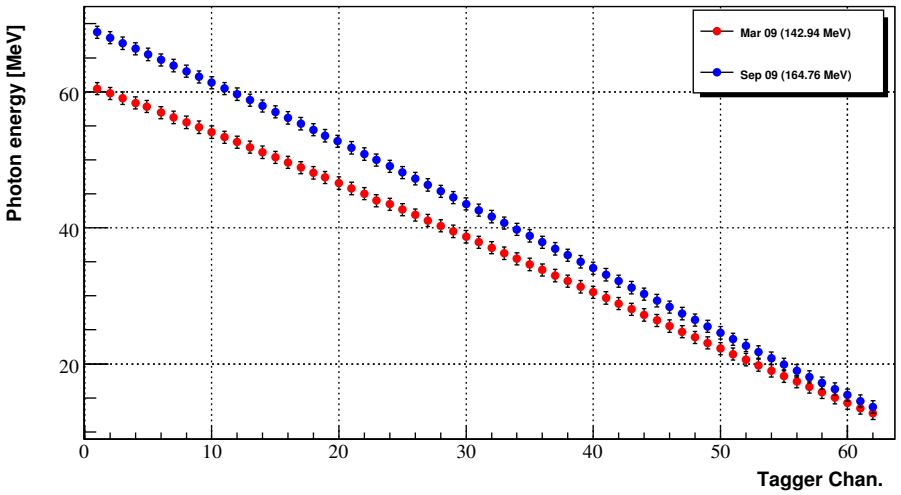

Figure 5.16: Tagged photon energy as a function of tagger channel. The higher tagger channels correspond to low energy photons. The error bars of 0.9 MeV, gives the width of each tagger channel.

5.5 Tagged Photon Energies

The photon energy calculation takes three main inputs: the primary electron beam energy, the field setting of the tagger dipole and the physical location of the focal plane detectors. The details of this are given in Sec. 3.5.3.

In the experiment discussed in this thesis, two different electron beam energies were used: 142.9 MeV in March 2009 and 164.8 MeV in September of the same year, which gave photon energy ranges (see Sec. 3.5.2) $\sim 12.72 - 60.45$ MeV and $13.67 - 68.76$ MeV respectively. Tagged photon energy as a function of tagger channel is given in Fig. 5.16 for the two primary electron beam energies used for data production. The energy resolution for each tagger channel is about 900 keV on average.

5.6 High-Rate Corrections

The measurement reported here was taken using a relatively high beam intensity, corresponding to an average electron counting rate in the range of 0.8 to 2.5 MHz per focal plane channel, as discussed in Chapter 3. Running with such a high intensity is known to give rise to a number of issues directly affecting the measured TDC yield and the electron scalers. The two possible effects are the so-called "Stolen Coincidences" and "Ghost Counts" which will be discussed briefly in the next two subsections. Running with a lower beam intensity led to instability in the beam time structure as discussed in Sec. 5.2.1.

A full treatment of ghost counts (Sec. 5.6.2) has not been attempted here as they have a very small effect and are quite complicated to calculate. It is worth mentioning that Myers et al. [211] are currently finalising a Monte Carlo simulation of the MAX-lab tagger electronics which in principle can be used to extract these corrections with a good level of precision. The tagger Monte-Carlo simulation is expected to be published shortly.

5.6.1 Stolen Coincidences

Stolen coincidences are defined as real events that failed to appear in the prompt peak of the target-tagger TDC spectra due to accidental electrons stopping the TDC unit before the real correlated electrons, i.e. "stealing" the true coincidence event. This effect decreases the extracted yield if no correction is applied. Detailed studies on this effect were made by Owens [212] and Hornidge [158].

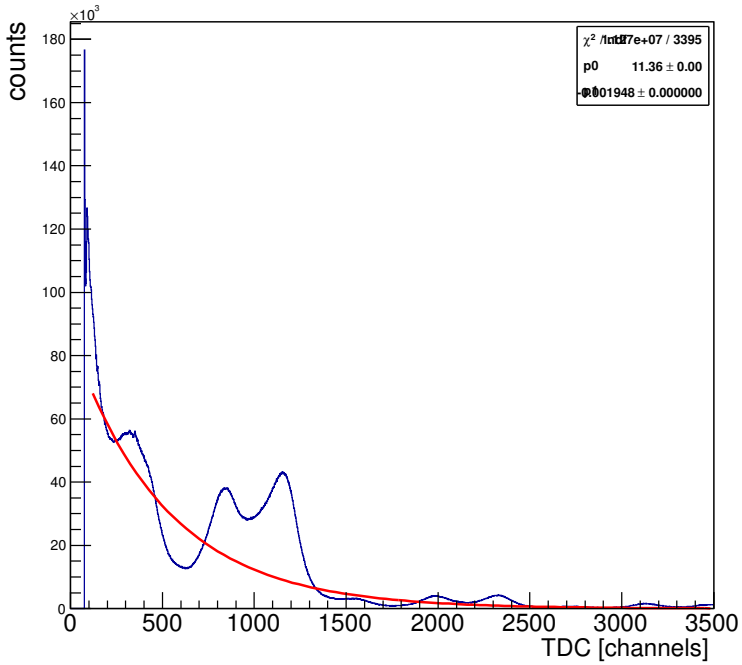

Figure 5.17: Typical HGSAT-tagger TDC spectrum. Ideally, the instantaneous electron rate in the focal plane ($\dot{R}$) is determined from the slope of the TDC spectrum exponential fit. However, the spectrum does not follow an exponential distribution and therefore it could not be used to determine the stolen coincidence correction.

The probability of stolen coincidences is proportional to the beam intensity. If the probability of n electrons arriving at focal plane channel i during time "t" after

the start of the TDC is given by [153][213]:

$$P(n,t)_i = \frac{(\dot{R}_i.t)_i^n}{n_i!} \times e^{-t\dot{R}_i} \tag{5.5}$$

then the probability of no counts in t is $P(0,t)_i = e^{-t\dot{R}_i}$ where $\dot{R}_i$ is the instantaneous rate in focal plane channel i. This can be used to calculate the stolen coincidence correction (ε_s):

$$\varepsilon_s = e^{-t_{peak}\dot{R}_i} \tag{5.6}$$

where t_{peak} is the position of the prompt peak relative to the TDC start time.

There are two conventional ways to determine $\dot{R}$, either using the average electron counts in the focal plane along with the beam duty factor, or from an exponential fit to the tagger TDC spectra. Unfortunately, there was no accurate method of determining the duty factor at the time when the $\gamma + {}^4$He measurement was taken and the exponential fit does not work due to the oscillations in the shape of the tagger TDC spectra as can be seen in Fig. 5.17.

Recently, Schröder devised a method to deal with this correction without the need to determine the instantaneous electron rate $\dot{R}$ [214]. The correction is independent of the shape of the TDC random spectra and solely relies on determining the ratio of the total number of counts in the TDC spectra (overflows included) to the number of counts above the beginning of the coincident peak:

$$\varepsilon_s = \frac{N_T}{N_s} \tag{5.7}$$

where N_T is the number of TDC stops above the start of the coincidence peak including the overflows and N_s is the number of TDC starts. The number of overflows is determined from the difference between the total number of TDC starts and the number of TDC entries in each of the 62 TDC channels. Fig. 5.18 shows the stolen coincidence correction for all of the TDC channels. The yield has to be divided by this correction in order to obtain the true yield.

5.6.2 Ghost Counts

An electron must be detected in two overlapped focal plane detectors, within a given coincidence time window, for it to be registered in any given tagger channel. If two uncorrelated electrons pass two channels sandwiching a third (Fig. 5.19) then it is possible that a count is registered in the third channel accidentally, a "ghost" count. If electrons "e$'$1" and "e$'$2" pass through tagger Ch(i) and Ch(i+2) then a count in Ch(i+1) could be registered[8] if a hit is received in both m and n+1 focal plane detectors within a resolving time of m/(n+1) coincidence unit.

[8] Given the two electron hits happened within the specified coincidence time window

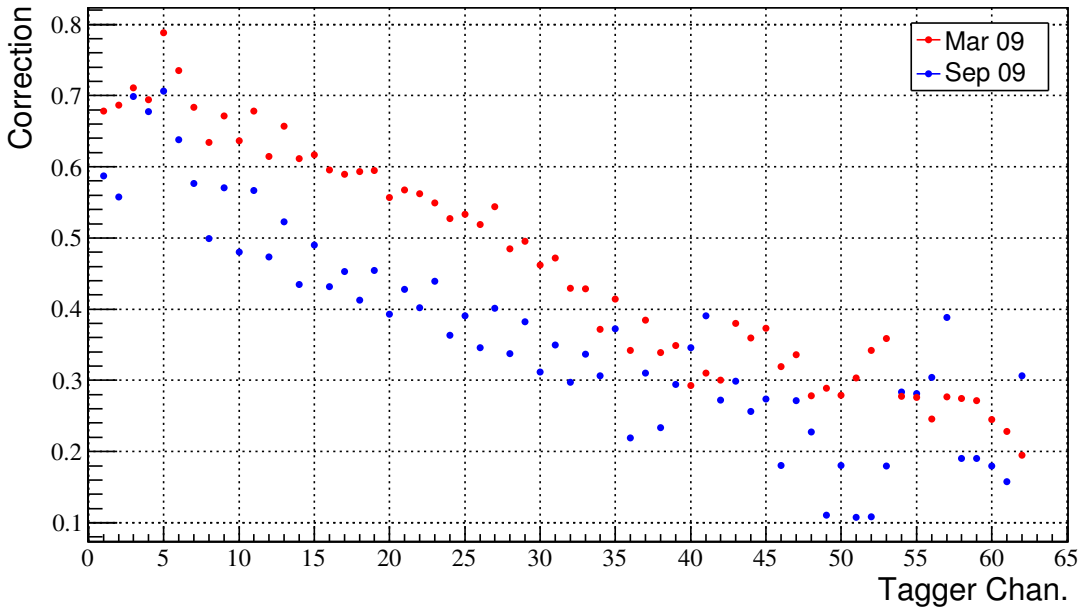

Figure 5.18: The correction for stolen coincidences for both March and September 09 runs as a function of the tagger channels. As with the tagger scalers shown in Fig. 5.14, the scatter seen in channels >34 is most likely due to discriminator threshold effects and different gains in the focal plane PMTs. Statistical error bars are too small to be visible.

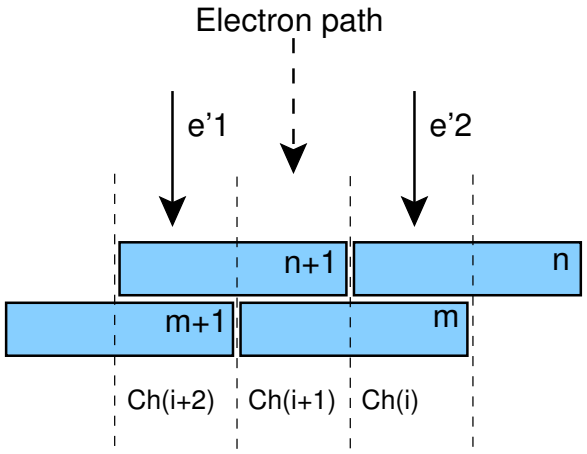

Figure 5.19: An illustration of how a ghost count is created. More details can be found in the text.

The effect of the ghost counts on the measurement is an apparent increase in the number of electrons registered by focal plane scalers which tends to decrease the normalised cross-sections. On the other hand, a ghost count could also occur in coincidence with the experimental trigger and show up in the TDC coincidence peak and hence increasing the apparent cross-section. The two effects may not cancel exactly but limit the size of this correction. It was estimated that this correction is around 1%[153] which is below the systematic errors estimated for this work.

5.7 Detection Efficiency Correction

A Geant4 based Monte-Carlo simulation was developed mainly to extract the HGSAT detection efficiency needed in the cross-section normalisation. Absolute determination of the detector efficiency was not possible as an energy calibration, necessary to determine the discriminator thresholds has yet to be completed. Thus, the HGSAT efficiency was calculated as a function of energy threshold using "data" generated by the Monte-Carlo simulation, always requiring the M_3 trigger condition (see Sec. 3.7.2 and 4.5.4) to be satisfied since it was the trigger condition used in the analysed data presented in this thesis. Previous experimental data on $\gamma + {}^4$He cross-sections in the E_γ >40 MeV region were used as a base with which to compare the present measurement in order to infer the detection thresholds, since previous data appear to be relatively consistent in this energy range. The inferred thresholds were then used to calculate the detection efficiency over the full energy range of the experiment.

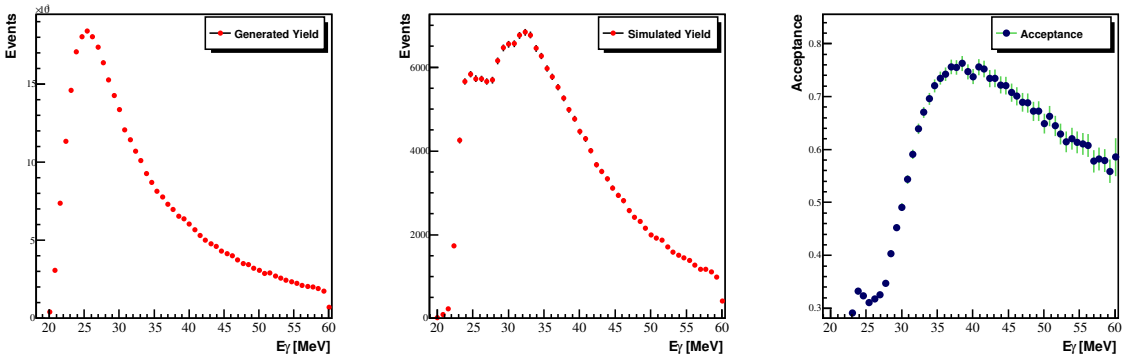

Figure 5.20: Efficiency calculation. Far left: Events as generated by the event generator (see Sec. 4.4.1). Middle: Events that passed all cuts, including the QDC software cuts applied in the offline analysis. Far right: Acceptance is calculated by dividing the middle spectrum by the one on the left. The cut conditions applied are: 2.3 MeV energy cut, M_3 multiplicity, PMT threshold of at least 1 photoelectron produced by any 3 PMTs of any HGSAT cell plus the QDC software cuts.

Energy and multiplicity cuts, PMT discriminator thresholds and software cuts used in the offline analysis were applied to the simulated data. The efficiency was

calculated by dividing the number of events that survived all cuts by the number originally generated. Fig. 5.20 shows the total number of events as produced by the event generator (far left), events that passed all cuts (middle) and finally the efficiency curve as a function of photon energy (far right). The cut conditions applied to generate the middle plot are: 2.3 MeV energy cut, M_3 multiplicity, PMT threshold of at least 1 photoelectron produced by any 3 PMTs of any HGSAT cell and in addition to the QDC software cuts. The details of the structure around ∼25 MeV and the location of the peak were found to depend on the values used in the cuts. Higher cuts results in a wider separation until the peak disappears. This highly suggests that the structure seen in the extracted yield shown in Fig. 5.6 at tagger channel 45 (corresponds to 25.54 MeV photon energy) is a real effect and most likely to be due to protons starting to escape the gas volume. Evaluation of the detection efficiency for different values of energy threshold and multiplicity cut is given in Ch. 4.

The efficiency rises from zero at photodisintegration threshold, peaking at 0.75 around 38 MeV energy and then gradually falling off. The efficiency is different for different reaction channels with $^4\mathrm{He}(\gamma, ^3\mathrm{He})n$ producing the greatest energy loss in the target. Over the present energy range only the ^{3}He stand a good chance of stopping in the target. Above ∼25 MeV most protons do not stop in the target gas, producing the cusp in efficiency at photon energies around 25 MeV. Stopping power and ranges of $\gamma + ^4$He breakup products as a function of incident photon energy are discussed in more detail in Sec. 4.4.2.

5.8 Systematic Uncertainties

The systematic uncertainties associated with this measurement come from six main sources:

- The yield extraction has a systematic uncertainty arising from the background subtraction and from fitting the prompt peak in the tagger-target TDC spectra. This quantity was estimated by varying the parameters of the two methods employed in obtaining the yield and subtracting the results. The systematic uncertainty was found to be around ±1.5% at photon energies with highest statistics $35 - 41$ MeV. Below 30 MeV and above 55 MeV incident photon energy, the uncertainty peaks at ±6% where the statistics are relativity poorer. For all other photon energies, the uncertainties were found to be about ±2.5%.

- The tagging efficiency was measured using two different methods: the "Lund" and the "Mainz" methods. Analysing the results from the two methods showed no significant discrepancy. Considering fluctuations in the beam position and the difference resulted in using the two methods, the systematic uncertainty associated with this quantity was estimated to be around ±2.5% and goes up to ∼ ±3% at photon energy < 32 MeV due to the reduced detection efficiency of the Pb-SciFi detector at these low energies. The significant drop in the detection efficiency of the Pb-SciFi detector at tagger channels > 50, correspond

to photon energies of $< 21\,\text{MeV}$, (Fig. 5.11) has no real impact on the total $\gamma + {}^4\text{He}$ cross-section where the reaction threshold is $\sim$20 MeV.

- The target thickness was calculated using measurements of the gas pressure and the length of the gas traversed by the photon beam. A small leak in the gas vessel resulted in a $\sim$1.5% decrease in the gas pressure for the data set that was analysed and presented in this thesis. Adding this to the pressure sensor intrinsic accuracy and room temperature fluctuations takes the systematic error up to $\sim \pm 3\%$.

- The electron beam energy is well defined, so the tagged-photon energy resolution is given by the width of the focal-plane counters, that is: $\pm 0.9\,\text{MeV}$.

- The systematic uncertainty associated with the stolen correction comes mainly from locating the start of the TDC coincidence peak which was determined by eye from the aligned tagger TDCs. Varying the start of the TDC coincidence peak location by a few channels both ways introduced an error of about $\pm 2.5\%$ on average, $\sim \pm 3.5\%$ at low photon energies and fall to $\sim \pm 1.4\%$ at $\sim$60 MeV. The systematic error in this correction will be assessed further using Myer's tagger simulation [211] upon its release.

- It is premature to make a reliable estimate on the systematic uncertainties associated with the acceptance correction until an energy calibration of detection thresholds has been made. Pending the energy calibration a rough estimate of around $\pm 30\%$ is made at the break-up photon energy of $\sim$20 MeV, falling to $\pm 10\%$ for photon energies $\geqslant 30\,\text{MeV}$.

Chapter 6

Results and Discussion

6.1 Overview

The results of a ^{4}He total photoabsorption cross-section measurement, performed using the active target technique are presented in this chapter. This is the first $\gamma + {}^4$He cross-section measurement using scintillations in a helium target as a means of detection of the photodisintegration break-up products. The results are compared with previous experimental data and to recent theoretical calculations made by Gazit et al. [38] and Quaglioni et al. [14]. The chapter concludes with a conclusion and recommendations for future work.

6.2 Results

The preliminary results of the total photoabsorption cross-section of ^{4}He as a function of incident photon energy (E_γ) measured using the HGSAT are given in Fig. 6.1. The cross-section peaks at $\sim$2.85 mb at the photon energy of $\sim$27 MeV. The HGSAT cross-section was obtained by normalising to previous total $\gamma + {}^4$He cross-section measurements above 40 MeV where more consistency in the dataset is observed. However, setting the discriminator threshold in the Monte-Carlo to match high energy data seems to produce low cross-section values below 25 MeV where the efficiency correction is very large and the systematic uncertainty correspondingly large. This suggests a deficiency in the current Monte-Carlo. The "one photoelectron" assumption in triggering a single PMT is probably not accurate and an overall energy calibration of HGSAT has still to be completed. Absolute determination of the efficiency is on-going, hence the results presented here should be treated as preliminary. It should be stated that without applying any efficiency correction the normalised total $\gamma + {}^4$He cross-section peaked at $\sim$1.8 mb at $\sim$36 MeV photon energy.

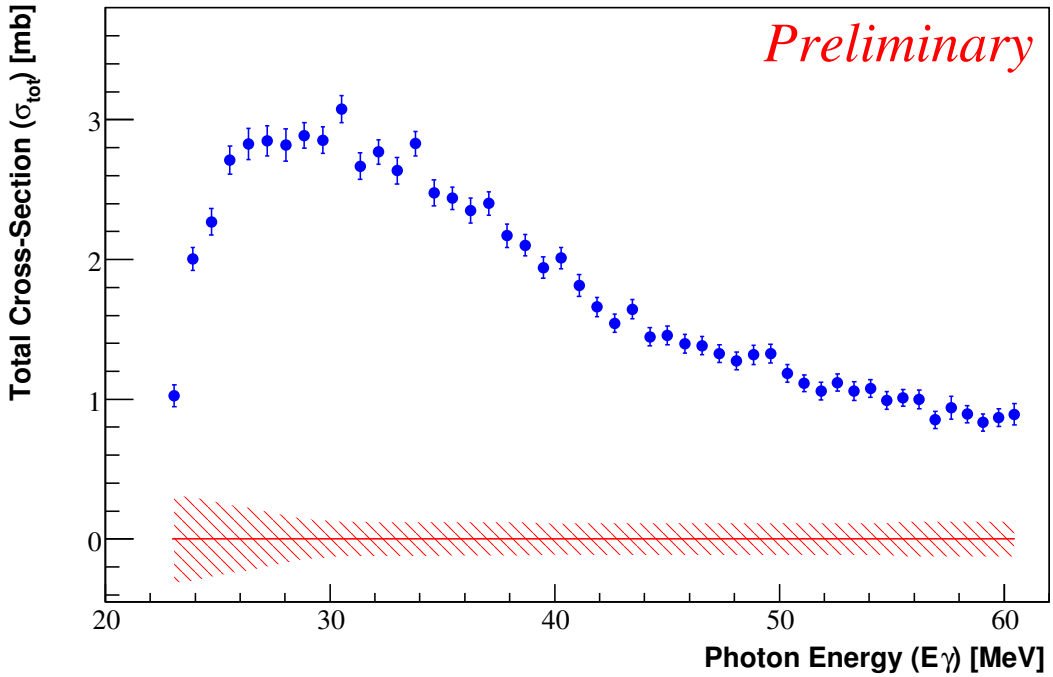

Figure 6.1: The total photoabsorption cross-section of ^{4}He as a function of photon energy (E_γ) measured using the HGSAT. The dashed area is the estimated systematic uncertainties associated with the measurement.

6.3 Comparison With Existing Data and Recent Theoretical Calculations

The preliminary results of the $\gamma + {}^4$He cross-section are shown in Fig. 6.2 in comparison with previous experimental data and the two recent theoretical calculations which include the three-body force effect NNN. The figure is zoomed in at photon energies $\sim 19.5 - 46$ MeV to offer a better visualization to the Giant Dipole Resonance (GDR) region. Experimental data of Arkatov et al. [48] above 40 MeV was mainly used for cross-section normalisation purposes. Although preliminary, the results of the present analysis are reasonably consistent with the calculations of Gazit at al. [38] and Quaglioni at al. [14] above the near-threshold region. The present, highly preliminary, cross-section is also compared with various data sets which are described in Sec. 1.4.2. Note that only the data of Arkatov [48], Wells [53], Shima [35] and Nakayama [54] are direct measurements of the total cross-section. The other data have been inferred from measurements of partial cross-sections. Apart from the Shima measurement [35], the present data follows the general trends in energy-dependence shown by previous measurements.

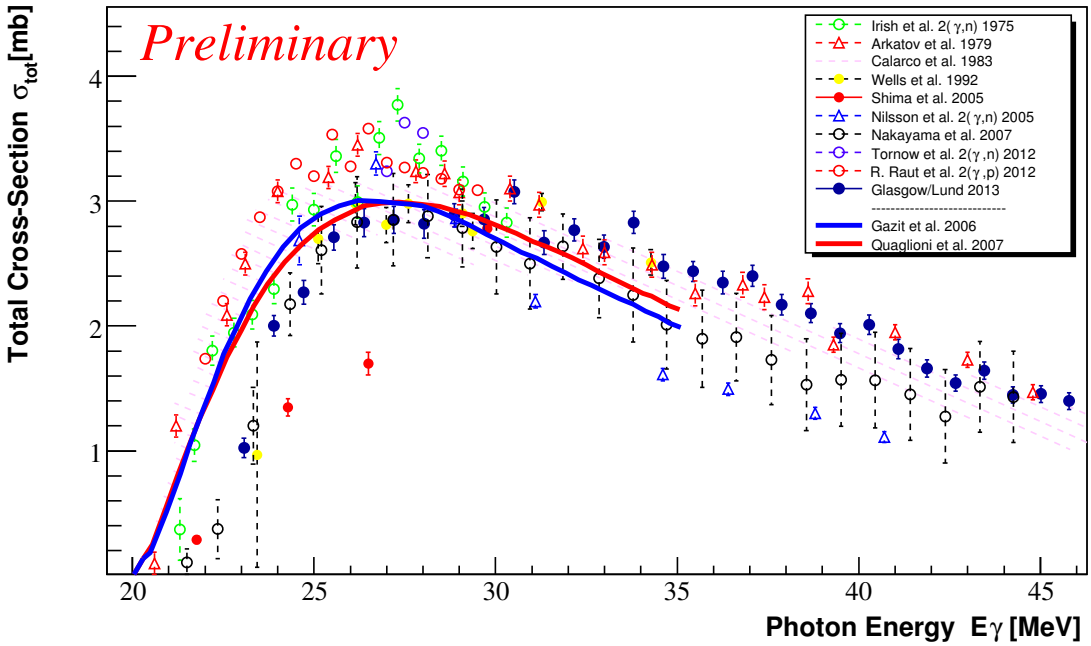

Figure 6.2: Comparison between the measured cross-section in this work (Glasgow/Lund 2013) and the recent theoretical calculations: Gazit (2006)[38], Quaglioni (2007)[14] and experimental data: Irish (1975)[56], Arkatov (1979)[48], Wells (1992)[53], Shima (2005)[35], Nilsson (2005)[39] Nakayama (2007)[54], Tornow (2012)[40] and Raut (2012)[55]. The dashed region is the sum of the recommended (γ, p) and (γ, n) based on an evaluation of the dataset made by Calarco at el. in 1983. All of the experimental data are retrieved from the EXFOR online library [57].

6.4 Conclusions and Future Work

For the preliminary results presented here to be finalised, the absolute efficiency of the HGSAT and corrections for rate-dependent effects in the tagger FP detector must be determined precisely. The experiment reported here was run with a relatively high-beam intensity, motivated by the desire to accumulate reasonable counting statistics in external neutron and gamma-ray counters and also to avoid instabilities in the beam time structure which were observed at lower intensities. This led us to apply a restrictive trigger condition for most of the data taking during the experiment to overcome issues with the DAQ system saturation. Running with such a high beam intensity and trigger condition led to a significant impact on the detection efficiency and to a sizeable rate dependent correction.

Until an energy calibration of HGSAT is completed, the applied energy thresholds will be uncertain. The detection efficiency depends strongly on the threshold, especially close to photodisintegration threshold. A calibration procedure, using the existing tagged photon data, is being devised and this will be checked against the

response to alpha sources. This calibration procedure is similar to that used to produce Fig. 4.26. From the data, the total measured pulse height is plotted against photon energy after random background has been subtracted. Fig. 4.26 shows the effect of the experimental trigger which does not have a clear defined energy cut off. However, a software energy cut can in principle clear most of the indeterminate hardware threshold region. Such a cut can be easily implemented in the simulation and therefore, the detection efficiency can be determined directly without necessarily converting the discriminator thresholds from mV to MeV units. Modelling of various reaction channels, which have different energy-dependent efficiencies is also being refined.

For stolen-coincidence corrections, we believe our treatment is correct, but nonetheless the corrections are large. The ghost correction has not been dealt with in the analysis presented in this thesis since it is estimated to be insignificant compared to the other effects. However, both stolen-coincidence and ghost corrections will be checked when the newly developed Monte-Carlo simulation of the MAX-lab tagger [215] becomes available. A way to eliminate the need of this correction is to use a Multi-hit TDCs instead of regular TDCs. This has been already planned for the next experimental rerun.

In conclusion, the preliminary total $\gamma + {}^4\mathrm{He}$ cross-section obtained using the Helium Gas-Scintillator Active Target (HGSAT) is very promising and already shows the general trends of recent theoretical calculations and results from a number of previous experiments. The author is confident that an absolute and precise determination of the cross-section is feasible and within reach using the HGSAT. The experiment will be rerun in 2013 at lower beam-intensity using more relaxed trigger conditions. With an energy calibration this should substantially reduce the current uncertainties in the measured cross-section.

Bibliography

[1] M. Beller, R. S. Cohen, and J. Renn. *Einstein in Context*. Science in Context. Cambridge University Press, 1993.

[2] H. Bethe and R. Peierls. Quantum Theory of the Diplon. *Royal Society of London Proceedings Series A*, 148:146–156, Jan. 1935.

[3] V. McLane. A short guide to the nuclear reaction data format. *Report BNL-NCS-63380*, 34(12), 2000.

[4] IAEA. Handbook on photonuclear data for applications, Cross sections and spectra. *Final report of a co-ordidnated research project*, 2000.

[5] International Atomic Energy Agency. IAEA Photonuclear Data Library . www.nucleus.iaea.org, 2013.

[6] Nuclear Data Center (NDC). Japanese Evaluated Nuclear Data Library. http://wwwndc.jaea.go.jp/nucldata, 2013.

[7] J. Chadwick. Bakerian Lecture. The Neutron. *Royal Society of London Proceedings Series A*, 142:1–25, Oct 1933.

[8] C. A. Bertulani. *Nuclear Physics in a Nutshell*. Princeton University Press, 2011.

[9] E. Epelbaum. Few-nucleon forces and systems in chiral effective field theory. *Prog.Part.Nucl.Phys.*, 57:654–741, 2006.

[10] K. G. Wilson. Confinement of Quarks. *Phys. Rev. D*, 10:2445, 1974.

[11] S. Weinberg. Phenomenological Lagrangians. *Physica*, A96:327, 1979.

[12] G. E. Brown, T. T. S. Kuo, and J. W. Holt. *The Nucleon-Nucleon Interaction and the Nuclear Many-Body Problem: Selected Papers of Gerald E. Brown and T. T. S. Kuo*. World Scientific, 2010.

[13] P. Vesely. The nucleon-nucleon interaction with the leading order relativistic effects. Lecture Notes in Physics. Mar. 2006.

[14] S. Quaglioni and P. Navrátil. The ^{4}He total photo-absorption cross section with two- plus three-nucleon interactions from chiral effective field theory. *Physics Letters B*, 652(56):370 – 375, 2007.

[15] J. Ahrens. The total absorption of photons by nuclei. *Nuclear Physics A*, 446(12):229 – 239, 1985.

[16] K. A. Snover. Giant Resonances in Excited Nuclei. *Annual Review of Nuclear and Particle Science*, 36:545–603, 1986.

[17] K. Goeke and J. Speth. THEORY OF GIANT RESONANCES. *Annu. Rev. Nucl. Part. Sci.*, 32:65(115), 1982.

[18] N. Harakeh and A. Woude. *Giant Resonances: Fundamental High-Frequency Modes of Nuclear Excitation*. Oxford Studies in Nuclear Physics. Oxford University Press, 2001.

[19] M. Goldhaber and E. Teller. On nuclear dipole vibrations. *Phys. Rev.*, 74:1046–1049, Nov. 1948.

[20] H. Steinwedel and J. H. Jensen. *Z. Nat.*, 5, 1950.

[21] Ph. CHOMAZ. Collective excitations in nuclei. *GRAND ACCELERATEUR NATIONAL D'IONS LOURDS-CAEN*, 1997.

[22] J. Speth. *Electric and Magnetic Giant Resonances in Nuclei*. International Review of Nuclear Physics Series. World Scientific Publishing Company Incorporated, 1991.

[23] D. Bohm and D. Pines. A Collective Description of Electron Interactions. I. Magnetic Interactions. *Phys. Rev.*, 82:625–634, Jun. 1951.

[24] Ioannis Daoutidis. *Relativistic Continuum Random Phase Approximation in Spherical Nuclei*. PhD thesis, Institut für Theoretische Physik T30, Physik Department, Technische Universität München, Germany, 2009.

[25] J. S. Levinger. The High Energy Nuclear Photoeffect. *Phys. Rev.*, 84:43–51, Oct. 1951.

[26] J. S. Levinger. Modified quasi-deutron model. *Physics Letters B*, 82(2):181 – 182, 1979.

[27] K. Gottfried. On the determination of the nuclear pair correlation function from the high energy photo-effect. *Nuclear Physics*, 5(0):557 – 587, 1958.

[28] J. Ryckebusch, M. Vanderhaeghen, L. Machenil, and M. Waroquier. Effects of the final state interaction in (γ, pn) and (γ, pp) processes. *Nucl.Phys.*, A568:828–854, 1994.

[29] Björn Nilsson. *High-Resolution Measurement of the ^{4}He(γ,n)Reaction in the Giant Resonance Region*. PhD thesis, Lund University, Lund, Sweden, 2003.

[30] S. S. M. Wong. *Introductory Nuclear Physics*. Wiley, 2008.

[31] V. D. Efros, W. Leidemann, G. Orlandini, and N. Barnea. The Lorentz integral transform (LIT) method and its applications to perturbation-induced reactions. *Journal of Physics G: Nuclear and Particle Physics*, 34(12):R459, 2007.

[32] E. R. Gaerttner and M. L. Yeater. The Photodisintegration of ^{4}He Nuclei by X-Rays from a 100-MeV Betatron. *Phys. Rev.*, 83:146–150, Jul. 1951.

[33] J. R. M. Annand et al. Measurement of Photoreactions on Helium Isotopes using Gas-Scintillator Active Targets. *Experimental Proposal For Lund MAXLab P.A.C.*

[34] J. R. Calarco, B. L. Berman, and T. W. Donnelly. Implications of the experimental results on the photodisintegration of ^{4}He. *Phys. Rev. C*, 27:1866–1875, May 1983.

[35] T. Shima, S. Naito, Y. Nagai, T. Baba, K. Tamura, T. Takahashi, T. Kii, H. Ohgaki, and H. Toyokawa. Simultaneous measurement of the photodisintegration of ^{4}He in the giant dipole resonance region. *Phys. Rev. C*, 72:044004, Oct. 2005.

[36] R. B. Wiringa, V. G. J. Stoks, and R. Schiavilla. Accurate nucleon-nucleon potential with charge-independence breaking. *Phys. Rev. C*, 51:38–51, Jan. 1995.

[37] B. S. Pudliner, V. R. Pandharipande, J. Carlson, S. C. Pieper, and R. B. Wiringa. Quantum Monte Carlo calculations of nuclei with A $\leqslant$ 7. *Phys.Rev.*, C56:1720–1750, 1997.

[38] D. Gazit, S. Bacca, N. Barnea, W. Leidemann, and G. Orlandini. Photoabsorption on ^{4}He with a Realistic Nuclear Force. *Phys. Rev. Lett.*, 96:112301, Mar. 2006.

[39] B. Nilsson, J.-O. Adler, B.-E. Andersson, J. R. M. Annand, I. Akkurt, M. J. Boland, G. I. Crawford, K. G. Fissum, K. Hansen, P. D. Harty, D. G. Ireland, L. Isaksson, M. Karlsson, M. Lundin, J. C. McGeorge, G. J. Miller, H. Ruijter, A. Sandell, and Schr

[40] W. Tornow, J. H. Kelley, R. Raut, G. Rusev, A. P. Tonchev, M. W. Ahmed, A. S. Crowell, and S. C. Stave. Photodisintegration cross section of the reaction ^{4}He(γ,n)^{3}He at the giant dipole resonance peak. *Phys. Rev. C*, 85:061001, Jun. 2012.

[41] V. D. Efros, W. Leidemann, and G. Orlandini. Response functions from integral transforms with a lorentz kernel. *Physics Letters B*, 338(23):130 – 133, 1994.

[42] Ward Andrew Wurtz. *Photodisintegration of Lithium Isotopes*. PhD thesis, Department of Physics and Engineering Physics, University of Saskatchewan, Saskatoon, Canada, 2010.

[43] N. Barnea and A. Novoselsky. Construction of hyperspherical functions symmetrized with respect to the orthogonal and the symmetric groups. *Annals of Physics*, 256(2):192 – 225, 1997.

[44] P. Navrátil and B. R. Barrett. No-core shell-model calculations with starting-energy-independent multivalued effective interactions. *Phys. Rev. C*, 54:2986–2995, Dec. 1996.

[45] A. Nogga, H. Kamada, Walter Gloeckle, and B. R. Barrett. The Alpha particle based on modern nuclear forces. *Phys.Rev.*, C65:054003, 2002.

[46] V. D. Efros, W. Leidemann, and G. Orlandini. Accurate Four-Body Response Function with Full Final State Interaction: Application to Electron Scattering off ^{4}He. *Phys. Rev. Lett.*, 78:432–435, Jan. 1997.

[47] N. Barnea, V. D. Efros, W. Leidemann, and G. Orlandini. Total ^{4}He photoabsorption cross section reexamined: Correlated versus effective interaction hyperspherical harmonics. *Phys. Rev. C*, 63:057002, Apr. 2001.

[48] Yu. M. Arkatov, P. I. Vatset, V. I. Voloshchuk, V. A. Zolenko, and I. M. Prokhorets. Experimental check of the sum rules for photodisintegration of he-4. *Voprosy Atomnoy Nauki i Tekhniki, Seriya Obshch. Data retrieved from EXFOR M0019001*, 4/10:55, 1979.

[49] R. Bernabei, A. Chisholm, S. d'Angelo, M. P. De Pascale, P. Picozza, C. Schaerf, P. Belli, L. Casano, A. Incicchitti, D. Prosperi, and B. Girolami. Measurement of the ^{4}He(γ,p)^{3}H total cross section and charge symmetry. *Phys. Rev. C*, 38:1990–1995, Nov. 1988.

[50] G. Feldman, M. J. Balbes, L. H. Kramer, J. Z. Williams, H. R. Weller, and D. R. Tilley. ^{3}H(p,γ)^{4}He reaction and the (γ,p)/(γ,n) ratio in ^{4}He. *Phys. Rev. C*, 42:R1167–R1170, Oct. 1990.

[51] L. Van Hoorebeke, R. Van de Vyver, V. Fiermans, D. Ryckbosch, C. Van den Abeele, and J. Dias. Direct measurement of the ^{4}He(γ,p_0) absolute cross section. *Phys. Rev. C*, 48:2510–2513, Nov. 1993.

[52] R. J. Komar, H.-B. Mak, J. R. Leslie, H. C. Evans, E. Bonvin, E. D. Earle, and T. K. Alexander. ^{3}He(n,γ)^{4}He cross section and the photodisintegration of ^{4}He. *Phys. Rev. C*, 48:2375–2384, Nov. 1993.

[53] D. P. Wells, D. S. Dale, R. A. Eisenstein, F. J. Federspiel, M. A. Lucas, K. E. Mellendorf, A. M. Nathan, and A. E. O'Neill. Elastic photon scattering from ^{4}He: Charge symmetry problem. *Phys. Rev. C*, 46:449–454, Aug. 1992.

[54] S. Nakayama, E. Matsumoto, R. Hayami, K. Fushimi, H. Kawasuso, K. Yasuda, T. Yamagata, H. Akimune, H. Ikemizu, M. Fujiwara, M. Yosoi, K. Nakanishi, K. Kawase, H. Hashimoto, T. Oota, K. Sagara, T. Kudoh, S. Asaji, T. Ishida, M. Tanaka, and M. B. Greenfield. Analog of the giant dipole resonance in ^{4}He. *Phys. Rev. C*, 76:021305, Aug. 2007.

[55] R. Raut, W. Tornow, M. W. Ahmed, A. S. Crowell, J. H. Kelley, G. Rusev, S. C. Stave, and A. P. Tonchev. Photodisintegration Cross Section of the Reaction ^{4}He$(\gamma, p)^3$H between 22 and 30 MeV. *Phys. Rev. Lett.*, 108:042502, Jan. 2012.

[56] J. D. Irish, R. G. Johnson, B. L. Berman, B. J. Thomas, K. G. McNeill, and J. W. Jury. Photoneutron Angular Distributions for 4He. *Canadian Journal of Physics, Data retrieved from EXFOR M0327018*, 53(8):802–811, 1975.

[57] Experimental Nuclear Reaction Data. www-nds.iaea.org/exfor/exfor.htm, 2013.

[58] B. Nilsson, J.-O. Adler, B.-E. Andersson, J. R. M. Annand, I. Akkurt, M. J. Boland, G. I. Crawford, K. G. Fissum, K. Hansen, P. D. Harty, D. G. Ireland, L. Isaksson, M. Karlsson, M. Lundin, J. C. McGeorge, G. J. Miller, H. Ruijter, A. Sandell, B. Schröder, D. A. Sims, and D. Watts. Measurement of the ^{4}He (γ, n) reaction from 23< E_γ <70 MeV. *Phys. Rev. C*, 75:014007, Jan. 2007.

[59] W. Crookes. Certain Properties of the Emanations of Radium. *Chem. News*, 87(241), 1903.

[60] T. Gray. Atoms and Eves. *Popular Science*, 270(6):68, Jun. 2007.

[61] J. B. Birks. *The theory and practice of scintillation counting*. Pergamon Press, 1964.

[62] W. R. Leo. *Techniques for Nuclear and Particle Physics Experiments: A How-to Approach*. Springer, Berlin, 2., Überarb. A. edition, Feb. 1994.

[63] A Ward. The Emission of Light in the Passage of Alpha Particles through Gases. *Proceedings of the Physical Society. Section A*, 67(9):841, 1954.

[64] S. S. Al-Dargazelli, T. R. Ariyaratne, J. M. Breare, and B. C. Nandi. The performance of a gas scintillation counter at high count rates. *Nuclear Instruments and Methods in Physics Research*, 200(2-3):341 – 344, 1982.

[65] R. Auderbert and S. Lormeau. *C. R. Acad. Sci., Paris*, 228:318, 1949.

[66] R. Auderbert and S. Lormeau. *C. R. Acad. Sci., Paris*, 230:956, 1950.

[67] R. E. Shamu. High-pressure gas scintillation counters. *Nuclear Instruments and Methods*, 14:297 – 301, 1962.

[68] J. W. Mayer. The "State-of-The Art" in Nuclear Particle Detectors. *Nuclear Science, IRE Transactions on*, 9(3):124 –134, Jun. 1962.

[69] E. Aprile, A.E. Bolotnikov, A.I. Bolozdynya, and T. Doke. *Noble Gas Detectors*. John Wiley & Sons, 2007.

[70] M. Mutterer, P. Grimm, H. Heckwolf, J. Pannicke, W. Spreng, and J. Theobald. Response of gas scintillators to heavy charged particles. In von Oertzen, W., editor, *Detectors in Heavy-Ion Reactions*, volume 178 of *Lecture Notes in Physics*, pages 63–79. Springer Berlin / Heidelberg, 1983. 10.1007/3-540-12001-7245.

[71] C. A. N. Conde and A. J. P. L. Policarpo. A gas proportional scintillation counter. *Nuclear Instruments and Methods*, 53:7 – 12, 1967.

[72] Policarpo. A. J. P. L., M. A. F. Alves, M. C. M. Dos Santos, and M. J. T. Carvalho. Improved resolution for low energies with gas proportional scintillation counters. *Nuclear Instruments and Methods*, 102(2):337 – 348, 1972.

[73] K. P. Schelhaas, M. Mutterer, J. P. Theobald, P. A. Schillack, G. Schrieder, and p. Wastyn. A two-dimensional gas-scintillation drift chamber for heavy-ion detection. *Nuclear Instruments and Methods*, 154(2):245 – 252, 1978.

[74] K. D. Mathis, M. Simon, and M. Henkel. A gas scintillation drift chamber for heavy ion detection. *Nuclear Instruments and Methods in Physics Research*, 225(2):407 – 412, 1984.

[75] T. Kobayashi, F. S. Bieser, T. J. M. Symons, and D. E. Greiner. A drift chamber for high-energy heavy ions. *Nuclear Instruments and Methods in Physics Research Section A: Accelerators, Spectrometers, Detectors and Associated Equipment*, 254(2):281 – 302, 1987.

[76] S. Hohara et al. Development of Gas Proportional Scintillation Counter for Light Heavy-Ion Detection. *AIP Conference Proceedings*, 769(1):773–775, 2005.

[77] Z. Sosin et al. Gas scintillation chamber for superheavy elements detection at GANIL. In *Acta Physica Polonica B*, volume 40, pages 741–745, Zakopane, Poland, 2009.

[78] M. Mutterer. Gas scintillation nuclear particle detectors. *Nuclear Instruments and Methods in Physics Research*, 196(1):73 – 81, 1982.

[79] G.F. Knoll. *Radiation detection and measurement*. Wiley, 2000.

[80] J. R. M. Annand et al. Measurement of the $\gamma + {}^4$He Total Photoabsorption Cross Section from 25 to 70 MeV. *Experimental Proposal For Lund MaxLab*, 1997.

[81] J. B. Birks. Excimers. *Reports on Progress in Physics*, 38(8):903, 1975.

[82] J. R. M. Annand, R. Al-Jebali, K. Livingston, D. Burdeinyi, V. Ganenko, K. Goloreshko, J. Brudvik, K. Fissum, K. Hansen, M. Lundin, L. Isaksson, and B. Schröder. Σ Asymmetry of ^{4}He(γ, n) with the MkIII Helium Active Target and Nordball. *Experimental Proposal For Lund MAXLab P.A.C.*, Mar. 2011.

[83] S. Kubota, T. Takhashi, and T. Doke. Mechanism of Scintillation of Helium, Helium-Argon, and Helium-Neon Gas Mixtures Excited by Alpha Particles. *Phys. Rev.*, 165(1):225–230, Jan. 1968.

[84] T. Iida, H. Hosoe, and I. Urabe. Kinetic Processes of the Scintillation in Helium Excited by Alpha Particles. *Journal of the Physical Society of Japan*, 49:1619–+, Oct. 1980.

[85] P. C. Hill. Ultraviolet continua of helium molecules. *Phys. Rev. A*, 40(9):5006–5016, Nov. 1989.

[86] P.P.W. Atkins and J. De Paula. *Atkins' Physical Chemistry*. Oxford University Press, Incorporated, 2002.

[87] C. Böehme et al. Gas Scintillation Beam Profile Monitor At Cosy Jülich. *BIW19 Preprint–Edited; preliminary green dot status*.

[88] T. Takahashi. Recombination Luminescence in the Scintillation of High Pressure Helium Gas Induced by Alpha Particles. *Journal of the Physical Society of Japan*, 24:561–+, Mar. 1968.

[89] M. G. Payne, C. E. Klots, and G. S. Hurst. Kinetic processes determining the time dependence of vuv emission in He. 63(4):1422–1428, 1975.

[90] Daniel Nicholas McKinsey. *Detection of Magnetically Trapped Neutrons:Liquid Helium as a Scintillator*. PhD thesis, Harvard University, Cambridge, Massachusetts, USA, Feb. 2002.

[91] G. Charpak. Emission and absorption of photons in gaseous detectors. In W. Oertzen, editor, *Detectors in Heavy-Ion Reactions*, volume 178 of *Lecture Notes in Physics, Berlin Springer Verlag*, pages 10–24, 1983.

[92] M. Stockton, J. W. Keto, and W. A. Fitzsimmons. Ultraviolet Emission Spectrum of Electron-Bombarded Superfluid Helium. *Phys. Rev. Lett.*, 24(12):654–657, Mar. 1970.

[93] D. M. Bartell, G. S. Hurst, and E. B. Wagner. Time-Dependent Studies of Vacuum-Ultraviolet Emissions from Helium. *Phys. Rev. A*, 7(3):1068–1078, Mar. 1973.

[94] D. N. McKinsey, C. R. Brome, J. S. Butterworth, S. N. Dzhosyuk, P. R. Huffman, C. E. H. Mattoni, J. M. Doyle, R. Golub, and K. Habicht. Radiative decay of the metstable $He_2(a^3\Sigma_u^+)$ molecule in liquid helium. *Phys. Rev. A*, 59(1):200–204, Jan. 1999.

[95] R. E. Huffman, J. C. Larrabee, and D. Chambers. New Excitation Unit for Rare Gas Continua in the Vacuum Ultraviolet. *Appl. Opt.*, 4(9):1145–1150, Sep. 1965.

[96] Y. Tanaka, A. S. Jursa, and F. J. Leblance. Continuous Emission Spectra of Rare Gases in the Vacuum Ultraviolet Region. II. Neon and Helium. *J. Opt. Soc. Am.*, 48(5):304–307, May 1958.

[97] Y. Tanaka, R. E. Huffman, and J. C. Larrabee. Recent improvements in rare gas continua in the vacuum ultraviolet region. *Journal of Quantitative Spectroscopy and Radiative Transfer*, 2(4):451 – 464, 1962.

[98] A. M. Boichenko, V. F. Tarasenko, and S. I. Yakovlenko. Nature of third continua in rare gases. 4071(1):255–270, 2000.

[99] H. Langhoff. The origin of the third continua emitted by excited rare gases. *Optics Communications*, 68(1):31 – 34, 1988.

[100] T. Griegel, H. W. Drotleff, J. W. Hammer, and K. Petkau. The third continuum of the rare gases emitted by heavy ion beam induced plasmas. 93(7):4581–4588, 1990.

[101] H. Yagisawa, H. Sato, and T. Watanabe. Accurate electronic energies of He_2^{++}. *Phys. Rev. A*, 16(4):1352–1357, Oct. 1977.

[102] J. Wieser, A. Ulrich, A. Fedenev, and M. Salvermoser. Novel pathways to the assignment of the third rare gas excimer continua. *Optics Communications*, 173(1-6):233 – 245, 2000.

[103] P. C. Hill. Ultraviolet continua of He_2^+. *Phys. Rev. A*, 43(5):2546–2549, Mar. 1991.

[104] D. N. McKinsey, W. H. Lippincott, J. A. Nikkel, and W. G. Rellergert. Trace Detection of Metastable Helium Molecules in Superfluid Helium by Laser-Induced Fluorescence. *Physical Review Letters*, 95(11):111101–+, Sep. 2005.

[105] R. J. Esterling and N. H. Lipman. Helium Gas Scintillation. *Review of Scientific Instruments*, 36:493–497, Apr. 1965.

[106] C. Rubbia and M. Toller. Pressure dependence of radiative processes in helium. *Nuovo Cim*, 10(758), 1957.

[107] R. L. Aamodt, L. J. Brown, and G. M. Smith. High Pressure 3He Gas Scintillation Neutron Detector. 37(10):1338–1340, 1966.

[108] K. Saito, H. Tawara, T. Sanami, E. Shibamura, and S. Sasaki. Absolute number of scintillation photons emitted by alpha particles in rare gases. *IEEE Transactions on Nuclear Science*, 49:1674–1680, Aug. 2002.

[109] D. N. McKinsey, C. R. Brome, S. N. Dzhosyuk, R. Golub, K. Habicht, P. R. Huffman, E. Korobkina, S. K. Lamoreaux, C. E. H. Mattoni, A. K. Thompson, L. Yang, and J. M. Doyle. Time dependence of liquid-helium fluorescence. *Phys. Rev. A*, 67:062716, Jun. 2003.

[110] P. Guazzoni and M. Pignanelli. Pressure dependence of radiative processes in helium. *Physics Letters A*, 28(6):432 – 433, 1968.

[111] W. R. Bennett, Jr. Optical spectra excited in high pressure noble gases by alpha impact. *Annals of Physics*, 18:367–420, May 1962.

[112] K. Saito, S. Sasaki, H. Tawara, and E. Shibamura. Application of scintillation in helium mixed with xenon to a position-sensitive detector. In *Nuclear Science Symposium Conference Record (NSS/MIC), 2010 IEEE*, pages 14 –18, Nov. 2010.

[113] S. A. Baldin, V. V. Gabrilovski, and F. E. Chukreev. Scintillation in helium at high pressures due to alpha-particles. *Journal of Nuclear Energy (1954)*, 8(4):247 – 252, 1959.

[114] P. Guazzoni and M. Pignanelli. On the performance of helium scintillation counters. *Nuclear Instruments and Methods*, 72(2):195 – 200, 1969.

[115] H. Morii, K. Mizouchi, T. Nomura, N. Sasao, T. Sumida, M. Kobayashi, Y. Murayama, and R. Takashima. Quenching effects in nitrogen gas scintillation. *Nuclear Instruments and Methods in Physics Research Section A: Accelerators, Spectrometers, Detectors and Associated Equipment*, 526(3):399 – 408, 2004.

[116] J. R. M. Annand et al. A Helium Gas-Scintillator Active Target for Photoreaction Measurement. 2006.

[117] Eljen Technology. Wave-length Shifting Paint EJ-298. http://www.eljentechnology.com, 2011.

[118] P. E. Thiess and G. H. Miley. *Nuclear Science, IEEE Transactions on, title=New Near-Infrared and Ultraviolet Gas-Proportional Scintillation Counters*, 21(1):125 –145, Feb. 1974.

[119] C. Eggler and C. M. Huddleston. Gaseous Scintillation. *Nuclear Science, IRE Transactions on*, 3(4):36 –38, Nov. 1956.

[120] T. W. Carr and S. Dondes. Direct measurement of the radiative lifetime and collisional quenching of the C3.PI.u state of nitrogen as studied by pulse radiolysis. *The Journal of Physical Chemistry*, 81(24):2225–2228, 1977.

[121] W. Tornow, H. Huck, H. Kober, and G. Mertens. Properties of high pressure nitrogen-argon and nitrogen-xenon gas scintillators. *Nuclear Instruments and Methods*, 133:435–443, Mar. 1976.

[122] J. R. M. Annand et al. Measurement of the $\gamma + {}^4$He Total Photoabsorption Cross Section from 25 to 70 MeV. *Experimental Proposal For Lund MAXLab P.A.C.*, 1998.

[123] J. R. M. Annand et al. Measurement of the $\gamma + {}^4$He Total Photoabsorption Cross Section using a Helium-Gas-Scintillator Active Target. *Experimental Proposal For Lund MAXLab P.A.C.*, 2000-2001.

[124] J. R. M. Annand et al. Measurement of Photoreactions on Helium Isotopes using Gas-Scintillator Active Targets. 2006.

[125] INDIUM CORPORATION OF AMERICA. Indium for sealing, Application note. 2011.

[126] PHOTONIS Technologies. Photomultiplier XP2262 manual. http://www.photonis.com, 2011.

[127] MAX-lab tagged photon facility. www.maxlab.lu.se, 2011.

[128] National Institute of Advanced Industrial Science and Technology (AIST). www.aist.go.jp, 2011.

[129] High Intensity Gamma-Ray Source (HIGS). www.tunl.duke.edu, 2011.

[130] Iskender Akkurt. (γ, n) *in light nuclei.* PhD thesis, University of Glasgow, Glasgow, Scotland, 1998.

[131] Andreas Reiter. *Differential photoneutron cross sections of light nuclei for neutron dosimetry.* PhD thesis, University of Glasgow, Glasgow, Scotland, 2004.

[132] J. W. Weil and B. D. McDaniel. The Production of Protons from Carbon by Monoenergetic Gamma Rays. *Phys. Rev.*, 92(2):391–400, Oct. 1953.

[133] J. Goldemberg. A Photon Monochromator for Bremsstrahlung Radiation. *Phys. Rev.*, 93(6):1426–1427, Mar. 1954.

[134] M. F. Shea, R. L. Walter, and W. C. Miller. *Phys. Rev.*, 5:226, 1960.

[135] J. S. O'Connell, P. A. Tipler, and P. Axel. Elastic Scattering of 11.5-17.7-MeV Photons by Au Measured with a Bremsstrahlung Monochromator. *Phys. Rev.*, 126(1):228–239, Apr. 1962.

[136] D. O. Caldwell, J. P. Dowd, K. Heinloth, and D. M Rousseau. Tagging System for High Energy Photons. *Rev. Sci. Instrum.*, 36(283), Sep. 1965.

[137] D. O. Caldwell, V. B. Elings, W. P. Hesse, G. E. Jahn, R. J. Morrison, F. V. Murphy, and D. E. Yount. Total Photoabsorption Cross Sections up to 18 GeV and the Nature of Photon Interactions. *Phys. Rev. Lett.*, 23(21):1256–1260, Nov. 1969.

[138] G. R. Brookes, S. Hinds, W. R. Rawlinson, M. D. Rousseau, D. W. L. Tolfree, and A. G. Wardle. A high resolution wide range photon tagging system. *Nuclear Instruments and Methods*, 85(1):125 – 131, 1970.

[139] P. Axel. Nuclear Studies With Tagged Photons, Nuclear Physics with Electromagnetic Interactions,Lecture Notes in Physics. 108:256–265, 1979.

[140] L. I. Schiff. Energy-Angle Distribution of Thin Target Bremsstrahlung. *Phys. Rev.*, 83(2):252–253, Jul. 1951.

[141] MAX-lab. MAX-lab Activity Report 2008-09, 2009.

[142] Mikael Ericsson. Private communication, 2011.

[143] Å. Andersson, M. Eriksson, P. Lindgren, L.-J.and Röjsel, and S. Werin. The MAX II synchrotron radiation storage ring. *Nuclear Instruments and Methods in Physics Research Section A: Accelerators, Spectrometers, Detectors and Associated Equipment*, 343(2-3):644 – 649, 1994.

[144] M. Sjöström, E. Wallén, M. Eriksson, and L.-J. Lindgren. The MAX III storage ring. *Nuclear Instruments and Methods in Physics Research Section A: Accelerators, Spectrometers, Detectors and Associated Equipment*, 601(3):229 – 244, 2009.

[145] W. J. Briscoe, B. Jason, K. G. Fissum, K. Hansen, L. Isaksson, M. Lundin, B. Nilsson, and B. Schröder. Plenary Talk: Nuclear physics program at MAX-lab. *Chinese Physics C*, 33:1159–1166, Dec. 2009.

[146] S. Werin, Å. Andersson, M. Bergqvist, M. Brandin, M. Eriksson, L. Johan-Lindgren, L. Malmgren, and H. Tarawneh. Commissioning of the 500 MeV Injector for MAX-lab. In *9th European Particle Accelerator Conference (EPAC)*, ISBN 92-9083-231-2, Lucerne, Switzerland, Jul. 2004.

[147] L. J. Lindgren and M. Eriksson. Experiences with the MAX accelerator system in the pulse-stretcher mode. *Nuclear Instruments and Methods in Physics Research Section A: Accelerators, Spectrometers, Detectors and Associated Equipment*, 294(1-2):10 – 14, 1990.

[148] L. Lindgren. Pulse-stretcher upgrade. *Nuclear Instruments and Methods in Physics Research Section A: Accelerators, Spectrometers, Detectors and Associated Equipment*, 492(1-2):299 – 304, 2002.

[149] S. Thorin, N. Cutic, F. Lindau, S. Werin, and F. Curbis. Photocathode operation of a thermionic RF gun. *Nuclear Instruments and Methods in Physics Research Section A: Accelerators, Spectrometers, Detectors and Associated Equipment*, 606(3):291 – 295, 2009.

[150] B. Anderberg, Å. Andersson, M. Demirkan, M. Eriksson, L. Malmgren, and S. Werin. The design of a 3GHz thermionic RF-gun and energy filter for MAX-lab. *Nuclear Instruments and Methods in Physics Research Section A: Accelerators, Spectrometers, Detectors and Associated Equipment*, 491(1-2):307 – 313, 2002.

[151] National Research Council (U.S.). Nuclear Physics Panel. *Nuclear physics.* Physics through the 1990s. National Academy Press, 1986.

[152] L. Lindgren and B. Anderberg. Septum magnet design. *Nuclear Instruments and Methods in Physics Research Section A: Accelerators, Spectrometers, Detectors and Associated Equipment*, 490(3):592 – 597, 2002.

[153] Bent Schröder. Private communication, 2012.

[154] MAX-lab tagged photon facility. Accelerator ELog 2009. http://np1.maxlab.lu.se:7713/Mar09/, 2009.

[155] J.-O Adler. The New Nuclear Physics Beam Line at MAX-lab. pages 194–201, Aug. 2001.

[156] MAX-lab. MAX-lab Activity Report 2007-08, 2008.

[157] J. M. Vogt, R. E. Pywell, D. M. Skopik, E. L. Hallin, J. C. Bergstrom, H. S. Caplan, K. I. Blomqvist, W. D. Bianco, and J. W. Jury. The photon tagging facility at the Saskatchewan Accelerator Laboratory. *Nuclear Instruments and Methods in Physics Research Section A: Accelerators, Spectrometers, Detectors and Associated Equipment*, 324(1-2):198 – 208, 1993.

[158] David Lee Hornidge. *Elastic Photon Scattering From Deuterium.* PhD thesis, University of Saskatchewan, Saskatoon, Canada, Spring 1999.

[159] M. Adler, J-O, M. Boland, and J. Brudvik. The upgraded photon tagging facility at MAX-lab. 2009.

[160] J. L. Matthews and R. O. Owens. Accurate formula for the calculation of high energy electron bremsstrahlung spectra. *Nuclear Instruments and Methods*, 111(1):157 – 168, 1973.

[161] D. W. Hertzog, P. T. Debevec, R. A. Eisenstein, M. A. Graham, S. A. Hughes, P. E. Reimer, and R. L. Tayloe. A high-resolution lead /scintillating fiber electromagnetic calorimeter. *Nuclear Instruments and Methods in Physics Research Section A: Accelerators, Spectrometers, Detectors and Associated Equipment*, 294(3):446 – 458, 1990.

[162] John R. M. Annand. Private communication, 2011.

[163] B. Herskind. The NORDBALL – A multidetector system for the study of nuclear structure. *Nuclear Physics A*, 447:395 – 412, 1986.

[164] S. E. Arnell, Roth H.A, Ö. Skeppstedt, J. Biakowski, M. Moszynski, D. Wolski, and J. Nyberg. A 2π neutron and γ-ray multiplicity filter for the NORDBALL detection system. *Nuclear Instruments and Methods in Physics Research Section A: Accelerators, Spectrometers, Detectors and Associated Equipment*, 300(2):303 – 311, 1991.

[165] Hengameh Navirian. Measurement of the Properties of Liquid-scintillator Neutron Detectors at MAX-lab. Master's thesis, Lund University, Lund, Sweden, 2005.

[166] Martin Karlsson. Absolute efficiency calibration of a NE-213 liquid scintillator using a 252-Cf source. Master's thesis, Lund University, Lund, Sweden, 1997.

[167] J. R. M. Annand et al. First In Beam Measurements with the MkIII Helium Active Target at MAX-lab, Lund Status Report, Oct. 2008.

[168] LUKE S. MYERS. *DEUTERON COMPTON SCATTERING BELOW PION THRESHOLD*. PhD thesis, University of Illinois at Urbana-Champaign, Illinois, USA, 2010.

[169] GE Intelligent Platforms. 616 VMEbus to PCI Bus Adapter Manual, 2010.

[170] M. Lundin. MAX-lab Activity Report 2005-06, 2005-06.

[171] I. Antcheva et al. ROOT - A C++ framework for petabyte data storage, statistical analysis and visualization. *Computer Physics Communications*, 180(12):2499 – 2512, 2009.

[172] CAEN. Technical Information Manual, V1190 A/B, VX1190 A/B, Feb. 2010.

[173] J. R. M. Annand. A fast module for pulse shape analysis. *Nuclear Instruments and Methods in Physics Research Section A: Accelerators, Spectrometers, Detectors and Associated Equipment*, 262(2-3):371 – 377, 1987.

[174] J. R. M. Annand et al. The MkIII Helium Active Target at MAX-lab, Lund Status Report, Sep. 2009.

[175] European Organization for Nuclear Research (CERN). http://public.web.cern.ch, 2011.

[176] S. Agostinelli et al. Geant4 - A simulation toolkit. *Nuclear Instruments and Methods in Physics Research Section A: Accelerators, Spectrometers, Detectors and Associated Equipment*, 506(3):250 – 303, 2003.

[177] J. Allison et al. Geant4 developments and applications. *Nuclear Science, IEEE Transactions on*, 53(1):270 –278, Feb. 2006.

[178] Fastrad Radiation 3D CAD V3 Software. http://www.trad.fr, 2011.

[179] Extensible Markup Language (XML). http://www.w3.org, 2011.

[180] M. Constantin, D. E. Constantin, P. J. Keall, A. Narula, M. Svatos, and J. Perl. Linking computer-aided design (CAD) to Geant4-based Monte Carlo simulations for precise implementation of complex treatment head geometries. *Physics in Medicine and Biology*, 55(8):N211, 2010.

[181] E. Alvarado. Geant4 optical photon processes forum, entry 9 Oct. 2009. Geant4 optical photon processes forum (Link), Oct. 2009.

[182] National Institute of Standards and Technology. http://www.nist.gov, 2012.

[183] Y. M. Chan and A. Dalgarno. The refractive index of helium. *Proceedings of the Physical Society*, 85(2):227, 1965.

[184] Agilent Technologies. Cary 300 UV-Visible Spectrophotometer. http://www.chem.agilent.com, 2012.

[185] Eljen Technology. EJ-510 Refelctive Paint for Plastic and Crystals. http://www.eljentechnology.com, 2013.

[186] UQG Optics. B270 Superwite. http://www.uqgoptics.com, 2013.

[187] Heraeus Quarzglas. Glass for Optics, Data and Properties. http://optics.heraeus-quarzglas.com, 2013.

[188] Geant4 Collaboration. Geant4 User's Guide for Application Developers Manual. Version: geant4 9.5.0(350), Dec. 2011.

[189] P. Colin, A. Chukanov, V. Grebenyuk, D. Naumov, P. Ndlec, Y. Nefedov, A. Onofre, S. Porokhovoi, B. Sabirov, and L. Tkatchev. Measurement of air and nitrogen fluorescence light yields induced by electron beam for uhecr experiments. *Astroparticle Physics*, 27(5):317 – 325, 2007.

[190] A. Levin and C. Moisan. A More Physical Approach to Model the Surface Treatment of Scintillation Counters and its Implementation into DETECT.,TRIUMF Preprint TRI-PP-96-64. Oct. 1996.

[191] GEANT Detector Description and Simulation Tool. Application Software Group. Computing and Networks Division, CERN:PHYS260–6 tp 260–7., 1993.

[192] Geant4 Collaboration. Physics Reference Manual. Version: geant4 9.4(539), Dec. 2010.

[193] S. Chauvie, S. Guatelli, V. Ivanchenko, F. Longo, A. Mantero, B. Mascialino, P. Nieminen, L. Pandola, S. Parlati, L. Peralta, M. G. Pia, M. Piergentili, P. Rodrigues, S. Saliceti, and A. Tnndade. Geant4 low energy electromagnetic physics. In *Nuclear Science Symposium Conference Record, 2004 IEEE*, volume 3, pages 1881 –1885 Vol. 3, Oct. 2004.

[194] S. Guatelli, D. Cutajar, B. Oborn, and A. B. Rosenfeld. Introduction to the Geant4 Simulation toolkit. *AIP Conference Proceedings*, 1345(1):303–322, 2011.

[195] Geant4. http://geant4.cern.ch, 2012.

[196] M. V. Kossov. Approximation of photonuclear interaction cross-sections. *The European Physical Journal A - Hadrons and Nuclei*, 14:377–392, 2002. 10.1140/epja/i2002-10008-x.

[197] Yu. M. Arkatov, P. I. Vatset, V. I. Voloshchuk, V. N. Gur'ev, V. A. Zolenko, and I. M. Prokhorets. SEARCH FOR 2+ STATES IN HE-4 BY PHOTODISINTEGRATION METHOD. *Yad.Fiz.31(1980)297, Data retrieved from EXFOR E1234.002*, 1980.

[198] J. Arends, J. Eyink, A. Hegerath, K.G. Hilger, B. Mecking, et al. MEASUREMENT OF TOTAL PHOTONUCLEAR CROSS-SECTIONS IN THE DELTA RESONANCE REGION. *Phys.Lett.*, 98B:423–426, 1981.

[199] M. MacCormick, G. Audit, N. d'Hose, L. Ghedira, V. Isbert, S. Kerhoas, L. Y. Murphy, G. Tamas, P. A. Wallace, S. Altieri, A. Braghieri, P. Pedroni, T. Pinelli, J. Ahrens, R. Beck, J. R. M. Annand, R. A. Crawford, J. D. Kellie, I. J. D. MacGregor, B. Dolbilkin, and A. Zabrodin. Total photoabsorption cross sections for ^{1}H, ^{2}H, and ^{3}He from 200 to 800 MeV. *Phys. Rev. C*, 53:41–49, Jan. 1996.

[200] Donald [GB/GB]; BNFL Instruments Limited Pelham House Calderbridge Cumria CA20 1DB GUNN, Richard. IMPROVEMENTS IN AND RELATING TO MONITORING EMISSIONS. *World Intellectual Property Organization*, Nov. 1999.

[201] S. Quaglioni, W. Leidemann, G. Orlandini, N. Barnea, and V. D. Efros. Two-body photodisintegration of ^{4}He with full final state interaction. *Phys. Rev. C*, 69:044002, Apr. 2004.

[202] ROOT A C++ framework for petabyte data storage, statistical analysis and visualization. http://root.cern.ch, 2013.

[203] J. F. Ziegler, M. D. Ziegler, and J. P. Biersack. SRIM – The stopping and range of ions in matter (2010). *Nuclear Instruments and Methods in Physics Research Section B: Beam Interactions with Materials and Atoms*, 268(1112):1818 – 1823, 2010.

[204] J. R. M. Annand et al. A Helium Gas-Scintillator Active Target for Photoreaction Measurements,In press., 2013.

[205] R. Spohr and K. Bethge. *Ion Tracks and Microtechnology: Principles and Applications*. Informatica International, Incorporated, 1990.

[206] M. Morháč. Processing and visualization functions. *Institude of Physics, Slovak Academy of Sciences, Bratislava, Slovakia*.

[207] M. Morháč, J. Kliman, V. Matousek, and I. Turzo. Background methods for multidimensional gamma-ray spectra. *Nuclear Instruments and Methods*, 401:113 – 132, 1997.

[208] C. G. Ryan et al. SNIP, a statistics-sensitive background treatment for the quantitative analysis of PIXE spectra in geoscience applications. *Nuclear Instruments and Methods*, 214:431–434, 1988.

[209] Jason Brudvik. Private communication, 2012.

[210] John R. M. Annand. Private communication, 2012.

[211] Luke Myers. Private communication, Aug. 2012.

[212] R. O. Owens. Statistical treatment of tagged photon experiments. *Nuclear Instruments and Methods in Physics Research Section A: Accelerators, Spectrometers, Detectors and Associated Equipment*, 288(23):574 – 584, 1990.

[213] Kevin Fissum. Private communication, Aug. 2012.

[214] B. Schröder. Comment on the correction for stolen trues in the case of single hit TDCs, MAX-lab, Lund University, Lund, Sweden. Oct. 2012.

[215] L. S. Myers, G. Feldman, K. G. Fissum, M. A. Kovash, A. M. Nathan, R. E. Pywell, L. Isaksson, and B. Schröder. Monte Carlo Simulation of the Photon-Tagger Focal-Plane Electronics at the MAX IV Laboratory, In press. 2013.